Progressive deformation, fluid flow and water-rock interaction in the Mexican Fold-Thrust Belt, Central Mexico

A DISSERTATION
SUBMITTED TO THE FACULTY OF THE GRADUATE SCHOOL
OF THE UNIVERSITY OF MINNESOTA
BY

Elisa Fitz-Díaz

IN PARTIAL FULFILLMENT OF THE REQUIREMENTS
FOR THE DEGREE OF
DOCTOR OF PHILOSOPHY

Peter Hudleston, Adviser

November, 2010

Acknowledgments

This thesis would not have been possible without the support of many institutions and people. I would like to thank in the first place my country, which through Conacyt (the Mexican Council of Science and Technology) sponsored the first three years of my PhD program. I also sincerely thank the National University Autonomous of Mexico and the University of Minnesota for funding my thesis research. I also deeply appreciate the support received from other institutions, including the Saint Louis University, the University of Arizona and the University of Lausanne, which allowed me the use of their facilities at special rates and provided me with a significant professional and personal experience.

I have no words to express how thankful I am to my advisor Peter Hudleston, from whom I have received the best guidance and support that a student can possibly have. This thesis might not reflect how much I have learned from him through these five years, not only in science but also from his excellent human quality. In the same way, I am very thankful to Gustavo Tolson for encouraging me to pursue this degree at the UMN and for his enormous support, without which it truly would not have been possible to complete this work.

I sincerely appreciate the support and feedback from Christian Teyssier, Karen Kleinspehn, and Emi Ito, the members of my evaluation committee, in every step of my degree completion. I am particularly in debt to Christian, not only for sharing with me some of his vast knowledge but also for his suggestions and encouragement to do analytical work abroad, and for putting me in contact with some of his collaborators.

Thanks to my brothers and sister in the field for making this project a beautiful adventure that I will ever remember with a big smile. Thanks Berlaine, Daniel and Alberto. Thanks also to Elena, Maria Fernanda, Antoni, Carlos and Yang, who also importantly contributed during the field work campaigns.

The geochemical and geochronological data presented in this thesis would not have been possible without the support of David Kirschner, Teresa Pi, Antoni Camprubi, Luc Siebenaller, Annia Fayon, Peter Reiners, Stefan Nicolescu, Victor Valencia, Jesús Solé, Torsten Vennemann, Consuelo Macias and Juan Pablo Bernal.

To the STAMP group, especially to Donna Whitney for sharing with me her opinions on some aspects of my thesis, and to the rest of the STAMP gang for always being supportive.

I can't tell how much I thank my parents Lucía and Miguel, to my brothers, and especially my partner in life, Carlos, for their love and unconditional support through all these years. I dedicate this effort to my grandmother Jovita Fitz, who taught me the happiness of satisfying curiosity and thank my uncle Mere for showing me the beauty of Earth Sciences.

I also thank my family in Minneapolis, my friends from the beginning (Bronie, Ioana, Ioan, Leo, Gilles, Donald, Rodolfo, Lucia, Pablito, Gaby and super Sharon), to the ones in the middle of the way (Yang and Erkan) and to the recent ones (Paola, Sara, Matt and Jen) for making my life through these five years fun and interesting.

Dedication

With hope, I dedicate this work to México and to my beloved people there.

Abstract

An integrated study of the Mexican Fold-Thrust Belt (MFTB) in central Mexico provides information on the evolution of the belt and the processes operating to produce structures and fabrics. Key questions addressed concern to the role of lithology in controlling the style of deformation, the role of fluids in facilitating deformation and the timing and sequence of structural development. Overall, the MFTB is thin-skinned and has properties consistent with the critical tapered wedge model of fold-thrust-belt development: there is a decrease in thickness, intensity of deformation and temperature of deformation towards the toe. Critical wedge theory, however, does not explain how deformation accumulates in the rocks within the wedge. In the MFTB, the deformation mechanisms that operate in different segments of the cross-section are strongly controlled by lithology. The dominant rocks in the sedimentary cover are Cretaceous carbonates that vary in facies laterally, with two large carbonate platforms flanked by more thinly bedded basinal carbonates. Kilometer scale thrusts dominate deformation in the platform carbonates (a more brittle behavior), and mesoscopic buckle folds and associated cleavage dominate deformation in the basinal carbonates (a more ductile behavior). Two phases of deformation are recognized, the first, D1 being more intense than the second, D2. The difference in facies distribution is the main reason for the difference between the MFTB and the fold-thrust belt in the southern Canadian Rocky Mountains, which is characterized by large thrust sheets and relatively few buckle folds.

Structural observations on the mesoscopic scale allow distinguishing veins (dominantly calcite) of several generations, emplaced early, during and late/after deformation (V1, V2 and V3 respectively). Analysis of $\delta^{13}C$ and $\delta^{18}O$ in calcite from veins and host-rock shows that the veins confined within thrust slices are isotopically buffered by the host rock and differ in isotopic composition from veins emplaced along major thrusts or cross cutting thrust-slices. The extent of isotopic buffering seems to be controlled by the amount and composition of the fluid interacting with the carbonate sequences rather than by the temperature, which varies between 100 to 300°C along the cross-section. Analysis of δD in water extracted from fluid inclusions trapped in the veins and in clay minerals strongly suggests rock interaction with meteoric fluids in the west (hinterland) and with fluids close to SMOW in the east (foreland) side of the cross-section. The influence of meteoric water was also more important late during D1 than in the early stages of deformation.

Stratigraphic constraints indicate that D1 started about 90 Ma on the western side of the MFTB in central Mexico and finished about 65Ma towards the east. Stratigraphic and structural observations in the foreland indicate that D2 took place after 65Ma. K/Ar ages of illite separated from layers of bentonite intensively sheared during folding of D1 lie between 84-77 Ma for one locality and between 64 and 71 in a second locality. Outcrop scale variations in age indicates that illite transformation and the closure of its K/Ar isotopic system are not only controlled by temperature but also by strain around the folds. The data suggest that it took about 5 to 7 Ma to develop individual folds, and this occurred within the time range constrained by stratigraphy. U-Th/He thermochronological ages determined in 21 zircon grains are overall consistent with stratigraphic ages and K/Ar ages.

Table of Contents

List of Tables

List of Figures

List of Appendices

Chapter 1

Introduction

The most spectacular mountain ranges on the Earth's surface are the result of continental involvement in plate consumption at convergent tectonic boundaries (Dewey and Horsfield, 1970). They are the topographical expression of mobile belts or orogenic belts, which consist classically of two zones: an internal zone (orogenic core, close to the plate boundary) affecting the entire crust, in which magmatism, metamorphism, ductile deformation, and erosion are common geological processes; and an external zone (foreland side) that involves the upper crust, where more brittle deformation, erosion and sedimentation take place (Dickinson, 1971). Fold-thrust belts are typically observed in the external parts of collisional orogens, such as in the Himalayas, or on the foreland side of subduction-related orogenic belts (Roeder, 1983), such as the Andes. Fold-thrust belts are common from Proterozoic times onwards, but could have formed also during the Archaean according to Lacroix and Sawyer (1995).

Fold-thrust belts are important features in many regards. Loading of the crust by growing fold-thrust belts produces foreland sedimentary basins, in which not only sediment but also organic matter accumulates, to be transformed into hydrocarbons upon burial and heating. These hydrocarbons are frequently trapped in the folds and thrusts within the belts. The process of simultaneous evolution of structures and sedimentary basins has been nicely illustrated in a number of recent models, such as the one by Stockmal *et al.* (2007).

According to Roeder (1983), there are two styles of deformation experienced by fold-thrust belts during continental contraction: **thin-skinned** and **thick-skinned**, which can occur either at different times or at different locations during orogenic development. The **thin-skinned** style is characterized by a stack of thrust sheets developed in non- or weakly metamorphic sedimentary rocks and formed above a sole thrust or detachment zone, which is normally localized along horizons of rocks mechanically weak near or at the cover-basement interface (Pfiffner, 2006). The **thick-skinned** style occurs when high angle reverse faults cut across the entire upper crust, and possibly also the lower crust, and thus both

basement and cover are involved in the deformation. The associated overall continental contraction is apparently less than that occurring in thin-skinned tectonics and the ensuing deformation might be characterized by warping of the basement-cover interface (Pfiffner, 2006). The classic example of thick-skinned tectonics is the Wyoming Foreland (Laramide) Province in the U.S (Eardley, 1963), while excellent examples of thin-skinned tectonics are those of the Canadian Rocky Mountains (Price, 1981) and the Sevier fold-thrust belt in the U.S. (Armstrong, 1968; Yonkee, 1982).

Mechanical models to explain the evolution of thin-skinned fold-thrust belts started with the classical work on the mechanics of thrusting by Hubbert and Rubey (1959), who invoked high pore fluid pressure to reduce friction along a thrust surface upon which a rectangular porous thrust block might be moved. Deformation within the rectangular block was not considered. The first mechanical model that attempted to explain the overall evolution of fold-thrust belts as distinct from the movement of individual thrust blocks was proposed by Chapple (1978), who took the fold-thrust belt to be represented by a perfectly plastic wedge, tapering towards the foreland and underlain by a weak basal layer. What is generally considered the first fully developed orogenic wedge theory is that proposed by Davis *et al.* (1983), who took the wedge concept from Chapple and applied it to a Coulomb material, modified to include the effect of pore pressure. These authors demonstrated the applicability of their approach to real fold-thrust examples. Improvements and refinements to the Davis *et al.* (1983) model have been made by the same authors in subsequent years, allowing for cohesion in the wedge and addition or removal of material at the upper and lower boundaries to simulate deposition/underplating and erosion (Dahlen *et al.*, 1984 and 1989; Dahlen, 1984 and 1990), keeping the central notion that a thrust belt develops with a taper that depends on the internal strength of the wedge material and friction along the base. Some predictions and considerations of this model are: 1) the wedge maintains the same shape as it grows – it is self similar; 2) deformation propagates from the rear towards the front of the wedge; 3) therefore, deformation is greatest towards the back of the wedge; 4) the rocks within the

wedge are everywhere at the point of failure during wedge development; 5) the thermal structure within the wedge is controlled by the geothermal gradient, the isotherms are only slightly modified by the deformation within the wedge; 6) the effect of temperature on deformation depends on the path that the rocks follow within the wedge during its growth and also on the distribution of the isotherms; 7) pore fluid pressure is an important factor in the wedges mechanics by reducing the value of the mean stress in the rocks within the wedge and along the detachment.

The important role that fluids play in the deformation of orogenic wedges was first recognized by Hubbert and Rubey (1959), and this role is also acknowledged by Davis and his co-workers, starting with Davis *et al*. (1983). The key role of fluids was also recognized by Elliott (1976) who considered the various deformation mechanisms operating in the motion of thrust sheets. Elliott applied his theory to explain thrust sheet emplacement in the southern Canadian Rocky Mountains.

In parallel with the theoretical developments on thrust belt mechanics have been developments on the geometry and kinematics of thrust belt emplacement, based on field observations of thrusts and folds. One of the earliest attempts to explain the kinematics of the Cumberland Thrust (in the foreland of the Appalachians) based on its geometrical characteristics was made by Rich (1934), who developed the concept of what is now referred to as fold-bend fold. Other key contributions were made by Dahlstrom (1969, 1970), with subsequent contributions by a large number of authors (e.g. Price, 1981; Boyer & Elliott, 1982; Suppe, 1983; McClay, 1992). Both the kinematics and mechanics of fold thrust belts have been investigated using physical models (e.g. Smit *et al*., 2003; Dixon, 2004) and numerical modeling (e.g., Stockmal *et al.*, 2007). In this thesis I present the results of an integrated study of the Mexican Fold-Thrust Belt (MFTB) along a cross-section in Central Mexico, in an effort to understand the evolution of the belt and the processes operating at different scales and at different times. The MFTB (Campa-Uranga, 1985) is thin-skinned, developed in

the foreland of the southern termination of the North American Cordilleran Orogenic Belt. This area was chosen because it is possible to observe a full cross-section of the MFTB, well exposed in a relatively narrow area (about 150 km in width). The MFTB has a wedge shape at the large scale, defined by a detachment zone slightly dipping towards the west and an average topographic surface gently sloping towards the east and the Gulf of Mexico coast. The critical taper model of fold–thrust belts provides a useful template for understanding the overall evolution of the MFTB. However, integrating local observations and measurements into a model of the whole fold-thrust belt is not a simple task because of the heterogeneity and anisotropy of the rocks on a wide range of scales. The problem has been tackled by employing a combination of different analytical tools to progressively build a picture, with each tool used to improve the picture and provide information for refining the application of other tools. The tools used include structural analysis, characterization of clays, fluid inclusion analysis, rare earth geochemistry and several geochronological methods. The thesis is divided into chapters that follow the general way in which the project has been tackled and that tracks this refinement in each stage. Each chapter of the thesis summarizes the main conclusions derived from each step in the analysis.

The first part of the research involved gaining an understanding of the large scale picture, and this is synthesized in Chapter 2. In this chapter the full cross-section of the MFTB is considered in light of orogenic wedge theory. To better understand the significance of the structures in the analyzed cross-section, a comparison is made with another section of the North American Cordillera in the southern Canadian Rocky Mountains. The latter cross-section is of similar width to the MFTB and is perhaps the best documented fold-thrust belt anywhere. In particular, the structures in the southern Canadian Rockies are well understood compared to those in the MFTB. Noting the similarities and contrasting the differences between these two cross-sections provides an opportunity to assess the role of stratigraphy in fold-thrust belt development.

More detailed descriptions of the structures and mechanisms of deformation in the MFTB are presented in Chapter 3. Also, in this chapter, a systematic kinematic analysis of mesoscopic scale folds is undertaken. This allows a better comprehension on how deformation is accumulated and propagated within the fold-thrust belt wedge.

Chapter 4 is a synthesis of the techniques used in and results obtained from an analysis of fluid flow and fluid-rock interaction during the deformation of the MFTB. This study involves different tools, including stable isotope geochemistry, clay mineral characterization and fluid inclusion analysis. The structural framework provided by the regional and mesoscopic-scale analysis of structures presented in chapters 2 and 3 is fundamental in designing the sampling strategy used and in arriving at a meaningful interpretation of the results.

In Chapter 5, the preliminary results of applying two techniques for constraining the age of deformation are summarized. The techniques used are K/Ar dating of illite and U-Th/He dating of zircon. The results, together with stratigraphic constraints, provide the basic elements of a spatial-temporal framework for interpreting the progression of deformation, syn-tectonic sedimentation, topographic evolution, and the influence of meteoric fluid on the deformation in the MFTB.

Chapter 2

Comparison of tectonic styles in the Mexican and Canadian Rocky Mountain Fold-Thrust Belt

Elisa Fitz-Díaz, Peter Hudleston and Gustavo Tolson

Geological Society of London, Special Publication on Kinematics and Tectonic Styles of Fold-Thrust Belts, In Press

Despite the fact that most fold-thrust belts around the world share many features, successfully explained by the critical wedge model, the details of their geometric evolution and tectonic style development are poorly understood. In the classic section of the southern Canadian Rocky Mountains the dominant tectonic style consists of imbricate thrust sheets with relatively little internal deformation of the individual slices. In the Mexican Fold and Thrust Belt (Central Mexico), the age of deformation, the overall structural pattern and the total amount of shortening are similar, but the individual thrust sheets exhibit much more internal deformation as manifest by meter-scale buckle folds. One of the differences between these localities is the lateral variation of facies resulting in massive platform limestone separated by thinly-bedded basinal limestone in the Central Mexico section. Strain is concentrated toward the margins between platforms and basins. In Canada, thick platform carbonates form continuous resistant units across the Front Range. Possible reasons for the differences in tectonic style between the two sections include the dominant lithology, distribution of lithologies, taper angle of the tectonic wedges, amount of friction along the basal detachment and the degree of anisotropy of the basin facies rocks.

2.1 Introduction

Fold-thrust belts are common features that developed on the edges of orogenic belts worldwide. Many have been well studied and their characteristic features established (Dahlstrom, 1970; Chapple, 1978; Boyer and Elliott, 1982; Price and Fermor, 1985; McClay, 1992). These features include the classic notions of forward propagation of thrusts, piggyback style, a basal *décollement*, and decreasing intensity of deformation towards the foreland. Most fold-thrust belts are wedge-shaped, and since the mid 1980's, the critical taper model of their development (Davis *et al.*, 1983; Dahlen *et al.*, 1984; Dahlen, 1990) has become generally accepted. Analogue and numerical models have been developed that are able to capture many of the basic features of fold-thrust belts and that are broadly consistent with the critical taper theory (e.g. Huiqi *et al.*, 1992; Stockmal *et al.*, 2007). From early studies it has been clear that most of the large folds in fold-thrust belts are intimately related genetically to the thrusts, and extensive studies of thrust-related folds, in the field and in analogue and numerical models, have established the nature of this relationship (e.g. Dahlstrom, 1969, 1970; Elliott, 1976; Suppe, 1983; McClay 1992; Wilkerson *et al.*, 2002; Spratt *et al.*, 2004).

Despite the many similarities among fold-thrust belts in general, there are significant differences among belts and along strike within individual belts. These reflect, among other things, differences in the strength of the basal detachment and the composition and distribution of the rocks in the fold-thrust wedge. In this contribution we compare basic elements of the structures developed roughly synchronously in two widely separated parts of a single orogenic

belt – the North American Cordillera. The sections we compare are a well-known section across the southern Canadian Rocky Mountains and a new section across the Sierra Madre Oriental in central Mexico. The dimensions of the fold-thrust belts in these two locations are similar, and both sections are dominated by carbonates. The structural style, however, is quite different. We compare structures in the two locations and speculate on what may be responsible for the differences.

2.2 Tectonic setting

The Rocky Mountain Fold-Thrust Belt (RMFTB) is located along the eastern edge of the North American Cordillera. Although it has a physiographic expression that is continuous from Alaska to southern Mexico (Fig. 2-1), it presents changes in width, structural style and age along strike. In southern Canada, the belt has a width between 100-200 km, is thin-skinned and is fold dominated to the north (Thompson, 1979, 1981) and thrust dominated to the south (Price, 1981). In the southwest USA, it widens to more than 1000 km and is divided into two parts: the Sevier and Laramide (Fig. 2-1, Armstrong, 1974). The Sevier fold-thrust belt is thin-skinned and its front is to the west of the Colorado Plateau (Armstrong, 1968; Yonkee, 1992). Its original width is not well known because it has been severely affected by Basin and Range extension in the Neogene. The Laramide province extends eastward of the Sevier fold-thrust belt into the continental interior from central Montana to northern Mexico. It is characterized by basement-involved or thick-skinned structures (Allmendinger *et al.*, 1982; Brewer *et al.*, 1982; Schmidt *et al.*, 1993). It is not clear how the Sevier and Laramide tectonic fronts continue to the south, partly because the traces of Laramide structures are not continuous for long distances along strike and partly because the Sevier structures seem to terminate along the trace of the Mojave-Sonora Megashear (Anderson and Silver, 2005). However, in a broad area in northern Mexico (Fig. 2-1), thin-skinned structures are cut by high angle reverse faults that involve blocks of basement (e.g. San Marcos and La Babia faults, Chávez-Cabello *et al.*, 2007), which suggests the presence of both Sevier and Laramide structural expressions. Farther south, the Sierra Madre Oriental is a clear topographical expression of the Mexican Fold-Thrust Belt (MFTB), a 100-250 km wide thin-skinned fold belt (Campa-Uranga, 1983; Eguiluz *et al.*, 2000). The MFTB extends from northern Mexico, where it is oriented NW-SE and its northern boundary coincides with the Mojave-Sonora Megashear trace, to central and southern Mexico, where it is narrower, changes orientation to N-S, and finally bifurcates, with one branch that continues along the Gulf of Mexico coast and the other that runs into the Morelos Guerrero platform (Fig. 2-1). One significant difference between the MTFB and its northern counterpart is the absence of a comparable continental foreland.

In addition to the striking variations in tectonic style along the North American Cordillera, there is a difference in deformation ages (Fig. 2-1). Detailed studies of plutonism and syn-orogenic basins in western Canada (Evenchick *et al.*, 2007), suggest that deformation started in Late Jurassic and propagated to the east through the Cretaceous. In the western USA, intensive orogenic plutonism has been documented in the Late Jurassic and continued until Late Cretaceous (e. g. Sierra Nevada and Idaho Batholiths, DeCelles, 2004; Giorgis *et al.*, 2008). Stratigraphic-sedimentological studies in syn-tectonic piggyback basins, however, suggest an Albian-Maastrichtian age for the Sevier deformation and a Campanian-Eocene age for Laramide structures (Dickinson *et al.*, 1988; DeCelles *et al.*, 1991; Lawton and Trexler, 1991; DeCelles *et al.*, 1995). In central Mexico, the age of syn-tectonic turbidites indicates a Middle Turonian-Santonian age for the western boundary of the MFTB (Hernández-Jauregui, 1997) and Paleocene to Early Eocene age for the frontal structures (López-Oliva *et al.*, 1998; López-Ramos, 1983). Absolute ages of deformation by Ar/Ar dating of illite extracted from fault gouge in different major thrusts in the RMFTB in Canada (Van der Pluijm *et al.*, 2006), Montana, USA (Solum and Van der Pluijm, 2007) and in the MFTB in central Mexico (Gray *et al.*, 2001), suggest that deformation along the front of the thin-skinned fold thrust belts from Canada to Mexico occurred between Maastrichtian and Early Eocene. Therefore, although there is no apparent physical continuity between the Sevier and MFTB fronts, their ages of deformation are contemporaneous and they were active until the Early Cenozoic. This is perhaps expected from the fact that subduction occurred continuously along the western margin of the continent during Mesozoic and early to mid Tertiary times (Scotese and Golonka, 1992). The subduction picture, however, is complicated by the presence of accreted terranes along the western margin of the continent, reflecting arc-parallel displacements during the Mesozoic of portions of crust now constituting the hinterland to the fold-thrust belt (e. g. Evenchick *et al.*, 2007).

Detailed field observations of the MFTB in central Mexico have been made and the results synthesized in a geologic map and cross section A-A'(Fig. 2-2), and we compare the structures displayed in this cross section with those of the classical cross section of the RMFTB in southern Canada (Fig. 2-3). The latter was chosen because of its similarity to the one in Mexico in width, amount of accommodated shortening, lithology (dominated by carbonates), and because they are both part of the same extensive orogenic belt and formed at least in part at the same time. It was also chosen because of the striking contrast in tectonic style. One important difference is the nature of the carbonates involved in the deformation. In Mexico they are Cretaceous in age with large lateral variations in facies over relatively short distances, while in Canada, they are

Paleozoic with a smooth westward transition from shallow to deeper water facies in the section studied, although elsewhere along-strike facies changes from platform to shaly facies occur (e.g. Spratt *et al.*, 2004, Fig. 2-4).

2.3 Mexican Fold-Thrust Belt (MFTB) in Central Mexico

The cross section of the MFTB in central Mexico is well exposed and the surface geology has been quite well studied (Imlay, 1944; Suter, 1980, 1984, 1987; Contreras and Suter, 1990; Carrillo-Martinez 1989, 1990, 1997; Carrillo-Martínez *et al,.* 2001) (see the map in Fig. 2-2 and cross section in Fig. 2-4a). Except for two borehole records close to the line of cross section, no sub-surface information is available in this area.

The fold and thrust structures displayed in this cross section define a body of deformed rocks that is wedge shape, tapers to the east, and involves mostly Mesozoic units that are dominated by Cretaceous carbonates. One particularity of these carbonates in central Mexico is the abrupt lateral change from thick platform facies (delineating El Doctor and Valles-San Luís Potosí platforms) to thinner basinal facies (Zimapán and Tampico-Misantla Basins). The platforms and basins are clearly defined on the geological map (Fig. 2-2) and cross section (Fig. 2-4a). A possible modern analogue would be the Bahamas carbonate platform and surrounding basins. The stratigraphic range of the units containing the carbonate banks extends from Neocomian to Cenomanian. In the Tampico Misantla Basin (on the eastern side of the cross section) these rocks have a thickness of about 600 m and lie on top of Jurassic red beds (200-500 m thick). To the south these red beds rest on a Paleozoic volcanic arc related sequence (Rosales-Lagarde *et al.*, 2005) and in some areas, according to borehole records, directly on Grenville age granulite gneisses (Eguiluz *et al.*, 2000). Lack of borehole data in the area and the considerable thickness of the Valles-San Luís Potosí Platform rocks, with an original thickness of more than 2 km, duplicated by thrusting, means it is not possible to determine what happens to the pre-Cretaceous units to the west. Pre-Cretaceous rocks do reappear on the western edge of the cross section (Fig. 2-4a), but they are very different in character to those exposed or inferred to the east. They have been interpreted to be a siliciclastic Permo-Triassic mélange overlain by Early Cretaceous marine volcaniclastic strata that are in turn overlain by Albian-Aptian deep-water carbonates (debris flow and talus facies). These units together constitute the Tolimán Sequences (Figs. 2-2 and 2-4a). They are separated from the Cretaceous carbonates to the east by the Higuerillas Thrust (HT in Figs. 2-2 and 2-4a).

Within the Tolimán Sequences, the siliciclastic mélange possesses a fabric that predates the deformation associated with the MFTB. The two overlying Cretaceous units show more complex deformation than Cretaceous rocks east of the Higuerillas Thrust. They are strongly deformed, and are affected by at least two generations of folds: isoclinal folds refolded into asymmetrical open folds generally verging to the east. These folds are severely affected by later faults. The contact between the lower unit and the mélange is strongly sheared, and that between the upper and lower units weakly sheared.

A possible reconstruction of carbonate facies distribution in the area suggests that the Higuerillas Thrust accommodates a stratigraphic separation on the order of 3 kilometers, the largest such associated with a thrust along the entire cross section. Just east of this thrust, El Doctor Platform is mostly cut by thrusts with kilometer scale displacements (see Fig. 2-4a) and large-scale related folds, although there is also evidence of smaller scale internal deformation in the form of abundant tectonic stylolites and veins within the thrust slices. Because the rocks of the Tolimán Sequences are different in facies and show evidence of a more complex tectonic history than rocks to the east, the western boundary of the MFTB for the purpose of this study is taken as the Higuerillas Thrust, which thus is taken to separate foreland from hinterland.

To the east of El Doctor Platform, the rocks in the Zimapán Basin have been shortened by kilometer scale thrusting close to the contact with El Doctor Platform (Fig. 2-5a). The individual thrust slices, however, show very strong internal deformation (Fig. 2-5b). In thinly bedded limestone layers, this is in the form of meter scale tight folds (Figs. 2-5 c and d) and in the shaly layers, in addition to open folds, a pervasive axial plane pressure-solution cleavage is also observed (Fig. 2-5e). Tight mesoscopic folds with eastward vergence and associated cleavage are present all across the Zimapán Basin, with a diminishing of thrusting eastward (Fig. 2-4a).

Structures in the Valles-San Luís Potosí Platform, which is cut by several kilometer scale thrusts, are similar to those in El Doctor Platform (Fig. 2-5a); although a major difference is a striking decrease in the intensity of tectonic stylolites and veins at the mesoscopic scale.

At the eastern edge of the fold-thrust belt, in the Tampico-Misantla Basin, deformation is mostly accommodated by folds of chevron style (Fig. 2-6a). These folds are tight close to the boundary with the Valles-San Luís Potosí Platform, and become progressively more open towards the front of the belt. Most deformation here is accommodated by east verging folding and bedding-parallel slip with internal deformation mostly in fold hinges, with little variation in layer thickness from limb to limb (Figs. 2-6b-d). Axial planes are mostly steep across the basin (Figs.

2-2i and 2-4a), but as the basal detachment zone is approached, they decrease in dip. The detachment zone is in a Late Jurassic carbonaceous horizon and is well exposed along a broad area (see map in Fig. 2-2). It separates folded Cretaceous carbonates above from slightly tilted Jurassic red beds below.

Near the western boundary of the Tampico-Misantla Basin the thrusts dip more steeply than they do to the east and appear to postdate folding, as suggested by thrusts cutting attenuated fore-limbs of folds, although no examples were observed in the field. Some of the thrusts could be coeval with the folds. The same is also true for the Zimapán Basin, and is different to what is observed in the platforms. In general, the large-displacement thrusts along the cross section are located in the interiors of the two platforms or at their eastern boundaries, where they produce stratigraphic offsets on the order of hundreds of meters. This, together with field observations and fold analyses, suggests that most of the shortening in the basins is accommodated by folding. The geometrical features described above are consistent with what is observed in cross sections to the north and to the south of the area (Eguiluz *et al.*, 2000), which have borehole records to provide control at depth.

Shortening within the wedge across the two Cretaceous platforms was determined by three methods, using 1) length of the base or top of the massive carbonate unit (see Fig. 2-6a), 2) comparing total widths of the platform in the unrestored, restored and palinspastically restored states, and 3) using the area occupied by the carbonate unit in the unrestored and restored states, assuming that both bed length and thickness (and thus area) are preserved and that all deformation is in the plane of the section. In the third method, the original thickness of the unit is known from measurements in the field and in boreholes. This method is one of several described by Hossack (1979). These result in average estimates of shortening of about 55% (corresponding to 20 km of shortening in the cross section) for El Doctor Platform and about 35% (~ 23 km) for the Valles-San Luís Potosí Platform. The latter is less than the value of 42% reported by Suter (1987) and Contreras and Suter (1990) for exactly the same cross section. The difference reflects the conservative way in which the cross section has been constructed.

To determine shortening in the basins, we analyzed trains of at least 5 single layer buckle folds of mesoscopic scale in the same stratigraphic unit (Tamaulipas Fm., Fig. 2-6c and 2-7b). We characterized the geometry of such folds in outcrop and calculated the minimum shortening by using the chord method. The chord method (Fig. 2-7b) was only applied to buckle folds in rocks that did not show significant internal deformation, such as chert layers (Fig. 2-5c). Folds

were analyzed in 10 outcrops in the Zimapán Basin, mostly on the eastern side (and the values obtained were extrapolated to the whole basin), and 14 outcrops in the Tampico-Misantla Basin, covering the whole width. Shortening (of 60-65%, at least 49 km) at the level of the Tamaulipas appears to be fairly uniformly distributed across the Zimapán Basin and to decrease (from 70 to 20%, with an average of 40%, about 30 km) eastwards across the Tampico-Misantla Basin (Fig. 2-4a). Offsets on thrusts and local anomalous thickening give rough estimates of shortening due to thrusting in the two basins of 10% and 5%. These are added to the shortening estimates due to folding to arrive at the values of 70% and 45% for total shortening across the Zimapán and Tampico-Misantla basins, respectively.

The limited stratigraphic range and thickness of strata of the rocks exposed across the full length of the cross section indicate that the wedge must have been thin and must have had a relatively low taper angle, which is consistent with the 2-2.5° dip westward of the detachment zone exposed near the east side of the cross section. However, we do not have direct evidence of the position of the basement or the basal décollement to the west of the cross section.

The current average topographic slope along cross section A-A' (Fig. 2-4a) dips from 1 to 1.3° to the east. An inferred paleo-topographic slope based on the reconstruction of structures varies from 3.0-3.8° to the east (Fig. 2-4a). This is consistent with burial conditions in the Zimapán Basin, interpreted from temperature of deformation (about 180°C) in this basin and towards the front of the cross section A-A' (about 70°C), determined with illite crystallinity analysis and considering a range of geothermal gradients from 23-30°C (Fig. 2-4a).

2.4 Rocky Mountains Fold-Thrust Belt in Southern Canada (CRMFTB)

Because of the excellent exposure, arguably the best characterized cross section of a fold-thrust belt anywhere is the one that runs sub-parallel to Highway 1 in Alberta and British Columbia, in the southern Canadian Rocky Mountains. We focus our attention on the Front Ranges and eastern edge of the Main Ranges (Figs. 2-3 and 2-4c), although data from the Foothills are also included. Cross section B-B' is based on a great deal of geological and geophysical information. The sedimentary rocks involved in the belt include a broad range of ages from Late Proterozoic to Late Cretaceous (Price, 1981, Price and Fermor, 1985). For the purposes of this paper these units are grouped into five suites. The first is a Proterozoic sequence of feldspathic to arkosic sandstone and argillite (Windermere Supergroup). The second consists of a Paleozoic sequence of shale that is the dominant lithology exposed in the Main Ranges, to

the west of the cross section (Fig. 2-4c). The third suite corresponds to Paleozoic platform and shallow water carbonates that thicken and changes to deep-water facies (shale) westward. This consists of two packages of Early to Late Paleozoic age that are represented separately in the map. These are the dominant lithologies in the Front Ranges (Figs. 2-3 and 2-4c and d). The fourth suite consists of Triassic-Jurassic marine shale, quartz sandstone and limestone. The fifth consists of Late Jurassic-Paleocene marine and non-marine siliciclastic and volcaniclastic deposits, which are dominant in the Foothills. Price (1981) suggested that these different units exert an important control on the nature and orientation of structures within the fold-thrust belt.

In the Foothills, closely spaced listric imbricate thrusts are observed in the Late Cretaceous units, and fault-related folds are also common (MacKay, 1996). Associated with these folds are folds not directly related to faults (probably buckle folds) of variable style and often complex geometry (e.g. MacKay, 1996; Soule and Spratt, 1996; Stockmal *et al.*, 2001). Wells reveal several large gently westward dipping thrust sheets of Paleozoic strata below the east-directed imbricates (Bally *et al.*, 1966). The eastern-most outcrops of the imbricates are marked by a triangle zone (Spratt *et al.*, 1993; Spratt and Lawton, 1996; Stockmal *et al.*, 1996), which is blind to the east of Fig. 2-4c (Slotboom *et al.*, 1996) and better exposed in the Turner Valley structure, just to the south of the section in Fig. 2-4c.

In the Front Ranges (Fig. 2-8a) the imbricate style is maintained, but the thrusts are more widely spaced and are developed in Paleozoic platform carbonates. The structures are well exposed and the thrust slices are dominated by the thicker carbonate units that stand out in the landscape, often giving the superficial impression of homoclinal sequences of undisturbed beds (Fig. 2-8a). Large fault-related folds mark hanging wall or footwall cutoffs and thrust terminations (Fig. 2-8b). There is little internal deformation in most of the platform carbonates, except in the vicinity of faults, where locally some of the units may show intense internal folding, such as in the Middle Cambrian Eldon Fm. limestones in the hanging wall of the McConnell thrust, near Mt. Yamnuska, or in the in the Jura-Cretaceous Kootenay Fm. (interbedded sandstones, shale and coal, Fig. 2-8c) in the footwall of the nearby Rundle Thrust (Cant and Stockmal, 1999).

In the Main Ranges, contemporaneous internal deformation in the Early Paleozoic shale and clastic Proterozoic rocks is widespread and pronounced, with the development of a pervasive cleavage and mesoscopic folds with vergence towards the east, which are more evident than large thrusts. With the exception of the Western Main Ranges, the deformation in cross section B-B'

(Fig. 2-4c) is dominated by thrust slabs, mostly more than 1 km thick in the Front Ranges and less than 1 km thick in the Foothills, stacked to the east.

Shortening in the Front Ranges of cross section B-B' (Fig 4c) was determined by the bed length method (Fig. 2-7a), selecting as the marker horizon the base of the Upper Devonian and vertical pin lines passing through the surface traces of the Fatigue and McConnell thrusts (Fig. 2-7a). The shortening thus derived is 70% (corresponding to about 110 km). The same method was used for the Foothills, above the Paleozoic rocks, using the Cretaceous Cardium Formation as the marker horizon, the trace of the McConnell thrust as the western end point and the eastern tip of the triangle zone as the eastern end (see Fig. 2-4d, the actual section used for the measurements was that of Price and Fermor, 1985). The shortening is about 50% (about 50 km), although it is not uniformly distributed. In the central part of the Foothills, bounded by the traces of the Waiparous and Old Baldy thrusts, shortening is almost 80% (at least 100 km in the studied cross section). Because of the presence of smaller scale thrusts and folds not accounted for in the cross section of Price and Fermor (1985), this estimate of shortening in the Foothills is certainly an underestimate.

An average dip of the detachment zone in the CRMFTB over the section studied is about 3.3° with a minimum dip of 2.5° in the Foothills. The current topographic slope varies between 1.3-1.6° to the east (maximum dip is shown in Fig. 2-4c) and a minimum inferred paleo-topography based on structural reconstructions varies from 3.5-5°. Some structural features of the CRMFTB and the MFTB are compared in Table 2-1.

2.5 Horizontal shortening and wedge geometry

Values of shortening obtained for fold and thrust belts, with significant discontinuities in displacement across faults and little internal deformation between faults, depend on the scale at which the measurements are made. The most meaningful results are obtained when the measurement 'box' is wide compared with the displacements on individual thrusts. The nature of thrust development also means that shortening between two vertical bounding lines may vary with stratigraphic level, typically decreasing with depth, as in-sequence thrusts are added from below (e.g. Lebel *et al.*, 1996). We assume here that shortening measured at an appropriate stratigraphic level is characteristic of the segment under consideration. With the limitations of the methods in mind, the sections in Figure 2-4 show that in general, for both fold and thrust belts, the shortening is greatest towards the hinterland and least towards the foreland. This phenomenon is predicted for critical taper models of subaerial wedges, since erosion in such wedges requires

continued deformation – and thus shortening – throughout the wedge to maintain the critical angle (Davis *et al.*, 1983). Continued displacement on older thrusts that develop in piggy back fashion is consistent with observations in the Front Range of the Canadian Rockies (Price, 2001), and also with finite element simulations of fold-thrust belts by Stockmal *et al.* (2007) and analog models (Dixon and Liu, 1992). In addition to an overall gradient in shortening, Figure 2-4 shows that the total shortening accommodated by the two fold-thrust belts is similar, within the uncertainties of the measurements – about 55% for the MFTB and 65% for the CRFTB. A significant difference between the two is that the stratigraphic section in the MFTB contains two carbonate platforms flanked by more pelitic facies. The shortening of the MFTB Platform carbonates is significantly less (55% and 35%) than the shortening accommodated by the basinal strata (about 70% close to the platform borders) on either side.

It is instructive to compare the overall shortening in the two sections with shortening in an idealized self-similar wedge and with the shortening pattern in finite element models (Stockmal *et al.*, 2007). In an ideal wedge, the percentage of internal shortening for a given amount of displacement between the 'backstop' and the rigid substrate below the wedge is a function of the taper angle (surface slope α plus basal slope β) and the thickness of the section from which the wedge is built. Figure 2-9 shows the ideal total percentage of shortening for three values of wedge taper angle and the dimensionless displacement of the backstop (displacement divided by thickness of the undeformed section). For comparison, the progressive shortening displayed by Models 7 and 8 of Stockmal *et al.* (2007) are also shown. In the Stockmal *et al.* models, for which the Canadian Rockies section shown in Figure 2-4c provided a rough prototype, relative displacements between backstop and sub-wedge crust of 240 km are associated with values of shortening of about 60% for taper angles of about 5.5-6.5° for model 7 and 5.0-5.5° for model 8. The taper angles of the fold-thrust belt in Canada and Mexico have diminished since the cessation of tectonism due to erosion - estimates suggest that about 2 km of strata have been removed at the deformation front in Canada (Nurkowski, 1984), and proportionately more would have been eroded farther back in the wedge. Thus, the current taper angles of about 4.0-5.0° for the CRMFTB and 3.5-4.0° for the MFTB are lower bounds to the values that existed at the time of wedge formation, for which our estimates are 6-8° and 5-7° respectively. One piece of geological evidence that supports the notion that the taper angle was higher for the CRMFTB than for the MFTB is the stratigraphic range of the rocks exposed at the surface in the two belts. In the CRMFTB these rocks are progressively older towards the hinterland whereas in the MFTB the strata exposed at the surface are of a much more restricted stratigraphic range. With a high taper

angle there will be greater uplift and erosion at the back of the wedge, bringing deeper rocks to the surface. The estimates of total shortening and taper angle for the two fold and thrust belts are indicated on Figure 2-9. It should be noted that the displacement of the backstop (on the horizontal axis of the plot) applies just to the segments of the fold and thrust belts for which shortening data was obtained (Doctor platform to the Tampico-Mislantla basin in the case of the MFTB and Front Range and Foothills in the CRMFTB). In other words, the 'backstop' is locally defined within the larger orogenic belt.

In a Coulomb wedge taper is controlled by the angle of internal friction of the wedge material, friction at the base, and pore fluid pressure (Davis *et al.*, 1983). Since the composition of the rocks in the two fold-thrust belts is similar (although the distribution of facies is different), it seems likely that the main reason for the difference in taper angle lies with basal friction: the lower the basal friction, the smaller the taper angle. Although only exposed in the middle of the Valles-San Luís Potosí Platform, there is good reason to believe from borehole data to the north and to the south of the area that (Neocomian) evaporites partially underlie the MFTB wedge and localize the basal detachment (Eguiluz *et al.*, 2000). In the CRMFTB the basal detachment (sole thrust) lies at the basement cover interface under the Main Ranges and Front Ranges and steps up into the Paleozoic section towards the Foothills, climbing further into the Mesozoic section towards the tectonic front. The décollement horizons involved are all in a carbonate/clastic units and will be associated with higher coefficients of friction than the inferred evaporite horizons under the MFTB.

It is instructive to explore what combinations of mechanical properties might satisfy the observed and inferred wedge geometries of the two fold and thrust belts. If we assume Coulomb behavior and a homogeneous wedge, the only properties that affect the taper angle are internal friction within the wedge, basal friction, and pore fluid pressure (Davis *et al.*, 1983) (although cohesion affects the frontal part of the wedge, resulting in a slightly concave upwards profile, Dahlen *et al.*, 1984). The results of applying the wedge model of Dahlen *et al.* (1984), with various combinations of basal friction and internal friction, are shown in Table 2-2, with the combinations that satisfy the geometry of the two fold and thrust belts, given the taper angles inferred from the geology. The range of values of internal friction and basal friction that match the inferred taper angles for the two sections are realistic and consistent with a weaker basal detachment under the MFTB for a fluid pressure ratio of 0.7.

2.6 Major controls on tectonic style

The most striking difference in structural style between the two fold-thrust belts is in the relative partitioning of deformation between displacement on thrust faults and internal deformation of the rock units. In the CRMFTB much of the deformation is accommodated by slip on faults, with a relatively small amount of internal deformation within individual stratigraphic units. In the MFTB much of the deformation is taken up by internal deformation within each stratigraphic unit, accompanied by mesoscale fold and cleavage development, with correspondingly less deformation taken up by displacement on thrusts.

The large-scale folding in the CRMFTB is associated with hanging wall or footwall cutoffs (fault bend folds) and thrust terminations along strike or in the displacement direction (fault-propagation folds or detachment folds). The anisotropy of the layers certainly influenced the growth and geometry of these folds, with bedding-parallel slip a key component of the deformation, but the main factor that controls the location, general shape and orientation of folds is the geometric accommodation required to allow slip on thrust faults. Large-scale folds of this type in the MFTB are restricted to the platforms.

In general the mesoscale folding in the MFTB is not directly associated with thrust faults but reflects a buckling instability of layers of different composition subjected to layer-parallel compression. Intense folding within a stratigraphic unit without much folding of the unit itself, a common phenomenon in the MFTB, suggests what has been referred to by Biot (1965) as internal buckling. This requires the layer in which the folds develop to possess anisotropy, which is the case for a unit made up of alternating layers of differing stiffness or viscosity. This phenomenon has been well documented in experiment and in nature (e.g. Cobbold *et al.*, 1971; Johnson and Fletcher, 1994, ch. 6). The centrifuge models of Dixon (2004) nicely illustrate the difference in behavior of juxtaposed massive units, simulating carbonate platforms, and strongly anisotropic softer units, simulating basinal facies. The massive units fail by thrusting and the anisotropic units by multilayer buckling. The models also show that the presence of platform facies cause partitioning of deformation in the wedge on a large scale, as is indicated for the MFTB in Figure 2-4a, with deformation concentrated in the basinal facies. The normal decrease in deformation towards the toe in a homogenous wedge is changed by the presence of a carbonate platform which may act as a competent ram to concentrate deformation ahead of the platform towards the foreland. This is seen in front of both the Doctor and Valles-San Luís Potosí platforms in the MFTB and in Models MO15 and MO17 of Dixon (2004). Field examples of the lateral transition in structural style from reef facies to shales facies in rocks above a thrust are given by Spratt *et al.*

(2004). This transition is orthogonal to the shortening direction rather than parallel to it as is the case for the MFTB.

All the folds illustrated in figures 5 and 6 are internal to particular stratigraphic units, and many of them can be characterized as either internal buckles or examples of true multilayer buckling (Schmid and Podladchikov, 2006). In some cases deformation becomes localized in fold limbs to produce distinctly asymmetric folds with strong bed thinning (Fig. 2-5c). The fold style is similar to that observed in the intra-unit buckle folds developed in the anisotropic layers in the analog models of Spratt *et al.* (2004). It also appears to be similar to the style observed in Mesozoic strata above blind thrusts in the Foothills in northern Alberta (Gabrielse and Taylor, 1982). The examples of natural folds described by Spratt *et al.* (2004) are long wavelength compared to the intra-unit folds in the basinal formations of the MFTB, and most appear to be fault related, unlike the small-scale folds in the models. Most of the mesoscale folds seen in the MFTB are buckles without ties to specific faults.

There are several possible reasons for the stark difference in structural style of the two fold and thrust belts. First, the presence of two carbonate platforms within the MFTB may have inhibited the development of long thrust slices and the large displacements associated with them. These two stiff platforms would have tended to localize deformation along their margins and inhibited large displacement thrusting. Second, the MFTB does not possess the equivalent of the extensive competent lithological units in the CRMFTB that provided stiffness to the sequence and resistance to internal buckling. In the CRMFTB the carbonates of the Devonian Palliser and Mississippian Rundle Group, sandwiching the shale-dominated Banff Formation, are generally considered to have formed a stiff beam that controlled thrust spacing and major folds (Currie *et al.*, 1962, Spratt *et al.*, 2004). If that was the case, it is unclear why the more anisotropic units in this package and in units above and below it, did not develop meso-scale buckle folds of the kind seen in the MFTB and, allowing for scaling to bed thickness, in the analog models of Dixon (2004) and Spratt *et al.* (2004). Third, the wedge geometry may have had an influence. In thin wedges with low taper angles there is less opportunity for thrust slices with long aspect ratios to develop. This is nicely shown in analog models. For example, in the sandbox models of Huiqi *et al.* (1992), the aspect ratio of the ‘thrust slices’ defined by shear bands in the sand increases with taper angle, which itself increases with basal friction (see Figs. 2-7 and 2-8 in Huiqi *et al.*, 1992). Thus the lower taper angle in the MFTB may have inhibited the development of large thrust sheets. These three factors, either separately or in combination, likely made the MFTB more susceptible to intra-formational deformation than the CRMFTB and the latter more susceptible to

the development of long thrust slices and imbricate thrust faulting with large displacements and little internal deformation.

2.7 Conclusions

Variations among different fold and thrust belts as well as along the strike of individual belts are well documented but, with few exceptions (e.g. Spratt *et al.*2004), the reasons for these differences have not been fully addressed systematically. By comparing and contrasting the style of deformation along two sections of the Rocky Mountain Fold and Thrust Belt we conclude that the broad geometry and structural evolution in both sections agrees with a critical wedge model. The major difference between the two sections is the relative amount of strain accommodated by slip along regional scale thrust faults (Southern Canadian Rocky Mountains) compared with the strain associated with internal deformation within the thrust sheets themselves (Mexican Fold-Thrust Belt).

The variation of internal deformation across the Mexican Fold and Thrust Belt is associated with the spatial distribution of carbonate platforms and intervening basinal sequences resulting in the juxtaposition of massively bedded and thinly bedded limestone packages whose response to shortening is markedly different. The anisotropy of the latter is such that the development of mesoscale buckling instabilities is widespread and shortening is preferentially accommodated by internal folding. The more competent and more massively bedded units apparently favor the development of longer wavelength thrusting instabilities. The relative lack of meso-scale buckle folds in the Southern Canadian Rocky Mountain section, despite the existence of thinly bedded limestone packages that would favor their development, may be due to the shielding effect of an effectively stiff carbonate-dominated unit in the central part of the section.

Whether these differences in tectonic style are related to the taper angle of the critical wedge is unclear, although numerical and analogue modeling suggests that wedges with more taper tend to develop larger thrust sheets, which is in agreement with our observations. Considering a tectonic wedge of a given lithology, friction along the basal décollement is directly related to the taper of the wedge, with higher angles resulting from higher values of basal friction. Thus, thin wedges with low taper angles favor internal deformation of thrust slices while thicker wedges accommodate strain by the imbrication of thrust sheets along regional thrusts with little or no internal deformation.

Figures and Tables

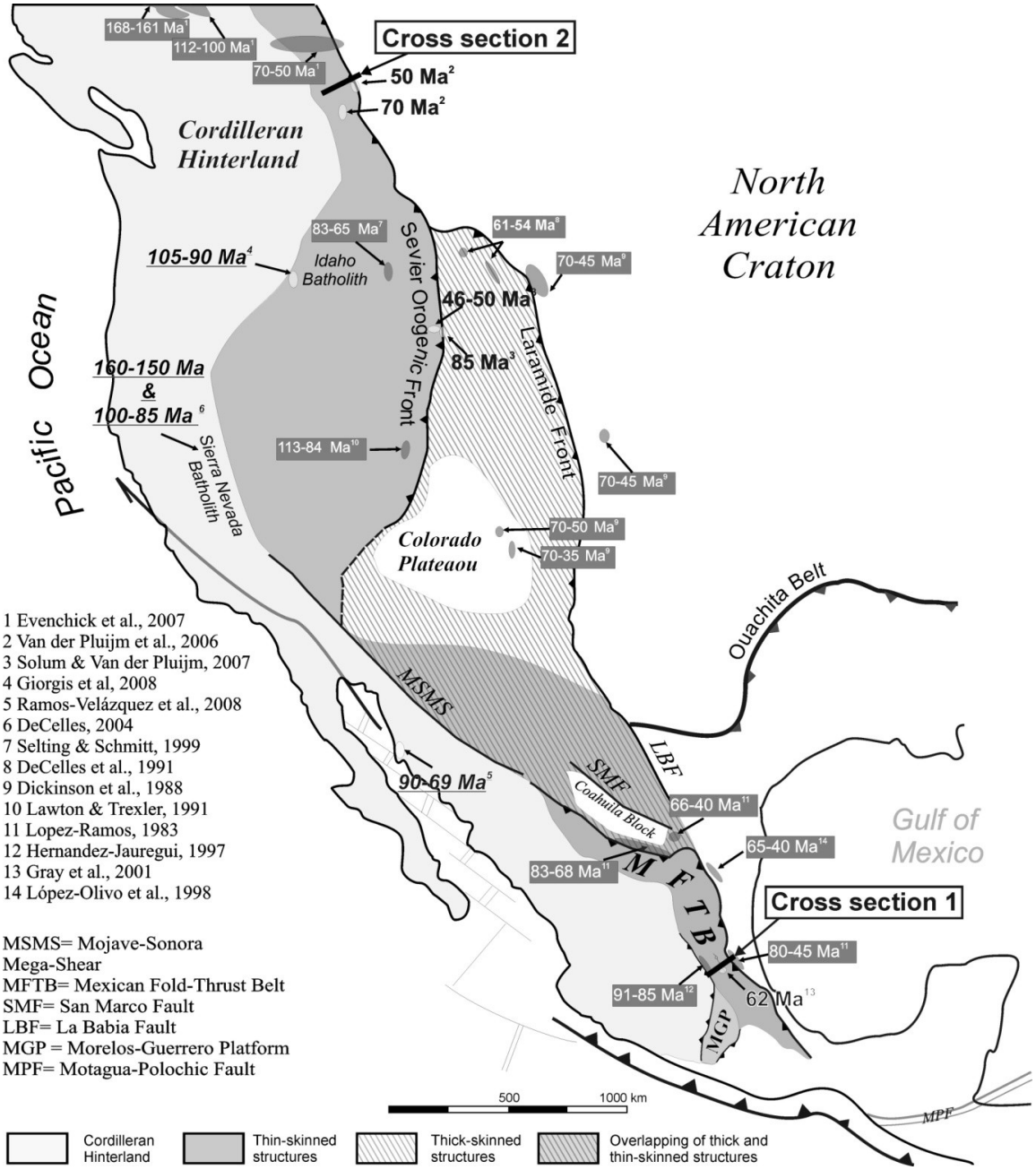

Figure 2-1. Generalized tectonic map of the North American Cordillera showing the differences observed in the fold-thrust belt along its eastern edge, together with ages of syntectonic plutons, basins and absolute ages of deformation (based on various sources as indicated, and Armstrong, 1974; Campa-Uranga, 1983; Anderson and Silver, 2005). The ages in grey boxes correspond to ages of syn-sedimentary basins, determined by means of biostratigraphy; underlined ages correspond to isotopic zircon ages from syn-tectonic intrusive rocks; and bold ages are fault-gouge illite Ar/Ar ages.

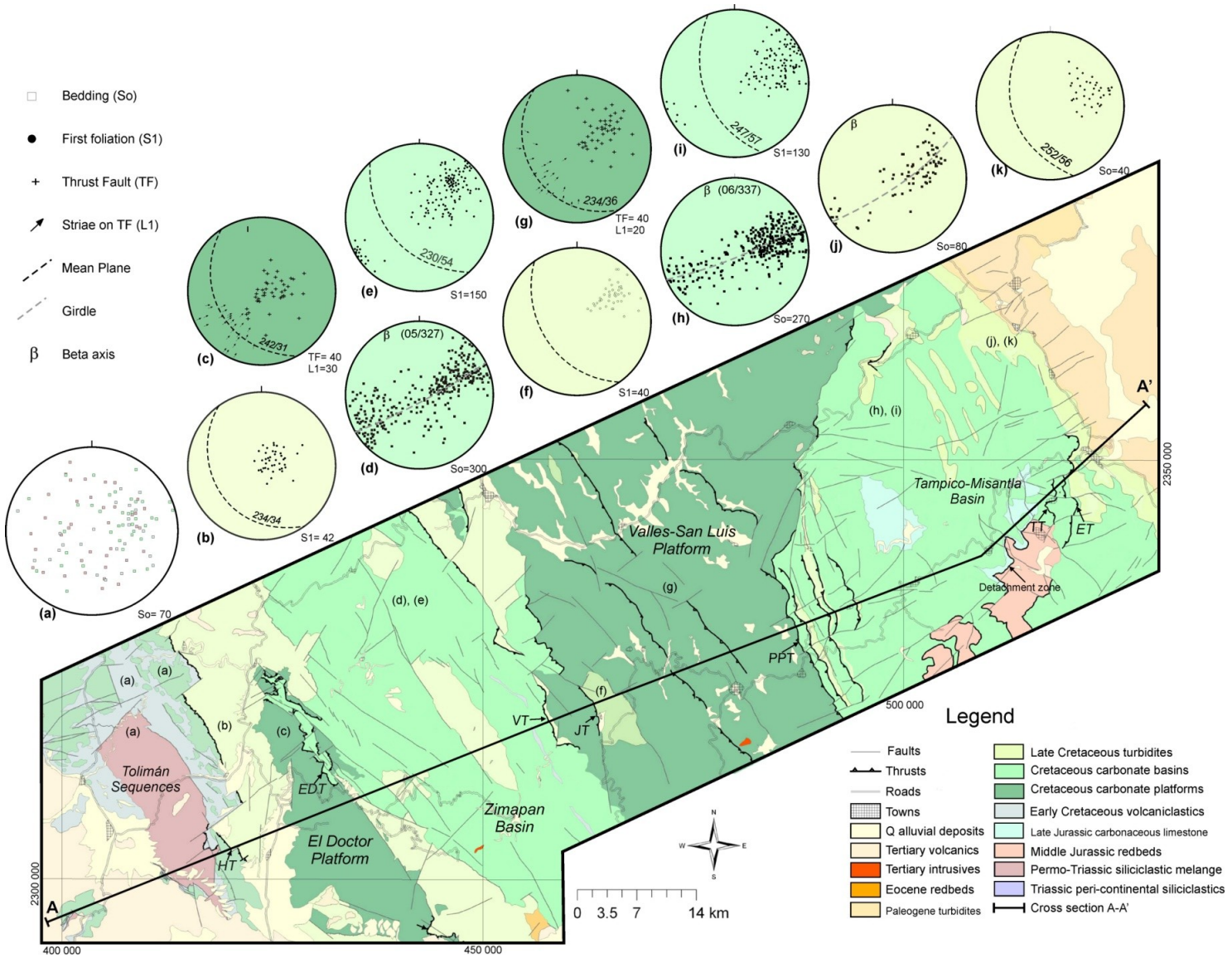
Bedding (So)
First foliation (S1)
Thrust Fault (TF)
Striae on TF (L1)
Mean Plane
Girdle
β Beta axis
(a)
So= 70
(b)
234/34
S1= 42
(c)
242/31
TF= 40
L1=30
(d)
So=300
(e)
230/54
S1=150
(f)
S1=40
(g)
234/36
TF= 40
L1=20
(h)
So=270
(i)
247/57
S1=130
(j)
So=80
(k)
252/56
So=40
Tolimán Sequences
El Doctor Platform
Zimapan Basin
Valles-San Luis Platform
Tampico-Misantla Basin
Detachment zone
EDT
HT
VT
JT
PPT
TT
ET
A
A'
2300 000
2350 000
400 000
450 000
500 000
0 3.5 7 14 km
Legend
Faults
Thrusts
Roads
Towns
Q alluvial deposits
Tertiary volcanics
Tertiary intrusives
Eocene redbeds
Paleogene turbidites
Late Cretaceous turbidites
Cretaceous carbonate basins
Cretaceous carbonate platforms
Early Cretaceous volcaniclastics
Late Jurassic carbonaceous limestone
Middle Jurassic redbeds
Permo-Triassic siliciclastic melange
Triassic peri-continental siliciclastics
Cross section A-A'

Figure 2-2. Simplified geologic map of the area studied in Central Mexico to show the geometry and extent of structures in map view, as well as the location of the cross section in Fig. 2-4a. In the upper part, equal-area lower hemisphere projections of structural data, measured along the line of section in different units, are keyed to map location, with the color of the stereoplot corresponding to the lithological unit in which measurements were made: (a) poles to bedding (So), Tolimán area; (b) poles to cleavage (S1) in Late Cretaceous turbidites in the footwall of Higuerillas Thrust; (c) poles to thrusts planes (TF) and slickenlines (L1) measured in El Doctor Platform; (d) poles to bedding (So) measured in mesoscopic folds in layers of Cretaceous carbonates of Zimapán Basin; (e) poles to axial plane cleavage (S1) of mesoscopic folds, in Cretaceous carbonates of Zimapán Basin; (f) poles to cleavage (S1) in Late Cretaceous turbidites in the footwall of Jiliapan Thrust; (g) poles to thrusts planes (FT) and slickenlines (L1) measured within Valles-San Luís Potosí Platform; (h) poles to bedding (So) measured in mesoscopic folds in Cretaceous carbonates layers of Tampico-Misantla Basin; (i) poles to axial plane cleavage (S1) in Cretaceous carbonates of Tampico-Misantla Basin; (i) poles to bedding (So) in Late Cretaceous turbidites to the front of the MFTB; (k) poles to axial plane cleavage (S1) in Late Cretaceous turbidites in the front of the MFTB. A-A' shows the line of cross section in Fig. 2-4a. HT=Higuerillas Thrust, EDT=El Doctor Thrust, VT=Volantín Thrust, JT=Jiliapan Thrust, PPT=Puerto de Piedra Thrust, TT=Tetitla Thrust, ET=Enramaditas Thrust.

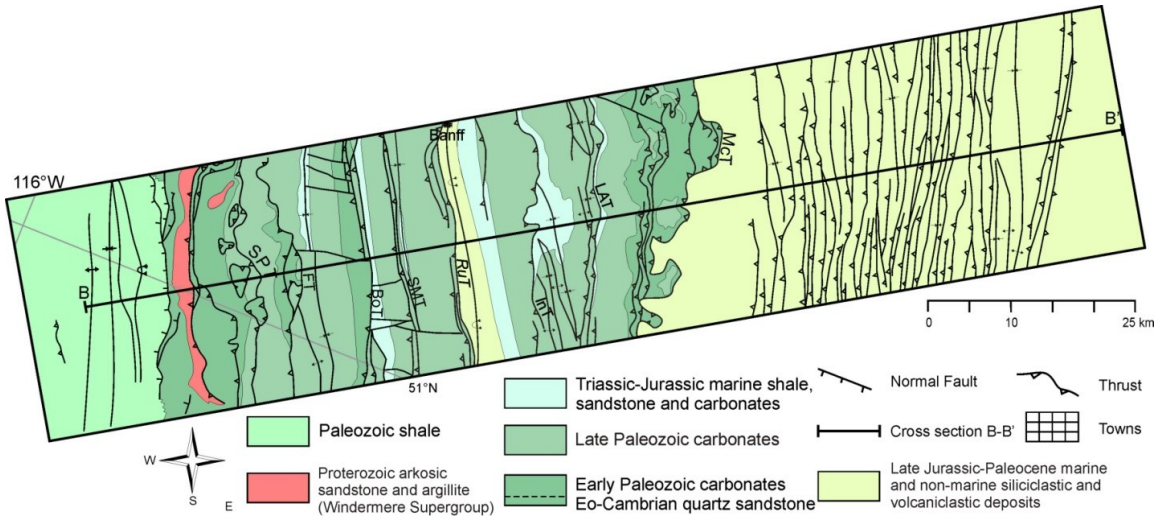

Figure 2-3. Generalized geological map of the Southern Canadian Rocky Mountain Front Ranges and Foothills along the Highway 1 transect to the west of Calgary (taken from Price and Fermor, 1985). Line B-B' corresponds to the section in Fig. 2-4c. SPT= Simpson Pass Thrust, FT=Fatigue Thrust, BoT= Bourgeau Thrust, SMT= Sulphur Mountain Thrust, RuT=Rundle Thrust, InT= Inglismaldie Thrust, LAT= Lac des Arcs Thrust, McT=McConnell Thrust.

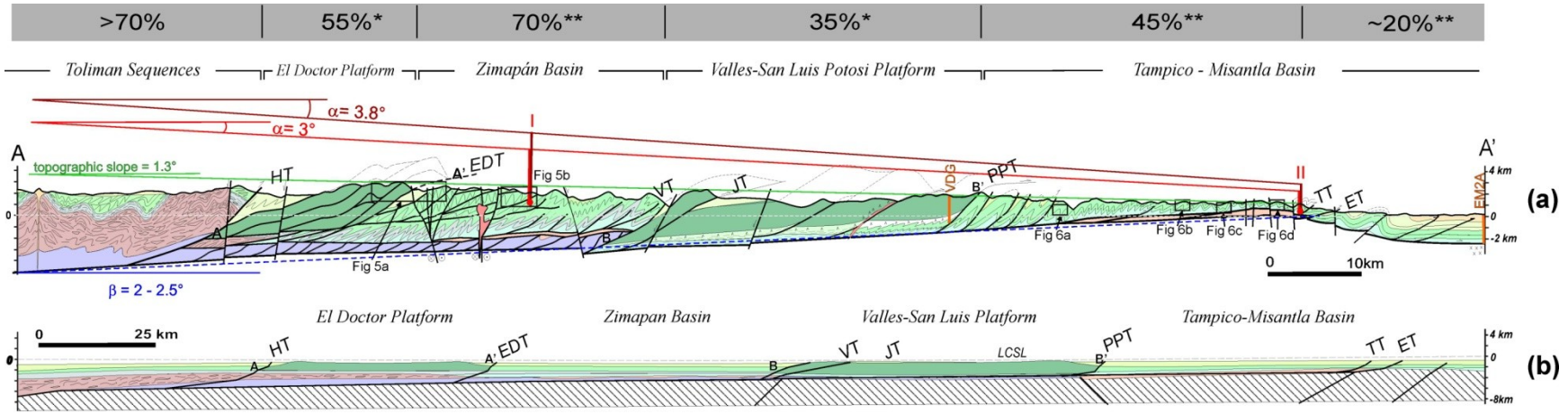

HT= Higuerillas Thrust, EDT= El Doctor Thrust, VT=Volantin Thrust, JT=Jiliapan Thrust, PPT= Puerto de Piedra Thrust, TT= Tetitla Thrus, ET=Enramaditas Thrust. EM2A & VDG correspond to El Maguey 2A and Valle de Guadalupe borehole records, taken from Suter (1987). LCSL=Late Cretaceous Sea Level -100m above the current sea level. Legend of sections (a) and (b) can be consulted in Fig. 2

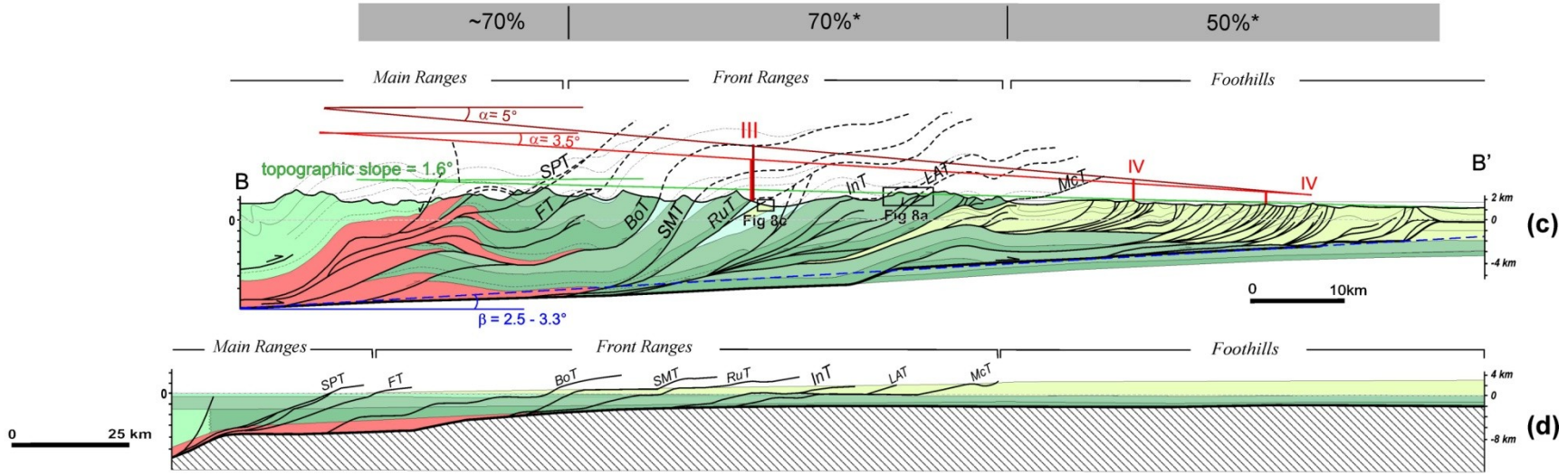

SPT= Simpson Pass Thrust, FT=Fatigue Thrust, BoT= Bourgeau Thrust, SMT= Sulphur Mountain Thrust, RuT=Rundle Thrust, InT= Inglismaldie Thrust, LAT= Lac des Arcs Thrust, McT=McConnell Thrust

Figure 2-4. Cross sections of the two fold-thrust belts in the foreland of the North American Cordillera. The locations and orientations of sections A-A' and B-B', with legends, are indicated in Figs. 2-2 and 2-3. (a) Admissible and partly schematic cross section of the Mexican Fold-Thrust Belt (section A-A' in Figs. 2-1 and 2-2) showing the variation of deformation style within the wedge. (b) Possible restoration of the section in (a) prior to deformation. Note the abrupt lateral changes in thickness and facies of the Cretaceous carbonates associated with the two platforms, and the disrupted basement at the east end of the cross section. (c) Balanced cross section of the Rocky Mountain Fold-Thrust Belt in southern Canada (Price and Fermor, 1985) along line B-B' in Figs. 1 and 3. (d) Palinspastic restoration of the sedimentary units (Proterozoic, Paleozoic and Mesozoic strata) of section (c) before deformation (Price and Fermor, 1985). Note the gradual increase in thickness of the different units towards the west. Figures 2-4 a and c are at the same scale, which is twice that of the palinspastic restorations in b and d. The amounts of shortening shown above (a) and (c) were determined using two methods (see the text and Fig. 2-7), one for thrust-dominated (*) and the other for fold-dominated segments (**). Blue lines in (a) and (c) show the average dip angle of the basal detachment zone inferred for the MFTB and reported in the CRMFTB. Red lines and brown lines in (a) and (c) show inferred paleo-topographic slopes for the end of the Cretaceous. In the MFTB the slope was determined using paleo-temperatures estimated at two localities (I and II), and calculating burial depth for a range of geothermal gradients. At locality I, a temperature (T) of 180°C was calculated from an illite crystallinity index of 0.48 (average of 6 measured samples). The value falls in the range of temperature of homogenization (170-190°C) of measured fluid inclusions in quartz of syn-tectonic veins from exactly the same locality. In locality II, a minimum burial temperature of 70°C was calculated from an average illite crystallinity index of 1.54. If we consider a minimum geothermal gradient of 23°C/km (Magoon *et al.*, 2001) and a maximum geothermal gradient of 30°C/km, we get estimates of burial depth of from 6.6 to 5.0 km for locality I and, from 2.2 to 1.5 km for locality II. Plotting these in cross section A-A', we obtain a gradient of from 3.0 to 3.8° to the east. For the CRMFTB, we used the thickness of the column (4-5.5 km) of rocks above the Lewis Thrust in Late Cretaceous calculated by Feinstein *et al.* (2007), and projected this as being directly above the Rundle Thrust on our line of section (point III in (c)). In the Foothills (point IV in (c)), we used the thickness of the overburden column calculated by Nurkowski (1984) for Late Cretaceous-Early Cenozoic times. We draw a line that approximately fits the burial depths and these values implying a range in gradient of 3.0 to 5.5 ° to the east. Labeled boxes in (a) and (b) show locations of photographs shown in Figs. 2-5, 2-6 and 2-8.

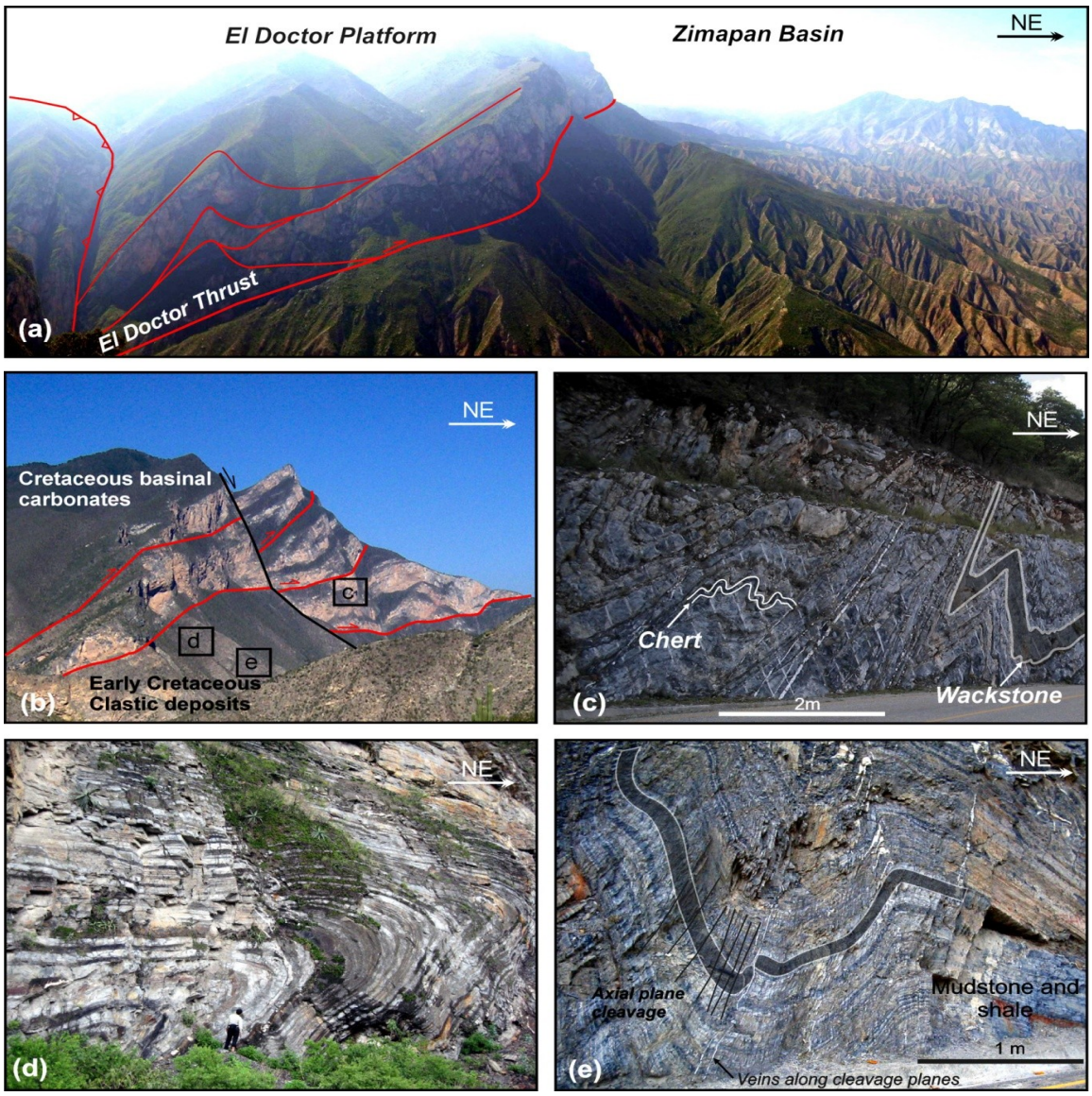

Figure 2-5. Examples of structures from the Mexican Fold Thrust Belt on the western part of the section (for locations see boxes in Fig. 2-4a). (a) Panoramic view of El Doctor Thrust from south of the Montezuma River. (b) Panoramic northward view of stacked thrust sheets of the Cretaceous Tamaulipas limestone in the Zimapán Basin, which at this scale does not seem to be internally deformed, but which in fact displays intense internal folding. (c) Tight mesoscopic folds in the interior of a thrust sheet of middle Cretaceous limestone, Tamaulipas Fm. Note the thickening in the fold hinges, except in the chert layers (to the left). (d) Gently inclined fold in Early Cretaceous shale and calcarenite layers. Note the variation in layer thickness around the fold. (e) Folds in layers of Early Cretaceous shale and mudstone. The folds are more open but the cleavage is more intense than in the limestone and sandstone layers. Note that the insets in (b) do not correspond to the actual locations of (c), (d) and (e), but rather indicate equivalent stratigraphic/structural positions where these folds are encountered.

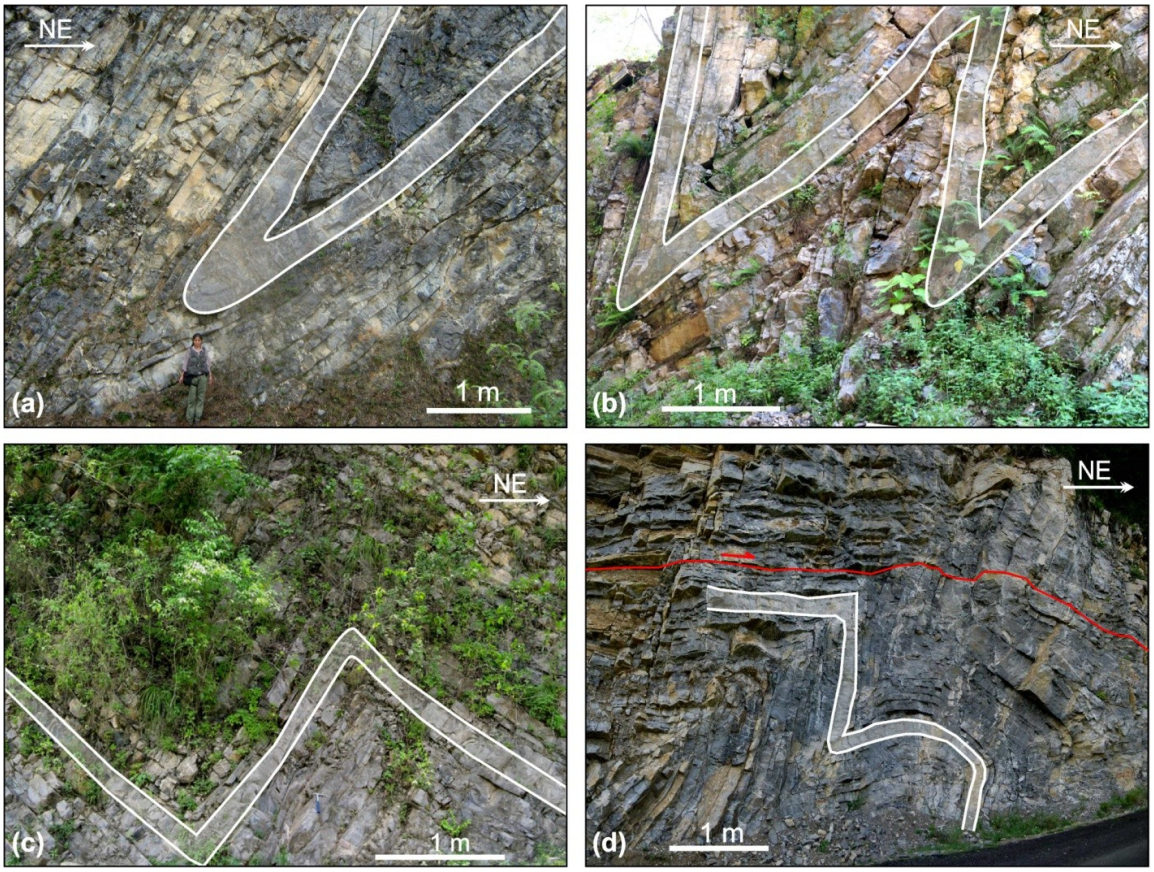

Figure 2-6. Examples of meso-scale structures to show variation in fold style along the same horizon of Middle Cretaceous basinal carbonates (Tamaulipas Formation) across the Tampico-Misantla Basin (TMB, for locations see boxes in Fig. 2-4a). (a) Tight folds with thickened hinges, typically observed on the western boundary of the basin. (b) Close chevron folds typically observed in the center of the basin. (c & d) Open folds observed towards the eastern side of the basin.

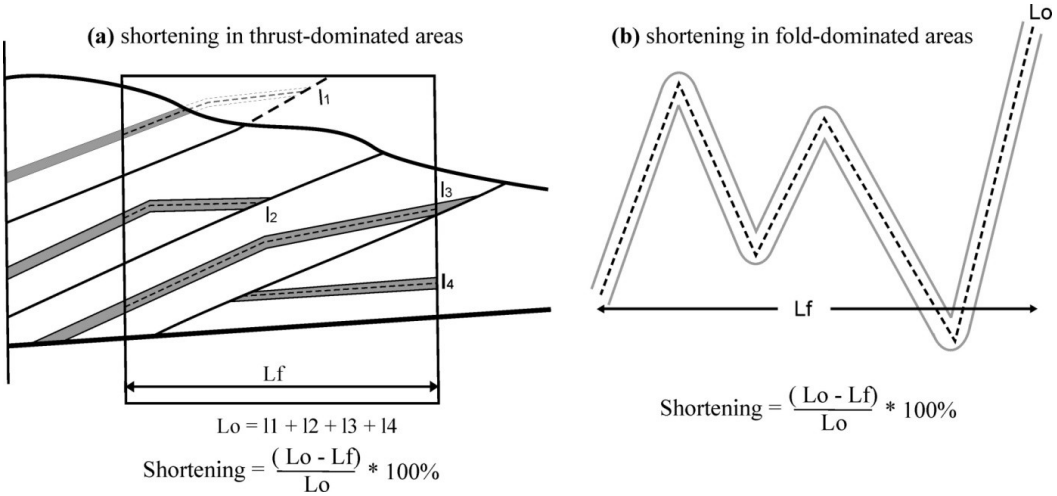

Figure 2-7. Methods applied to determine shortening: (a) using line length in the platforms of the MFTB and for the CRMFTB where thrusts are the dominant structure, including eroded segments of the marker horizon; (b) in the basins, where the dominant structures are buckle folds, we used fold arc length to determine shortening. We applied the second method only in trains of upright folds in Cretaceous carbonates, in layers that did not show significant variations in thickness or a pervasive axial plane cleavage (in some horizons of limestone and chert).

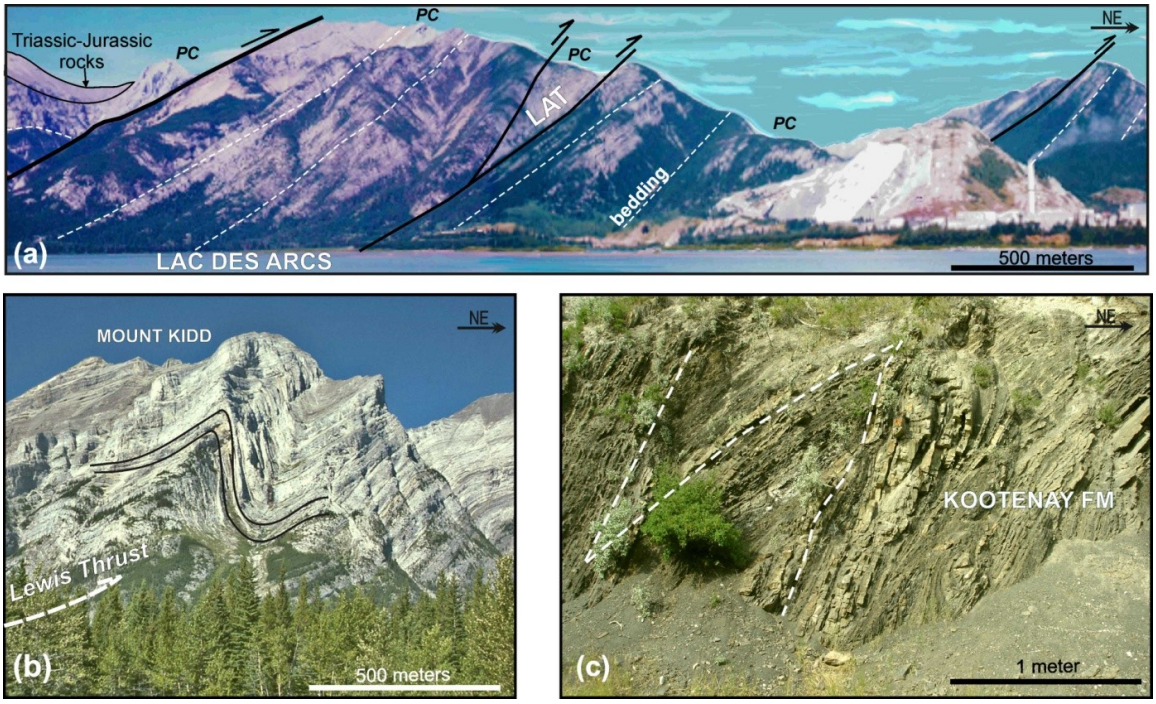

Figure 2-8. Examples of structures in the Canadian Rocky Mountains (for locations see boxes in Fig. 2-4c). (a) Panoramic northward view of Front Range structures (across Lac Des Arcs) with repetition of mostly Upper Paleozoic carbonates (PC) and little change in bedding dip (white dashed lines) across several thrusts. To the west, Triassic-Jurassic units cover the Paleozoic units. Nowhere in the MFTB section is there such uniformity of dip on this scale. (b) Paleozoic carbonates at Mount Kidd, folded in connection with the northern termination of the Lewis thrust. (c) Tight mesoscopic chevron folds in shale and sandstone layers of the Jurassic-Cretaceous Kootenay Fm. in the core of the Mount Allan Syncline, under the Rundle Thrust in the Front Ranges (see Cant and Stockmal, 1999, for more photographs and description of the rocks and structures in this location).

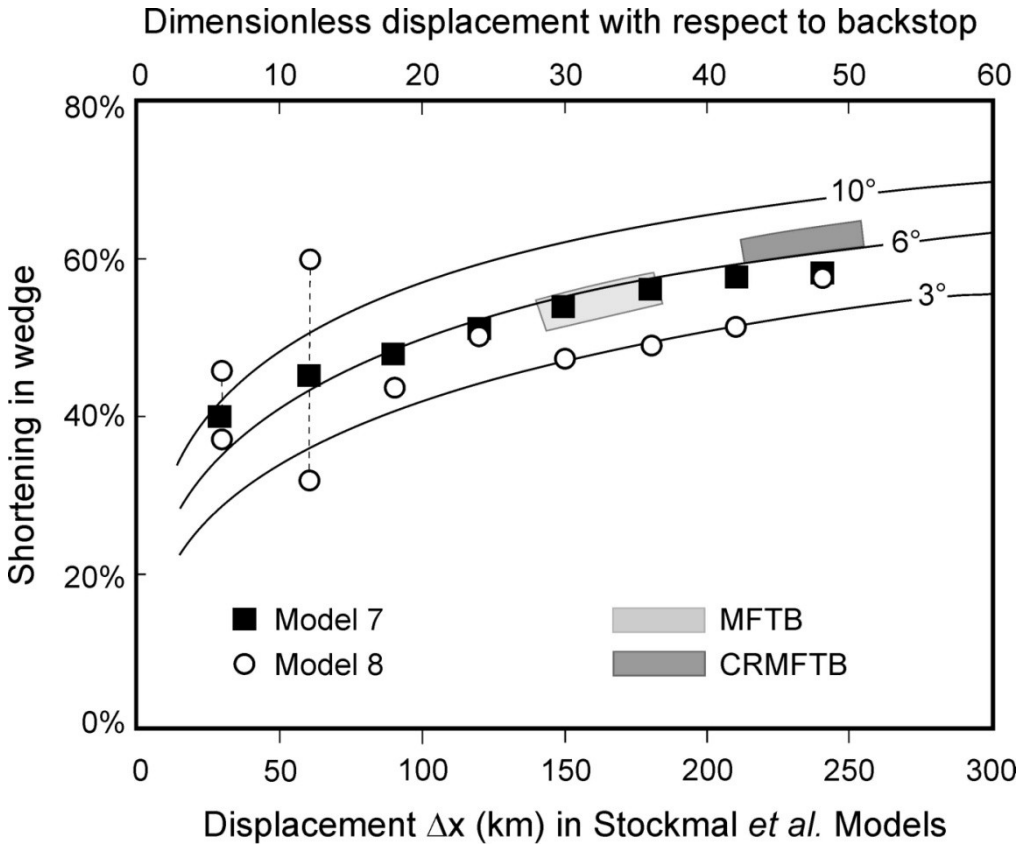

Figure 2-9. Data for numerical models and approximate fields corresponding to the MFTB and CRMFTB compared with theoretical shortening in a self-similar critically tapered wedge for three different taper angles (surface slope α plus basal slope β: 3°, 6° and 10°) as a function of the relative displacement between the backstop and the rigid sub-wedge substrate, for wedge development from strata of uniform thickness and assuming no erosion. The black squares and open circles indicate the shortening developed in finite element Models 7 (three-detachment, with erosion and no sedimentation) and 8 (three-detachment, erosion and sedimentation to base level) respectively of Stockmal *et al.* (2007), for which the CRMFTB is a rough prototype. The two circles joined by dotted lines at 30 and 60 km displacement represent alternative positions of the toe at incipient development of a new thrust in the numerical models. The discrete nature of thrust spacing and displacement on a scale not markedly different from that of the displacement of the backstop result in considerable deviation of the data points from a smooth curve, especially towards the left of the figure, and especially for Model 8, involving erosion and sedimentation (see Stockmal *et al.*, 2007, for more details of the models). Dimensionless displacement is displacement divided by thickness of the strata fed into the wedge at the toe. The shaded areas represent the ranges of inferred values of taper angles and internal wedge shortening for the two fold and thrust belts.

Table 2-1. Comparative table outlining the differences and similarities between the Mexican Fold-Thrust Belt (MFTB) and the Rocky Mountain Fold-thrust Belts in southern Canada (CRMFTB).

	CRMFTB section	**MFTB section**
Width	125 km	150 km
Dip of the detachment zone, β	2.5-3.3° to the west	2-2.5° to the west
Current surface slope	1.3-1.6° to the east	1-1.3° to the east
Inferred topographic slope, α	3.5-5°	3.0-3.8°
Inferred critical taper angle (α + β)	6-8.3°	5-6.3°
Stratigraphic range of rocks involved in deformation	Proterozoic-Late Cretaceous	Triassic-Eocene
Dominant Lithology	Carbonates (Paleozoic platform) in the Front Ranges, clastic units in the Foothills and Main Ranges	Carbonates (Cretaceous platforms and basins)
Lateral facies changes	Smooth-transitional at the scale of tens of km, except in transition from Front Ranges to Main Ranges (abrupt in the third dimension)	Abrupt at the scale of tens of km, associated with platforms
Amount of Shortening	70%	60% (minimum)
Maximum vertical displacement along thrusts	5 km	2.5 km
Scale of deformation	Typically kilometer scale in the Front Ranges	Typically meter scale
Dominant structures	Thrusts	Folds
Axial plane cleavage	Pressure-solution and slaty cleavage in the Main Ranges	Pressure-solution dominant to the rear and center of the cross section, but also present to the front

Table 2-2. Comparative table showing critical taper angles in an ideal subaerial wedge, and combinations of basal friction, μ_b, and internal friction, μ, that are consistent with inferred taper angles for the MFTB and CRMFTB. The taper angle ($\alpha + \beta$) is approximated by: $\alpha + \beta = \frac{\beta + (1-\lambda_b)\mu_b}{1 + (1-\lambda)K}$ (from eq. 21 in Dahlen *et al.*, 1984). This equation is valid for non-cohesive wedges and to cohesive wedges far from the toe. β is the dip of the detachment; $\boldsymbol{\alpha}$ is the topographic slope; λ and λ_b are the ratios of fluid pressure to total vertical pressure in the wedge and in the detachment, respectively. Taper angle is sensitive to pore fluid pressure, with fluid pressure build up in the detachment and the wedge itself having opposite effects on the taper angle. We have no direct evidence for what fluid pressure might have been at the time of wedge formation. Certainly it was elevated above hydrostatic ($\lambda \approx 0.44$), because of the abundance of veins in both the MFTB and CRMFTB. If fluid pressure is high just in the detachment (say $\lambda_b = 0.9$), taper angles are all too low. We take for this comparison $\lambda = \lambda b = 0.7$. μ_b is the basal coefficient of friction. The coefficient of internal friction, $\mu = \tan \varphi$, is embodied in the coefficient K (see Dahlen *et al.*, 1984, eq. 18a). Note that $\mu_b \leq \mu$ for a wedge to exist. To achieve the critical taper inferred for the MFTB we need a wedge with a weak detachment and relatively low φ or an intermediate-strength detachment and a high φ (shaded in pale gray). For the CRMFTB, we require a strong detachment and a relatively high φ, or an intermediate-strength detachment and an intermediate φ in the rock to achieve the inferred critical taper (shaded in deep grey). There is a small zone of overlap in conditions that matches both of the fold and thrust belts. Geological data suggest a weak detachment for the MFTB, and the range of matching φ for the inferred critical taper are typical for limestones (φ=25-30°, Sydney, 1966). Stockmal *et al.* (2007) took a value of φ=38° for the strongest material in their models, and values of basal friction consistent with such a value and the inferred tapers can be found for MFTB ($\mu_b = 0.5$) and CRMFTB ($\mu_b = 0.7$).

Very Weak Detachment (μb=0.35)																
φ	25				30				35				40			
β	2	2.5	3	3.5	2	2.5	3	3.5	2	2.5	3	3.5	2	2.5	3	3.5
α	3.8	3.6	3.5	3.4	3.1	3.0	2.8	2.6	2.5	2.3	2.1	1.9	1.9	1.7	1.4	1.1
α+β	**5.8**	**6.1**	**6.5**	**6.9**	**5.1**	**5.5**	**5.8**	**6.1**	**4.5**	**4.8**	**5.1**	**5.4**	**3.9**	**4.2**	**4.4**	**4.6**

Intermediate Detachment (μb=0.5)												
φ	30				35				40			
β	2	2.5	3	3.5	2.0	2.5	3.0	3.5	2.0	2.5	3.0	3.5
α	5.0	4.9	4.8	4.6	4.1	3.9	3.7	3.5	3.2	3.0	2.8	2.5
α+β	**7.0**	**7.4**	**7.8**	**8.1**	**6.1**	**6.4**	**6.7**	**7.0**	**5.2**	**5.5**	**5.8**	**6.0**

Solutions for α and β in the range estimated for the MFTB

Solutions for α and β in the range estimated for the CRMFTB

Overlapping solutions

Strong Detachment (μb=0.7)								
φ	35				40			
β	2.0	2.5	3.0	3.5	2.0	2.5	3.0	3.5
α	7.3	7.2	7.0	6.8	5.3	5.1	4.9	4.6
α+β	**9.3**	**9.7**	**10.0**	**10.3**	**7.3**	**7.6**	**7.9**	**8.1**

Chapter 3

The role of folding in the development of the Mexican Fold-Thrust Belt

Elisa Fitz-Diaz, Gustavo Tolson, Peter Hudleston, Daniel Bolaños-Rodríguez, Berlaine Ortega-Flores and Alberto Serrano Vázquez

Geological Society of America, Special Publication on the Laramide Orogeny in Mexico, in review

The Mexican Fold-Thrust Belt in central Mexico has overall characteristics that fit the critical tectonic wedge model. It is thin-skinned, forward propagating, tapers towards the toe (the east), and displays an overall decrease in deformation towards the toe. The internal structures and heterogeneity of deformation are not typical of fold-thrust belts; however, due to the presence of two large carbonate platforms, flanked by more thinly bedded basinal carbonates. Kilometer scale thrusts dominate deformation in the platform carbonates (a more brittle behavior), and mesoscopic buckle folds and associated cleavage dominate deformation in the basinal carbonates (a more ductile behavior). Total shortening across the belt, including both platforms and basins, is about 55-65%, with higher values in the basins than in the platforms and a concentration of deformation near the platform borders. The dominant mechanism of folding in the basinal rocks is buckling, with thin chert horizons behaving as single layers and limestone, shaly limestone interbeds buckling as multilayers, with a dominant chevron style. A significant shear component of the deformation is indicated by monoclinic fold symmetry, with a consistent sense of vergence of top towards the foreland. Strain and strain history are estimated from mesoscopic analysis of fold geometry and internal strain distribution at several locations across the basin. This information is used to assess overall kinematics and progressive deformation in the basins, which involves both shortening and shear components. The implications of this for the kinematics of the fold-thrust belt are discussed.

3.1 Introduction

Fold-thrust belts are one of the most common tectonic features worldwide, and their basic characteristics, tectonic style, and kinematics have been established by study of natural examples (e.g., Armstrong, 1968; Price and Fermor, 1985; Philippe *et al.*, 1996; McQuarrie, 2004) and by numerical and physical modeling (e. g. Huiqi *et al.*, 1992; Dixon, 2004, Stockmal *et al.*, 2007 and Simpson, 2009). Excellent descriptions of the structural characteristics of fold-thrust belts were provided by Dahlstrom (1969) and Boyer and Elliott (1982). Key features are the overall forward propagation of deformation, piggy-back style, the presence of a basal décollement, and decreasing intensity of deformation towards the foreland. Most fold-thrust belts are wedge-shaped, and since the mid 1980's, the critical taper theory of their development (Davis *et al.*, 1983; Dahlen *et al.*, 1984; Dahlen, 1990) has become generally accepted and is supported by field observations and by numerical and physical models.

Although increasingly sophisticated numerical codes allow many features of fold-thrust belts to be simulated and the effects of key controlling parameters to be assessed, they do not fully explain the variations of deformation styles along a cross-section at multiple scales of observation. The results of numerical simulations, in conjunction with theory, do however; provide an excellent guide when studying natural examples, and study of natural examples in turn provides information that allows models and theory to be refined. When combined iteratively, all these approaches lead to a better understanding of deformational processes within fold-thrust belts.

The Mexican Fold-Thrust Belt (MFTB), like virtually all fold-thrust belts, is wedge-shaped thin-skinned. It has been the subject of a number of regional studies (Campa-Uranga, 1983; Padilla y Sánchez, 1986; Eguiluz *et al.*, 2000). We present here the results of a structural analysis along a cross-section of the MFTB in central Mexico, for which the regional characteristics have been previously documented in classical papers by Suter (1987) and Carrillo-Martínez *et al.* (2001). In the present work, we attempt to relate local deformation on the mesoscopic scale to the overall deformation of the fold-thrust belt. In an earlier work (Fitz-Díaz *et al.*, in press, Chapter 2) we focused our attention on the large scale deformation and an interpretation of the structures in terms of critical taper wedge theory. In that paper also we compared and contrasted the geometrical, lithological and tectonic features of central Mexico with those of the classic cross-section of the Southern Canadian Rocky Mountains.

We present here detailed qualitative and quantitative information from a study of small scale buckle folds, developed in carbonates in two basins traversed by the studied cross section. The geometrical analysis of these folds allows us to locally estimate the strain and its variation along the cross-section. Additionally, a careful qualitative analysis of fold-related veins, axial plane cleavage and fold geometry, give us clues to the kinematics of folding and more broadly the evolution of the MFTB.

We use data on fold geometry and strain, based on observations at key outcrops, to relate mesoscopic scale folding to deformation at the scale of the basins in a kinematic model. This, together with information on deformation in the platforms allows the effects of lithological variations within the wedge as a whole to be assessed.

3.2 Regional Framework

Subduction along the western margin of North America and associated accretion of terranes swept from reaches of the Pacific Ocean is considered to be responsible for the formation of the Cordilleran orogen (Coney *et al.*, 1980; Coney and Evenchick, 1994; Armstrong, 1974; DeCelles, 2009). One of the consequences of such accretionary or collisional processes is the shortening of sedimentary rocks in the foreland, giving rise to the formation of fold-thrust belts, a prime example of which is the Rocky Mountains Fold-Thrust Belt (RMFTB) in western North America. Although the RMFTB seems to be a continuous feature along the eastern edge of the cordillera, it shows some marked variations along strike. In southern Canada, the RMFTB is relatively narrow and has a thin-skinned deformation style, with a width between 100 and 200 km. In the southwest USA, it widens to more than 1000 km and is divided into two tectonic elements: the Sevier and

Laramide fold-thrust belts (Fig. 3-1, Armstrong, 1968 and 1974). The Sevier fold-thrust belt is thin-skinned and its front is to the west of the Colorado Plateau (Armstrong, 1968; Yonkee, 1992). The Laramide province extends eastward of the Sevier fold-thrust belt into the continental interior from central Montana to northern Mexico. It is characterized by basement-involved (thick-skinned) structures (Allmendinger *et al.*, 1982; Brewer *et al.*, 1982; Schmidt *et al.,* 1993). It is not clear how the Sevier and Laramide tectonic fronts continue to the south. Nevertheless, in a broad area in northern Mexico, low angle thrusts and related folds are cut by large scale high angle reverse faults that involve blocks of basement (e. g. San Marcos and La Babia faults, Chávez-Cabello *et al.*, 2007). This suggests an overlapping of both Sevier and Laramide deformation styles in this area (Fig. 3-1). The age of the RMFTB for the segment Canada-USA ranges from Late Jurassic to Eocene (Armstrong, 1974; DeCelles, 2004; DeCelles *et al.*, 1995; Van der Pluijm, 2006; Evenchick *et al.*, 2007).

Further south, the Mexican Fold-Thrust Belt (MFTB) is expressed topographically in the Sierra Madre Oriental. It is thin-skinned and 100-250 km wide (Campa-Uranga, 1983 and Eguiluz *et al.*, 2000), extending from northern Mexico, where it is oriented NW-SE and its northern boundary is parallel with the Mojave-Sonora Megashear trace (Fig. 3-1, Anderson and Schmidt, 1983; Anderson and Silver, 2005), to central and southern Mexico. At its southern end, this belt narrows, changes orientation to N-S, and finally bifurcates, with one branch that continues along the Gulf of Mexico coast and another that runs through the Morelos Guerrero platform (Fig. 3-1).

This study is focused on a well exposed cross-section of the Mexican Fold-Thrust Belt (MFTB) in Central Mexico (Fig. 3-1). The chosen transect is oriented ENE-WSW, and in only 150 km we can see a full cross-section of the MFTB, with a relief of about 3000 m. In this area, the MFTB shows a dominant thin-skinned deformation style, with an overall wedge shape tapering towards the east.

3.2.1 Stratigraphy

The stratigraphy of the area was first described in the 1940s (Imlay, 1944) and has been subsequently refined in a number of papers (Segerstrom, 1961; Suter 1980, 1984 and 1990; Carrillo-Martínez, 1989; Wilson and Ward, 1993; Carrillo-Martínez *et al.*, 2001, Dávila-Alcocer *et al.*, 2009). The rocks are mostly Cretaceous carbonates, with lateral facies changes associated with different paleogeographical elements across the region. These elements are, from east to west: the Tampico-Misantla Basin, the Valles-San Luis Potosí Platform, the Zimapán Basin, and

El Doctor Platform (Carrillo-Martinez, 1997; Suter, 1987 & 1990). To the west the Cretaceous rocks are in fault contact with a suite of rocks here grouped as the Tolimán Sequences (Figs. 3-2 and 3-3). The paleogeographic elements and the stratigraphy of the area play a major role in the characteristics of the deformation, as we will see in the following sections.

In Figure 3-2, a characteristic stratigraphic column is presented for each area. Each column includes the regional stratigraphic nomenclature, graphical representation of lithology for the different units, age, a rough estimate of thickness and the shortening phases observed. On the eastern side of the transect, the Tampico-Misantla Basin is characterized by a sedimentary record that starts in the Triassic?-Jurassic with continental sandstones and conglomerates (Huizachal and Cahuasas Fms., undifferentiated) uncomformably deposited on a basement of Grenville age granulite gneiss. Above these units, a eustatic sea-level rise caused an incursion of the sea from the Pacific Ocean (Ochoa-Camarillo, 1996) and resulted in the deposition of calcarenites and carbonaceous shale (Santiago Fm.) with a strong influence of continental organic matter. These rocks in turn were covered in the Early Cretaceous by thinly-bedded black mudstone with abundant chert bands (Taman, Pimienta and Tamaulipas Fms.), and then by two packages of clastic sediments, one Late Cretaceous in age (Agua Nueva, San Felipe and Mendez Fms.) and another Paleocene-Eocene in age (Velasco, Chicontepec, Tanlajas and Chalma Fms.). This last package is the dominant lithology in the foothills of the Sierra Madre Oriental (Suter, 1987 & 1990, Fig. 3-2a). The Valles-San Luis Potosí Platform (VSLPP) is characterized by about 2000 m of massive to thickly-bedded Cretaceous platform limestone and dolostone (Abra and Tamabra Fms., Suter, 1987), with evaporites at the base (Guaxcamá Fm.). These rocks are Berriasian-Cenomanian in age and rest on top of the Santiago Fm. They are covered by Late Cretaceous clastic deposits (Soyatal Fm., Fig. 3-2b). The VSLPP is overthrust along its western margin by rocks of the Zimapan Basin (Figs. 3-2c, 3-3 and 3-4), which consist of Early Cretaceous thinly bedded basinal limestones with chert bands and calcarenites (Tamaulipas and Trancas Fms.), deposited on top of Tithonian-Berriasian volcaniclastics and covered by Late Cretaceous calcareous turbidites (Soyatal Fm.). The stratigraphic changes between the units of the Zimapan Basin are all transitional. On the western margin of the basin, the rocks are overthrust by the massive Cretaceous limestones (El Doctor Fm.) and Late Cretaceous calcareous turbidites (Soyatal Fm.) of the El Doctor Platform paleogeographical element (Fig. 3-2d). In Figures 3- 2 and 3-3 carbonates of similar ages and facies (e. g., platform and basinal carbonates) are indicated using the same color. Figure 3-3c is a reconstruction in cross-section of the facies distribution prior to deformation.

Although basement rocks are not exposed along the cross-section, they have been reported in borehole records along the eastern edge of the Tampico-Misantla Basin (and are so interpreted in the cross-section of Fig. 3-3b). Some blocks of the basement have been dragged to the surface along major thrusts and are exposed few kilometers to the south of the area. We infer the presence of Jurassic redbeds under the carbonates of the Zimapan Basin from borehole records to the south of the area. It is also likely that Permo-Triassic volcaniclastic rocks underlie the rocks of the Zimapan Basin and El Doctor Platform, based on the field observations by Rosales-Lagarde *et al.* (2005) to the south of the studied area. According to these authors, these units are involved in the deformation.

3.2.2 Geometry of the wedge

A tapered orogenic wedge model was originally proposed by Chapple (1978), and the first fully developed wedge theory was developed by Davis *et al.* (1983), who demonstrated the applicability of the approach to submarine fold-thrust wedges. Improvements and refinements to this model have been made since then (Dahlen *et al.*, 1984; Dahlen, 1990). In this model, the cited authors assumed a Mohr-Coulomb behavior of a homogeneous material within the wedge, and a mechanically weaker material along the basal detachment. Dahlen *et al.* (1984) demonstrated that the geometry of a subaerial wedge (given by the critical taper angle which is the sum of the topographic slope angle and the dip of the detachment) is characteristic for a particular combination of: strength of the rock within the wedge (given by the coefficient of internal friction); frictional resistance along the detachment; pore fluid pressure ratio (hydrostatic/lithostatic pressures) within the wedge and along the detachment.

On the regional scale, the MFTB displays a wedge shape typical of thin-skinned fold-thrust belts (Fig. 3-3a). This wedge tapers towards the east, in the same direction that the topography decreases and the detachment fault ascends to the surface. In a previous study, an average critical taper angle between 5 and 6.3° was calculated for the studied cross-section (for details see Fitz-Diaz *et al.*, in press). This is consistent with taper angles in cross-sections of the MFTB to the north and to the south of the area (Eguiluz *et al.*, 2000), which have borehole records and seismic profiles to provide control at depth. The limited stratigraphic range and thickness of strata of the rocks exposed across the full length of the cross-section are consistent with a relatively thin wedge.

The lateral facies changes along the cross-section (as evident from the stratigraphic columns of the different paleo-geographical elements – see Fig. 3-2) can be expected to have locally

modified the critical taper angle, or in other words controlled whether some segments experienced displacement over internal shortening. As an example, there is a marked difference in amount of shortening experienced by the VSLPP and the adjacent TMB (Fig. 3-3). This difference in behavior can be explained by the difference in internal strength of the units above the detachment and a difference in frictional resistance along the detachment, both of which favored slip over shortening in VLSPP and shortening over slip in the TMB. The massive dolomitized limestone of the VSLPP was stronger than the well bedded carbonaceous mudstone interbedded with shale and chert of the TMB and the frictional resistance of evaporites under the VLSPP would have been less than the frictional resistance of the carbonaceous shale under the TMB. A difference in taper angle – lower associated with the VSLPP and higher associated with the TMB – is linked to the difference in the relative importance of basal slip versus internal shortening (Fitz-Díaz *et al.* in press).

In the following sections, the characteristics of deformation, both qualitatively and quantitatively, will be described for each paleogeographical element. These data will allow us to test the predictions we can make by applying the orogenic wedge model.

3.3 Deformation within the wedge

The large-scale structures within the MFTB wedge are shown in the cross-section of Figure 3-3b. This cross-section is an admissible and partially schematic representation of structures at the kilometer scale. In the following paragraphs, details on the structures on a smaller scale are described, including geometry, kinematics and mechanisms of deformation and their variations along the cross-section and among the different stratigraphic units.

On the western side of the study area, El Chilar Complex rocks exhibit a complex pattern of deformation (Figs. 3-2e and 3-3a and b). This complexity is the result of at least three events of shortening including: 1) an old anastomosing, block-in-matrix fabric, referred to here as pre-D1, which occurred under low grade metamorphic conditions, given that tectonic chlorite and sericite developed on the foliation; 2) tight folding of the pre-D1 fabric, with a well developed axial plane cleavage (S1); the folding and the cleavage are associated with D1; 3) open folding of the D1 folds related to low angle thrust faults, these structures being designated as D2. Pre-D1 structures seem to predate any deformation related to the MFTB because they do not affect the Cretaceous units that uncomfortably overlie El Chilar Complex. D1 and D2 structures do, however, affect the Early to Late Cretaceous rocks lying on El Chilar Complex. These structures are represented by tight folds (D1) refolded by more open folds (D2), both fold episodes being associated with an

axial plane cleavage (S1 and S2). S1 cleavage is folded by D2 to form a spaced S2 crenulation cleavage. Also associated with D2 are younger, low-angle thrusts faults, which cut the early folds.

D1 and D2 structures are developed in rocks across the MFTB, as indicated on the left hand side of the column on the stratigraphic charts (Fig. 3-2). D1, as represented by folds and thrusts, seems to have been the main tectonic event that built up the Sierra Madre Oriental and, across the whole belt, accommodated considerable amounts of shortening (several hundred kilometers, Fig. 3-3b). Based on stratigraphic constraints, this event seems to have taken place from Turonian to Maastrichtian times in the studied region (see Fig. 3-2). D2, on the other hand, is characterized by gentle folds and meter-scale displacement on late thrust faults. It affected most of the Cretaceous strata in the area, and is the only deformation that affected the Early Cenozoic clastic deposits in the foothills. Evidence for this last statement comes from: 1) the complex deformation in the Late Cretaceous clastic deposits (Soyatal Fm. Fig. 3-4a) on the western side of the cross-section; and 2) the unconformity that separates Late Cretaceous clastic deposits (Mendez Fm., Fig. 3-4b), with D1 folds and a strong S1 axial plane cleavage, from Early Cenozoic clastic deposits (Velasco Fm., Fig. 3-4c), in which S1 is absent. Both D1 and D2 structures have a vergence towards the NE throughout the MFTB.

The main focus of this study is on the D1structures, since we consider that D1 contributed the most to the development of the MFTB. The small amount of shortening and weak development of folds during D2 makes it possible to find D1 structures almost in their original position. A large amount of structural orientation data was collected along the cross-section and this is presented in equal-area projections in Figure 3-5. All these data are consistent with a general direction of transport and shortening towards the NE along the entire cross-section, with local deflections (on the order of ten degrees) in the orientation of the structures in the different paleogeographical elements. The data also indicate that there is refraction of axial plane cleavage associated with the different lithologies within the Zimapán and Tampico-Misantla basins.

Along the line of section (AA’ in Fig. 3-3), the style and intensity of deformation vary depending on the position along the section and on lithology, which is characterized by the carbonates of the two platforms and the lateral facies changes from the platforms into the two basins (Figs. 3-2 and 3-3). In the following paragraphs, the characteristics of the deformation will be summarized for the platforms and the basins and the boundaries between them.

3.3.1 Deformation in the Platforms

The deformation in the platforms is dominantly brittle; thrust dominated and can only be considered penetrative at a kilometer scale (Figs. 3-6a, b and c). The folds in the thick platform carbonates are very wide and are controlled by the geometry of the thrusts: they are mostly fault-bend folds (Suppe, 1983), although in relatively thin layers, fault-propagation folds (Suppe, 1983) can also be observed. Except for strong grain-scale deformation concentrated along thrust zones, in the interior of the thrust sheets the deformation is negligible at a metric scale and is accommodated by scarce veins and well-spaced stylolites. To represent these structures in the regional cross-section we took into account structural data and observations at the surface (e. g. Fig. 3-6a), borehole records from the surrounding areas, and the typical geometric relationships between thrusts and fault-related folds and the inferred wedge-shaped geometry of fold-thrust belts (Fitz-Diaz *et al.*, in press, Chapter 2) as well as the basic rules for cross-section balancing.

Stratigraphic studies and structural observations in the area (Segerstrom, 1961 and Hernández-Jáuregui, 1997) indicate that the original thickness of El Doctor Platform (EDP) (between 800 and 1200 meters) is triplicated by thrusting for at least half of its width. In a similar way, the thickness of the Valles-San Luis Potosi Platform (VSLPP) was partially duplicated, and relatively less shortened than El Doctor Platform. Estimates of shortening, determined by three different methods, are about 55% for EDP and about 35% for the VSLPP. The latter is somewhat less than the value of 42% reported by Suter (1987) and Contreras and Suter (1990) for exactly the same cross-section. The difference reflects the conservative way in which we constructed the cross-section.

In both platforms, the average strike of the major thrusts is roughly N150°. The slickenlines measured on these surfaces indicate a direction of transport towards N50-60° (Figs. 3-5a and b). With the exception of a few small scale back-thrusts, no major structures with reverse vergence were observed in the study area.

3.3.2 Deformation in the basins

Deformation and associated shortening in the basins was far higher than in the platforms and was accommodated mostly by meter-scale buckle folds (folds unrelated to faults). In the Zimapán Basin (ZB), the folds exhibit a rather ductile style of deformation, as evidenced by a considerable thickening and thinning of the layers in the hinge and in the limbs, respectively (Fig. 3-7), indicating penetrative deformation at the grain scale. In the Tampico-Misantla Basin, however,

fold style indicates less ductile behavior, as evidenced by smaller thickness variations and the presence of small faults and fractures in association with folds (Fig. 3-8).

In the Zimapán Basin most folds are tight to isoclinal, and their geometry is strongly controlled by the lithology (Fig. 3-7). In clastic carbonates (e. g. Soyatal and Trancas Fms.), folds are relatively open with rounded hinges and with a strong axial plane cleavage. They commonly are class 1C and occasionally class 2 of Ramsay (1967). Limestone layers interbedded with chert and shale (Tamaulipas Fm.), typically show tight to isoclinal folds with angular hinges (*chevron* style), and less commonly are associated with a pressure-solution cleavage. Fold styles are fairly homogeneous within stratigraphic horizons across the basin. Most of the folds in the Zimapán Basin are asymmetrical with an axial plane cleavage striking NW-SE and dipping about 60° to the SW (Figs. 3-5 e-j). Nevertheless, along stratigraphic transitions the axial planes of folds are sub-horizontal, sub-parallel to the contact. Figure 3-7a is a schematic cross-section to show structural style in the middle of the ZB. It shows the striking variations among the different stratigraphic units, which maintain their stratigraphic position across the basin. There is no significant variation in trend of the fold axes among the different stratigraphic packages (Figs. 3-5e, g and i), however, there are systematic differences in dip of the axial plane cleavage, which is generally greater in the younger units (Figs. 3-5f, h and j).

At least 5 generations of fold-related veins can be recognized in the limestones of the ZB. The earliest are two generations of early veins (parallel and oblique to bedding) affected by folding; these are followed by two different types of syn-tectonic veins that accommodated layer extension and occasionally shear between the layers during folding; and finally veins emplaced along attenuated forelimbs of asymmetrical folds and cutting the axial plane cleavage. There is an additional generation of vertical veins unrelated to folding. The early and syn-tectonic veins are relatively abundant, but the younger ones are more widely spaced.

In the Tampico-Misantla Basin (TMB), folds vary in style from isoclinal (approaching the western boundary of the TMB) to more open towards the east. Most are typical buckle folds of *chevron* style, except those near the VSLPP which are more rounded and have thickened hinges and attenuated limbs. The average trend of the fold axes is about N340 for most of the units and on average is about 20° different in a clockwise sense from the average trend in the ZB (Figs. 3-5k, m and o). The axial plane cleavage is weak to incipient overall in the TMB, and in general dips more gently in the Early Cretaceous units as it approaches the detachment zone (Figs. 3-5l, n

and p). Asymmetry of the folds decreases to the surface, as sketched in Figure 3-8a and illustrated in the photographs.

Fold-related veins are far less abundant in the TMB than in the ZB. It is common to find three generations of them: veins parallel to bedding, *en echelon* arrays of veins that accommodated shear parallel to bedding, and extensional veins normal to bedding positioned in the outer arc of folds. It is also common to find high concentrations of veins along thrust planes or along the detachment zones. These have a thickness on the order of few centimeters, lengths of tens of centimeters and commonly accommodate sub-horizontal extension. Later tectonic veins, unrelated to folds or thrusts are rather scarce.

To estimate the amount of shortening accommodated by folding in the basins, we applied a systematic analysis of fold geometry across the basins along the same stratigraphic horizon. We chose for this the Tamaulipas Fm. because it is present in both basins, because it is relatively thick (~600 meters), because it is mechanically competent and because, unlike the shale or carbon rich units (i.e., the Trancas, Tamán, Pimienta and Santiago Fms.), it did not develop a strong axial plane cleavage. Because of these properties, according to buckling theory, we may expect this horizon to have exerted a controlling influence on deformation in the basins and also to provide representative estimates of the overall shortening in these basins.

The geometrical analysis applied here involves several steps. First, we selected trains of well exposed near–upright to upright chevron folds. Folds at a total of 20 outcrops, 7 across the ZB and 13 across the TMB, were analyzed. For each train of folds we measured the orientation of limbs and fold axes. For trains of folds that did not show evidence of flattening (as suggested by a change in thickness of the layers around the fold), we compared the presumed initial length (l_o) of layers prior to folding with the horizontal distance between the same end points after folding (l_f), as shown in Figure 3-9a. This provides a measurement of shortening strain accommodated by folding. For folds that showed evidence of flattening, we first estimated the amount of flattening, by restoring the layers to constant thickness (as illustrated in Fig. 3-9b). Then with image analysis we removed the flattening strain, after which we calculated the shortening due to buckling alone by applying the same technique as for the folds that did not show flattening (Fig. 3-9a). Finally, we added the shortening due to buckling and that due to flattening to calculate the total shortening (Fig. 3-9c and d).

The average shortening estimates (of at least 5 individual folds) for each analyzed train of folds are plotted against distance from the western edge of the cross-section, for each of the two

basins, in Figure 3- 9c and 3-9d. The data in Figure 3-9c are for the western half of ZB. On the left note that the shortening due to buckling is fairly homogeneous across the basin, indicating that buckle folding reduced the horizontal length of Tamaulipas Fm. by about 45%. The central graph in Figure 3-9c indicates that shortening due to flattening is less homogenous than that due to buckling, but is more variable, as evidenced by the error bars. It averages about 20%. The graph on the right combines shortening due to buckling and flattening for each fold train. It indicates a total shortening strain due to folding of 60-65%, which corresponds to 60 km across the whole basin. Figure 3-9d, shows the corresponding data for the TMB. Note that shortening due to buckling (Fig. 3-9d, left) is a maximum close to the boundary of the basin with the VSLPP and decreases eastwards towards the toe of the fold-thrust wedge, with an average of about 45%. The amount of shortening due to flattening shows a similar trend (Fig. 3-9d, center), with a maximum of 22% on the western edge of the basin, and essentially none on the eastern edge (front of the MFTB). The sum of the two components of shortening (Fig. 3-9d, right) is about 60% on the western side of the TMB, decreasing to about 20% at the eastern edge (the front of the MFTB). This corresponds to 35 to 40 km reduction in length. In addition to the shortening due to folding, there is some offset on minor thrusts and some amount of thickening of layers during the early stages of folding. Estimates of shortening due to thrusting and bed thickening prior to folding in the two basins are 10% and 5%, respectively. These can be added to the shortening estimates due to folding to arrive at estimates of total shortening across the Zimapán and Tampico-Misantla basins of 65% and 45%, respectively. In the case of the TMB shortening decreases from 65% in the west to 20% in the east (Fig. 3-3).

Values of shortening for each of the major paleogeographical elements, including the platforms and basins, encountered along the line of cross-section are shown above the cross-section in Fig. 3-3b. In general, shortening increases modestly from east to west, and this observation is in agreement with the critical-taper orogenic wedge model that predicts that more deformation is accumulated at the rear of the wedge than at the front (Davis *et al.*, 1983). However, because of lithological heterogeneity, the gradient is not smooth, with deviations that depend on lithology. The platforms exhibit less overall shortening than the basins, although the western platform (EDP) accommodates more shortening than the eastern one (VSLPP). The two basins each accommodated more shortening than either of the platforms, but the western basin (Zimapán) accommodated more shortening than the eastern one (TMB). Thus both basins accommodated more shortening than the adjacent platforms (Fig. 3-3c). Although the deformation is accentuated towards the boundaries of the Zimapán basin, the fold analysis

suggests that the internal deformation of the basinal limestone is very homogeneous across the basin (Fig. 3-8c). In the TMB, by contrast, we can see a gradient of deformation accommodated by folding in the Tamaulipas Fm. that decreases towards the foreland.

3.3.3 Deformation along the platform/basin boundaries

The boundaries between the basins and platforms along cross-section AA' in Fig. 3-3 are typically observed as sharp tectonic contacts, in the form of thrusts. Considerable vertical displacements are accommodated along these thrusts. The stratigraphic offsets are largest to the west, on the order of a few kilometers (e. g. the Higuerillas and El Doctor Thrusts, Fig. 3-3c), and decrease towards the east, the front of the MFTB, where they accommodate displacements of about a kilometer to a few hundred meters (e. g. Enramaditas Thrust, Fig. 3-3c). The thrusts have a constant strike of NW-SE and dip towards the SW. Their dip is shallower towards the front of the fold-thrust belt, and the lineation on the thrust planes indicates a consistent direction of transport towards the NE. Most of the thrust zones exhibit, at least in part, a brittle fabric. Towards the west, deformation associated with the Higuerillas, El Doctor and El Volantín Thrusts exhibits a dominant cataclastic fabric, which locally, in fine grain horizons, becomes a calci-mylonite. The cataclastic fabric is commonly cut by later reverse faults. Towards the east (e. g. Jiliapan, Puerto de Piedra and Enramaditas) a coarser grained brecciated fabric is more common associated with the thrusts, although finer cataclasites also developed in shale-rich horizons.

Thrust-related veins are thicker and more abundant along the Higuerillas and El Doctor Thrust zones and on the western side of El Doctor Platform. Such veins are thinner and less abundant along the easternmost thrusts. This might suggest that less fluid circulated along the eastern thrusts during deformation, associated with the smaller displacements on these thrusts, consistent with the predictions of Hubbert and Rubey (1959).

3.4 Age of deformation

As shown in Figure 3-1 of Fitz-Diaz *et al.* (in press), there are two main orogenies in western North America involving Cretaceous age rocks. These are traditionally known as the Sevier and the Laramide. They have been well studied since the beginning of 20th century in the central part of the cordillera, and their ages relatively well documented in recent decades (Armstrong, 1968; Allmendinger *et al.*, 1982 Brewer *et al.*, 1982; Yonkee, 1992 and Schmidt *et al.,* 1993). However, it is not yet well understood how the effects of these two orogenies are reflected in the cordillera to the south into the Mexican Fold Thrust Belt. This is partly because there is not a clear continuation of the fronts of the Sevier or Laramide fold-thrust belts to the south, as a result of a

number of younger fault systems, and partly because the traces of the main Laramide thrusts are not continuous for long distances.

In northern Mexico, low-angle thrusts and related folds are cut by high angle reverse faults (e. g. La Babia and San Marcos). The latter, according to Chávez-Cabello *et al.* (2007) were originally normal faults formed during the opening of the Gulf of Mexico, in the Middle Jurassic, and were apparently reactivated on multiple occasions. One of the most important reactivations occurred, according to the same authors, in the Paleocene-Eocene during the Laramide orogeny. This coexistence of thin and thick-skinned structures in Cretaceous limestones makes it likely that both, Sevier and Laramide structures are recorded in northern Mexico, in the overlapped area in Figure 3-1.

In the studied area in central Mexico, there are no large stratigraphic separations associated with any of the high-angle reverse faults related to D1. In the cross-section AA' of Figure 3-3, the MFTB has a wedge shape and is bounded below by a detachment zone, typical of thin-skinned fold-thrust belt (Fig. 3-3a). If there are high-angle faults cutting this detachment, displacements on them must be small. Even the late shortening structures (D2) are represented by low-angle reverse faults and related folds (Fig. 3-10 a). Based on these structural characteristics, we consider that the MFTB has more affinity in style with the Sevier fold-thrust belt than with the Laramide.

Stratigraphic relationships in the studied cross-section, which can be consulted in Figure 3-2, suggest that syntectonic sedimentation (Soyatal Fm., Fig. 3-4a) on the western side of the cross-section started in the Turonian (Hernández-Jaúregui, 1997). On the other hand, similar clastic deposits at the front of the MFTB (Mendez Fm., Fig. 3-4b) were strongly deformed during D1, as evidenced by a pervasive axial plane cleavage (S1), which is cut by younger thrust faults, presumably during D2. The Mendez Fm. is uncomformably covered by younger clastic units (Velasco Fm.) which are cut by spaced thrust faults with displacements on the order of meters (Fig. 3-4c) and in which S1 is absent. The unconformity that separates these two units coincides, according to López-Oliva *et al.* (1998), with the K/T boundary. All these facts together, indicate that D1, the deformation event that contributed most to the development of the MFTB in central Mexico, started in the west in the Turonian (about 90 Ma) and ended to the east in the Maastrichtian (about 65 Ma). Also, the second shortening event, D2 that affected these rocks occurred after the Maastrichtian.

To the north, syntectonic basins in the Sevier fold-thrust belt have a range of age between Cenomanian-Maastrichtian (Lawton and Trexler, 1991; Selting and Schmitt, 1999; DeCelles, 2004), while those associated with the Laramide structures are younger, with a range of ages between Maastrichtian and Eocene (Dickinson *et al.*, 1988 and DeCelles *et al.*, 1991). The oldest syn-tectonic basins in the Sevier belt coincide with the age of syn-tectonic magmatism in the Sierra Nevada and Idaho Batholiths to the west (DeCelles, 2004 and Fig. 3-1 in Fitz-Díaz *et al.*, in press).

Comparing our data with the ages of the classic Sevier and Laramide orogenic belts indicate that D1 deformation in the MFTB seems to have occurred at least in part during the Sevier Orogeny. Also, D2, the second episode of deformation in the MFTB, that accommodated minor shortening, seems to be coincident in time with the Laramide Orogeny. In this portion of the MFTB the deformation style of Laramide age structures (D2), however, does not correspond to the thick-skinned basement-involved style displayed by Laramide structures in the type location of the Western US.

3.5 The role of the platforms in the deformation of the basins

In a Coulomb critically-tapered wedge the taper angle is controlled by the angle of internal friction of the wedge material, friction at the base, and pore fluid pressure (Davis *et al.,* 1983). The angle of internal friction and fluid pressure (expressed as the lithostatic/hydrostatic pressure ratio) exert important controls on the deformation of rocks within the wedge. On the other hand, friction and the fluid pressure along the underlying detachment also play a critical role in determining the critical taper angle, and determining whether or not the wedge is displaced or thickened through internal deformation.

The platformal and basinal rocks in the MFTB constitute two distinct facies, despite the fact that the dominant lithologies of both are carbonates. The platform carbonates are massive or thickly bedded and are mainly calcite and dolomite. On the other hand, the basinal carbonates (calcite rich) are typically thinly bedded, with interbeds of carbonaceous mudstone, chert, and thin (<1 cm) layers of shale.

Platforms and basins present striking differences in the style of deformation, which is thrust-dominated in the platforms, and fold dominated in the basins. Reasons for such differences are explained in the previous chapter. Independently of the variations in the deformation style, shortening of the MFTB Platform carbonates is significantly less (55% for the EDT and 35% for

the VSLPP) than the shortening accommodated by the basinal strata (about 70% close to the platform borders) on either side. This deformation could be controlled by changes in the angle of internal friction which could have been enhanced in the platforms by the presence of dolostone along the borders of the platforms and diagenetic dolomite mixed with calcite in the interior of the platform, which is scarce in the basins.

This difference in the amount of shortening makes it easy to visualize the platforms as relatively rigid objects, representing local backstops concentrating shortening in the adjacent basins. For this to occur, the displacement along the detachment zone underneath the platforms must be facilitated by a "weaker rock". In the western side of the area underneath EDP and the ZB, the lack of seismic information or borehole records makes it difficult to predict the lithology along the *décollement*. In VSLPP, however, borehole records in the surrounding areas and the exposure of anhydrite towards the base of the platform (Fig. 3-3a and b), makes it likely that the detachment lies within these weak rocks, facilitating displacement. This is not the case for the TMB, where strongly sheared carbonaceous shale and limestone of the Santiago Fm. is pervasively present in the detachment zone. The rocks of the Santiago Fm. are mechanically stiffer than evaporites, therefore less efficient in accommodating displacement.

The combination of a competent massive dolomitized limestone within the VSLPP and a weak detachment, make it possible that the VSLPP accommodated a small internal shortening and a large displacement, locally acting as a "backstop" that induced deformation in the TMB. The deformation in the TMB, as in the ZB, was accommodated by internal buckling (Biot 1965), folding unrelated to faulting, and that was the result of stress applied parallel to a multilayer that possesses anisotropy (alternating layers with different viscosity and stiffness). This phenomenon has been documented in nature and experiments (e. g. Cobbold *et al.*, 1971).

Because of the mechanical contrast between platforms and basins, the platforms play a major role in establishing boundary conditions for the deformation of the basins. In the ZB, there is an intense internal deformation of fairly constant magnitude (Fig. 3-9c) and a constant orientation of structures within the same stratigraphic horizon. These characteristics can be related to the fact that this basin is confined between two platforms. In the TMB, however, there is a deformation gradient from west to east (Fig. 3-9d), corresponding with a a (fixed) boundary to the west (the VSLPP) and a free boundary to the east (the toe of the MFTB).

3.6 Kinematics of deformation within the basin

3.6.1 Representative vertical sections

Two well exposed sections in the middle of the Zimapán and Tampico-Misantla Basins (Figs. 3-7a and 3-8a) were chosen to analyze fold kinematics. In these two sections we analyzed fold-geometry to estimate strain at the different stratigraphic/structural levels. The estimated finite (total) strain is characterized by the axial ratio of the strain ellipse and orientation of the long axis of this ellipse, θ'. In deciding how to estimate strain we took into account qualitative field observations interpreted in light of folding theory. This allowed the selection of an appropriate method to estimate strain. For the quantitative analyses we applied a number of different methods, including: the one described in Figure 3-9 (which is based on Ramsay 1974), the Wellman method (Wellman, 1962; Shah and Srivastava, 2006), the method of Aller *et al.* (2008), and estimating strain within the layers by analyzing distortion of calcispherulid shells with the Rf/phi method (Dunnet, 1969; Lisle, 1985). The results are presented in the second column of Table 3-1.

In each section, several different stratigraphic/structural horizons or levels could be distinguished, taking into account the dominant lithology and folding style (tightness, asymmetry, hinge shape, and presence/absence of pressure-solution cleavage). Each horizon was assigned a thickness (with precision of ± 100m) on the basis of field observation, and a characteristic column was drawn for each basin.

Figure 3-7 illustrates the dominant folding styles within the different horizons in the Zimapan Basin. This section shows how deformation was accommodated in the upper units of the Zimapan Basin – the Tamaulipas and Trancas formations (see Fig. 3-4c for reference) – and the transition between these units and between these units and those above and below. The two units remain in their original stratigraphic position, and their overall thickening seems to be due to folding. The Tamaulipas Formation consists of mudstone and wackestone interbedded with abundant chert bands and thin layers of shale, while the Trancas Formation is dominantly carbonate siltstone interbedded with calcarenite and volcanic greywacke. In the Tamaulipas Formation, the deformation is mostly accommodated by asymmetric, steeply inclined, tight to close folds and pressure-solution cleavage is only observed in the shale layers. In contrast, deformation of the Trancas Formation is accommodated by close to open folds with rounded hinges and a pervasive pressure-solution cleavage. In the lithological transitions the asymmetry of folds is accentuated and the dip of the axial planes reduced, sometimes to the point that it becomes sub-parallel with

the contact. One way to explain these variations in axial plane dip is to relate them to ramps and flats of major thrust faults, in such a way that the low angle axial plane folds develop associated with shear along flats, while the steeper axial plane folds develop adjacent to ramps. However, the amount of displacement required to produce the observed shortening should also produce significant stratigraphic off-sets or anomalous thickness variations in the different units, and these are not observed.

Figure 3-8 illustrates the dominant folding styles within the different horizons in the Tampico-Misantla Basin (the thickness-scaled representation can be consulted in Fig. 3-10b). It includes most of the stratigraphic units involved in the deformation within the wedge down to the detachment zone (see Fig. 3-4c). All the units preserve their stratigraphic positions without duplication, except for the Tamaulipas Formation in the upper part of the cross-section, which is duplicated by thrusting. This section includes slightly deformed redbeds (Cahuasas Fm.) under the detachment; strongly sheared and faulted carbonaceous shale (lower part of Santiago Fm.) along the detachment; recumbent folds in association with thrust faults developed in carbonaceous limestone with scarce chert bands (upper part of Santiago Fm.); above this gently to moderately inclined asymmetrical tight folds with sharp hinges in carbonaceous shale with abundant shear bands (Tamán and Pimienta Fms.); above this upright chevron folds in layers of non carbonaceous limestone with chert bands (Tamaulipas Inferior Fm.); and above this steep folds in thinly bedded limestone with chert bands (Tamaulipas Superior Fm.). We can see that in general, the axial planes of folds are steeper upwards and become sub-parallel to the detachment zone in the lower portions of the section. This gradual variation in axial plane dip can be explained in the framework of the orogenic wedge model by small differences in the strength of the rocks in the detachment and within the wedge, and with smooth stratigraphic transitions. This kind of fold profile has been observed in analogue models focused on analyzing deformation in carbonate basins influenced by the presence of adjacent platforms (see Fig. 3-2 of Dixon, 2004), a situation analogous to that in the MFTB.

3.6.2 Kinematic models

We analyze the variation in fold style and finite strain in the two vertical sections represented by the structures illustrated in Figs. 3-7 and 3-8 by considering two kinematic models. In doing so we make these general simplifying assumptions: (1) Deformation is plane strain and there is no volume change. (2) The deformation producing the asymmetrical folds is a combination of pure shear and simple shear, and the long axis of the bulk total strain ellipse (represented by angle θ') is parallel to the axial planes of the folds. (3) The trains of asymmetrical chevron folds in the ZB

and TMB were formed in two stages: first one of buckling that gave rise to symmetrical chevron folds, followed by flattening that produced the observed changes in layer thickness and that helped develop asymmetry. (4) The deflection of the axial planes of the folds from the vertical is due to simple shear, which also contributed to the development of fold asymmetry and different limb lengths. (5) Discrete displacement along the contacts between the different stratigraphic units can be neglected. We indicate in the cross-section the places where thrust faults were observed in the field.

Assumptions 2 and 3 are supported by Dixon's (2004) analogue models, for which he analyzes the effect of a stiff platform on the deformation of an adjacent softer well-bedded basinal unit. His physical models show that in most cases the basinal layers develop symmetrical buckle folds that preserve layer thickness in the initial states of deformation and progressively become asymmetrical and inclined, with thickened fold hinges.

The analysis of the geometry of trains of chevron folds in the same horizon along the whole cross-section of Figure 3-3c strongly supports assumption (3). Assumption (4) is also supported by Dixon's analogue experiments and the analysis strain associated with the trains of chevron folds in this study (Fig. 3-9). The folds analyzed in the ZB and on the western side of the TMB exceeded the locking angle for chevron folds (Ramsay, 1974) and accommodated a shortening of close to 45% (after removing flattening), while the folds towards the eastern side of the TMB show a progressively more open interlimb angle and do not show evidence of flattening, suggesting that they did not reach the locking angle. These variations in geometry from much evolved folds in the ZB to less deformed folds at the front of the fold-thrust belt, strongly support the idea of the basinal layers being initially deformed by buckling, giving rise to trains of symmetrical chevron folds, followed by flattening, which accentuated the asymmetry, in a deformation that involved both pure shear and simple shear. The fact that pressure solution is locally important suggests that assumption 1 is not fully satisfied, and the fact that different units (e.g. the Tamaulipas and Trancas formations in the ZB) exhibit different pervasiveness of pressure solution cleavage implies further that assumption 5 is not fully satisfied.

3.6.2.1 Pure Shear + Simple Shear models

The different units in the representative sections in the two basins are scaled according to thickness in Figure 3-10. and the rock columns so produced provide the basis for two different kinematic models. In the first model (Figs. 3-10a and b, for ZB and TMB respectively) we assume that the different units (1 to 10, in Figs. 3-10 a and b) experienced a homogeneous pure shear in a first stage of deformation, followed by different amounts of simple shear necessary to

produced folds with the observed asymmetry, as expressed by variations in the axial plane dip of the folds in Figs. 3-7 and 8). Mathematically this is expressed by the linear transformation matrices, $\boldsymbol{D}_{ps}$ and $\boldsymbol{D}_{ss}$, which combined are equivalent to a transformation $\boldsymbol{D}$.

$$\boldsymbol{D} = \boldsymbol{D}_{ss}\boldsymbol{D}_{ps} = \begin{pmatrix} 1 & \gamma \\ 0 & 1 \end{pmatrix}\begin{pmatrix} k & 0 \\ 0 & 1/k \end{pmatrix} = \begin{pmatrix} k & \gamma/k \\ 0 & 1/k \end{pmatrix} \qquad 1)$$

where the pure shear in the horizontal (x-direction) is given by k and the simple shear by γ. We applied a pure shear (k=0.5) corresponding to a maximum shortening of 50% taking into account the 45% shortening that we estimated through the analysis of chevron folds (Fig. 3-9) and taking into account the fact that buckled layers experience a small amount of homogenous shortening prior to fold growth at nearly constant limb length (e.g. Hudleston and Treagus, submitted).

Our reference direction (x-axis) is horizontal, since shortening is sub-parallel to this direction. By applying a bulk pure shear (k=0.5) to the layers, we can produce upright buckle folds with an interlimb angle of between 65-70°, as sketched in figures 3-10a and b. The amounts of simple shear that must be added to this to produce folds with axial plane dips similar to the ones observed in the field (column 5 in Table 3-1, which is the median value of the range given in column 3) are given in the sixth column of Table 3-1. The sketches in figures 3-10a and b illustrate how pure shear might produce folding by bucking in a first stage of deformation and how asymmetry and flattening of folds can be related to the subsequent simple shear.

Even though this simple model illustrates the overall effects of buckling and flattening during folding, the axial ratio of the finite strain ellipse associated with the folds in each horizon, as calculated from eq. 1 (Column 4 in Table 3-1) is either larger or smaller than our estimated ranges (Column 2 in Table 3-1). We therefore consider an alternative model.

3.6.2.2 General shear kinematic model

There are two differences between the first model outlined above and the second model. One, we do not assume that the horizontal shortening experienced by all units in the rock column is the same, and two, we substitute general shear for the model in which simple shear precedes pure shear. We follow the method and nomenclature of Tikoff and Fossen (1993) in combining simple shear and pure shear into general shear, in which the two components occur simultaneously. The basic assumptions 1 through 5 above remain the same. The deformation matrix is now given by:

$$\boldsymbol{D} = \begin{pmatrix} k & \Gamma \\ 0 & 1/k \end{pmatrix} \qquad 2)$$

where Γ is the effective shear, $\Gamma = \frac{\gamma(k - 1/k)}{2\ln k}$.

In general shear every finite strain ellipse (characterized by its axial ratio and orientation) is the result of a unique combination of k and Γ. By using the average estimates of strain magnitude and orientation in the two characteristic cross-sections, determined from the strain analysis using the folds, and using equation 2 and the equations given in Appendix B of Ramsay and Huber (1983) we calculated k and Γ for each horizon for the two analyzed cross sections (1-10 in Fig. 3-10). The results are given in the columns 9 and 10 of Table 3-1, and represented diagrammatically in Fig. 3-10c and d.

We see in Table 3-1 and Fig. 3-10 c and d that the pure shear and simple shear components vary among the ten different horizons in the two analyzed cross-sections. In the case of the Zimapan basin, the variations in folding style and the amounts shortening (k) and shear (Γ) required to match the estimated finite strains in the different horizons are not systematic. More shortening and less shear is required to produce the steeply inclined asymmetrical folds, while less shortening and more shear is required to produce the nearly recumbent folds under a general shear regime (Table 3-1). The alternating distribution of steeply inclined and almost recumbent folds in the analyzed cross-section (Fig. 3-10 a and c) might be due partly to stratigraphic heterogeneity and partly due to the nature of the propagation of deformation within the basin. If deformation in the Zimapan Basin developed without internal thrusts, then the shortening should be almost independent of stratigraphic level, regardless of the mix of pure shear and simple shear, with the whole package riding eastwards on the basal detachment. If there are internal thrusts, and they developed in the classic piggy back, forward propagating style, then we would expect to see less shorting at deeper levels, reflecting the progressive incorporation of deeper stratigraphic units into the wedge (see for example the detailed measurements of shortening by Lebel *et al.*, 1996, in the Foothills of the Canadian Rockies). The fact that we do not observe significant internal thrusts, which would repeat stratigraphy, and the fact that there is not a simple pattern of increase in shortening upwards, suggest either that there was some minor out-of-sequence thrusting to create irregular variations in the amount of shortening with depth (as illustrated in Fig. 3-11a), or that there is more complex deformation partitioning in the basinal strata that does not involve duplication of units by thrusting. It is not surprising that the shortening within individual units

might be variable, although the fold data in Fig. 3-9 suggest that shortening on average is fairly const across the basin.

In the TMB (Figs. 3-10b and d and 3-11b), the situation is simpler. The pure shear (shortening) component of deformation increases towards the upper part of the section, in the younger units, while the simple shear component decreases. This systematic variation is commonly observed in fold-thrust belts that experience in-sequence forward propagation of thrusts (Elliott, 1976, Boyer and Elliot, 1982) where the strength between the detachment and the rocks within the wedge are not very different. This phenomenon has been documented in the foreland of the Canadian Rocky Mountains Fold-Thrust Belts, where shortening is mostly accommodated by thrusting (Lebel *et al.*, 1996); as well as in physical experiments (Dixon, 2004). In the TMB, however, later out of sequence thrusts might have accentuated deformation in the upper part of the Tamaulipas Fm.

3.7 Conclusions

Deformation in the Mexican Fold Thrust Belt is thin-skinned and occurred in two phases, D1 and D2, with D1 being far the most important in producing the observed structures. D2 gave a modest penetrative overprint to D1 and is also manifest in kilometer spaced small displacement thrusts. The occurrence of syn-tectonic turbidites (Soyatal Fm.) suggests that D1 on the western side started in the Turonian and finished in the East in the Maastrichtian. The absence of D1 structures in Paleogene clastic deposits to the front of the MFTB indicates that D2 can be as old as the Paleocene-Eocene. D1 structures might be related in time to the Sevier Orogeny, while D2 structures might be the manifestation of the Laramide Orogeny in the area.

A systematic study of D1 structures along a cross-section in central Mexico, allows us to analyze the role of the stratigraphy in the deformation of the marine sedimentary cover within the fold-thrust belt wedge and along the detachment. The carbonate cover sequence is mechanically heterogeneous as a result of lateral facies variations corresponding to paired platform-basin depositional environments, resulting in more or less competent rock packages. This mechanical heterogeneity favored different deformation styles (dominated by km-spaced thrusts in the platforms and by mesoscopic folds in the basins) with different amounts of overall shortening deformation being accommodated in the different segments. Vertically, the stratigraphy controls variations in strength between the detachment and the rocks within the wedge which in turn plays an important role in the distribution of strain within the wedge.

The geometry of mesoscopic folds in the different stratigraphic units in the basins shows a consistent geometry. Based on observations and measurements of these folds, we estimated and averaged strain for distinct stratigraphic units within each basin and the transition zones between units. The overall pattern of strain, and strain magnitude and orientation within each unit/stratigraphic level, can be accounted for by models involving pure shear and simple shear. In the models we assumed that the folds originated as symmetric upright chevron folds and that their current inclined orientation is a result of simple shear, with their axial planes parallel to the maximum bulk finite extension direction. In one model we assumed that shortening is constant within each basin and the same at all stratigraphic levels. This does not give a good match to the strain magnitudes at the various levels. In a second model we assumed general shear and computed the amounts of pure shear and simple shear required to produce the strains determined from the fold measurements. For the Zimapan Basin, this model, with some out-of- sequence thrusting or with some other form of strain partitioning could explain the observed strain pattern. For the Tampico-Misantla Basin, this model, involving normal in-sequence thrusting can well explain the observed strain variations

Overall, we get a reasonable approximation of the average strain in the basins if we weight the contributions of pure and simple shear in the general shear model by the thickness of the different horizons.

We finally conclude that mesoscopic analysis of folds provides a good means of estimating strain in fold-dominated parts of fold-thrust belts and provides the basis for developing kinematic models of deformation in fold-thrust belts and the evolution of basins during deformation. .

Figures and Tables

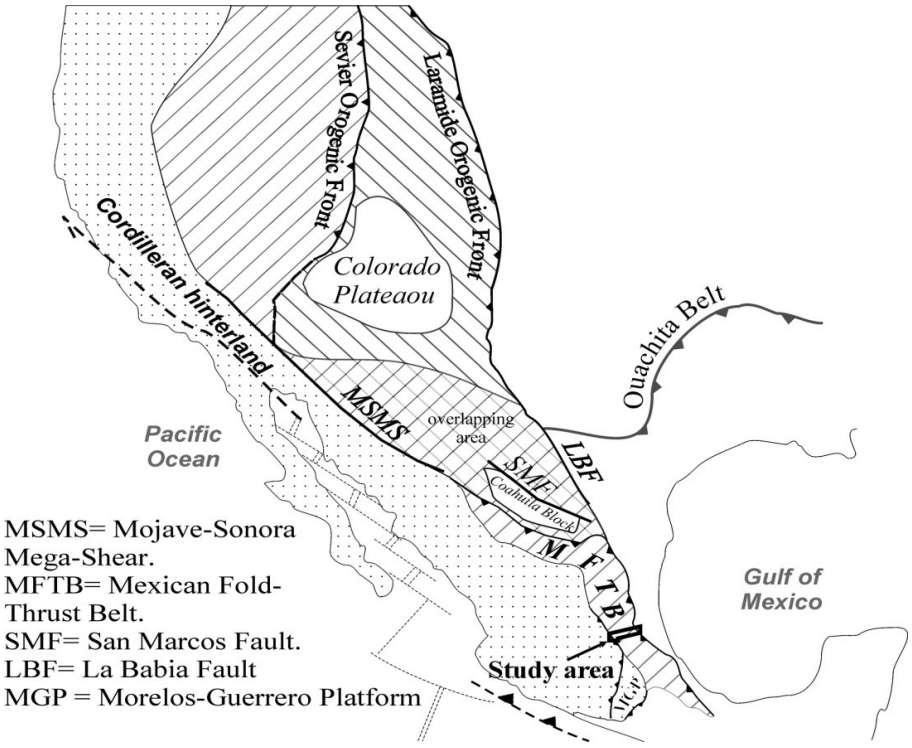

Figure 3-1. Generalized tectonic setting of the North American Cordillera showing the differences observed in the fold-thrust belt along its eastern edge (modified from Fitz-Diaz *et al*., 2010, in press).

Figure 3-2. Chart synthesizing stratigraphic and lithological variations of units along the studied cross-section, with characteristic columns for each major paleogeographic element. Each column displays the characteristic lithology of the different stratigraphic units, with their formational names, age constraints and estimated thicknesses. Also indicated are the units which show field evidence for have been affected by pre-D1, D1or D2 deformations. This stratigraphical information is a summary from a number of works (Imlay, 1944; Sergerstrom, 1961; Suter 1980, 1984 and 1990; Carrillo-Martínez, 1989; Carrillo-Martínez et al., 2001; Hernández-Jaúregui, 1997; Dávila-Alcocer et al., 2009) and new age constraints from detrital zircon dating. Thickness estimates come from borehole records and field observations. The grey dashed lines correlate units deposited between Berriasian and the upper limit of Cenomanian. Notice the abrupt facies changes in the different paleogeographic elements for this time range. Figure 3-2. Chart synthesizing stratigraphic and lithological variations of units along the studied cross-section, with characteristic columns for each major paleogeographic element. Each column displays the characteristic lithology of the different stratigraphic units, with their formational names, age constraints and estimated thicknesses. Also indicated are the units which show field evidence for have been affected by pre-D1, D1or D2 deformations. This stratigraphical information is a summary from a number of works (Imlay, 1944; Sergerstrom, 1961; Suter 1980, 1984 and 1990; Carrillo-Martínez, 1989; Carrillo-Martínez et al., 2001; Hernández-Jaúregui, 1997; Dávila-Alcocer et al., 2009) and new age constraints from detrital zircon dating. Thickness estimates come from borehole records and field observations. The grey dashed lines correlate units deposited between Berriasian and the upper limit of Cenomanian. Notice the abrupt facies changes in the different paleogeographic elements for this time range.

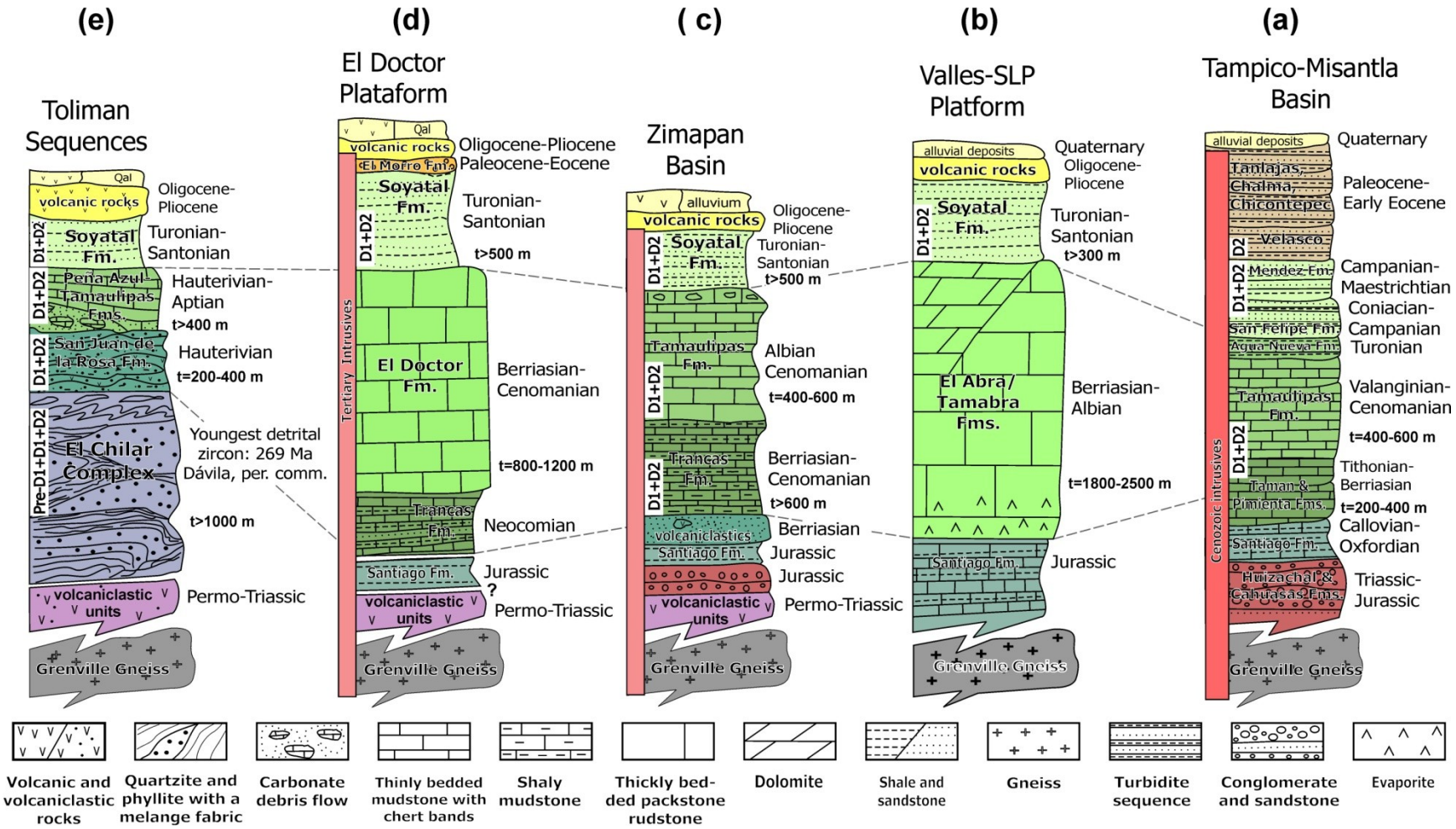
(e)
Toliman Sequences
Qal
volcanic rocks
Oligocene-Pliocene
D1+D2
Soyatal Fm.
Turonian-Santonian
D1+D2
Peña Azul Tamaulipas Fms.
Hauterivian-Aptian
t>400 m
D1+D2
San Juan de la Rosa Fm.
Hauterivian
t=200-400 m
Pre-D1+D1+D2
El Chilar Complex
Youngest detrital zircon: 269 Ma
Dávila, per. comm.
t>1000 m
volcaniclastic units
Permo-Triassic
Grenville Gneiss
(d)
El Doctor Plataform
Qal
volcanic rocks
Oligocene-Pliocene
El Morro Fm.
Paleocene-Eocene
Soyatal Fm.
Turonian-Santonian
t>500 m
D1+D2
Tertiary Intrusives
El Doctor Fm.
Berriasian-Cenomanian
t=800-1200 m
Tranças Fm.
Neocomian
Santiago Fm.
Jurassic
?
volcaniclastic units
Permo-Triassic
Grenville Gneiss
(c)
Zimapan Basin
alluvium
volcanic rocks
Oligocene-Pliocene
D1+D2
Soyatal Fm.
Turonian-Santonian
t>500 m
Tamaulipas Fm.
Albian-Cenomanian
t=400-600 m
D1+D2
Tranças Fm.
Berriasian-Cenomanian
t>600 m
volcaniclastics
Santiago Fm.
Berriasian
Jurassic
Jurassic
volcaniclastic units
Permo-Triassic
Grenville Gneiss
(b)
Valles-SLP Platform
alluvial deposits
volcanic rocks
Quaternary
Oligocene-Pliocene
D1+D2
Soyatal Fm.
Turonian-Santonian
t>300 m
El Abra/ Tamabra Fms.
Berriasian-Albian
t=1800-2500 m
Santiago Fm.
Jurassic
Grenville Gneiss
(a)
Tampico-Misantla Basin
alluvial deposits
Quaternary
Tantajas, Chalma, Chicontepec
Paleocene-Early Eocene
D2
Velasco
D1+D2
Mendez Fm.
Campanian-Maestrichtian
San Felipe Fm.
Coniacian-Campanian
Agua Nueva Fm.
Turonian
Tamaulipas Fm.
Valanginian-Cenomanian
t=400-600 m
D1+D2
Cenozoic intrusives
Taman & Pimienta Fms.
Tithonian-Berriasian
t=200-400 m
Santiago Fm.
Callovian-Oxfordian
Huizachal & Cahuasas Fms.
Triassic-Jurassic
Grenville Gneiss
Volcanic and volcaniclastic rocks
Quartzite and phyllite with a melange fabric
Carbonate debris flow
Thinly bedded mudstone with chert bands
Shaly mudstone
Thickly bed-ded packstone rudstone
Dolomite
Shale and sandstone
Gneiss
Turbidite sequence
Conglomerate and sandstone
Evaporite

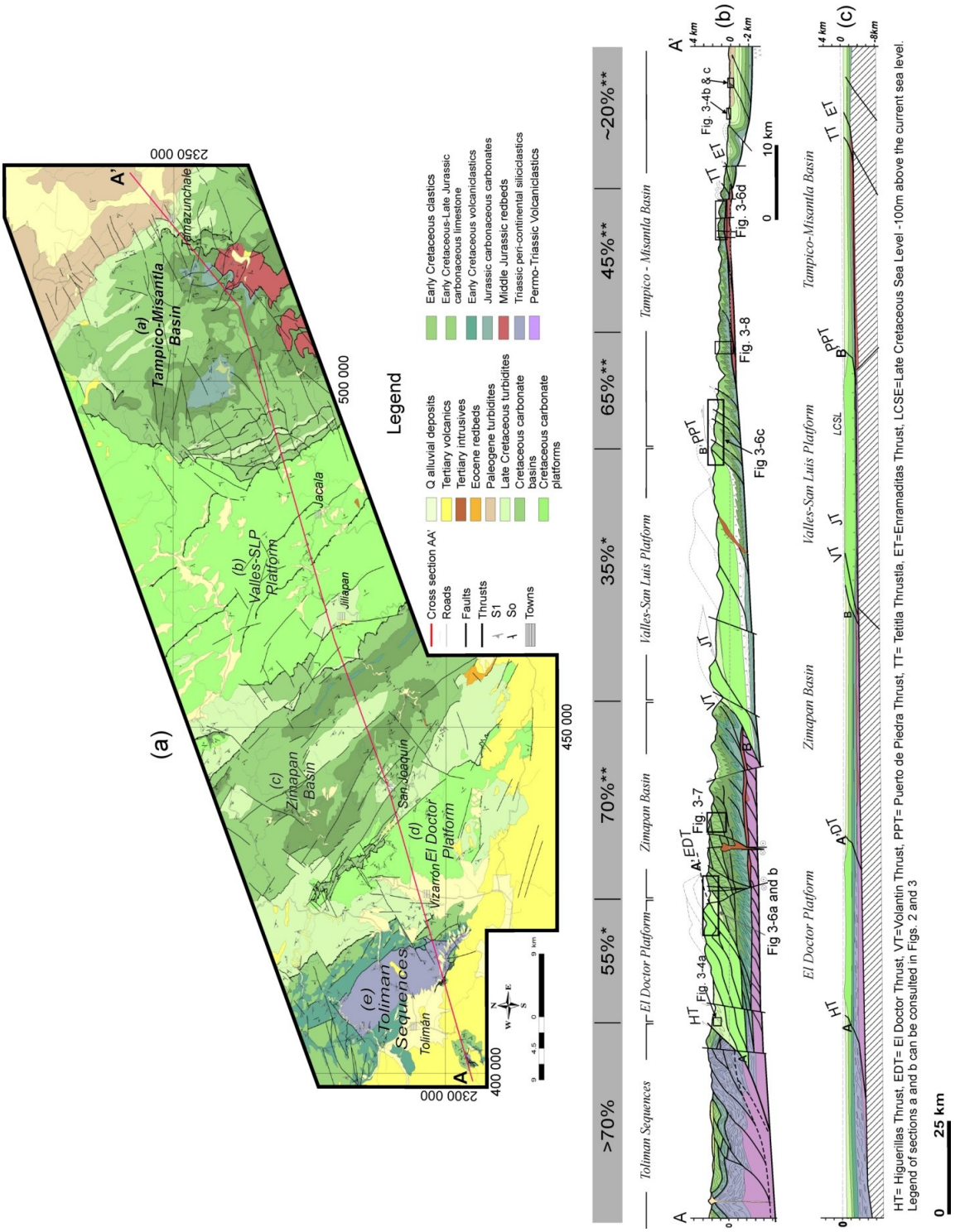

Figure 3-3. (a) Simplified geologic map of the study area in Central Mexico, showing the location of the cross-section AA'. The location of this area in the North American Cordillera is shown in Fig. 3-1. (b) Admissible and partly schematic cross-section of the Mexican Fold-Thrust Belt (cross-section AA') showing the variation of deformational style within the wedge. (c) Restored cross-section AA' showing the distributions of carbonate facies prior to deformation. Modified from Fitz-Díaz *et al.*, in press.

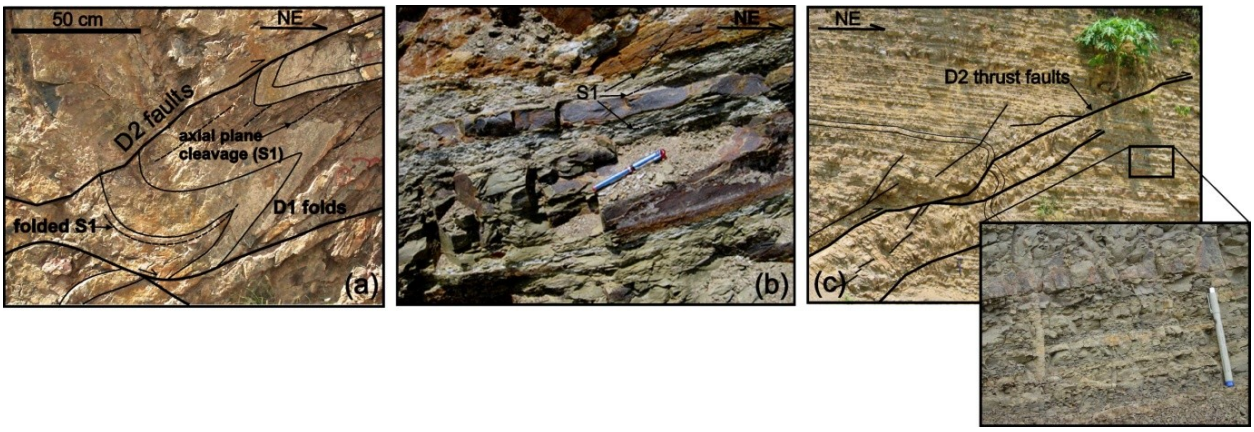

Figure 3-4. (a) Calcarenite and shale of the Soyatal Fm. in the footwall of the Higuerillas Thrust, showing a complex deformation. Note the tight folds, with an associated axial plane cleavage (S1), refolded and affected by later thrust faults. (b) Calcarenite, siltstone, and shale of the Mendez Fm. in the foothills of the MFTB, showing tight folds and a pervasive axial plane cleavage (S1), which in some places is cut by low-angle faults. (c) Calcarenite, siltstone, and shale of the Velasco Fm. to the front of the MFTB, affected by a low-angle thrust fault that accommodates meter scale displacement. Notice the absence of cleavage in the zoomed image.

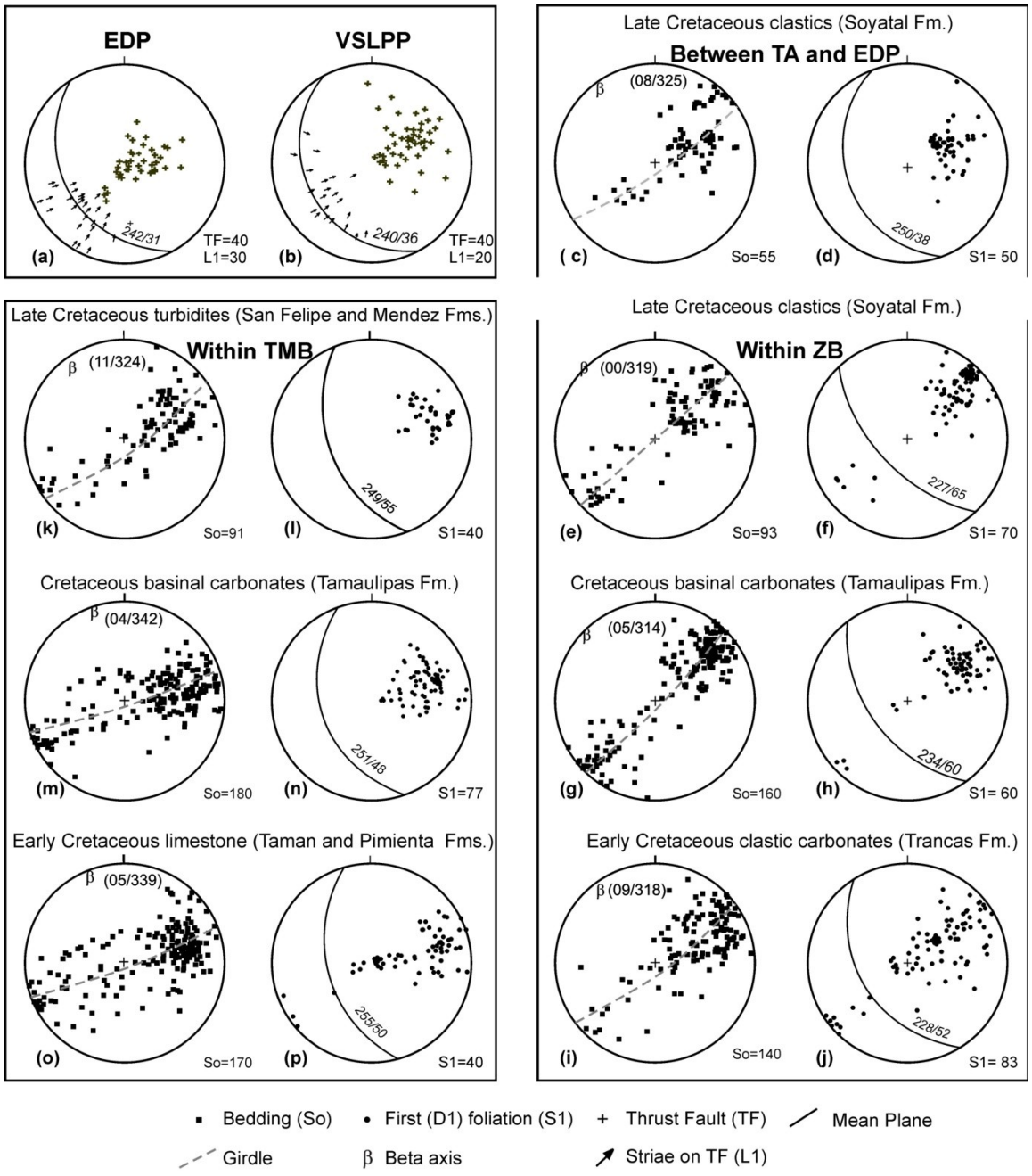

Figure 3-5. Equal-area lower hemisphere projections of structural data, measured in different units, within the different paleogeographical elements (see Fig. 3-3 for reference). Note the deflection in orientation of the beta axis of folds and S1 in the ZB and TMB.

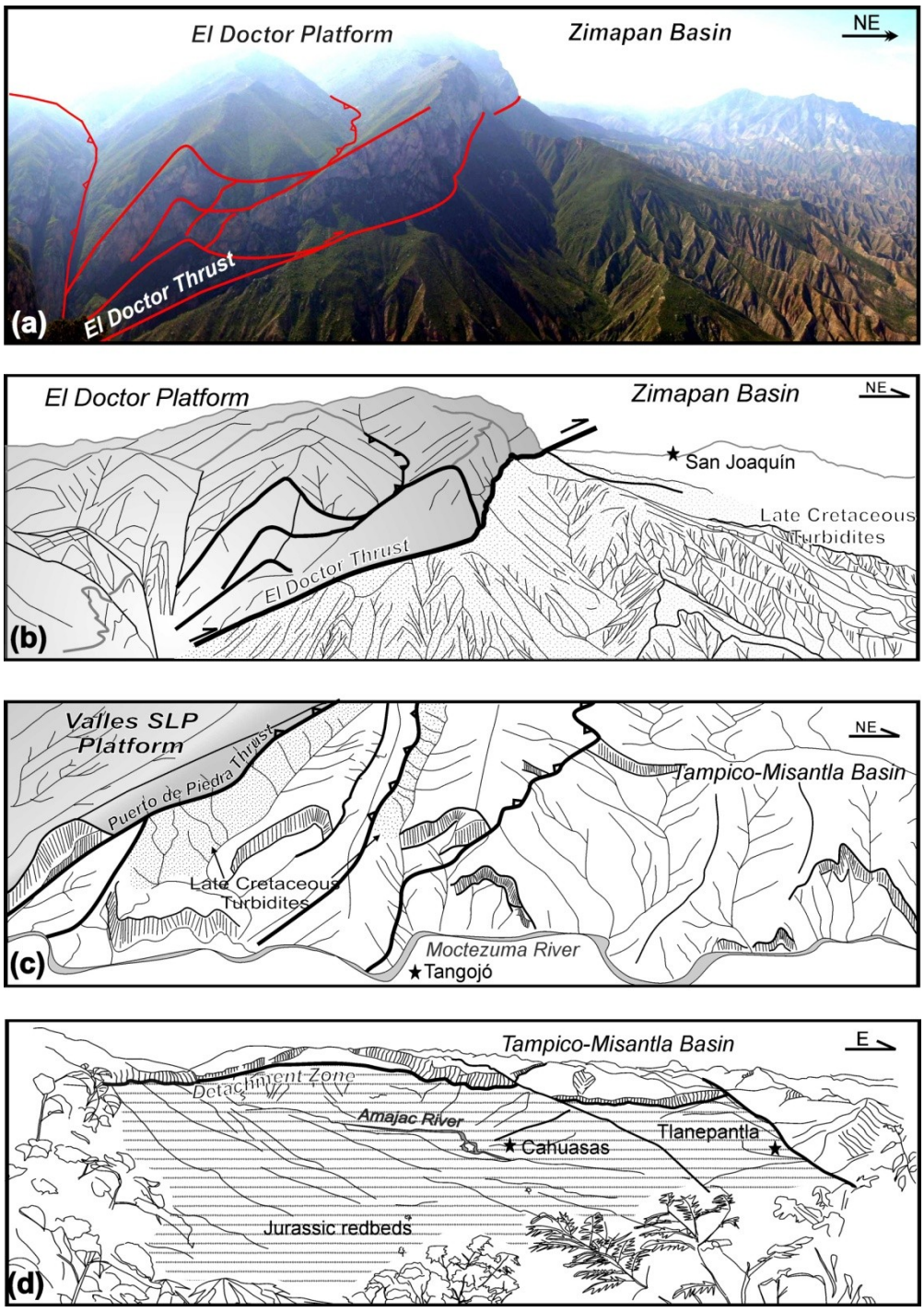

Figure 3-6. Kilometer scale viewof structures in the study area. (a) and (b) Picture and sketch of the contact between El Doctor Platform and Zimapán Basin along the northern margin of the Moctezuma River. (c) Sketch of the panoramic view of the contact between Valles-San Luís Potosí Platform and the Tampico-Misantla Basin along the Moctezuma River. (d) View of the northern side of Amajac River in the Cahuasas area, where the basal detachment of the MFTB is exposed. This detachment is located along the strongly sheared Santiago Fm., which is positioned between (relatively undeformed) Jurassic redbeds and (strongly folded) Cretaceous basinal limestones. In grey, platform carbonates; in white, basinal carbonates; dots, late cretaceous turbidites; dashes, Jurassic redbeds.

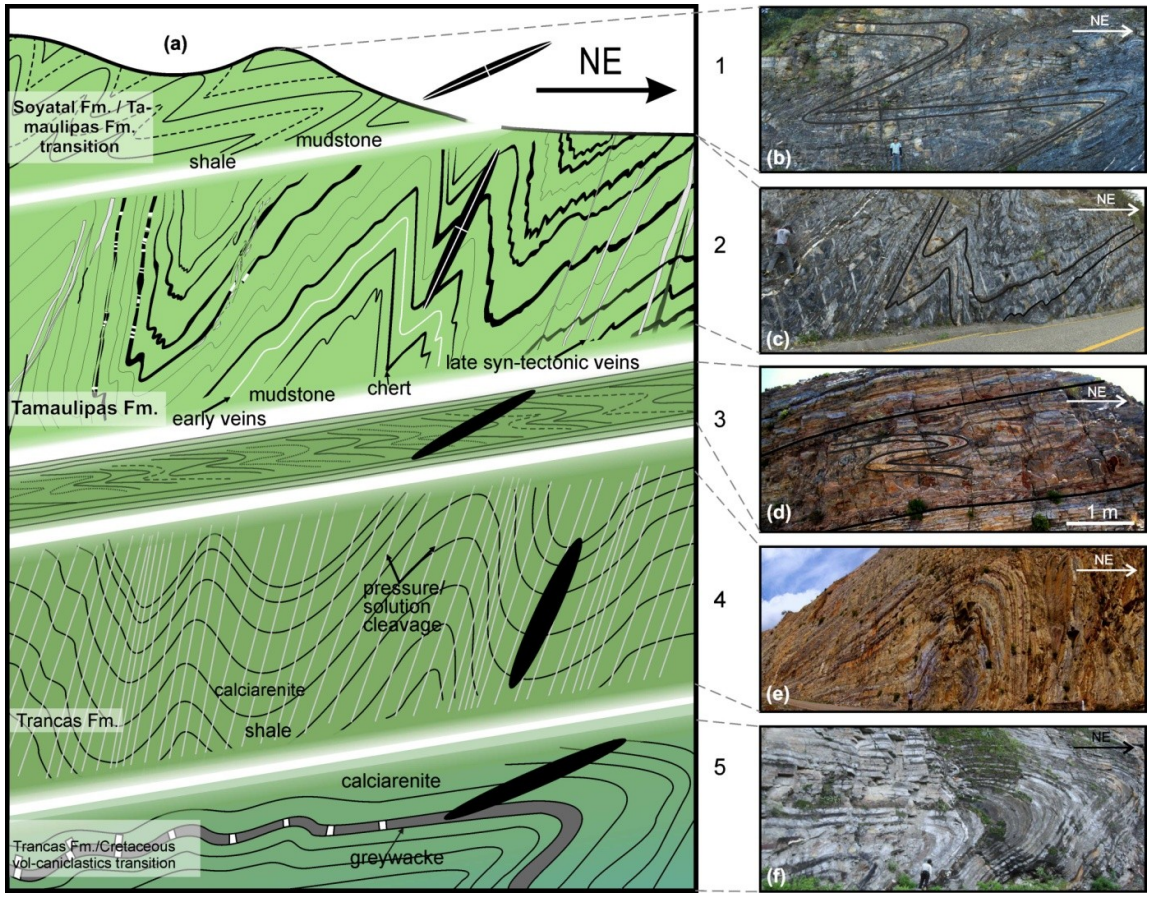

Figure 3-7. (a) Schematic but realistic representation of a typical section in the middle of the Zimapán Basin, showing the dominant styles of folding observed in the different lithological units exposed within the basin. Truncation of the folds at the boundaries of the units is not implied - the folds are presumed to decay towards the boundaries or to deflect the boundaries, since the stratigraphic sequence is preserved across the basin. (b) Typical gently inclined folds observed in mudstone interbedded with calcareous shale, interpreted by stratigraphic position as the transition between Tamaulipas and Soyatal Fms. These folds show considerable amounts of flattening, evidenced by their tightened hinges. (c) Typical folds in mudstone layers interbedded with chert and thinner layers of shale of the Tamaulipas Fm. The folds in the limestone layers are asymmetrical and steeply inclined; they show angular hinges and strong variations in the thickness of the layers, with attenuated forelimbs and thickened hinges. (d) Gently inclined folds in shaly limestone layers interbedded with calcarenite, also showing thickened hinges. (e) Asymmetrical, almost upright fold, in shale layers of Trancas Fm. Note the pervasive axial plane cleavage associated with this fold. (f) Nearly recumbent fold in layers of calcarenite and volcanic greywacke near the transition between the Trancas Fm. and a volcaniclastic sandstone unit.

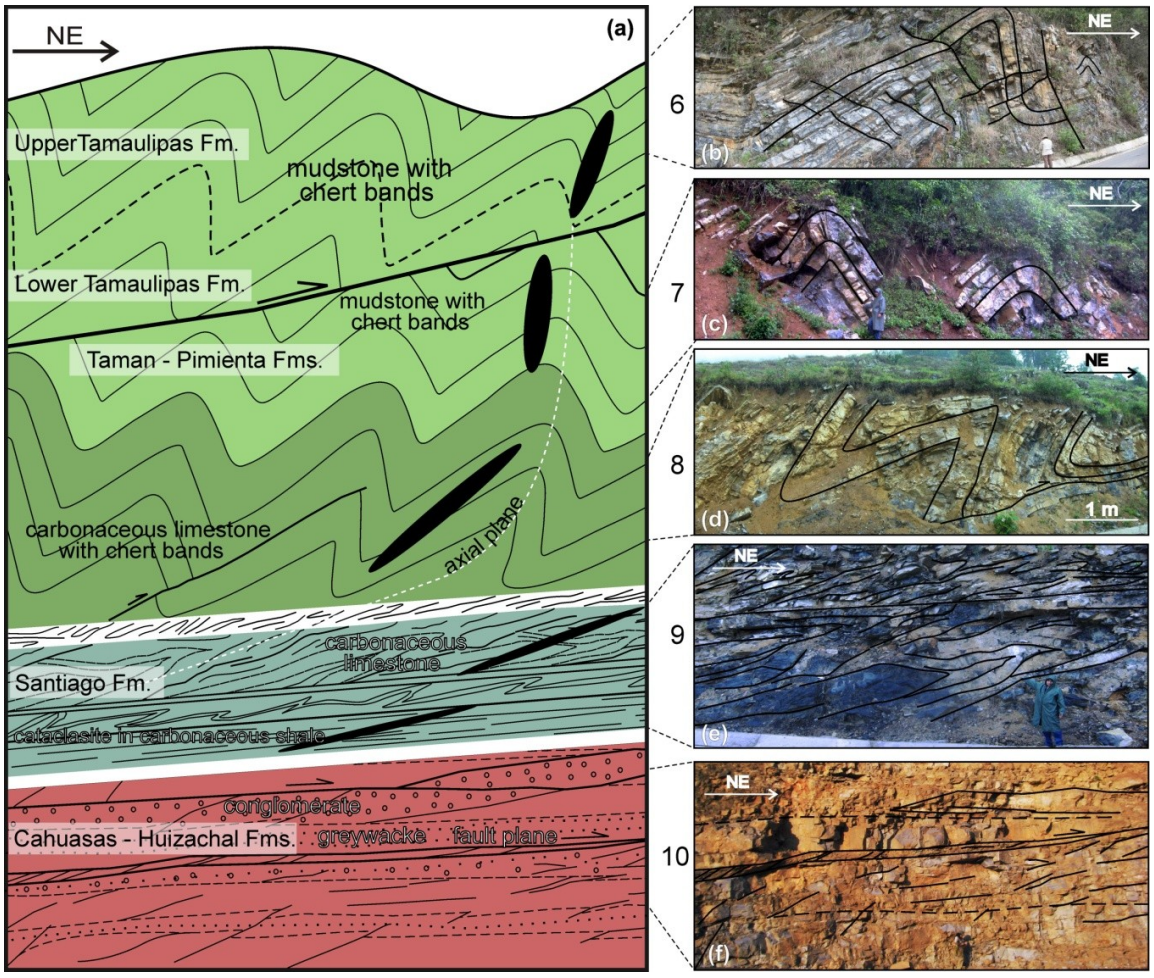

Figure 3-8. (a) Schematic but realistic representation of a typical section in the middle of the Tampico Misantla Basin, showing the geometrical variations in folds observed in the different stratigraphic units exposed. Except for the contact between the Jurassic redbeds and Santiago Fm., and the thrust fault represented in the upper part of the sketch, as in Figure 3-7 the truncation of the folds at the boundaries of the units is not implied - the folds are presumed to decay towards the boundaries or to deflect the boundaries. (b) Asymmetric, almost upright folds in limestone layers of the Tamaulipas Fm. Note the lack of significant variation in thickness of the layer around the fold. (c) Upright close folds in relatively thick layers of the Lower Tamaulipas Fm. (d) Moderately inclined asymmetric folds in carbonaceous limestone of the Taman Fm. The hinges of these folds are thickened, suggesting flattening after buckling. (e) Strongly sheared carbonaceous shale of the Santiago Fm., in which deformation was accommodated partly by isoclinal, nearly recumbent folding and partly by faulting. (f) Low-angle thrusts in continental conglomerate interbedded with quartz rich sandstone.

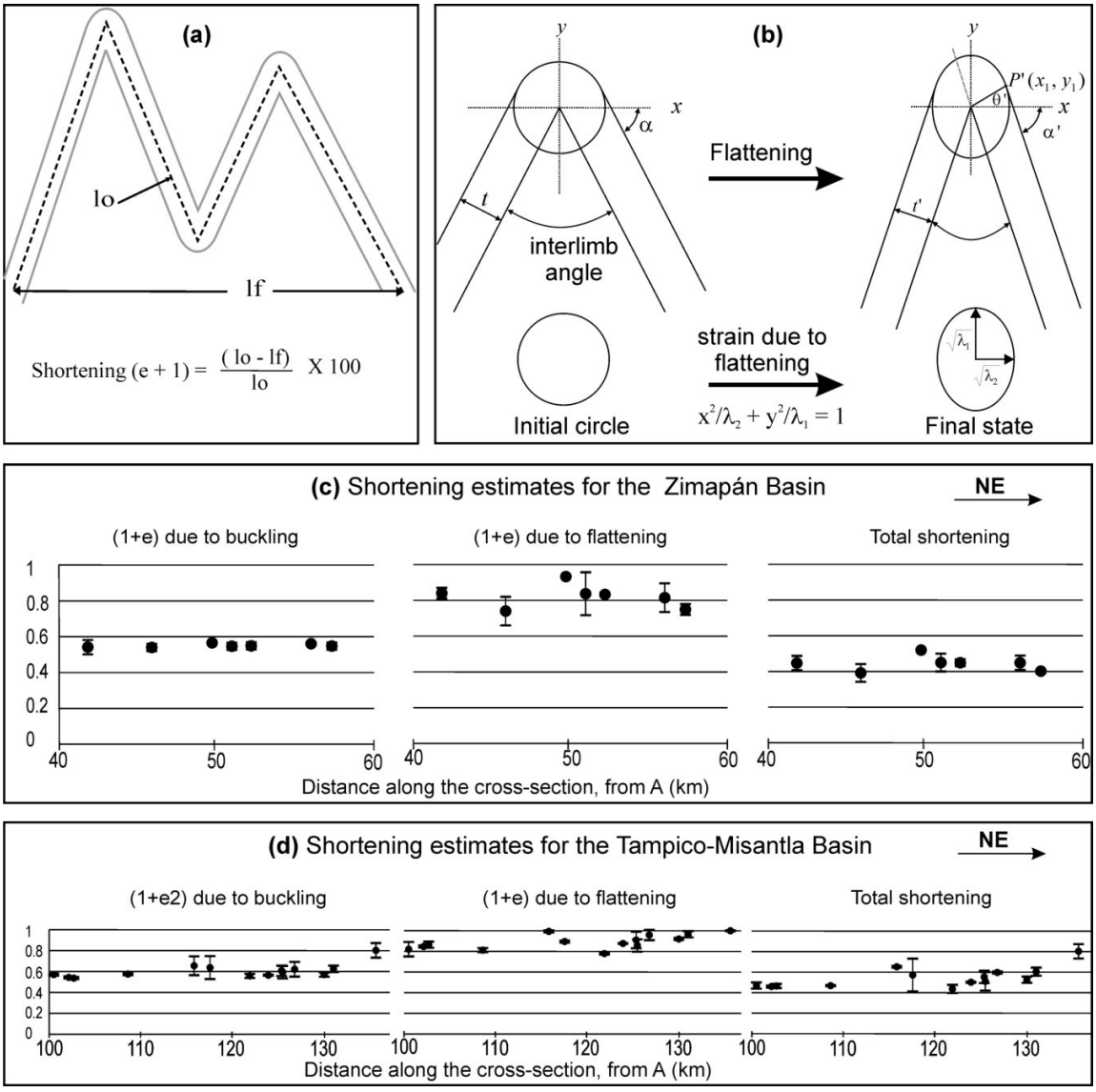

Figure 3-9. Illustration of two methods used to determine shortening in the basins, where the dominant structures are buckle folds, some of which experienced flattening. (a) Direct length of arc method. This was applied only in trains of upright chevron folds in layers that did not show significant variations in thickness or a pervasive axial plane cleavage; (b) Method for determining shortening due to flattening, which takes into account the following geometrical considerations: 1) Following Ramsay (1974), we take chevron folds to have linear limbs and the outer arc of the hinge to be defined by a circle centered at the vertex of the inner arc, with radius equal to the thickness (t) of the layer, which does not change during buckling. 2) If a homogenous flattening is now imposed perpendicular to the axial plane of the fold, the circumscribed circle in the hinge transforms into an ellipse corresponding to the strain ellipse due to flattening. Most of the flattened chevron folds used in this analysis showed elliptical outer arcs in the hinges. Circumscribed ellipses in individual folds, on planes perpendicular to the fold-axes, were retro-deformed to circles (using a computer graphics package) to find the flattening strain. Once flattening was removed, the method in (a) was used to find pre-flattening shortening. We also applied the method described by Ramsay (1974) to determine shortening in chevron folds which gives similar results. (c) Averaged shortening for each train of folds analyzed in the Zimapan Basin plotted against distance from the western edge of the cross-section, for buckling, flattening and for the combination of buckling plus flattening. (d) As in (c) for the Tampico-Misantla Basin.

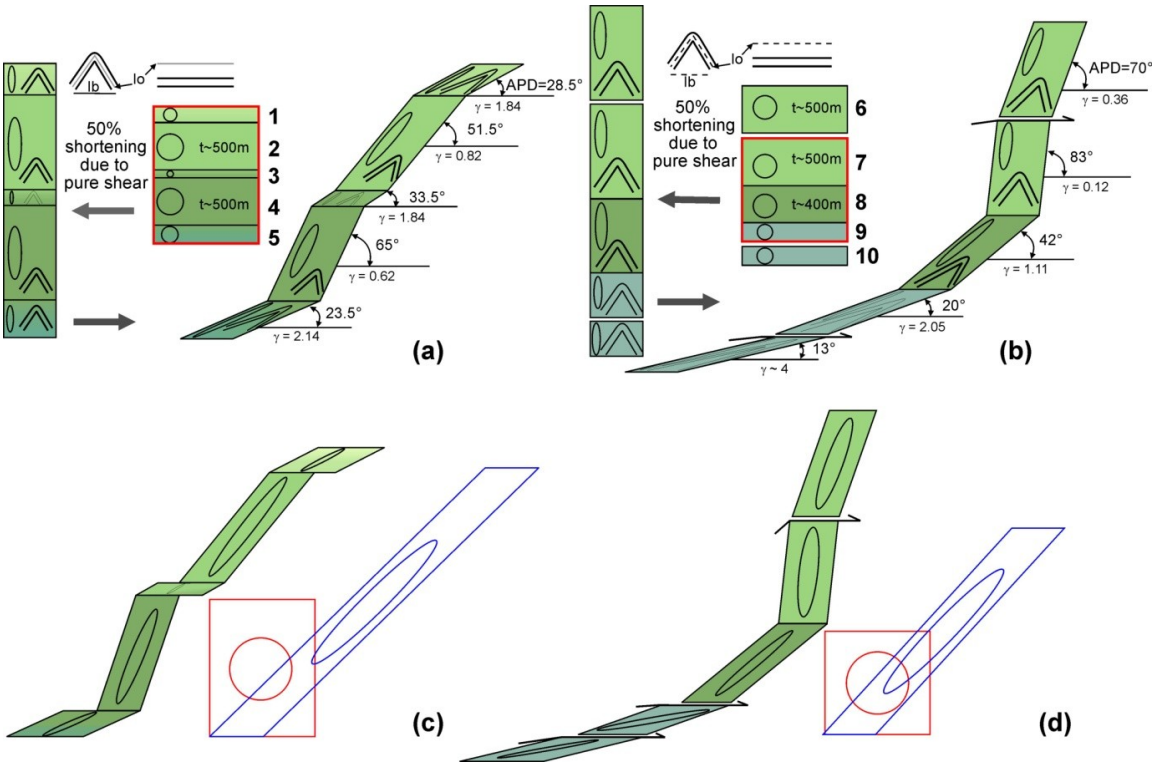

Figure 3-10. Kinematic models to explain the variation in folding styles observed in typical sections of the Zimapán (a) and Tampico-Misantla (b) basins. The left hand columns in (a) and (b) are from the columns in Figs. 3-7a and 3-8a, respectively, with scaled thicknesses of the units. (a,b) Kinematic models involving a homogeneous pure shear followed by simple shear. (c,d) Kinematic models similar to those in (a) and (b) , but involving general shear with the components k and Γ applied to match the estimated strain in the different horizons of the two basins,. On the right sides of (c) and (d) we show the average strain for these sections, found by weighting k and Γ according to the thickness of each horizon. APD= axial plane dip. See text and Table 3-1 for details.

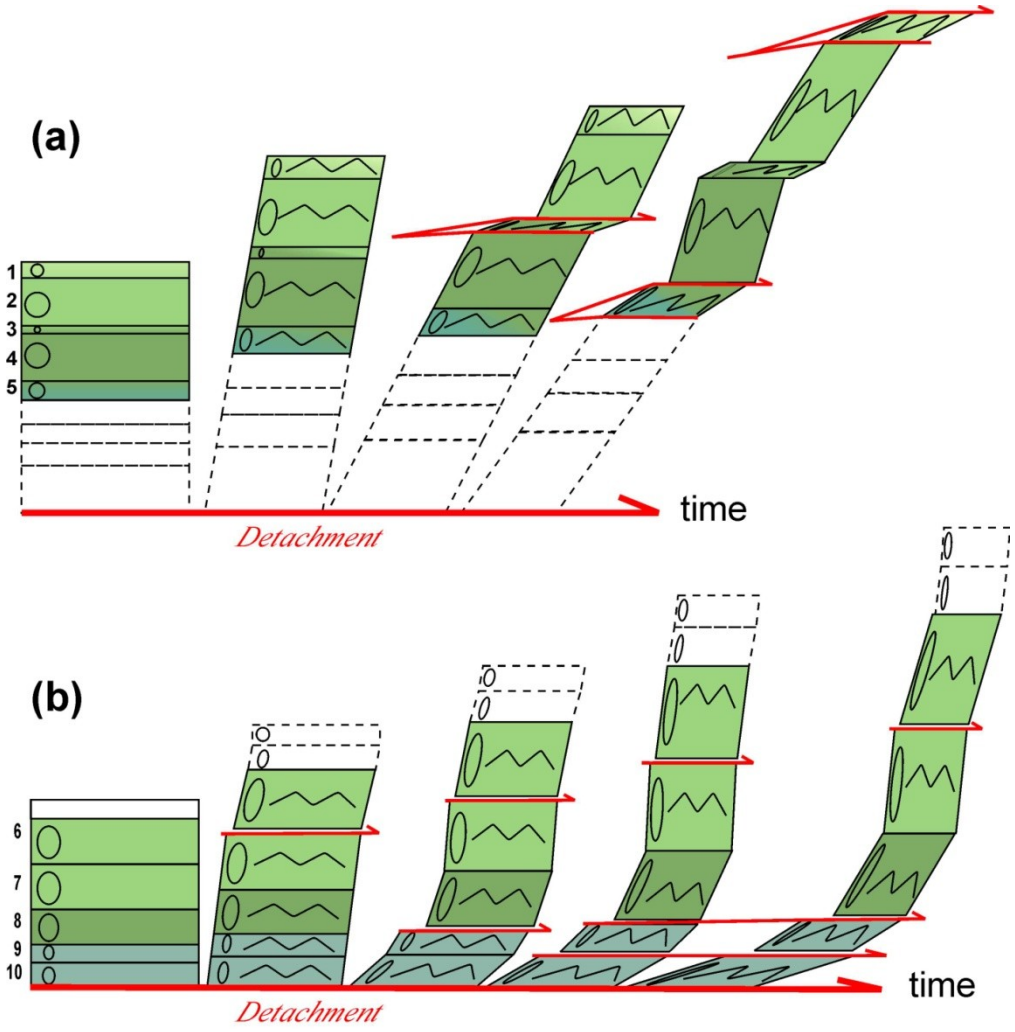

Figure 3-11. Possible paths of progressive deformation for the two basins. (a) For the Zimapan basin, with focused out of sequence shear along the horizons with near recumbent folds. The lower units are not exposed and are represented by dashed lines. (b) For the Tampico-Misantla Basin, with focused in sequence shear along certain horizons to account for the decrease in shortening with depth. See text for further explanation.

Table 3-1. Comparative chart of axial ratios and orientations of the strain ellipse calculated in the kinematic models consisting of pure shear followed by simple shear, general shear, as well as estimates from fold analysis.

Horizon number	Estimates from folds		Pure Shear then Simple Shear, k=0.5			Strain ellipse input for General Shear model		Strain components in General Shear		
	R	θ'	R	θ'	γ	R	θ'	k	γ	Γ
1	10-13	25-32	17.5	28.5°	1.84	11.5	28.5°	0.63 ±0.03	2.99 ±0.96	3.1 ±0.97
2	7-12.5	40-63	6.8	51.5°	0.82	9.75	51.5°	0.43 ±0.03	1.75 ±1	1.95 ±1
3	9-14	29-38	17.5	33.5°	1.73	11.5	28.5°	0.63 ±0.03	2.58 ±0.61	2.75 ±0.64
4	6.5-9.5	57-73	4.9	65°	0.62	8	65°	0.41 ±0.03	1.07 ±0.56	1.25 ±0.67
5	8.5-14.5	20-27	25.3	23.5°	2.14	11.5	23.5°	0.73 ±0.03	2.95 ±0.71	3.00 ±0.71
6	5-6.4	68-72°	4.5	70°	0.36	5.7	70°	0.45 ±0.02	0.7 ±0.1	0.79 ±0.1
7	4.2-5.5	82-85°	4.1	83.5°	0.12	4.65	83.5°	0.46 ±0.03	0.21 ±0.6	0.24 ±.06
8	9-14	36-44°	9.8	40°	1.11	11.5	40°	0.47 ±0.02	2.36 ±0.35	2.6 ±0.4
9	18-25	16-24°	34.3	20°	2.05	21.5	20°	0.65 ±0.05	4.22 ±0.5	4.35 ±.5
10	25-36	10-16°	7	13°	4	30.5	13°	0.83 ±0.12	5.25 ±0.5	5.30 ±0.5

R = Axial Ratio = (1+e1) / (1+e2); θ'= inclination of (1+e1); k = (1+e2), pure shear component of the deformation matrix; γ= tan ψ=simple shear component; Γ=effective shear strain in general shear.

Chapter 4

Fluid flow and water-rock interaction during deformation of carbonate sequences in the Mexican Fold-Thrust Belt

Elisa Fitz-Díaz, David Kirschner, Peter Hudleston, Luc Siebenaller, Antoni Camprubí, Gustavo Tolson and Teresa Pi Puig

Submitted to the Earth and Planetary Science Letters journal

Analysis of mesoscopic structures and related veins allows the history of deformation and role of fluids to be established for part of the central Mexican Fold-Thrust Belt (MFTB), which developed in mostly carbonate rocks with prominent lateral facies changes associated with two platforms and two basins. Fluids played a key role in the deformation, both physically and chemically, by reducing strength and inducing extensional fracturing through raised pore pressure and by providing the medium for solution transfer on the grain scale. Veins are the result of fluid-rock interaction and preserve portions of water related to deformation as fluid inclusions. Facies strongly control deformation styles, with thrusts dominant in the platforms and folds dominant in the basins, and also influence fluid behavior by controlling both porosity and permeability. Structural observations allow distinguishing veins (dominantly calcite) of several generations, emplaced early, during and late/after deformation (V1, V2 and V3 respectively). δ13C and δ18O analyses in calcite from veins and host-rock show that the veins confined within thrust slices are isotopically buffered by the host rock and differ in isotopic composition from veins emplaced along major thrusts or cross cutting thrust-slices. δD analyses of fluid inclusions and clay minerals strongly suggest rock interaction with meteoric fluids in the west (hinterland) and with fluids close to SMOW in the less deformed eastern (foreland) side of the cross-section. We propose a conceptual model that explains the differences in vein-rock isotopic composition, the differences in isotopic composition of aqueous fluids active during deformation, and the progression of clay de-hydration reactions as being related to variations in temperature and intensity of deformation in a growing tectonic wedge.

4.1 Introduction

Fluids play a major role in the development of fold-thrust belts by facilitating sliding along major thrusts and by reducing the effective stresses needed for slip on a basal décollement and on fractures within thrust slices through the effect of elevated pore-fluid pressure (Hubbert and Rubey, 1959). Fluids also provide the means for pressure-solution and solution-transfer at the grain-scale within the rock mass (e.g., Durney, 1972). In addition, fluids are active in the development of veins commonly observed in nature that develop in zones of extension in macroscopic structures, such as folds, that reflect overall shortening (e.g., Ramsay, 1967) or shear (e.g., Hudleston, 1989; Cosgrove, 1993).

The effect of fluids on the development of fold-thrust belts and accretionary prisms has been addressed at length in the literature. Some approaches have considered fluid behavior on the scale of the system as a whole (Hubbert and Rubey, 1959; Davis *et al.*, 1983; Dahlen *et al.*, 1984; Dahlen, 1990), while others have examined the behavior on the scale of individual structures (Hilgers *et al.* 2006; Fischer *et al.*, 2009). Perhaps the best opportunity to study the details of how fluids behave in a tectonic prism is afforded by active accretionary prisms (e.g., von Huene and Lee, 1982; Davis *et al.*, 1983; Moore *et al.*, 1991), linked to studies of older prisms, now exposed, in which the effect of fluid activity on a longer time-scale has been imprinted in the rocks and veins (e.g., Rye and Bradbury, 1988; Vrolijk *et al.*, 1988; Fisher and Byrke, 1990; Fisher and

Brantley, 1992; Moore and Vrolijk, 1992). The tools applied to the problem include structural analysis, geochemical and isotopic analysis, microscopy, spectroscopy, X-ray diffraction, and fluid inclusion studies. Such an approach allows (1) a better understanding of fluid transport mechanisms and fluid-rock interaction during deformation (Cox, 1987; Kirschner and Kennedy, 2001; Richards *et al.*, 2002; Cox, 2007), (2) estimating pressure and temperature conditions of deformation (Fyfe and Kerrich, 1985; Foreman and Dunne, 1991; Crispini and Frezzotti, 1994; Hodgkins and Stewart, 1994; Hilgers, 2006; Fischer *et al.*, 2009), and (3) inferring chemical conditions during precipitation and the possible sources of fluids active during deformation (Grant *et al.*, 1990; Kirschner *et al.*, 1993; Travé *et al.*, 2007; Sample, 2010).

This study examines fluid flow and water-rock interaction along a section of the Mexican Fold-Thrust Belt (MFTB). It takes as its starting point a structural analysis at different scales of observation, from regional to microscopic (Fitz-Díaz *et al.*, in press, Chapter 2) and an associated kinematic analysis (Chapter 3). Within this structural/kinematic framework, we examine the role of fluids during deformation, including kilometer-scale thrusting, mesoscopic folding, and grain scale pressure-solution and solution transfer. To achieve this, we apply various petrographic, microthermometric, geochemical and isotopic tools. The particular questions we address in this paper are: What are the effects of lateral facies variations in the carbonate sequences on fluid-rock interaction within the wedge? How does temperature affect water-rock interaction during deformation? What is the reservoir of fluids active during deformation?

4.2 Regional Framework

The Cordilleran Orogen extends along the western margin of North America and is the result of accretionary processes (Coney *et al.*, 1980; Coney and Evenchick, 1994) related to subduction from Jurassic to Early Cenozoic times (Armstrong, 1974; DeCelles, 2004; Evenchick *et al.*, 2007). In the internal (western) part of the Cordillera, accretion of allochthonous terranes (Coney *et al.*, 1980; Campa, 1983), magmatism and metamorphism were the dominant geological processes. In the external (eastern) part, however, shortening in the rocks of the autochthonous sedimentary cover associated with deformation at very low metamorphic grade prevailed. The eastern part of the Cordillera constitutes the Rocky Mountain Fold-Thrust Belt (RMFTB), which has its southern counterpart in the MFTB (Fig. 4-1).

In the study area the MFTB is only 150 km wide, and the deformed rocks are dominantly carbonates. Sedimentary and stratigraphic studies in the area (Imlay, 1944; López-Ramos, 1983; Suter 1980, 1984, 1987; Valencia-Islas, 1996, Carrillo-Martínez *et al.*, 2001), including

unpublished reports by PEMEX, indicate that the sedimentary sequence is determined by four paleogeographical elements: two thick carbonate platforms, El Doctor Platform (EDP), about 1 km thick, and the Valles-San Luis Potosí Platform (VSLPP), about 2.5 km thick; and two thinner packages of basinal carbonates, regionally known as the Zimapán Basin (ZB) and the Tampico-Misantla Basin (TMB, Fig.4-2). The two platforms consist of Neocomian-Cenomanian thickly bedded to massive wackestones, packstones and rudstones with abundant fragments of mollusks and benthic foraminifera. The basins are characterized by sections of 300-700 m thick Berriasian-Cenomanian thinly bedded limestones, interbedded with thinner shale and bentonite layers. Details of the stratigraphy can be found in Suter (1987).

The MFTB shows all the elements of an orogenic wedge (Davis *et al.*, 1983). It is thin-skinned, wedge shaped, tapering to the east (Fig. 4-3), and the gradient of deformation increases towards the back of the wedge (Fitz-Díaz *et al.*, in press, Chapter 2). The detachment separates a deformed sedimentary cover from an undeformed crystalline basement in the front of the cross-section (eastwards). The stratigraphic changes within the sedimentary cover play a major role in how the deformation is accommodated within the wedge and in the evolution of the fold-thrust belt.

Deformation in the platforms is dominated by thrusts and fault-related folds at a kilometer scale, and by fractures (Fig. 4-4a), veins and stylolites at a mesoscopic scale. In contrast, the deformation in the basins is more ductile and is dominated by mesoscopic buckle folds with a strong axial-plane pressure-solution cleavage and fold-related veins that are pervasive throughout the cross-section (Figs. 4-4b-d), although thrusts are also present within the basins.

Analysis of structures on a mesoscopic scale is presented in Chapter 2. The spatial-temporal variations of upright chevron folds that characterize the two basins indicate two stages of fold growth: the first one by buckling, which accounted for 45-55% of the shortening, followed by a second one of flattening that contributed up to 20% shortening, to produce a total shortening of 65-75%. Folds in the Tampico-Misantla Basin show a gradient of deformation that varies from 20% at the front of the basin to 65% near its western boundary. The folds in the Zimapán Basin accumulated an overall shortening of 70-75%, with some variation within the basin and the highest amounts at the margins (Fig. 4-3).

Another prediction of the orogenic wedge theory is that rocks exposed to the rear of a wedge are subjected to deeper and therefore higher temperature conditions than the rocks exposed at the front. So it happens in the MFTB, where temperature has been determined by microthermometry

of fluid inclusions (Gray *et al.*, 2001, and new data in this paper), illite crystallinity, and vitrinite reflectance (Valencia-Islas, 2006; Ortega-Flores, 2010). Such data show a gradient in the thermal conditions of deformation from about 80°C in the front of the MFTB to about 190°C on the western boundary of the Tampico Misantla Basin, 200-250°C in the Zimapán Basin, and more than 300°C in the rocks of the carbonates in the western edge of the cross-section (Fig. 4-3).

4.3 Methodology

4.3.1 Structural Framework

The overall wedge shape of the MFTB is inferred from surface mapping and borehole data, and various section-balancing techniques (Fitz-Díaz *et al.*, in press) were applied to produce the section shown in Fig. 4-3. Two main phases of deformation (D1 and D2) affected the rocks of the fold-thrust belt (Chapter 3), D1 being the major event that produced thrusts, folds, and a penetrative axial planar cleavage (S1) in the Trancas, Soyatal and Santiago formations. D2 modified the D1 structures to produce open folds, and a crenulation cleavage (S2) affecting the S1 cleavage. D2 is the only event that affected Paleogene sequences in the easternmost part of the section. Through a careful structural-kinematic analysis we distinguish veins emplaced before, during and after the main shortening event (D1). In the platforms, scarce millimeter-size veins (V0) formed parallel to diagenetic stylolite peaks, and are perpendicular to stylolite average surfaces (and bedding). No preferred orientation in strike was detected in these veins. Early veins (V1) are strongly affected by folding and shear; they are named V1a when they are extensional veins emplaced between strata and V1b when they are oblique to bedding. Syn-tectonic veins (V2) helped to accommodate local extension and shear during the main deformation event within limestone layers; depending on the timing of their emplacement, they are named V2a (extension and shear accommodation structures), or V2b (dominantly extension-related structures). When indistinguishable they are simply labeled as V2. V3 veins postdate V2 veins, are entirely made up of calcite, almost vertical and crosscut many layers.

4.3.2 Sampling strategy

4.3.2.1 In major thrusts

Major thrusts, especially those at or near the boundaries between paleogeographical or paleotectonic features, are visualized as fluid channel ways from the wedge during deformation. If the rocks affected by thrusting are carbonates with characteristic $\delta^{13}C$ and $\delta^{18}O$ values (around 0‰ with respect to the PDB) fluids with a different isotopic composition circulating through the

fault zones would likely leave a distinct isotopic imprint in recrystallized and new calcite formed during deformation. To investigate this, we took samples along profiles centered at each thrust 'plane' and out into the hanging-wall and foot-wall (Fig. 4-4a). Sample spacing was tighter in the fault zone and loosened outwards; the most distant rock samples were assumed to be isotopically unaffected by thrust-driven fluids (Fig. 4-4a). 209 samples of limestone, cataclasites and veins were collected in seven localities, T1 to T7 (see Figs. 4-2 and 4-3 and Table 4-1 for location and Appendix 4-1 for descriptions). The samples were prepared to allow more detailed structural observations at small scale and the selection of material for geochemical and isotopic analyses. About 5 mg of powder samples were obtained by micro-drilling for such analyses from every significant feature on each hand sample. Micro-sampling was normally done at the center of calcite veins and on calcite mega-crystals, carefully avoiding inclusions of other minerals and rock fragments. Sampling on carbonate rocks was done in homogeneous cement-rich areas. In fault rocks, micro-samples were taken in different shear domains (micro-breccia with veins, fault gouge, cataclasite or calci-mylonite). However, some of these domains (e.g. pink iron oxide-rich cataclasites) could not be analyzed because they are poor in calcite (see Appendix 4-1).

4.3.2.2 In mesoscopic structures

Outcrops showing evidence for local, meter-scale (e.g. Fig. 4-4b) to grain-scale deformation and clear vein crosscutting relationships were selected for study. The sites are located within thrust slices in the platforms and basins (Figs. 4-2 and 4-3, Table 4-2). Figures 4-4 c and d show the distribution and abundance of fold-related veins in two well-exposed outcrops in the Zimapán and Tampico-Misantla Basins.

For $\delta^{13}C$ and $\delta^{18}O$ analyses in calcite, 5 to 8 samples of host rocks, in continuous columns starting at over 20 cm from veins and deformed zones to ensure isotopic preservation (see Fig. 4-4b), were obtained. Such samples were taken from the central part of individual limestone layers in order to avoid contamination. At least 5 samples from every vein generation (see Fig. 4-4b) were taken. The number of samples in every site allows testing for homogeneity and to obtain statistically representative values for each generation of veins and host rock. A total of 209 samples were taken for $\delta^{13}C$ and $\delta^{18}O$ at the different localities (see Figs. 4-2 and 4-3 and Table 4-1 for location and Appendix 4-2 for details of samples).

4.3.3 Mineralogical and fluid inclusion analyses

δD_{water} was analyzed in fluid inclusions from vein calcite and quartz samples. To do this, single crystals were separated from different vein generations from six localities. We also

collected 16 illite/smectite-rich clay samples for δD analyses from bentonite layers in five outcrops (TMB1, TMB3, ZB2, ZB3 and ZB4).

To assess the temperature of formation of the veins, 14 samples were collected for microthermometry of fluid inclusions. The samples come from syn-tectonic (V2) calcite and quartz veins emplaced in chert layers in outcrops ZB3 and T1.

4.3.4 Illite-Smectite characterization

The bentonite samples were prepared following the recommendations of the IGCP 294 IC working group (Kisch, 1990). An unaggressive procedure was used for clay separation, which included: rock crushing, dispersion of powder in de-ionized water in an ultrasonic probe, separation of the fraction < 2μm by gravity settling, and washing and concentrating this fraction by centrifugation, and finally preparing this for X-ray diffraction (XRD) by sedimentation onto round glass slides. The coarse, medium and fine clay fractions were not separated, since we assumed that clay minerals in bentonite are authigenic and that there are not variations in the clay mineralogy of different size fractions. The concentration of the suspension was controlled to make sure that the weight of clay in the dried slide exceeded 2.5 mg/cm^2. The measurements were done in a Shimadzu XRD-6000 diffractometer, with a voltage of 40kV and a filament current of 30mA, using CuKα radiation and a graphite monochromator. The clay samples were examined by XRD in the air-dried form, saturated with ethylene glycol (EG) and in samples heated at 550°C. All the preparations were measured over a 2θ angle range of 2-70° (air-dried) and 2-40º (glycolated and heated) in steps of 0.02° and 2 seconds integration time. The profiles were analyzed using Shimadzu software. The illite crystallinity (IC) was measured using the FWHM (full-with-half maximum) parameter of the 10Å illite peak on oriented clay preparations of the <2 μm fraction (Kübler, 1967, 1968; Kübler and Jaboyedoff, 2000; Warr and Rice, 1994) with the results expressed in terms of the Bragg angle 2θ.

Illite identification and the percentage of smectite in mixed illite/smectite layers was estimated by using the methods described by Srodon (1984), Srodon and Eberl (1984), Reynolds (1992) and Moore and Reynolds (1997). The Intensity ratio index (Ir, Srodon and Eberl, 1984) was calculated by comparing the intensity ratio (peak height ratio) of the 001 and 003 reflections from the air-dried and the glycolated samples. Peak positions (d-spacing) were standardized against the quartz 100 peak taken at 4.26 Å.

In order to obtain statistically representative Illite crystallinity (IC) values, duplicates were analyzed for all samples. All the measurements were done under the same analytical

conditions and calibrated using international reference materials (NIST 675 and NIST 640d). No inter-laboratory standardization procedure was done (as suggested by Warr and Rice, 1994) since the purpose of this paper is to note variations of IC values rather than to obtain the absolute values.

4.3.5 Fluid inclusions

Two types of analysis were carried out in fluid inclusions: microthermometry and δD in inclusion water. For microthermometric analysis, 14 double polished thin sections of syntectonic calcite and fibrous quartz veins emplaced in chert bands were prepared. In 4 of them (2 from each T1 and ZB3 localities) homogenization temperatures (Th) were obtained. Ice-melting temperatures (Tmi) were obtained from fluid inclusions trapped in quartz fibers from the ZB3 locality. Workable fluid inclusions are scarce and display diameters ~10 µm. Primary (formed during the grain growth) and secondary fluid inclusion associations (along late microfractures) were selected for microthermometry (Fig. 4-5) by using the criteria of Goldstein and Reynolds (1994) and Touret (2001; Fig. 4-7a). The primary inclusions are typically distributed in growth zones in quartz fibers (Fig. 4-7b) and in clusters in calcite. Primary fluid inclusions are less abundant but bigger than secondary fluid inclusions. Secondary fluid inclusions are typically distributed along microfractures that cut quartz crystals and calcite twins (see examples in Figs. 4-7b-d). Inclusions showing evidence for necking, leakage, and other post-trapping modifications were identified and not used for microthermometry (Goldstein and Reynolds, 1994). Th and Tmi were obtained using a Linkam THMS 600 thermal stage (at the Instituto de Geología, UNAM), with a precision of ±0.2°C and ±2°C at low and high temperature determinations, respectively. Salinities were calculated with the equations of Bodnar and Vityk (1994).

4.3.6 Stable isotope analysis

4.3.6.1 $\delta^{13}C$ and $\delta^{18}O$ analyses in carbonates

Powdered samples of limestone, vein calcite and fault-rock were analyzed in a Micromass Isoprime mass spectrometer (at Stable Isotope Lab, Saint Louis University) to determine their $\delta^{13}C$ and $\delta^{18}O$ compositions. Samples of about 0.5 to 1 mg were made to react with H_3PO_4 at 90°C for at least one hour prior to analysis. One in-house standard was analyzed for every five unknowns. The in-house standard values of $\delta^{13}C = 2.33‰$ and $\delta^{18}O = 24.72‰$ were calibrated against NBS-19 standard values of 1.95‰ and 28.64‰, respectively. The standard deviations of in-house standards in individual sets of analyses (generally 30 analyses for each set) were 0.02 to 0.08‰ for $\delta^{13}C$ and 0.10 to 0.15‰ for $\delta^{18}O$.

4.3.6.2 δD analyses in illite/smectite

Analyses of δD in phyllosilicates were made with an ultra-high temperature Eurovector system (HT-PyrOH) connected to a Micromass Isoprime mass spectrometer (at the Stable Isotope Lab, Saint Louis University). Less than 1 mg of sample or standard was loaded into a silver capsule and pyrolized at 1800°C in a carbon reaction tube. Liberated gas was separated in a heated GC column and admitted online into the spectrometer. International (NBS22, NBS30) and in-house standards (coumarin, urea, kaolinite) were analyzed before, during, and after the analyses of the unknowns with standard deviations of < 2‰ after correcting for sample-size effects and "stretch".

4.3.6.3 δD analyses in fluid inclusions

For δD analyses in fluid inclusions, calcite was separated from quartz. 3-5 g of calcite were handpicked under a petrographic microscope. Quartz (0.5 to 2 g) was then separated from the leftover material by dissolving the remaining calcite with 10% diluted HCl in iterative steps. Fluids were then extracted from the inclusions by decrepitation, at 400°C for calcite and 600°C for quartz, in a closed cryogenic system. Samples of inclusion water that decrepitated at 100°C step heating intervals were also collected: from 200° to 400°C for calcite and from 200° to 600°C for quartz. The purpose of step heating was to look for isotopic differences in inclusions decrepitating at different temperatures. Bulk H_2O was trapped in Pyrex tubes. H_2O and CO_2 from water and hydrocarbon-bearing fluid inclusions (Appendix 4-2) were separated following the methodology of Vennemann and O'Neil (1993) and were also trapped in Pyrex tubes. Once these were sealed the pipes were inserted into a muffle furnace at 500°C for 15 min prior to mass-spectrometric analysis. δD analysis were done on a Finnigan Mat-Delta S mass spectrometer equipped with a dual inlet system (reference gas and sample). In-house, MOW and LIPE standards were used for corrections. These analyses were done in the Stable Isotope Lab at the University of Lausanne.

4.4 Results

4.4.1 Structural Analysis

The veins in the major thrust zones are most diverse texturally (Table 4-2), and are always calcite rich. Some of them predate faulting and are mechanically accumulated by shear along the thrust zone. Other veins were emplaced syn-tectonically to faulting, and once formed they behaved rigidly. Some veins with calcite megacrystals cut cataclastic fabrics.

In both basins there are extensional veins emplaced along the bedding (V1a) and shear veins that predate folding oblique to bedding (V1b; Figs. 4-4b-d). These are subsequently folded or sheared, and at a grain-scale they are affected by pressure solution, as evidenced by two generations of stylolites (one parallel to bedding and another oblique that cuts the first one; Figs. 4-5a and b). V1a veins are formed essentially by calcite and quartz in fibrous and elongate-blocky fabrics, in the terminology of Bons (2000). V1b veins typically exhibit blocky and elongate blocky textures, and dominantly (>85%) formed by calcite. Most of the V1 veins are affected by micro-fractures, twins (types II and III of Buckhart, 1993) and crystal-plastic deformation. These veins are more abundant in the Zimapán Basin than in the Tampico-Misantla Basin (Fig. 4-4 c and d, Table 4-2).

V2 veins are contemporaneous with folding and shear zones related to the main shortening event. They are typically found in the outer arcs of fold hinges accommodating extension (V2a in ZB), in *en-échelon* arrays, accommodating local shear zones around folds (V2 in TMB, Figs. 4-4d and 4-5c), or sub-perpendicular to axial planes, accommodating extension in attenuated limbs (V2b, Figs. 4-4b-d). In some outcrops several generations of syn-tectonic veins are found. V2 veins typically show planar vein-rock interfaces, are sheath shaped and confined to one or a few strata. They are almost 100% calcite when emplaced in limestones (Figs. 4-5c and d), and quartz content increases (up to 15%) in veins hosted by sandstones or chert (Fig. 4-5e). They exhibit fibrous (e.g. Fig. 4-5c-e), blocky-elongate and blocky textures (e.g. Fig. 4-5f), and the crystals show late deformation in the form of micro-fractures and (in calcite) deformation twins (Type II and III of Burkhart, 1993; Fig. 4-5f). Fibrous and blocky-elongate veins display fluid and solid inclusion trails sub-parallel to the vein walls, suggesting dominant crack-sealing (Ramsay, 1980; Fig. 4-5f).

Late veins (V3) are less abundant than V1 or V2 (Figs. 4-4c and d, Table 4-2) and are better developed on the western side of the study area (DP and ZB). They are commonly meter-spaced, vertical, several meters long, and unconfined to specific layers. They are made up of reddish semitransparent calcite, commonly with “dog tooth” crystals in open spaces. In other cases they show banded or crustiform textures with variegated coloring.

4.4.2 Clay analysis

Bentonite may constitute up to 30% (to the east of the cross-section AA’) of the series. On the other hand, XRD analyses in basinal limestone layers indicate that the amount of clay in them is negligible.

Interbedded shale and bentonite are rich in illite-smectite and quartz, have minor amounts of kaolinite, and may also have chlorite and K-feldspar. These were not sampled, to avoid contamination due to authigenic-detrital phase mixing (Srodon *et al.*, 2002). We assume that illite in the bentonite samples was produced from smectite only during diagenesis or deformation as indicated in other studies (Weaver, 1979; Compton *et al.*, 1999; Abdioglu and Arslam, 2005). X-Ray diffraction patterns of clay fractions indicate that mixed-layer clays are mostly illitic, with an increasing proportion of illite with deformation.

Illite crystallinity (IC) and Ir index vary regionally and range 0.23 to 1.5 and 0.87 to 6.80 (Fig. 4-6a), respectively: low illite crystallinity and more smectite interstratified with illite were obtained towards the front of the cross-section whereas high illite crystallinity and almost pure illite occur at the back of the wedge. Thus, following Srodon and Eberl (1984) the easternmost locality (TMB1) belongs to the predicted diagenetic trend, whereas localities TMB3, ZB3 and ZB4 follow the predicted metamorphic trend (Fig. 4-6b).

4.4.3 Microthermometry of fluid inclusions

In locality T1, the homogenization temperatures (Th) measured in primary fluid inclusion associations range 280º to 350°C (Fig. 4-7e), and in ZB3 ranges 180º to 230°C. The Th in secondary fluid inclusion assemblages in ZB3 averages 160°C (Fig. 4-7f). Such temperatures are consistent with those reported by Gray *et al.* (2001). The temperatures of ice melting of primary fluid inclusions in quartz from veins in ZB3 range from -4.5º to -5.2°C, and calculated salinities range from 7.17 to 8.14 wt. % NaCl equiv.

Fluid inclusions in syntectonic veins in the Zimapán Basin belong to the H_2O-NaCl system, as extraction of water in a cryogenic system (for δD analysis) produced tiny amounts of CO_2 and no residual gases were detected after isolating water and CO_2. However, hydrocarbons and probably N_2 occur in fluid inclusions from the Tampico-Misantla Basin V1 and V2 veins. CO_2 from fluid inclusions was analyzed in 2 samples (Appendix 4-2) and their $\delta^{13}C_{VPDB}$ composition (-34 to -6‰) suggests the presence of hydrocarbons.

4.4.4 Stable isotope geochemistry

4.4.4.1 In major thrusts

In Figure 4-8 the C and O isotopic values are plotted vs. distance for all sampling localities. In the two westernmost localities, T1 and T2, the $\delta^{18}O$ ranges of 10 to 15 ‰ in veins are distinctly lower in the fault zone than in the hanging wall and foot wall. In contrast, the $\delta^{18}O$ values to the east range from 24 to 27 ‰ for Cretaceous carbonates (Ferket *et al.*, 2003; Weissert

and Erba, 2004) and do not change within fault zones for localities T3 to T7. The locations that show the least variation in $\delta^{13}C$ across fault zones are T1, T4 and T7; eastwards to the two studied basins (Fig. 4-3). By contrast, along the thrusts on the western boundaries of these basins (in T5 and T3) $\delta^{13}C$ values are as low as -5‰, which might have been caused by hydrocarbons circulation along these faults. Similar variations are observed in the hanging wall, veins and cataclasites at T5, on the western side of the Valles-SLP Platform. Stronger variations (about 15 ‰) occur at T2 on the western side of the El Doctor Platform in both the footwall platform carbonates and the fault rocks.

4.4.4.2 In mesoscopic structures

In Fig. 4-9, $\delta^{18}O$ is plotted vs. $\delta^{13}C$ of veins and host limestones. In the two basins, values of $\delta^{18}O$ and $\delta^{13}C$ for the V1 and V2 veins are very similar to their values in host rocks. In the western platform (DP1), isotopic values for host rocks and V1 and V2 veins are very similar, but V3 veins are not. In the eastern platform (Valles-SLP Platform), by contrast, V1 and V2 veins have lower values of ^{18}O and ^{13}C compared to the host rock.

4.4.4.3 Clays and fluid inclusions

δD values in clay range from -41 to -72 ‰ (Fig. 4-10a). Clays from the eastern side of the cross-section have higher values in deuterium compared to those in the west. A similar trend is observed in δD in inclusion water from V1 and V2 veins, except that the range of values is broader in V1 (0 to -61 ‰ Fig. 4-10a) than in V2 (-33 to -58 ‰), with a greater overlap with the range in clays. V3 shows the lowest values among the veins (-60 to -70 ‰).

4.5 Interpretation

4.5.1 Wedge mechanics as deduced from vein analysis

The presence of veins of different generations in the MFTB is evidence for fluids operating at different scales throughout the deformation history. Vein types relate to fracture modes (e. g., mode I-extensional or mode II-shear, Table 4-2), while vein textures provide information about the velocity of material transfer into the vein with respect to the opening or strain rate (Bons *et al.,* 2000). Along major thrusts, which dominate in the platforms and their boundaries in the MFTB, multiple generations of veins indicate the intermittent passage of fluids and fracture filling. The veins were formed from distant source fluids and were probably transported as mobile hydro-fractures (Fisher and Byrke, 1994; Bons, 2001) during the different thrusting pulses. In contrast, syntectonic veins in the basins typically have sheath shapes, are

confined within strata and show dominantly blocky elongate and fibrous textures (Table 4-2), indicating that the material in the veins is locally derived and that the rate of vein opening (strain) was faster than the transportation of material inside the vein, implying that the most likely mechanism of transport was diffusion (Kirschner *et al.*, 1994; Bons *et al.,* 2000).

In the platforms it is common to see mm-thick veins (V0) emplaced along stylolitic interfaces, along roughly vertical planes oriented normal to the average stylolite surface. Since stylolites are overall parallel to bedding and are cut by syntectonic cleavage, we assume that they are diagenetic in origin and were roughly horizontal when formed. According to Bjørlykke (1989), stylolites can be formed within a range of 1500-2000 meters in depth. This constrains the vertical stress (σv), which, according to Anderson (1951), corresponds to a principal stress. Figure 4-11 shows schematically the state of stress responsible for the formation of these extensional veins and stylolites in Mohr circle representation (plot labeled as V0). Fluid pressure must have been sufficiently elevated to allow extensional veins to be emplaced, and stress difference small enough, $(\sigma_1 - \sigma_3) < 4Ts$ (Ts=tensile strength), that shear failure did not occur.

V1 veins, emplaced parallel to bedding, are omnipresent along the cross-section; they can be observed within the thrust slices in the platforms and in the basinal carbonate layers. This has important implications for the stress history of the area, because these must have been emplaced at a time when the pore fluid pressures were supra-lithostatic, with the vertical stress (σv) being the smallest principal stress (σ_3), and with a modest stress difference, $(\sigma_1 - \sigma_3) < 4T$, which allowed fractures to open against the vertical load and the veins to be emplaced between horizontal strata, prior to folding and thrusting (Fig. 4-11-V1). This phenomenon has been commonly observed elsewhere and has been successfully explained in other fold-thrust belts (Jessell *et al.*, 1993; Hilgers *et al.*, 2006). In the study area it likely occurred after tectonic compressional stresses begun to occur, eventually causing the E-W horizontal stress to become the maximum stress. The injection of veins parallel to bedding was probably facilitated by the fact that initially Ts across bedding planes is smaller than Ts for isotropic rock. The emplacement of these veins would have the combined effect of episodically lowering pore fluid pressure and increasing the tensile strength across bedding as the weak contacts between strata welded due to vein emplacement. Increasing tectonic stress would tend to re-pressurize pore fluids after each failure event. After many bedding-parallel veins had been emplaced, and the difference in tensile strength (Ts) between bedding normal and isotropic rock had been reduced, conditions were optimum for the production of the V1b veins, which are oblique to bedding and are commonly observed in both basins cross-cutting V1a veins (parallel to bedding). These are interpreted as

veins filling mixed mode fractures that may develop when (σ_1 - σ_3) is between 4T and 5.66T (Hancock, 1985; Sibson, 1998).

As tectonic compressional stresses increased, the stress difference eventually became large enough, (σ_1 - σ_3) > 5.66T, so that the shear strength of the rocks was overcome and thrust faults were produced (Fig. 4-11-V2). The large thrust faults in the platforms formed at this time. At the same time, compressive stresses in the basins produced folds, mostly by ductile deformation, but also with centimeter-scale veins of varying orientations and opening modes (Fig. 4-11-V2). I is likely that tectonic stresses increased slowly and intermittently, with some release after each fracturing or fault-slip event. This is reflected in the crack-seal textures in the syn-tectonic veins and is consistent with numerical models of the growth of the tectonic wedges that involve episodic slip on faults (e.g. Strayer *et al.*, 2001; Stockmal *et al.*, 2007). In addition there may be deformation hardening (Kilsdonk and Wiltschko, 1988) that will tend to broaden the deformation in the rock mass. As tectonism ceased, compressive stresses relaxed. In the absence of continued compression, the wedge (see Chapter 2) became unstable and a gravitational collapse followed, inducing extension (Fig. 4-11-V3). During this stage the maximum stress became vertical again. This explains the formation of extensional veins V3. The stress difference was small enough that tensile failure produced V3 veins in the westernmost platform. By contrast, in the Zimapán Basin, normal faulting occurred in addition to V3 veining, indicating that stress differences were eventually great enough for shear failure.

4.5.2 Implications from $\delta^{18}O$ and $\delta^{13}C$ data

Isotopic analyses in calcite from 'undeformed' limestone in the hanging walls and footwalls of major thrust zones and from associated cataclasites and veins (Fig. 4-8) can be summarized as follows:

1. Most of the limestones more than a meter away from the thrusts show carbon and oxygen isotopic values typical of Cretaceous carbonates (Weissert and Erba, 2004). However, the two westernmost thrusts (Fig. 4-8, T1 and T2) and T5 show relatively low $\delta^{13}C$ values in the host rock limestone. The fact that the two westernmost thrusts (T1 and T2) show the most pronounced isotopic anomalies is not fortuitous and probably reflects the accumulation of deformation damage in the rock over a more prolonged period of time and the most pronounced topography buildup relative to eastern most areas during the development of the fold-thrust wedge.

2. In cataclasites, the negative anomalies in $\delta^{13}C$ are larger than in veins and host rock at T2, T3, T5 and T6. In the fault zone at T2 the lowest $\delta^{13}C$ values were recorded (≤-15‰), not

only in the cataclasites but also in the host El Doctor Platform footwall limestone. This locality is a special case since, even though the contact between the two carbonate units is a thrust, these units are in their normal stratigraphic positions (Fig. 4-3). Along the surface contact there is paleo-karst and paleo-soil development on top of the platform prior to the deposition of syntectonic turbidites above (Hernández-Jauregui, 1997). To produce such a low $\delta^{13}C$ isotopic exchange with a light carbon source (likely, organic matter) is necessary. Such a source could have been in association with paleo-soils and karsts. There are also low $\delta^{13}C$ values in both the thrust zone and the hangingwall at T1 and to a lesser extent T5 on the western side of Valles-San Luís Potosí Platform. This feature is accentuated on the hinterland side of the platforms and may be linked to gentle erosion on the western side, compared to the abrupt propagation fronts of thrust slices, which allows soil development and infiltration of meteoric fluids.

The $\delta^{13}C$ anomalies in most of the cataclasites in the thrusts bounding the Zimapán and Tampico-Misantla Basins on their western sides (T3 and T6) are probably caused by the presence of hydrocarbons, or due to mobilization of ^{13}C-rich calcite by pressure-solution. Western thrusts are longer lived than the eastern, therefore such anomalies reflect a longer thrusting history, organic matter maturation and escape along the thrusts. Hydrocarbons were likely locally derived because the carbonate sequences in the area, especially basinal limestones, are rich in organic matter (Valencia-Islas, 1996). The lowest $\delta^{13}C$ values observed in thrust zones on the western edge of the Zimapán and Tampico-Misantla basins (Figs. 4-3, 4-8, T6 and T3) suggest hydrocarbon transformation is highly controlled by the deformation paths within the wedges. This last is because the deformation determines the thickening within the wedge, and therefore burial conditions.

3. The largest shifts in $\delta^{18}O$ occur in calcite megacrystals from late veins, and were observed only in the two westernmost thrusts (T1 and T2); $\delta^{18}O$ shifts (with respect to the host rock) are more accentuated in calcite veins than in cataclasites. In other thrusts $\delta^{18}O$ is the same in veins, cataclasites, and host rocks (Fig. 4-8, T1 and T2). $\delta^{18}O$ shifts in calcite from veins in the fault zones were probably caused by meteoric water, provided that the veins show no $\delta^{13}C$ variation. Meteoric fluids probably infiltrated the westernmost part of the cross-section and were squeezed along major faults. There is less carbonate in the rocks on the western edge of the cross-section to provide isotopic buffering. The absence of significant $\delta^{18}O$ drifts in other thrusts (T3 to T7) suggests that (1) the fluid circulating through them was compositionally close to that of the carbonate rocks, (2) they were volumetrically limited, or (3) there was enough time under

appropriate temperature conditions for isotopic equilibration to be approached (Kirschner and Kennedy, 2001).

The $\delta^{13}C$ and $\delta^{18}O$ values in V1 and V2 veins (fold and shear-related veins developed in thrust slices) are very close to those in the enclosing host rocks (except for locality PV1). However, most of the values in V3 veins differ from those in host rocks. $\delta^{13}C$ and $\delta^{18}O$ from V1 and V2 veins from locality VP1 are roughly distributed along a line with a positive slope that could represent a 'mixing line' (Phillips *et al.*, 2005) between a fluid poor in heavy carbon and oxygen and host rocks (Fig. 4-9).

Since deformation occurred between 90 and 65 Ma, based on stratigraphic constraints (Chapter 3), the overall rate of deformation, which is linked to the dissolution-precipitation rate, is slower than the isotopic exchange rate between calcite and water (Cole, 2000; Chacko *et al.*, 2001). V1 veins are assumed to have formed at about the same temperature (roughly 70º to 100°C) elsewhere, while V2 veins formed at 100° to 250°C (Fig. 4-12a), according to temperature determinations from fluid inclusion, illite crystallinity, and vitrinite analyses (Valencia-Islas 1996; Gray *et al.*, 2001; Fitz-Díaz *et al.*, in press; Ortega Flores, 2010). V3 veins formed at 70º to 160°C (Muñoz-Máximo, 2010, Fig. 4-12a).

The isotopic composition of calcite of V2 and host rocks is similar; this has two possible explanations: 1) a large amount of fluid in the reservoir with a similar composition to the host rock; 2) restricted amount of pore fluid with an initially different composition which was buffered during deformation. We know that temperature varies along the cross section (from 100-300°C). This temperature range, however, does not seem to have an effect on the isotopic exchange between host rocks and fluids during the emplacement of V1 and V2 in the basins and in DP1 (Fig. 4-9). However, V3 veins in DP1 and ZB4, and V1 and V2 veins in VP1 are likely to have been affected by fluids with low $\delta^{13}C$ and $\delta^{18}O$ values, and these were probably meteoric. Such fluids probably inflowed during the late extensional phase in the western part of the study area, including the El Doctor Platform and the Zimapán Basin.

The data also suggest that the Valles-San Luis Potosí Platform behaved as an open system during the shortening stage of deformation. Otherwise, calcite veins were initially buffered and recrystallized or reprecipitated during deformation. This could be due to brittle deformation allowing the inflow of low-temperature meteoric fluids (~160°C, Fig. 4-12a; Valencia-Islas, 1996; Gray *et al.*, 2001). The influence of meteoric water is reflected in the 'mixing line' trend (Fig. 4-9-VP1). Although rocks of the adjacent Tampico-Misantla Basin were

shortened under lower temperatures (90º to 190°C) than those of the Valles-SLP Platform, the similar isotopic compositions of vein calcite and host rocks in the basin suggests that temperature was not the main factor controlling isotopic exchange. The influence of meteoric fluids was limited in the basin, which behaved as a quasi-closed system for fluids during deformation. Fluids in the basin would likely have been formational water or basinal brines, which is compatible with evidence from fluid inclusion analysis in other parts of the MFTB (Fischer *et al.*, 2009; González-Sánchez *et al.*, 2009).

4.5.3 δD and sources for fluids during deformation

Unlike the $\delta^{18}O$ values, most of which have been buffered by the host rock due to intense fluid-rock interaction, δD from fluid inclusions and illite/smectite preserves better the original signature of aqueous fluids. Because δD in fluid inclusions from V1 and V2 veins decreases westwards, a feature that may be the result of the increasing interaction between pore water and meteoric water, which probably infiltrated through the abrupt topography at the back of the wedge. V3 veins show the lowest δD values (-70 to -60‰) and, as part of a network of sub-vertical extensional veins, they could have provided pathways for the inflow of meteoric fluids. The values recorded are similar to those of recent meteoric water in Mexico (Wasserman *et al.*, 2009). δD for Cretaceous meteoric water could have been lower than present values due to higher average annual temperatures at that time.

For the δD analyses in heating steps it is assumed that primary inclusion fluids were released at higher temperatures and have higher δD values than secondary inclusions. The exception is a V1 vein from ZB1 where all steps yielded low δD values (Fig. 4-10b). It is suggested that δD values (-11 to 0 ‰, Appendix 4-2) from fluid inclusion water in V1 in the easternmost localities is possibly closest to the original composition of formational water, as these values are the closest to SMOW. In the same localities, δD ~ -15‰ was obtained for water in isotopic equilibrium with the clay minerals at 80°C during diagenesis and V1 emplacement, following equations by Yeh (1980) and Hyeong and Campuano (2004). This composition is also close to both present and Cretaceous SMOW (Fig. 4-12b). Similar cases were reported by Compton *et al.* (1999) and Eslinger and Yeh (1986).

There is no evidence for metamorphic or magmatic fluids during deformation, and there is no Cretaceous to Paleogene magmatism in the study area. The deformation occurred at very low metamorphic grade and the Grenville gneiss basement was only affected by brittle shear along the detachment zone, with no associated metamorphism. Only clay dehydration (smectite to

illite) in deformed bentonite layers (interbedded with basinal limestones) occurred. Such a reaction is in accordance both with temperature and strain, as well as with δD values in clays and fluid inclusions.

The presence of diagenetic stylolites indicates that the Cretaceous carbonates were buried to a depth of ≥2 km (Bjørlykke, 1989), at which depth the porosity of the rock would be 10 to 20% of the total volume (e. g., Schmoker and Gautier, 1989), or perhaps less, as cementation might have sealed a considerable amount of the pore volume (Bjørlykke *et al.*, 1997). During this process expandable clays could have taken up sea water. Compaction of shaly layers could have decreased permeability due to the alignment and growth of platy-shaped clays, thus elevating the pore and clay fluid confinement within the layers. During the formation of V1 such water was the likeliest vehicle for dissolution-precipitation, and some was trapped in primary fluid inclusions. Part of this water was expelled from the basin as deformation progressed and rock porosity was further reduced. Based on the obtained temperatures of deformation, a reasonable estimate of the maximum burial depth at the front of the cross-section (assuming a surface temperature of 25°C and a geothermal gradient of 25°C/Km) is 3 to 4 km, where porosity would have been reduced at ~10% (e. g., Schmoker and Gautier, 1989). Thus pore fluids, essentially formational water, at the peak of the deformation were probably <10% of the total volume. Then, if formational water was the total budget available to produce V2 veins (Fig. 4-4b-d), it had to be re-used during deformation and/or increased by adding up meteoric fluids, since according to experimental observations the water/calcite volume ratio to precipitated veins is far larger (10^5 to 10^6, Lee and Morse, 1999) that the reservoir (rock porosity)/host rock volume ratio of the deformed rocks.

4.6 Discussion

The basic ideas that lead to the correlation between the mechanics of deformation and fluid-rock interaction within the MFTB wedge are illustrated in Figure 4-13. The model presented in Figure 4-14 integrates structural, isotopic and fluid inclusion data, to account for temperature (T), effective pressure, clay dehydration reactions, and fluid-rock interaction during the progressive growth of the fold-thrust belt. The model starts with the formation of V1 veins (Fig. 4-14a). These formed when compressive tectonic stresses first built up, causing σ1 to switch from vertical to horizontal, but at a time when σh did not differ much from σv. The tectonic stress would have enhanced the pore fluid pressure, which must have exceeded the lithostatic load (σv, Fig. 4-11-V1) for the veins to form. $\delta^{13}C$ and $\delta^{18}O$ in vein calcite are equilibrated with host limestones. At this stage, most of the rock volume would have been under the sea; therefore the

fluids (volumetrically restricted to primary porosity) active during deformation were formational waters with a δD close to SMOW.

In a second stage (Fig. 4-14b), shortening by thrusting and folding on the western side of the cross-section created vertical thickening in El Doctor Platform and ZB. Such thickening led to an increase in temperature on the western side of the cross-section, related to the regional geothermal gradient. Thickening also resulted in emergence of the rocks above sea level. Once exposed to atmospheric conditions, the rocks interacted with meteoric fluids. Since the platforms include few impervious clay horizons and experienced mostly brittle deformation, the faults and fracture network that developed in them probably allowed meteoric fluids to percolate. Such fluids would have interacted to some extent with the rock within the thrust slices, thus introducing low δD water into primary fluid inclusions in V2 veins and secondary inclusions in V1. Some meteoric water likely reached deeper levels in the wedge and finally interacted with foreland rocks, thus decreasing the overall δD in pore water. In the basins, limestones interbedded with impervious shales prevented meteoric fluid penetration and contributed to raising pore fluid pressure to supra-lithostatic conditions. The V2 veins were emplaced under these conditions. However, in the platforms the major thrusts and probably part of the fracture network were still connected to the surface, which would have kept the pore-fluid pressure to infra-lithostatic conditions.

In a third stage, as the wedge grew eastwards, the Valles-SLP Platform and the Tampico-Misantla Basin would have experienced similar conditions to those in the El Doctor Platform and Zimapán Basin during the previous stage. Meanwhile the El Doctor Platform and Zimapán Basin continued to shorten and thicken (Fig. 4-14c). At this stage, the tectonic stresses probably peaked, since the wedge then reached its maximum thickness, deepest burial conditions, and therefore also maximum temperature of deformation at the base and at the rear of the wedge (Figs. 4-11-V2 and 4-12a-V2). Extensional V2 veins confined to layers were still developing in the ZB, suggesting that the pore-fluid pressure was still, at least intermittently, supra-lithostatic. Unlike the latter case, in the platforms, especially the Valles-SLP Platform, the $\delta^{13}C$ and $\delta^{18}O$ in V2 veins are lower than in host rocks, pointing to the occurrence of meteoric water and low fluid-rock interaction (T of deformation in the Valles-SLP Platform was ~160°C). The $\delta^{18}O$ and $\delta^{13}C$ values in V1 in the Valles-SLP Platform also differ from those in host rocks, indicating that V1 calcite probably re-crystallized or was re-precipitated during deformation. In the Tampico-Misantla Basin, in contrast, $\delta^{18}O$ and $\delta^{13}C$ in V1 and V2 are equilibrated with the host rocks, although the temperature of deformation is lower there than in the Valles-SLP Platform. This is

probably because of the relatively confined fluid conditions within the basin, which was thus less susceptible to the influence of meteoric fluids than the platforms nearby.

Field evidence and microthermometric data indicate that V3 veins on the western side of the study area were emplaced at lower temperatures than V2 veins. Their isotopic composition was not completely buffered by the host rock, but rather is the result of interaction between isotopically lighter fluids, probably meteoric, and the host limestones. The *en-échelon* distribution of some V3 vein arrays indicates conditions of higher confining pressure in the Zimapán Basin than in the El Doctor Platform. In the latter, sub-vertical veins up to a few hundred meters long suggest more open and connected pathways to the surface. Further evidence for such differences in conditions is that V3 veins in some localities in the Zimapán Basin are isotopically buffered by host rocks, whereas in the El Doctor Platform they are not. Also, temperatures of homogenization in V3 are higher in the Zimapán Basin than in the El Doctor Platform, so it is interpreted that V3 veins in the Zimapán Basin formed deeper than those in the El Doctor Platform. δD values in V3 support the idea of meteoric water influence (Fig. 4-14d).

Mesoscopic structural observations indicate that most of V1 and V2 veins in the basins formed under confined conditions during tectonic shortening. However, the δD signatures indicate a progressive influence of meteoric fluids (Fig. 4-13). The $\delta^{13}C$ and $\delta^{18}O$ signatures of veins were probably buffered without much change in δD because the volume of formational fluids was limited. These fluids then welled up into basinal carbonates through microcracks and cleavage surfaces. Also, infiltration of meteoric fluids was possible along bedding planes after the exposure by erosion of folded layers (Fig. 4-14c).

4.7 Conclusions

The structural and kinematic analysis of mesoscopic shortening structures at a regional scale, together with proper stratigraphic constraints, allows understanding of progressive deformation and the role of fluids during deformation within the Mexican Fold and Thrust Belt. Lateral facies variations of carbonate sequences played a major role in controlling deformation styles: thrusting being dominant in the massive carbonate platforms and folding being dominant in basinal sequences. Major thrusts within and at the borders of platforms, together with associated fracture networks were efficient pathways for fluids. Fluid pathways in the basinal carbonate facies are not so obvious because fold-related veins were emplaced between and within limestone layers, interstratified with shales and bentonites. Nevertheless, isotopic studies point to the influence of meteoric fluids during deformation to a variable extent.

δD analysis in fluid inclusions water from veins emplaced early, during and after the main deformation event (V1, V2 and V3, respectively) along the studied cross-section, indicate a progressive influence of meteoric fluids with time and from west to east. δD in illite/smectite shows a similar trend and range of values, thus additionally suggesting that fluids during deformation interacted with clays as smectite transformed into illite. Since fluid pathways for meteoric water are not conspicuous at a mesoscopic scale in basinal carbonates, it is likely that fluids moved into and through these rocks through microcracks and by means of solution transfer.

C and O isotopic compositions of veins and basinal limestones indicate an intense interaction between pore fluids and host rocks, early and during deformation and over different strain conditions, at 90º to 300°C. This strong interaction resulted in isotopic equilibrium between the veins and the host rock. However, such isotopic buffering did not occur in some localities of the Valles-SLP Platform, probably due to the extensive influence of meteoric fluids. $\delta^{13}C$ and $\delta^{18}O$ along transects of major thrusts provide evidence for the passage of meteoric water on the two westernmost thrusts, and for the occurrence of hydrocarbons on the western boundaries of the basins. The latter observation suggests that the flow of hydrocarbons is asymmetric and is influenced by the flow of rocks during deformation. In other words, the flow of hydrocarbons was extensively controlled the orogenesis.

There is a very good correlation between the temperature of deformation, the influence of meteoric fluids, and clay dehydration reactions along the studied cross-section. This is consistent with the critical taper orogenic wedge theory, which predicts that the deformation starts at the back end of the wedge (the western side of the cross-section), and progresses towards the foreland, thus incorporating more strata as the wedge grows and thickens, increasing the temperature of deformation of the rocks under deepening burial conditions. Then, faster exhumation at the rear of the cross-section occurred. This scenario provides a longer time for the rocks on the western side of the cross-section to be exposed to meteoric water.

Figures and Tables

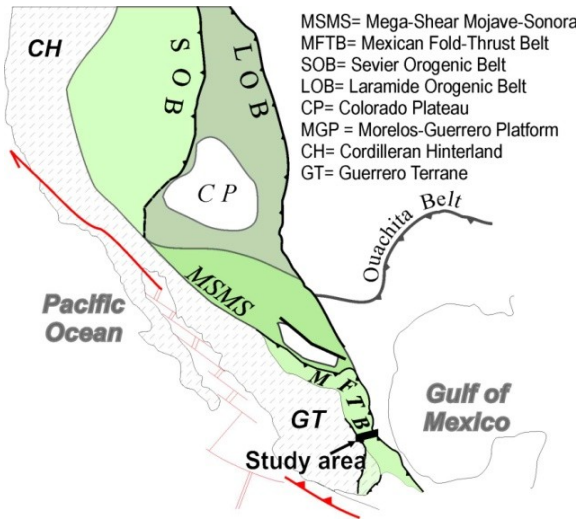

Figure 4-1. Generalized tectonic map of the Cordilleran Orogenic Belt showing the tectonic setting of the Mexican Fold-Thrust Belt (MFTB) and the location of the study area in Central Mexico.

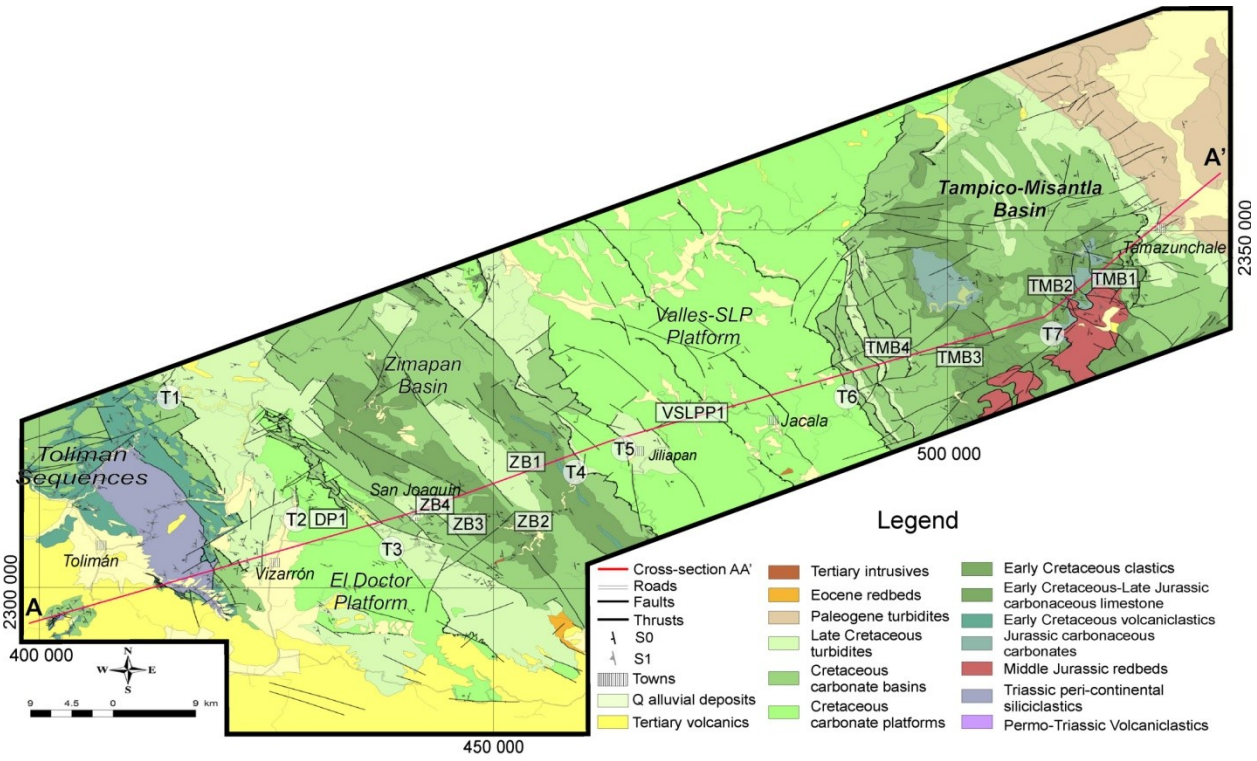

Figure 4-2. Geological map of the study area, the location of which is shown in Fig. 4-1. The sampling stations listed in Table 4-1 are indicated by letters and numbers. Modified from Fitz-Díaz *et al.* (in press).

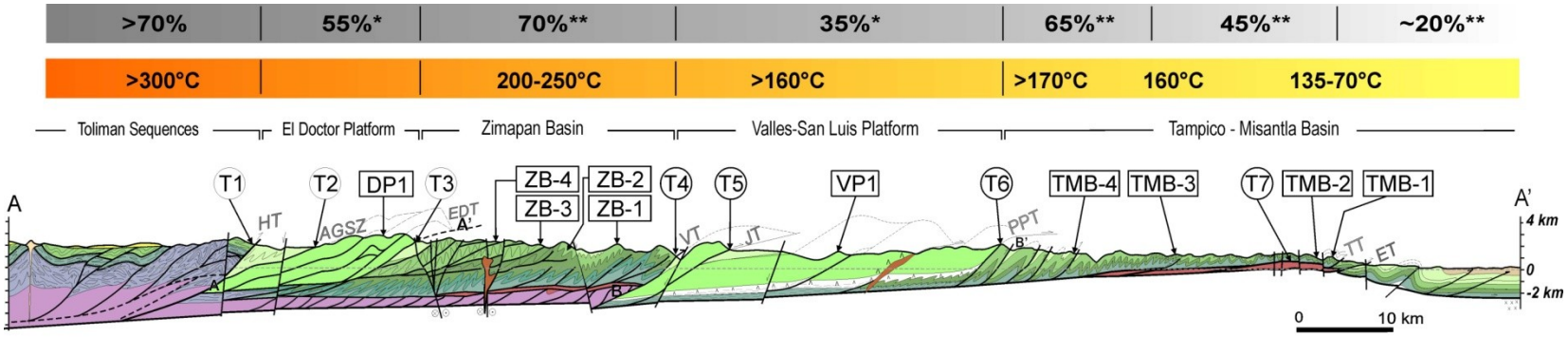

HT= Higuerillas Thrust, AGSZ= Arroyo Grande Shear Zone, EDT= El Doctor Thrust, VT=Volantin Thrust, JT=Jiliapan Thrust, PPT= Puerto de Piedra Thrust, TT= Tetitla Thrustla, ET=Enramaditas Thrust.
*shortening estimates by using balancing cross section techniques, ** shortening estimates by using fold analysis.

Figure 4-3. Geological cross-section along the line A-A' in Fig. 4-2. The sampling localities are projected onto the line of section. Estimates of shortening and temperature of deformation are indicated in the gray and orange bars above the cross section.

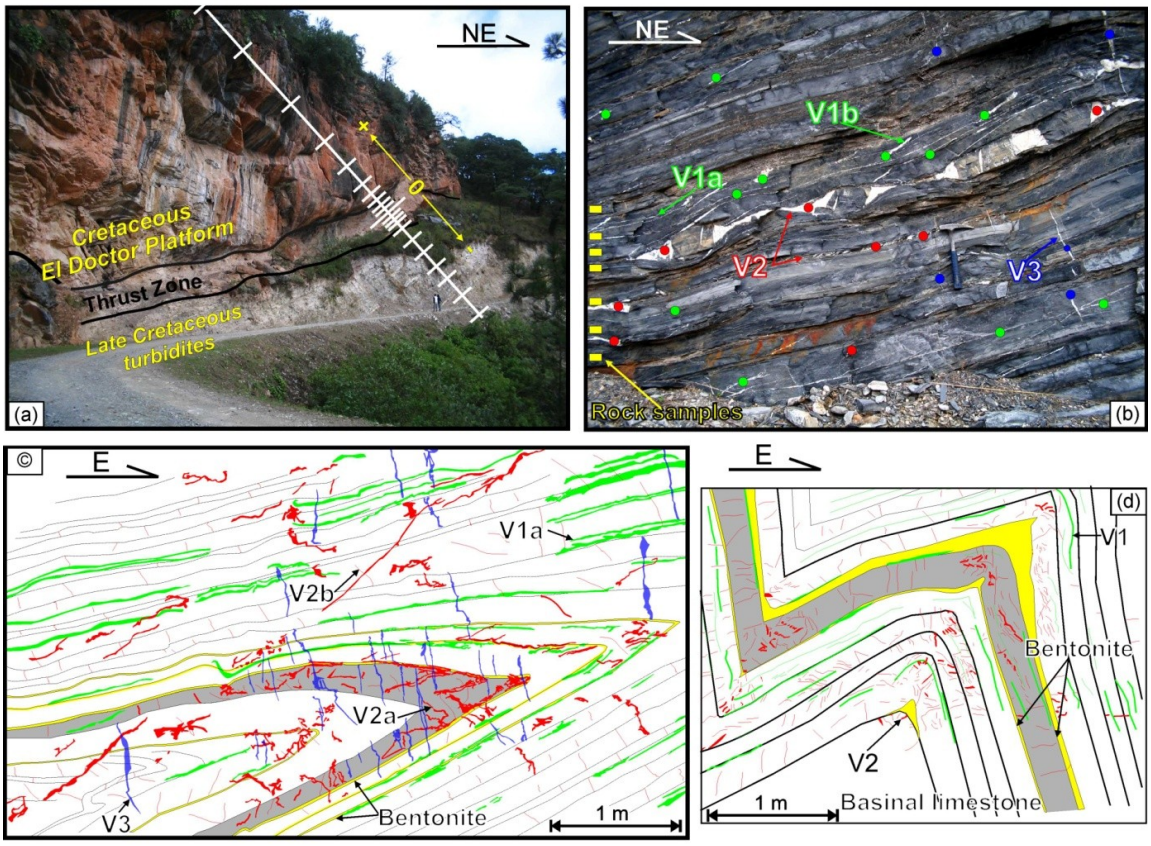

Figure 4-4. Photographs and sketches of selected outcrops. (a) El Doctor Thrust, showing how sampling was carried out for stable isotope analysis. (b) Different generations of fold-related veins in outcrop. (c) and (d) Distribution of different generations of fold-related veins in mesoscopic folds from the Zimapán and Tampico-Misantla basins, respectively. The vein generations are color coded (green for V1, red for V2 veins and blue for V3)

Figure 4-5. Examples of analyzed veins. (a) and (b) Sawn surfaces to show early veins, V1, which were early emplaced between limestone layers during D1. They are typically boudinaged and also affected by two generations of stylolites, one that strongly affects the vein wall, and a later one oblique to bedding. The internal fabric is commonly modified by later shear. (c) Sawn surface to show syntectonic calcite fibrous vein, V2. (d) Thin section slide of a V2 fibrous calcite vein showing trails of solid and fluid inclusions, under plain polarized light. (e) Cathodoluminiscence image of a V2 vein emplaced in a siltstone layer, showing the distribution of calcite and quartz fibers. (f) Blocky texture of calcite in a V2 vein with type II and III deformation twins (Burkhart, 1993), under plain polarized light. (g) Blocky texture of a V3 calcite vein.

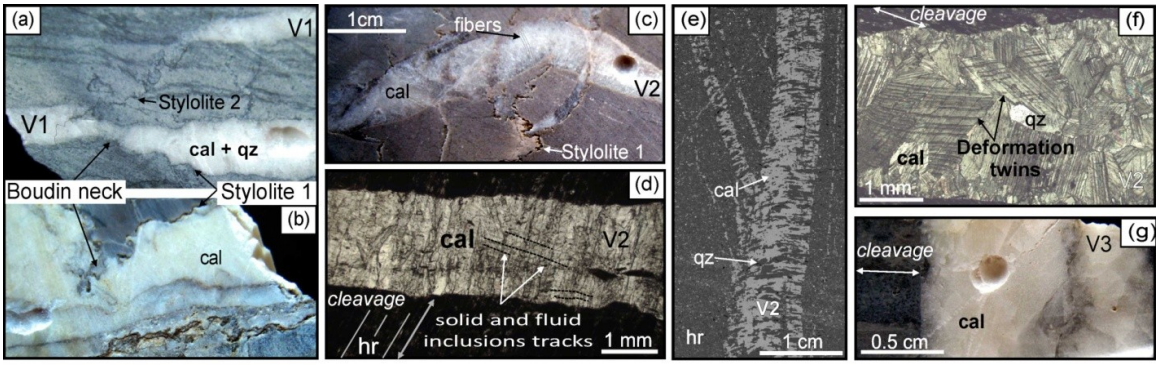

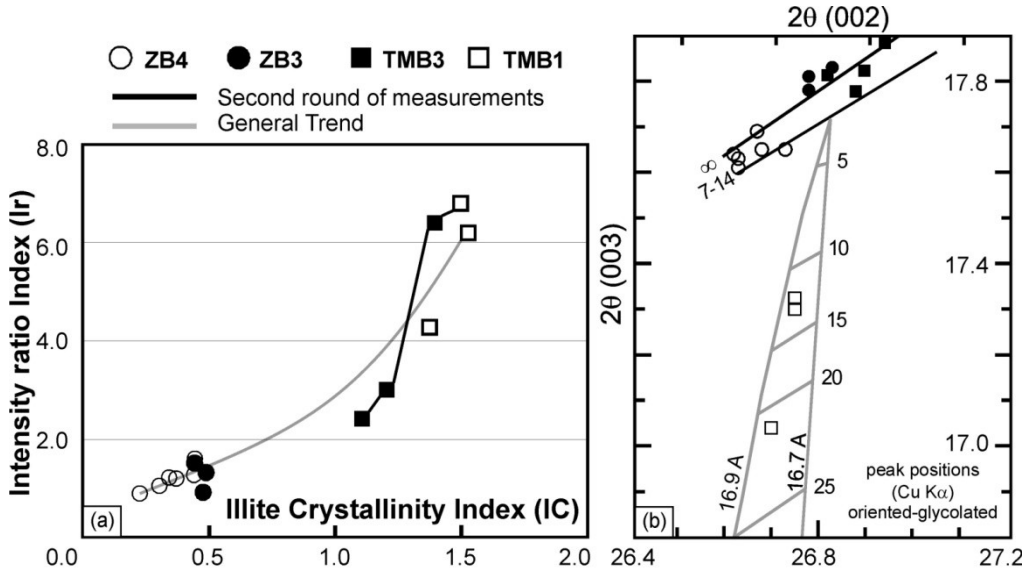

Figure 4-6. Analyses of clays. (a) The relationship between illite crystallinity (IC) and intensity ratios (Ir, Srodon and Eberl, 1984) measured in illite extracted from bentonite collected from four localities along the cross-section. Although the samples were run separately, they display the same trend. (b) The relationship between the peaks of the reflections from planes 002 and 003 in glycolated preparations of illite. Samples from the easternmost locality in the Tampico-Misantla Basin fall into the field of diagenesis (delineated in gray) while illite from localities in the Zimapán Basin falls on the metamorphic path (delineated in black).

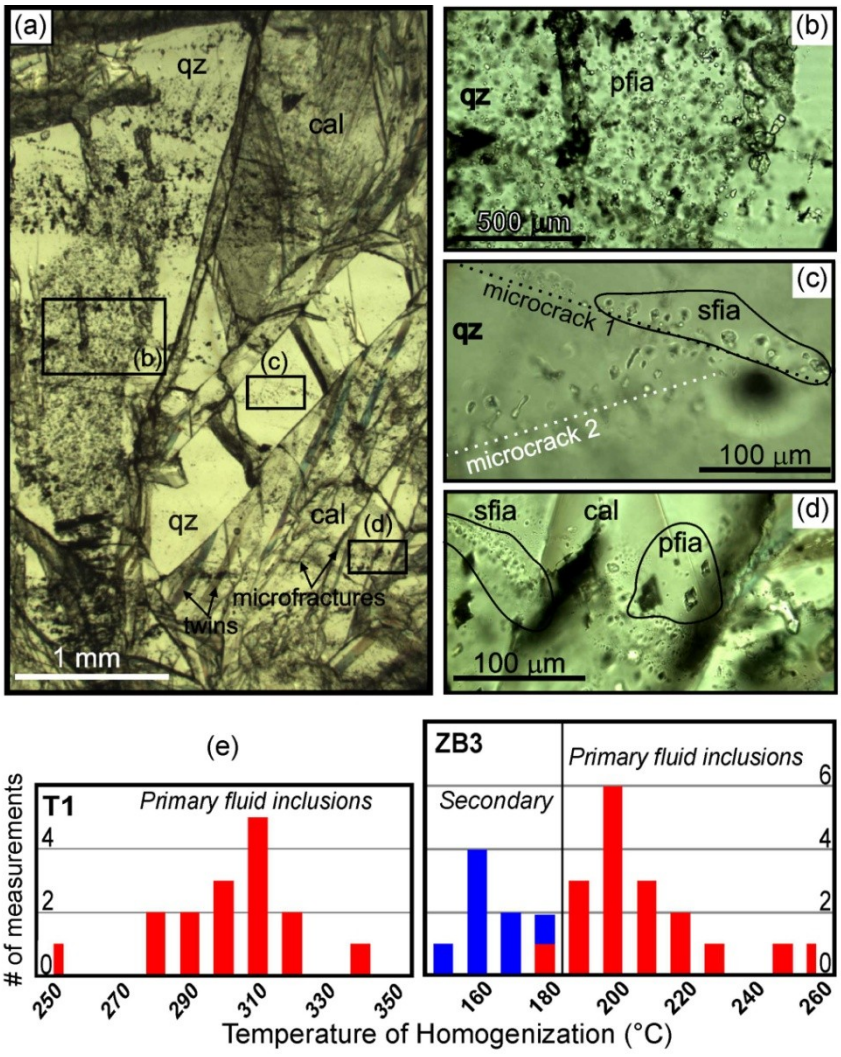

Figure 4-7. Fluid inclusions in veins. (a) Quartz and calcite fibers in a V2 vein where the distribution of primary fluid inclusion associations (pfia) is shown in an internal zone of an euhedral quartz crystal, and the secondary fluid inclusion associations (sfia) are hosted along fracture planes. (b) Close-up showing random distribution of pfia in quartz. (c) Closer view of microfractures hosting several small secondary inclusions. (d) pfia and sfia in a calcite fiber. Notice the difference in size and abundance of the primary and secondary fluid inclusions. (e) Histograms showing temperatures of homogenization in primary and secondary fluid inclusions in syntectonic veins from localities T1 and ZB3.

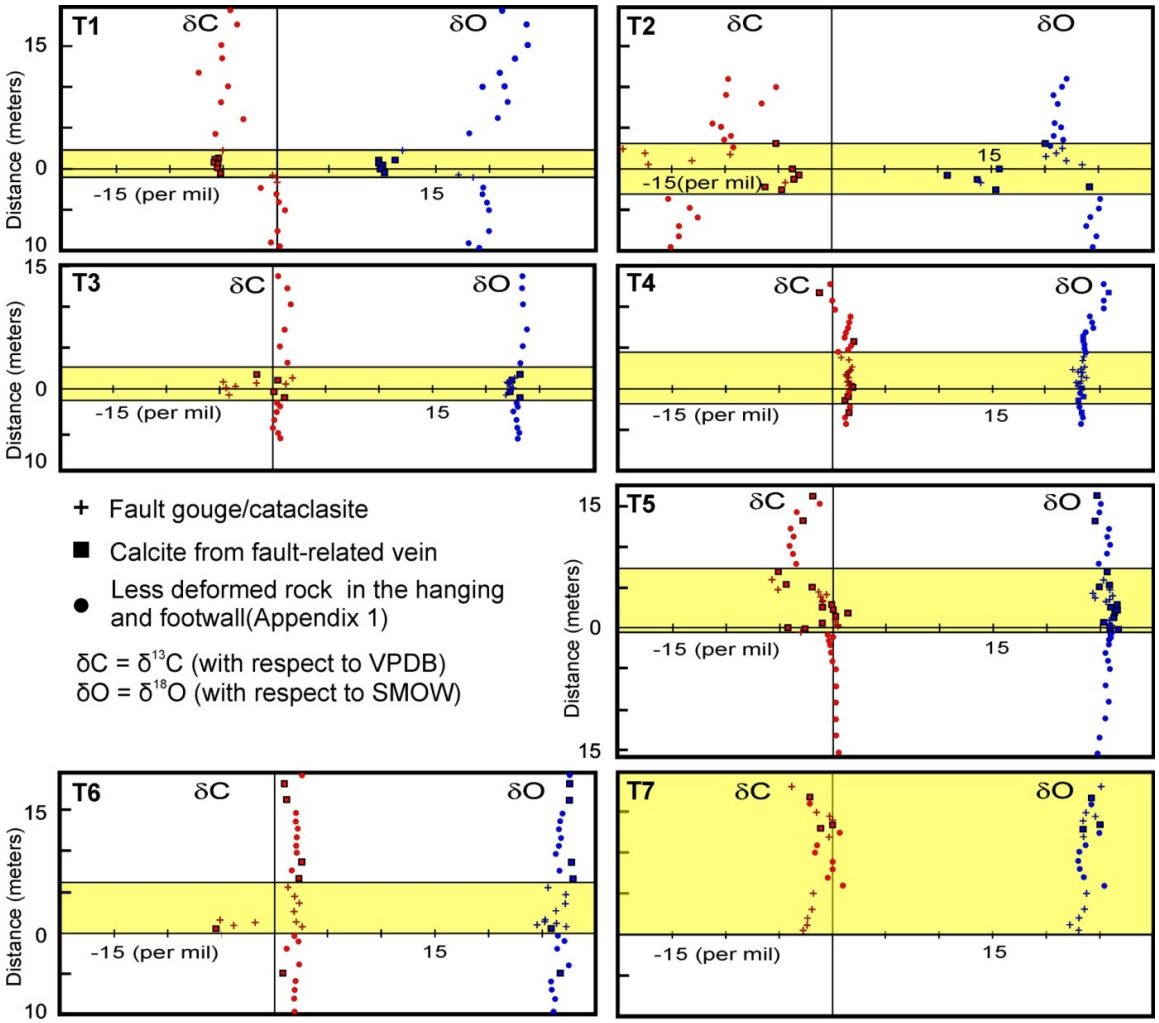

Figure 4-8. $\delta^{18}O_{VSMOW}$ and $\delta^{13}C_{VPDB}$ determinations in calcite veins, cataclasites and surrounding carbonate rocks along seven transects of major thrusts (as indicated in the upper left of each diagram). The isotopic values (‰) are plotted against distance, with the origin at the center of the most highly deformed zone in the thrust zone (the highlighted area). Sample locations are identified on Figs. 4-2 and 4-3.

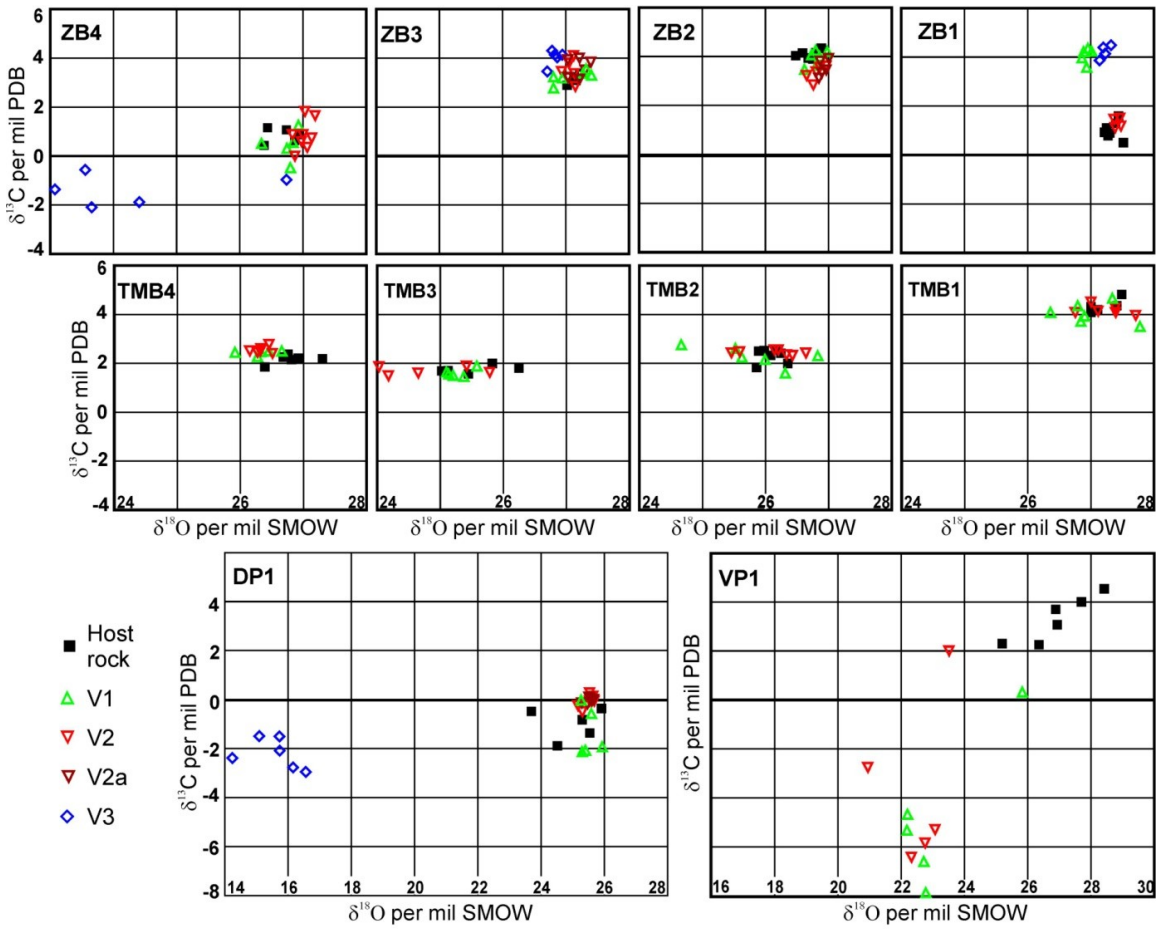

Figure 4-9. $\delta^{18}O_{VSMOW}$ vs. $\delta^{13}C_{VPDB}$ determinations in calcite from limestones and fold-related veins V1, V2 and V3 veins in ten different outcrops, keyed on the upper left on each diagram. V1 and V2 have $\delta^{18}O$ and $\delta^{13}C$ signatures close to their host rock 24‰ - 28‰, and -1‰ to 4‰, respectively, except for locality VP1. V3 veins in ZB4 and ED1 are strongly depleted in ^{18}O and slightly depleted in ^{13}C, while V3 veins in ZB1 are enriched in ^{13}C with respect to the host rock.

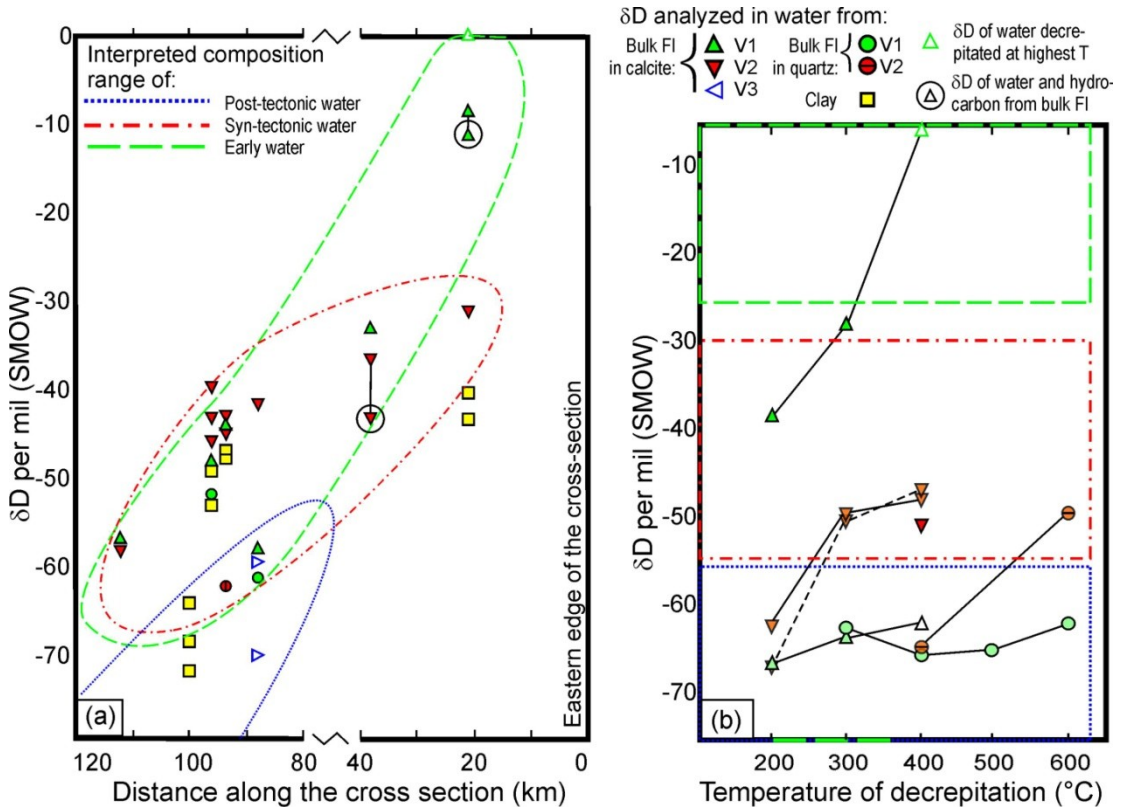

Figure 4-10. δD of water in fluid inclusions in veins, and of water in isotopic equilibrium with clays. The V1, V2 and V3 veins were collected along the cross-section and the clays from bentonite layers. (a) From water extracted at 400°C in calcite, 600°C in quartz, and 1500° in clay vs. distance along the cross-section (zero corresponds to the eastern edge, A' in fig.2). δD values correlate with both temperature and intensity of deformation, and all make a consistent trend in an inverse correlation. (b) δD values measured in water extracted from fluid inclusions within calcite and quartz at 100°C heating steps (from 200 to 400°C in calcite and from 200 to 600°C in quartz), whenever extracted water was available. Note the positive correlation between δD and temperature of extraction.

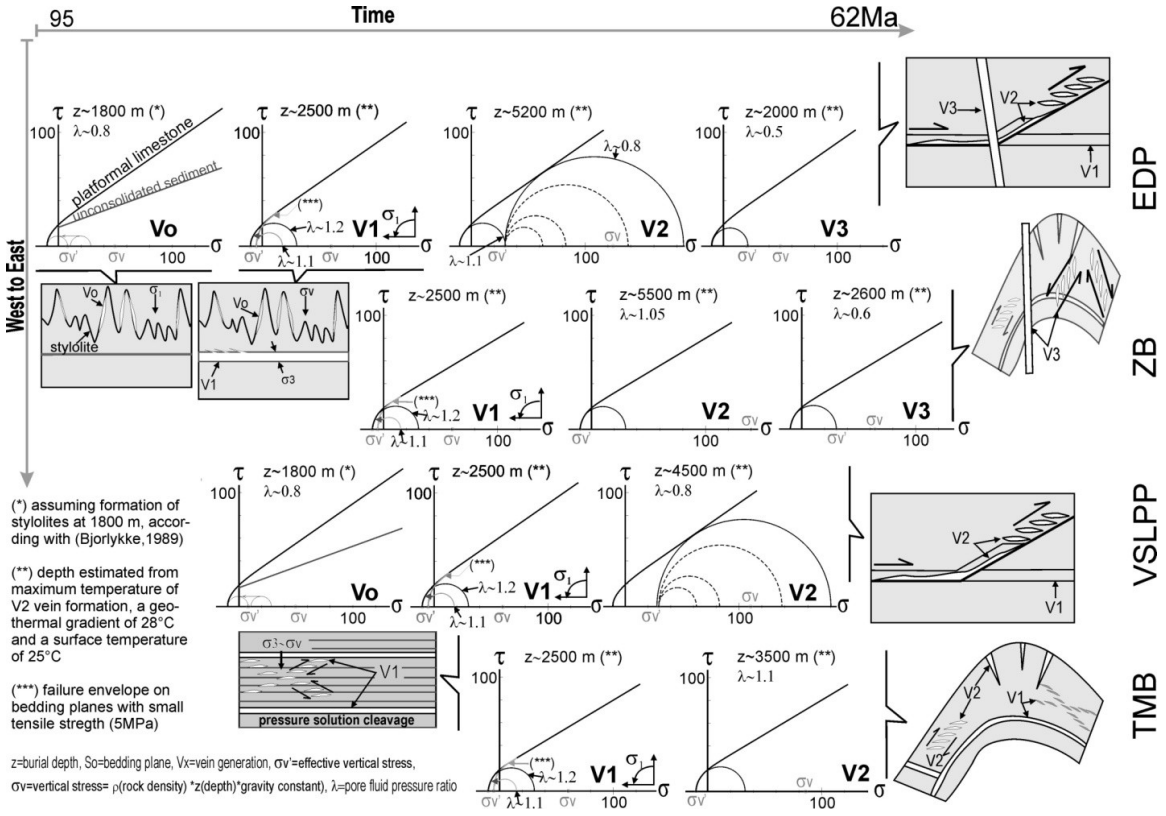

Figure 4-11. Inferred stress history within the wedge, based on relative abundance of vein types (extensional vs. shear) in each generation (V1, V2 and V3), burial depth (inferred from temperature of deformation, Fig. 4-12a), and constraints and theoretical considerations (Griffith, 1921; Byerlee, 1978; Sibson, 1998; Mandl, 2000). Failure mode is assumed to be combined Griffith/Mohr Coulomb (e. g., Price, 1966). Failure envelopes differ for different stages of deformation and limestone types (platformal and basinal). During the emplacement of V0 veins we assumed a poorly consolidated host rock with an angle of internal friction of 20°. During the emplacement of V1, we assumed a tensile strength (Ts) of 5 MPa along bedding, and angles of internal friction of 35° for platformal limestones (as they are dolomitized) and of 30° for basinal limestones (Sydney, 1966). During emplacement of V2 and V3 veins, we assumed a Ts of 10 MPa along bedding, and angles of internal friction of 35° for platformal limestone (dolomitized) and of 30° for basinal limestone. Criteria proposed by Sibson (1998) were utilized in drawing the Mohr circles and for calculating the pore fluid pressure ratios by accounting for estimated burial depths from temperature of deformation.

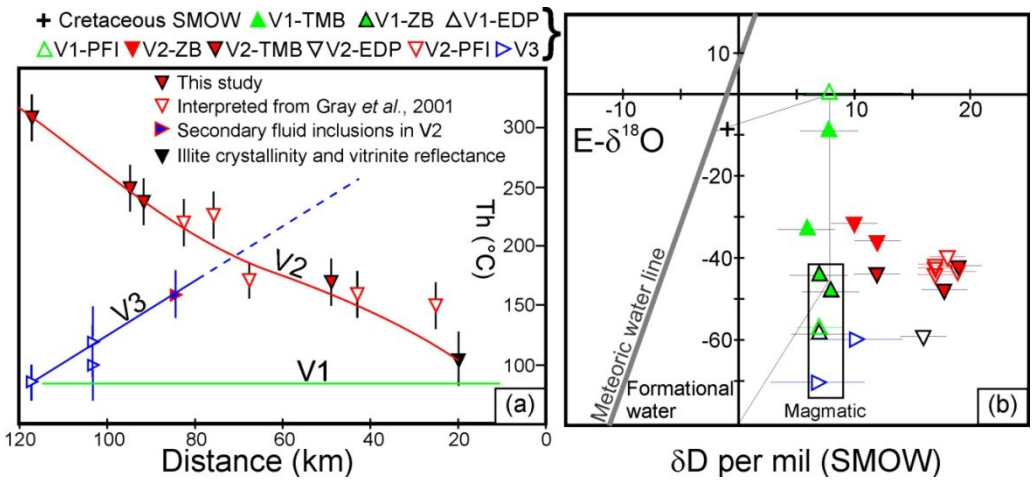

Figure 4-12. Temperature of deformation and isotopic composition of water from fluid inclusions. (a) Temperature profile for V1, V2 and V3 during deformation, based on a compilation of microthermometry of fluid inclusions reported in the area from this work (in solid symbols) and works by Valencia-Islas (1996), Gray *et al.* (2001) and Muñoz-Máximo (2010), in open symbols. The temperature ranges are in accordance with other thermometric methods (illite crystallinity, vitrinite reflectance, thermochronology) applied in the area. (b) $\delta^{18}O$ vs. δD plot for water from different vein generations and comparison with the meteoric water line and other possible sources of water. The range of $\delta^{18}O$ in fluid inclusions was calculated from $\delta^{18}O_{calcite}$, by assuming equilibrium and assuming the ranges of temperature of deformation (as for plot a), and equilibrium-state equations by O'Neil (1969) and Zheng (1994). The meteoric water line is based on measurements of recent meteoric water in Mexico (Wassenaar *et al.*, 2009), which does not significantly differ from Craig's (1961) meteoric water line. The envelopes for formational and magmatic waters were taken from Taylor (1974). The SMOW composition for Cretaceous times comes from (Eslinger and Yeh, 1986). Open symbols correspond to fluid inclusions released at the highest temperatures during decrepitation, presumably primary (green for V1, red for V2 veins and blue for V3 veins). IC = illite crystallinity, VR = Vitrinite Reflectance, pfia = primary fluid inclusion association, sfia = secondary fluid inclusion association.

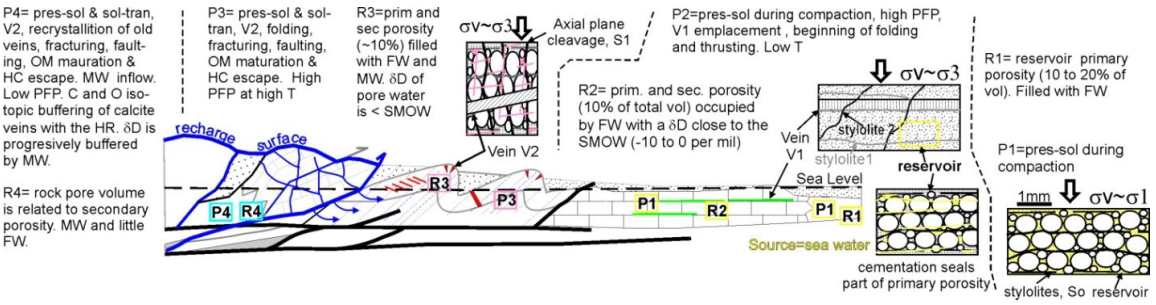

Figure 4-13. Synthesis of basic ideas and concepts discussed in the tectonic evolution model of the MFTB, further explained in Figure 4-14. Px=processes and conditions during deformation, Rx=reservoir, PFP=pore fluid pressure, T=temperature, FW=formational water, MW=meteoric water, OM=Organic Matter, HC=hydrocarbons, C=carbon, O=oxygen, pres-sol=pressure-solution, sol-tran=solution transfer, vol=volume, prim=primary, sec=secondary, σv=vertical stress.

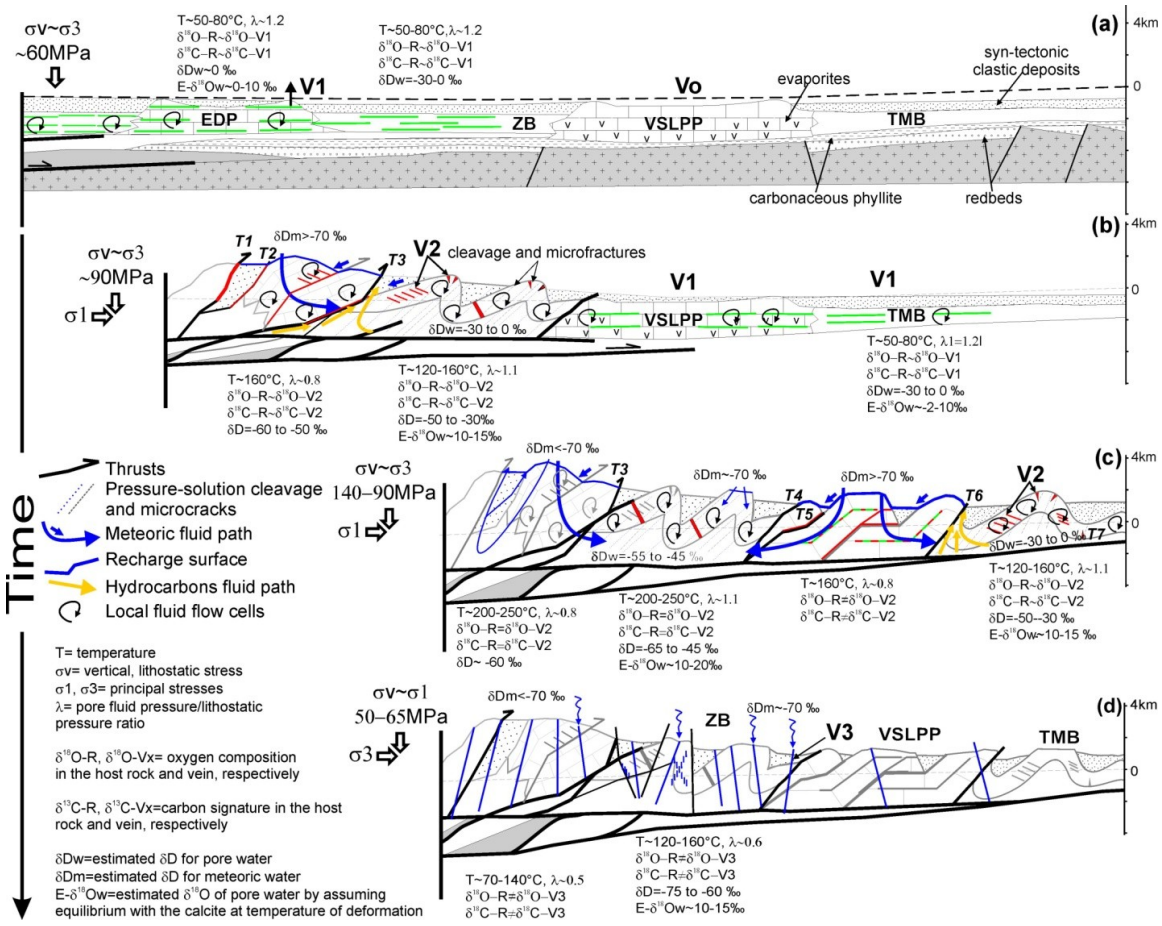

Figure 4-14. Conceptual model scenarios for the tectonic evolution of the MFTB. Each stage (a to d) shows the possible temperature of deformation, state of stress, pore fluid-pressure, and isotopic signature of aqueous fluids during deformation at different locations within the wedge. It also includes possible paths for aqueous fluids and hydrocarbons during deformation.

Table 4-1. List of samples and analytical methods applied

Sampling Locality	Paleogeographical Element	Coordinates (UTM)		Analysis			
		Latitude	Longitude	$\delta^{18}O$ & $\delta^{13}C$ in calcite	δD in fluid inclusions	δD in Illite-Smectite	clay analysis
T1	Tolimán Sequences, Higuerillas Thrust	2327861	414409				
T2	EL Doctor Plat., western boundary	2310383	429611				
T3	ZB, western boundary, El Doctor Thrust	2306474	438744				
T4	Zimapán Basin, eastern boundary, Volatín Thrust	2316548	459120				
T5	Valles-SLP Platform, Jiliapan Thrust	2320090	463823				
T6	Tampico-Misantla Basin, western boundary, Puerto de Piedra Thrust	2327403	488033				
T7	TMB, detachment zone	2324707	517033				
TMB1	Tampico-Misantla Basin	2334710	519126				
TMB2	Tampico-Misantla Basin	2340418	513206				
TMB3	Tampico-Misantla Basin	2334457	504135				
TMB4	Tampico-Misantla Basin	2331187	494461				
VP1	Valles-San Luis Potosí Platform	2325153	468068				
ZB1	Zimapán Basin	2318737	453221				
ZB2	Zimapán Basin	2309151	454054				
ZB3	Zimapán Basin	2311027	449760				
ZB4	Zimapán Basin	2311201	441909				
DP1	EL Doctor Platform	2312661	429611				
	Microthermometry of fluid inclusions in quartz from syn-tectonic veins						

Table 4-2. Structural, textural and compositional characteristics of the various generations of veins observed in the four different facies zones identified along the cross-section. Key: E = extension, S = shear related, SE = dominantly shear and some extension, ES = dominantly extension and some shear; b = blocky, be = blocky elongate, f = fibrous texture, c = crustiform, bd = banded. Cal/Qz (%) = rough estimate of calcite abundance (per weight) with respect to quartz in veins.

Vein type	Location	Typical			Cal/Qz (%)
		Length	Width	Texture	
V1- E	TMB	cm-m	1-3cm	b,be	>95
V1- E	VSLPP	cm-m	1-3cm	b, be	~100
V1-E	ZB	cm-m	1-3cm	be, f, b	>85
V1- ES	EDP	cm-m	1-3cm	b, be	~100
V1a- E	ZB	cm-m	1-3cm	f, be, b	>80
V1b- S	ZB	5-30 cm	0.5-2 cm	be, b	>90
V2- SE	TMB	1-10 cm	0.5-3 cm	be, f, b	~100
V2- S	VSLPP	cm-m	1-5 cm	b, be	~100
V2a-SE	ZB	1-10 cm	1-3cm	be, b	>85
V2b-E	ZB	1-30 cm	1-3cm	f, be, b	>85
V3- ES	ZB	3-x m	0.5-10 cm	c, bd	~100
V3- E	EDP	3-x m	1-20 cm	b, c	~100

UNIVERSITY OF MINNESOTA

Chapter 5

Age of deformation in the Mexican Fold-Thrust Belt in Central Mexico, preliminary results

Elisa Fitz-Díaz

The Mexican Fold-Thrust Belt (MFTB) was deformed in two shortening phases, a more intense D1 followed by a less intense D2. Stratigraphic constraints indicate that D1 started about 90 Ma on the western side of the MFTB in central Mexico and finished about 65Ma towards the east. Stratigraphic and structural observations in molasse type deposits in the foreland indicate that D2 took place after 65Ma. K/Ar ages of illite extracted from layers of bentonite intensively sheared during folding of D1 gave a range of ages between 84-77 Ma for one locality and between 64 and 71 in a second locality. In general, these ages are consistent with the stratigraphic constraints. Outcrop scale variations of illite properties and ages indicate that illite transformation and the closure of its K/Ar isotopic system are not only controlled by temperature (presumably the same everywhere in an outcrop) but also by strain variations in the folded bentonite layers. U-Th/He thermochronological ages determined in zircon gave a range of ages between 143-42Ma in seven different localities along the studied cross-section. The two westernmost (59-95Ma) and the two easternmost (143-42Ma) localities show the largest variability in ages of single zircon grains, while ages of zircons from two localities in the central part of the cross section, in the Zimapán Basin (58-62 Ma) and western side of the Tampico-Misantla Basin (64-67 Ma), are consistent among themselves and with the stratigraphic constraints. These ages indicate that the rocks were exhumed (cooled) after deformation, and thus they are also consistent with stratigraphic constrains. The significance of K/Ar ages in illite and U-Th/He ages from zircons are discussed.

5.1 Introduction

The development of fold thrust belts includes processes of deformation, uplift, erosion, sedimentation and in some cases low grade metamorphism (Dickinson, 1971). The orogenic wedge theory (Davis *et al.*, 1983; Dahlen *et al.*, 1984 and 1989; Dahlen, 1984 and 1990) explains how all these processes may occur at different times and places during the evolution of a fold-thrust belt. Deformation within the wedge produces thickening and therefore topography. Topography in turn enhances the processes of erosion and sedimentation, the effects of which are recorded in the rocks within the wedge now exposed at the surface (Koons, 1990; Beaumont *et al.*, 1992; Boyer, 1995; Cruz *et al.*, 2008). These linked phenomena have been observed in a number of natural examples (e. g. Beck *et al.*, 1988; Dickinson *et al.*, 1988; DeCelles, 1994) and analyzed by use of physical and numerical models (Storti and McClay, 1995; Mugnier *et al.*, 1997; Stockmal *et al.* (2007).

Another effect of deformation thickening in a fold-thrust belt is the increase of pressure (P) and temperature (T) at which deformation occurs within the wedge. Pressure and temperature can in turn induce formation of new minerals, if appropriate lithological/chemical conditions exist. Deformation thickening also indirectly affects the exhumation rates, which are expected to be faster towards the rear of the wedge where the topographic elevation is also higher (Dahlen and Barr, 1989; Dahlen, 1990; Cruz *et al.*, 2008). This complex combination of interacting factors allows a broad spectrum of structures formed at different P-T conditions to be exposed at the wedge surface.

It has been successfully demonstrated that thin-skinned fold-thrust belts develop broadly according to the orogenic wedge model (Davis *et al.*, 1983). In natural examples, however, the rocks involved in the deformation are not homogenous, and this has an impact in the heterogeneous nature of the deformation observed within fold-thrust belts (Price, 1981; Boyer and Elliott, 1992; Fitz-Díaz *et al.*, 2010). Having this complex scenario of conditions in mind is critical to the successful application of techniques to estimate the age of deformation in fold-thrust belts and the correct interpretation of such ages.

One indirect method for constraining the age of deformation is the dating of syntectonic sedimentary deposits. This requires a careful combination of detailed stratigraphic and structural analysis to ensure that sedimentation and deformation were contemporaneous. The resolution and the applicability of techniques (either paleontological or isotopic) to determine the age of the deposit vary depending on the availability of fossil record or datable authigenic minerals. Because of this, the ages of syntectonic deposits are commonly meaningful at the scale (spatial and temporal) of the deposit. There are outstanding studies of syntectonic deposits that have provided insight into the evolution of the North American Cordillera (Dickinson *et al.*, 1988), DeCelles (1994 and 2004) and Evenchick *et al.* (2007) and of the Pyrenees foreland (Burbank, 1992; Castelltort, 2003). This valuable approach requires detailed stratigraphic work that commonly takes a long time compared to other thermochronological and geochronological approaches to dating deformation. Although the analysis of syn-tectonic deposits provides valuable information on the history of tectonic activity in a region, it has the limitation that it is not generally possible to establish a direct correlation between a sedimentary deposit and a particular structure or episode of deformation.

Another way to constrain the age of deformation in fold-thrust belts is by applying low-temperature thermochronology. Thermochronological techniques are based on fundamentals of radiogenic isotope systematics and on the knowledge of the closure temperature (Tc) of the isotopic system/mineral of interest (Reiners *et al.*, 2005; Harrison and Zeitler, 2005). Geochronology helps to determine the age of formation of minerals by quantifying daughter isotopes derived from radiogenic isotopes in a mineral that is assumed to behave as a closed system after its crystallization (Faure and Mensing, 2005). Thermochronology, on the other hand, estimates the time at which a mineral closed its system for a particular isotope at a temperature that is lower than the temperature of crystallization. Thermochronology allows the interpretation of apparent cooling ages based on a detailed interpretation of the thermodynamic and kinetic properties of minerals with radiogenic elements (e.g. apatite, zircon and titanite) from

experimental work, together with modeling of the production of daughter isotopes (e.g. He), and the accumulation of such isotopes within a mineral, considering loss by volume diffusion (Dunai, 2005; Ketcham, 2005). In combination with geochronology, thermochronology allows estimating not only ages but also the rate of processes such as exhumation, to be inferred from cooling rates (Reiners *et al.*, 2005). Details on the history, theory and applications of thermochronological techniques can be consulted in Reiners and Ehrls (2005).

In fold-thrust belts, in which deformation occurs at temperatures lower than 300°C, some suitable methods to determine cooling ages are: fission track analysis in zircon and apatite; and U-Th/He in titanite, zircon and apatite. Closure temperatures for these systems are given by Reiners *et al.* (2005). Because of its abundance, its mechanical resistance, its chemical stability and its relative purity (it does not host many solid or fluid inclusions), zircon is probably the most feasible mineral for low T thermochronology and U-Th/He is more suitable technique than fission track analysis (Reiners, 2005; Tamagi and O'Sullivan, 2005). For all these reasons, together with the fact that temperatures of deformation in fold-thrust belts are high enough to reset the U-Th/He system, U-Th/He zircon dating is a good option for determining cooling ages and interpreting exhumation ages and rates in fold-thrust belts (Spotila, 2005; Cecil *et al.*, 2006).

Illite dating is probably the most common technique used for dating deformation and diagenesis in fold thrust belt environments (Pevear, 1999). Illite originates from the reaction of smectite with a K bearing phase (solid or fluid, Abdioglu *et al.*, 2005). The formation of pure illite ($2M_1$ polytype) has intermediate stages, for instance illite-smectite interlayers (1M/2M1 polytype), which in a later stage are interlayered with a purer illite polytype ($2M_1$, Pevear, 1999). These stages form part of a continuous Arrhenius type of reaction from smectite to muscovite and this is believed to be mainly controlled by temperature (Srodon and Erls, 1984). More recently, however, detailed analysis of transects along fault zones have shown that this reaction is also very sensitive to strain (Vrolijk and Vander Pluijm, 1999; Casciello *et al.*, 2004). These characteristics together make illite suitable for deformation dating (Lyons, 1971; Foland *et al.*, 1992; Van der Pluijm *et al.*, 2001). Illite is produced in an irreversible reaction, which is partially a deformation driven reaction, linked to the fact that illite hosts potassium in its structure.

Nevertheless, there are some analytical challenges posed in using illite to determine the age of deformation. Its fine grain size make analysis difficult, and the fact that illite is typically found in clastic deposits and fault rocks means that authigenic illite is frequently mixed with detrital illite (Meunier *et al.*, 2004). Separating authigenic from detrital illite is fundamental in

getting representative ages of deformation or diagenesis. The mixture of authigenic with detrital illite would give older apparent ages (Pevear, 1999; Meunier *et al.*, 2004). One way to examine for detrital contamination is by dating different size fractions, since the detrital/authigenic illite proportion typically increases with grain size, as does age (Clauer and Chaudhuri, 1994; Pevear, 1999; Van der Pluijm *et al.*, 2001; Lerman and Clauer, 2005). One way to avoid detrital illite contamination is by analyzing illite in bentonite, in which smectite and kaolinite are alteration products of volcanic (e. g. glass, plagioclase and feldspar) materials during diagenesis and further reactions that involve these clays and a source of K produce illite as temperature and/or strain increase (Abdioglu *et al.*, 2005; Compton and Vennemann, 1992; Casciello *et al.*, 2004).

Apparent ages of authigenic illite that are too young have been also documented and these can be due to ^{40}Ar loss by diffusion, which is sensitive to the clay size (Lerman and Clauer, 2005). Another reason for getting apparent younger ages in authigenic illite can be due to the duration of K accumulation stage (growth stage) of illite compared to the analytic error of the dating technique (Meunier *et al.*, 2004). Despite these limitations, illite dating has been successfully applied to age determinations of deformation in a number of brittle faults around the world, and it has provided meaningful ages for interpreting burial and exhumation histories of sedimentary sequences (Kralik et al., 1987; Cosca et al., 1992; Vrolijk and Van der Pluijm, 1999; Zwingmann and Mancktelow, 2004; Van der Pluijm *et al.*, 2006; Solum and Van der Pluijm, 2007, Sasseville *et al.*, 2008; Clauer *et al.*, 2008).

The purpose of this work is to determine the age of deformation in the Mexican Fold-Thrust Belt in central Mexico. For this, previous studies on stratigraphy of the area, especially on syn-tectonic turbidites are reviewed. U-Th/He ages in zircon from volcaniclastic and siliciclastic sequences and K/Ar ages in illite from bentonite layers interbedded with carbonates have been determined at different localities along the cross-section (Fig. 5-1). The significance of such ages in the evolution of the Mexican Fold-Thrust Belt, in terms of the propagation of deformation and of the cooling of the rocks within the wedge is discussed.

5.2 Geological Framework

The studied cross-section (Fig. 5-1) is of the deformed cordilleran foreland, locally known as the Mexican Fold-Thrust Belt (Fitz-Díaz *et al.*, 2010, Chapter 2). Most of the rocks involved in the deformation form part of the sedimentary cover which includes, at the base: Triassic-Jurassic siliciclastic sediments (El Chilar Fm. on the western side of the cross-section and Cahuasas Fm. on the east), which are covered by Jurassic-Early Cretaceous volcaniclastic

rocks (San Juan de la Rosa Fm.) to the west (in the Tolimán area, Fig. 5-1), and by Cretaceous carbonates towards the foreland (see Fig. 3-2 in Chapter 3 for details and Fig. 5-1). The carbonates account for most of the volume of rocks involved in the deformation and they change facies laterally, there being two basins and two platforms (from west to east: El Doctor Platform, Zimapán Basin, Valles-San Luis Potosí Platform and Tampico-Misantla Basin, Fig. 5-1). Two main phases of deformation (D1 and D2) affected the rocks of the fold-thrust belt, with D1 the major event that produced thrusts, folds, and a penetrative axial planar cleavage (S1) in the volcaniclastic formations and in syntectonic turbidites. S1 is more widely spaced in the carbonates (Chapter 3). D2 modified the D1 structures to produce open folds, and a spaced cleavage (S2) affecting the S1 cleavage in the volcaniclastic rocks. D2 is the only event that affected Paleogene clastic sequences in the easternmost part of the section (Fig. 3-2, Chapter 3).

The nature and distribution (exposure) of rocks within the MFTB was important in choosing appropriate geochronological methods and in designing the sampling strategy. Knowledge of the deformation and thermal conditions of deformation within the wedge were also taken into account. The results from the structural analysis presented in chapters 2 and 3 show a gradient in the intensity of deformation that increases to the west of the cross section, or in other words from the front to the rear of the fold-thrust belt wedge. Microthermometry of fluid inclusions also indicates a similar gradient of the temperature of deformation, which increases from about 100°C on the foreland side of the cross-section to above 300°C to the west (Fig. 4-12, Chapter 4). Details of the stratigraphy and structure are given in chapters 2 and 3.

Samples for zircon U-Th/He dating were collected in localities Z1 to Z7, shown on the cross-section of Figure 5-1. Most of the samples come from siliciclastic and volcaniclastic rocks (Fig. 5-1). In locality Z1 the samples are of quartzite from a Triassic siliciclastic assemblage. The sample from locality Z2 comes from an Early Cretaceous volcaniclastic sandstone layer (San Juan de la Rosa Fm., Fig. 3-2 in Chapter 3). Z1 and Z2 are the western-most localities, at the highest elevations (about 2500 meter above sea level) in the cross-section. In localities Z3 and Z4 the samples were taken in the same stratigraphic unit, a Late Jurassic volcaniclastic sandstone package exposed at the base of Trancas Fm. (Chapter 3). These rocks are exposed on the western side of the Zimapan Basin and both samples were taken at slightly different elevations (900 and 1100 m, respectively) in the core of the Bonanza anticline. The localities are 5 km apart along the fold hinge. Samples taken at Z5 and Z5' come from Late Cretaceous turbidites (San Felipe Fm., Chapter 3) and were collected at elevations of 1800 and 800 meters above sea level, respectively. These rocks were taken in the footwall rocks of the Puerto de Piedra-El Lobo Thrust zone (Fig. 5-

1). At localities Z6 and Z7 samples were taken from Triassic-Jurassic redbeds (Cahuasas Fm., Fig. 3-2 in Chapter 3). These are not strongly affected by the deformation since they are located below the main detachment zone of the fold-thrust belt.

For illite dating 15 samples of bentonite interbedded with Cretaceous basinal limestones were collected for illite characterization and K/Ar dating. These samples come from four localities, two of them located within the Zimapán Basin (I-1 and I-2 in Fig. 5-1) and two in the Tampico-Misantla Basin (I-3 and I-4, Fig. 5-1).

5.3 Methodology

5.3.1 U-Th/He zircon dating

5.3.1.1 The isotopic system

U-Th/He dating is based on the fact that ^{4}He is produced by intermediate, radioactive daughter products of ^{238}U, ^{235}U and ^{232}Th by α-decay. Since He is an inert gas, it is unable to chemically bond in silicates at high temperatures and because of that He atoms tend to be lost from U-bearing minerals. This leads to U-Th/He ages that are much younger than the age of mineral formation (Harrison and Zeitler, 2005). Experimental work has constrained closure temperatures of the U-Th/He system in different minerals, and the closure temperature depends on the rate of cooling of the mineral. For example, experimental work indicates that the closure temperature for zircon is of 175-193°C when cooled at a rate of 10°C/Ma (Reiners, 2005).

5.3.1.2 The samples

Zircons from the sandstone and siltstone samples collected in the field were separated by applying routine techniques that include: rock crushing and grinding, washing/shaking of the powder in the Wilfley table to concentrate heavy minerals; magnetic separation, and finally concentration of zircon grains by using heavy-liquids (this work was carried out at the UNAM and UMN). Unfortunately no apatite with the required quality (inclusion free) was found in the samples for U-Th/He dating; because of that the work was focused on zircon.

5.3.1.3 The analytical procedures

In U-Th/He dating the parent and daughter nuclides are measured in the same aliquot (same zircon grain) since U and Th concentration might vary among crystals (Reiners, 2005). This makes grain selection a critical step in the application of this technique. Typically, euhedral zircon grains, with a width between 75-150 μm were selected. These grains were photographed and measured (length and width in two orthogonal faces and pyramid height), for the purpose of

calculating surface area, by approximating the grains to a model shape of a perfect tetragonal bi-pyramidal zircon crystal (Reiners, 2005).

After measuring, single zircon grains were wrapped in niobium caps before they were degasified in a high-vacuum system by heating with a laser beam above 1100°C for 15 minutes. The niobium caps allow a homogenous distribution of heat around the grain and prevent grain damage by avoiding direct laser incidence on the grain. The gas extracted from zircon is spiked with 0.1-1 pmol of ^{3}He and then the $^{3}He/^{4}He$ ratio is measured in a gas-source quadrupole mass spectrometer. The ^{4}He concentration (the unknown daughter radioisotope in zircon) is calculated from this ratio and corrected for background and mass interferences. The parent nuclides (U and Th) are measured in the degassed zircon by using isotope dilution and solution (ICP-MS). A total of 21 U-Th/He ages (Table 5-1) were obtained at the U. of Arizona Radiogenic Helium Dating Laboratory with the help of Peter Reiners and Stefan Nicolascu.

5.3.2 Illite K/Ar dating

5.3.2.1 The isotopic system

Like U-Th/He, the K/Ar dating method also involves the production of an inert gas (^{40}Ar), by the decay of ^{40}K. Therefore the same theoretical principles as for helium are applied to argon, such as loss by diffusion at high temperatures. Muscovite, for instance, is a K bearing mineral and has a closure temperature for Ar between 300 and 350°C (Hames and Bowring, 1994). Illite is an intermediate K bearing mineral (formed and transformed between 40 to 200°C, Srodon and Erls, 1984) of a continuous reaction from smectite to muscovite typically observed in metapelites (Meunier, 2005). However, since illite behaves as a solid solution during part of its growth history, the isotopic closure of argon in illite depends on other factors besides temperature, such as the speed of the smectite-illite transformation, strain and grain size (Vrolijk and Van der Pluijm, 1999; Casciello *et al.*, 2004; Lerman and Clauer, 2005).

5.3.2.2 The samples

Given the nature of illite, it is imperative that a number of considerations be taken into account prior to its use in K/Ar dating. In the first place, to avoid mixture between authigenic and detrital illite, only bentonite layers were sampled. The bentonite layers are interbedded with limestone layers which experienced folding by bucking. A description of the studied outcrops and structural analysis and interpretation are presented in Chapter 3. These indicate that the folding mechanism affecting this multilayer system (limestone, bentonite and shale) was flexural slip, which induces a considerable amount of shear in the incompetent layers (bentonite). In

symmetrical folds the flexural slip model suggests that shear is the same in the two limbs, decreasing to zero in the hinge (Figure 5-2). The heterogeneous distribution of strain around the asymmetric folds requires a case by case analysis based on the final geometry of individual folds (see Chapter 3). In other to test the effects of strain on illite (from bentonite) properties, three samples from different parts (limbs and hinge) of previously well studied folds were taken from four outcrops. In outcrop I-2, three extra samples were taken around a fold hinge (for a total of 15 samples, Table 5-2).

5.3.2.3 The analytical procedures

The bentonite samples were prepared following the recommendations of the IGCP 294 IC working group (Kisch, 1990). An unaggressive procedure was used for clay separation, which included: rock crushing, dispersion of powder in de-ionized water in an ultrasonic probe, separation of the fraction < 2μm by gravity settling, washing and concentration of this fraction by centrifuge, and finally preparation for X-ray diffraction (XRD) by sedimentation onto round glass slides. The next step was the determination of the mineralogy of the bentonite samples by applying XRD (Table 5-2). Illite characterization included determining the illite crystallinity index (IC), intensity ratio index (Ir) and the crystallite size (CS). Details of the methodology followed are given in section 3.3 of Chapter 4. In order to obtain statistically representative IC values, duplicates were analyzed in all cases. The analyses were carried out at the Institute of Geology, UNAM.

The clay samples selected for dating did not contain K-feldspar, chlorite or other mineral phases that could be a source for K or Ar in the size fraction smaller than 2μm. Only a few milligrams of the illite concentrates were used for K-Ar dating. The K-Ar dating was done by Jesús Solé at the Institute of Geology, UNAM, by using known techniques for measuring K and Ar isotopes with mass spectrometry and by using laser heating and melting for gas extraction. The details of this method are given by Solé (2009).

5.4 Results

The U-Th/He ages determined in zircons in sandstones from the 7 localities are given in Table 5-1. These include the correction due to He lost by volume diffusion (Reiners, 2005). The error is related only to the analytical procedure. The column to the right shows some U-Pb ages analyzed in detrital zircons from the same samples (Dávila-Alcocer *et al.*, 2009), and these indicate that, as expected, in all the cases the crystallization age of the zircons is older than the thermochronological age.

Ages from zircon in the two westernmost localities Z1 and Z2, which are located in the same assemblage of rocks, give a range of U-Th/He ages between 59 and 95 Ma. The two zircons dated in locality Z3 gave ages of 84 and 62 Ma. Three zircons from Z4 gave more consistent ages, between 58-61 Ma. A similar consistency is observed in the three ages in zircons from locality Z5, 64-67 Ma. Two zircons from Z5' gave younger ages (55 and 48 Ma). Zircons from locality Z6 also show a variation of cooling ages from 43 to 143 Ma, while ages in Z7 also show a high variation, between 103 and 43 Ma.

The results from illite characterization and K/Ar dating are synthesized in Table 5-2. Plots of illite properties (IC, Ir and CS) from the four analyzed outcrops along the cross section show a good correlation among them (Fig. 5-3). In the plot of Figure 5-3a we can observe that the illite crystallinity index (IC) shows a positive correlation with the intensity ratio index (Ir); in other words the larger the IC values (lower crystallinity) the larger Ir (more illite-smectite interlayers are present in the illite grains). By contrast, Figure 5-3b, shows a negative correlation between IC and the crystallite size index (CS), which indicates that larger illite grains are also more crystalline. In Figure 5-3c we also see a negative correlation between CS and Ir, which indicates that the crystallite size in samples of illite with more interlayer smectite is smaller than it is in pure illite samples, which have larger crystals with a better organized lattice (more crystalline).

There are first order trends in the data related to their location along the cross-section. For instance, the Ir and IC are smaller in the samples taken in the Zimapán Basin than those in the Tampico-Misantla Basin. The values of CS, however, are larger in the western basin (Figs. 5-1 and 5-3),

At the outcrop scale, the Ir index does not show any systematic variation around a fold. CS and IC, however, show second order variations around the folds, depending on the position within the fold from which the sample was taken (e. g. hinge or attenuated limb in asymmetrical folds).

The oldest K/Ar ages of illite were determined in samples from the western-most locality, I-1 (76-85 Ma). The oldest age in this outcrop was obtained from the sample taken at the hinge of the fold (85 Ma). Younger ages were determined in locality I-2 (71-64 Ma), and again the older ages were determined at the hinges of the folds (an anticline-syncline pair), while the youngest ages were determined in the overturned limb of these asymmetric folds (Fig. 5-4). In general, there is a good agreement between the K measured in the samples and a semi-quantitative estimate of it by comparing the main peaks of the clays (illite, kaolinite and chlorite) in the

corresponding diffractogram. This comparison supports the assumption that the K is hosted in no other phase of the clay fraction but illite. The only sample that does not show a good agreement is sample number 15, in which the other source of K is feldspar (Table 5-2), therefore this apparent age probably does not correspond to the age of formation/closure of illite.

5.5 Discussion

5.5.1 Wedge-scale implication of ages

The syn-tectonic nature and the biostratigraphic age (91-85MA) of the clastic deposits (Soyatal Fm.) on the western side of the studied cross-section (El Doctor Platform and Zimapán Basin, Fig. 5-1) were documented in great detail by Henández-Jaúregui (1997). This work, together with detailed micropaleontological analysis of similar deposits (Mendez Fm.) on the foreland side of the MFTB by López-Oliva *et al.* (1998) helps to constrain the age of the main event of deformation (D1) of the Mexican Fold-thrust Belt at between 90-65 Ma (Fig. 3-2 in Chapter 3). The Paleogene age of molasse (Velasco Fm.) deposited above the Mendez Fm., together with the fact that these rocks do not register the deformation associated with D1 and are affected only by small-displacement thrusts of D2, indicate that the second shortening event in this area was less intense and took place in the early Cenozoic.

The U-Th/He ages from zircons taken from two localities (Z-1 and Z-2) are 76 and 83 Ma for locality Z-1 and range between 59 and 95 Ma for Z-2 (Fig. 5-1). These samples were taken from rocks of the Tolimán Sequences which constitute an assemblage of relatively allochthonous units thrust over Cretaceous carbonates to the east. The Tolimán Sequence rocks show the most complex and intense deformation in the area, and at higher temperatures (above 300°C, Fig. 4-12, Chapter 4) than elsewhere. According to the orogenic wedge theory these rocks would have experienced the maximum burial conditions in the area (high enough to reset the U-Th/He system in the zircons) relatively early during deformation, followed by a relatively fast exhumation. If these rocks had remained together during deformation, zircons from localities Z-1 and Z-2 should be similar and show the oldest cooling ages in the whole cross-section. The ages from Z-1 (76 and 83 Ma) overlap with the age (91-85 Ma) of syntectonic deposits (Soyatal Fm.) to the east. The U-Th/He ages in the zircons from sample Z-2, however, show greater variation (59-95 Ma), and this does not satisfy these predictions. This variability in age could be due to partial resetting of the isotope system because the U-Th/He closing temperature was never achieved (Mitchell and Reiners, 2003) or to later He loss by volume diffusion that varied among the zircon grains. The latter could have been caused by re-heating of the rocks at the surface by wild fires or human

activity, for example (Mitchell and Reiners, 2003). Five zircons from the Zimapán Basin (Z-3 and Z4) show consistent cooling ages between 58-62 Ma, with the exception of Z3-1. These ages are consistent with the temperature of deformation estimated in this area (200-250°C), that allowed the zircons to reset, and with the age of deformation for this basin constrained by stratigraphy and a later cooling during exhumation. Consistent ages were also observed for the three zircons from Z5 (64-67 Ma), which make sense with estimates of temperature of deformation (190-160°C) from fluid inclusion microthermometry and with the age of syntectonic deposits in this portion of the cross-section (older than 65 Ma). Two zircons from Z5' gave younger ages (48 and 55 Ma), even though the samples were collected along the same thrust zone a few kilometers along strike in the same stratigraphic unit. Z5' was collected 1 km below Z5 in elevation, on the bed of a major river. Thus these cooling ages could be controlled by different erosion rates between these two localities. Finally, zircons from redbeds in the Tampico-Misantla Basin (localities Z6 and Z7) in the foreland of the cross-section gave ages younger than the age of the deposit and show the largest variation compared to the other locations. Since temperature of deformation in this area never reached 160°C, it is likely that these zircons were not fully reset.

U-Th/He ages from the Zimapán and Tampico Misantla basins make sense with the age of deformation constrained using biostratigraphic analyses, and with the estimates of temperature of deformation. It is difficult, nevertheless, to find a deeper significance of these. This is partially due to the limited amount of data and to the fact that no detailed sampling, controlling elevation in the different localities was done that would allow determining exhumation rates associated with the later evolution of the MFTB.

5.5.2 Small scale age resolution

As a first order approximation, the K/Ar illite (64-84 Ma) ages are consistent with the stratigraphical constraints (90-65 Ma) of deformation in the region. There are, however, some variations in the clay properties and ages at the scale of the outcrop that deserve a closer look. Figure 5-4 shows the distribution of sampling spots in two outcrops I-1 (a) and I-2 (b), and their corresponding clay properties data and K/Ar ages. The ages obtained in locality I-4 will not be discussed here since they might not be reliable due to the presence of K-feldspar in theclay fraction that could affect the total K concentration in the sample, giving anomalously young age estimates.

In the fold from locality I-1, the Ir index is pretty much the same in the three sampled spots (close to 1), which indicates that illite is almost pure, or in other words the amount of

interlayer smectite in the grains is negligible. The illite crystallinity index however is smaller in the hinge than in the limbs indicating more crystalline illite (fewer lattice imperfections) in the hinge of the fold compared to the limbs. The illite crystallite size is also larger in the hinge. IC and CS, on the other hand show about the same values in the limbs as in the hinge. The K-Ar ages determined in illite are also close to each other in the limbs (about 77 Ma) and younger than the age found in the hinge by about 7 Ma.

Samples from locality I-2 were taken in a pair of steeply inclined asymmetrical chevron folds (a syncline-anticline pair) that have the particularity that the inverted limb in the anticline is strongly attenuated (layers are three times thinner than in the long limb, Fig. 5-2) and the hinge is thickened compared to the long limb. The Ir index does not show a large or systematic variation around the fold in the 6 analyzed samples and is greater than 1, indicating the presence of a small amount of smectite interlayers in illite grains. However, the illite is more crystalline and its CS is larger in the attenuated limb of the fold (sample 9, Table 5-2) than in the hinges (4, 5, 6 and 8) and in the long limb (7, Fig. 5-4b). Ages from the samples in the anticline hinge (4-6) vary between 67 and 71 Ma, and the age of the normal limb of the syncline (7) falls within this range. Ages from the overturned-attenuated limb and the syncline hinge (samples 9 and 8) are about the same, 64 Ma, and thus about 3-7 Ma younger.

The temperature of deformation in fold-thrust-belts is assumed to be due to the geothermal gradient (Dahlen and Barr, 1989). If temperature was the only factor controlling the clay reactions, illite transformation and ultimately the closure of the K-Ar isotopic system would be expected to be the same among samples in the same outcrop, and thus the ages should be the same – there should be no variation in age around the analyzed folds. One factor that varies around the folds and that might explain the observed difference in age is strain. In previous work strain has been recognized as playing an important role in illite transformation (Casciello *et al.*, 2004) and thus in the resetting of the K-Ar isotopic system (Vrolijk and Van der Pluijm, 1999).

In our interpretation of these data we make the following assumptions: 1) detrital illite is absent in the sampled bentonite layers; 2) illite found in the samples was produced in a continuous reaction that included the alteration of volcanic glass and minerals to smectite and the reaction of smectite with a K-rich phase in the presence of water to produce illite-smectite interlayers; 3) illite-smectite interlayers kept transforming during the deformation of the MFTB to become pure illite; 4) the deformation in the bentonite layers is relatively high compared to that in the limestone layers, due to relative competence and strain partitioning of shear parallel to bedding during

flexural-slip folding in multilayers (Ramsay, 1974); 5) the thermal history is homogenous at the scale of the fold; 6) the relatively small strain related to later 'passive' folding did not reset the K/Ar ages of illite in the hinges of the folds (Chapter 3). We propose 3 fold-kinematic models, illustrated in Fig. 5-5, to account for the variation in illite age around the folds in I-1 and I-2.

In Chapter 3 the kinematics of folding in localities I-1 and I-2 (Fig. 3-7 b and c, and Fig. 3-10 of Chapter 3) is discussed with more detail. One of the conclusions from that study is that the folds in the basinal carbonates were formed in two stages, an early stage of active folding, followed by a second stage of passive folding. The first stage, which included buckling (Biot, 1965) with flexural slip as the main mechanism, gave place to trains of chevron folds in multilayers. During passive folding, the main mechanism was flattening that accounted for a small amount (10%) of additional shortening (Chapter 3). The flexural slip mechanism implies deformation partitioning among competent and incompetent layers, which accentuates shear in the incompetent layers such as bentonite. During early stages the deformation should be similar at every point along the folded layer but in later stages shear mostly occurs in the limbs. The strain concentrated in the fold limbs should be about the same for symmetrical folds formed under pure shear.

Asymmetrical folds, which typically show an inclined axial plane and different limb lengths, are the result of the combination of pure shear and simple shear and the strain accumulated among the limbs is different, and is commonly accentuated in the fore-limb.

Two models to explain age variation around fold in I-1 are proposed. In Model I (Fig. 5-5a) the age in the hinge corresponds to the beginning of bucking, while the age in the limbs corresponds to the end of buckling. Illite was formed and recrystallized during the early stages of folding throughout the layer. As the fold grew, illite in the hinge did not experience significant further deformation while illite in the limbs experienced enhanced deformation, since flexural slip increases with limb dip and is nonexistent at the hinge. Deformation continued in the limbs until the folds reached the locking angle when the illite transformation stopped and the K/Ar isotopic system closed. The alternative interpretation, Model II, proposes that the isotopic system of illite remained open throughout buckling. During flattening the deformation of the rocks was not passive but quasi-passive, with shear still being accommodated in the limbs but not at the hinge. In this case 84 Ma would correspond to the end of buckling while 77 Ma would correspond to the very end of folding (active and further passive folding included). In either case, the correspondence in age in the limbs indicates that the deformation ended in them at about the same

time and after roughly the same strain had accumulated in the two limbs. This last point can be observed by comparing layer-thickness variations in the fore and back-limbs with respect to the hinge.

Unlike the fold at I-1, in the fold-pair at I-2 there is a strong difference in layer-thickness between the back-limb and fore-limb, which implies a different deformation history. A kinematic model to explain the age distribution is proposed that takes this difference into account (Fig. 5-5b). Since the age in the back-limb falls within the range of the ages in the anticline hinge it is possible that folding by buckling (related to D1) occurred or ended between 67-71Ma. The younger ages from the fore-limb and the syncline hinge are about the same and this can be due to the fact that the hinge sample was taken right at the boundary between the hinge and the fore-limb. The fact that the layers in the fore-limb are strongly strained and give younger ages indicates that this limb, unlike the back-limb, probably evolved to become shear bands. These shear bands could have formed late during D1, or perhaps be related to D2 in the area.

5.6 Conclusions

The U-Th/He ages determined in zircons from localities Z4 and Z5, as well as the K-Ar ages determined in illite extracted from bentonite layers in the Zimapán Basin are in agreement with stratigraphic constraints placed on the age of deformation in the studied cross-section of the Mexican Fold-Thrust Belt. Second order (outcrop scale) illite age variations in individual outcrops may be controlled by the fold kinematics and deformation history in different parts of the folds, in particular between hinges and limbs. Late stage passive folding, which accounts for a relatively small amount of strain quasi-homogenously distributed in the outcrop, probably does not have an effect on illite properties and ages, except perhaps in the limbs. Based on the obtained results, illite properties and ages together may provide a useful tool for determining the age of folding. More detailed work on well-characterized folds could help test folding mechanisms. This fold-dating method, together with strain analysis, has potential for determining not only the timing of deformation but also strain rates.

Figures and Tables

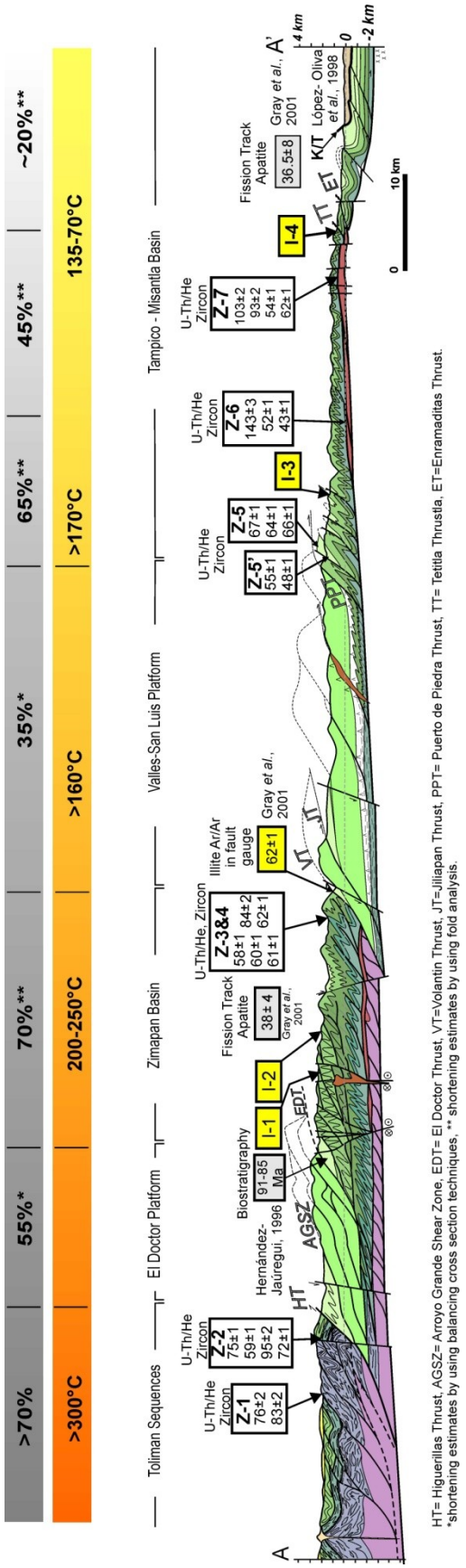

HT= Higuerillas Thrust, AGSZ= Arroyo Grande Shear Zone, EDT= El Doctor Thrust, VT=Volantin Thrust, JT=Jiliapan Thrust, PPT= Puerto de Piedra Thrust, TT= Tetilla Thrustla, ET=Enramaditas Thrust.
*shortening estimates by using balancing cross section techniques, ** shortening estimates by using fold analysis.

Figure 5-1. Regional cross-section of the study area showing the distribution of sampling localities for illite analysis and U-Th/He cooling age analysis, and other stratigraphic, geochronological and thermochronological ages reported in literature for this area. These include: stratigraphic constraints, fission track ages in apatite, and Ar-Ar ages determined in illite from fault gouge.

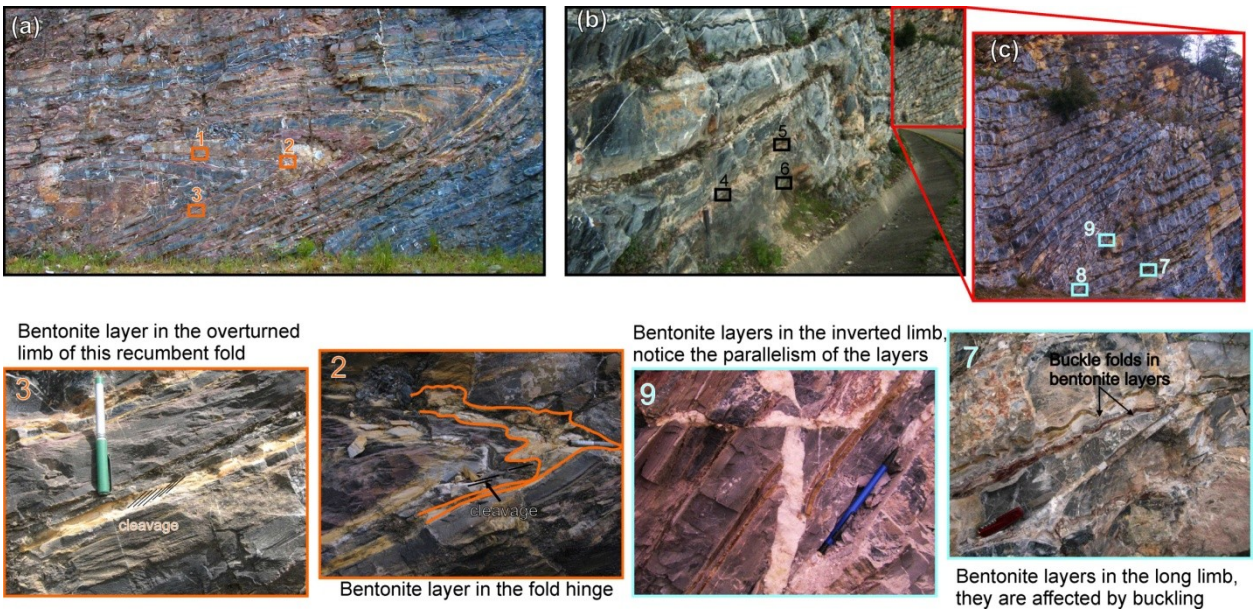

Figure 5-2. Outcrops where samples were taken of bentonite interbedded with limestone (Tamaulipas Fm., see Fig. 3-2 in Chapter 3) for illite characterization and K/Ar dating. (a) Recumbent fold sampled in locality I-1. (b) and (c) Asymmetrical fold sampled in locality I-2. 2, 3, 9 and 7 are close-ups of the sampled bentonite layers.

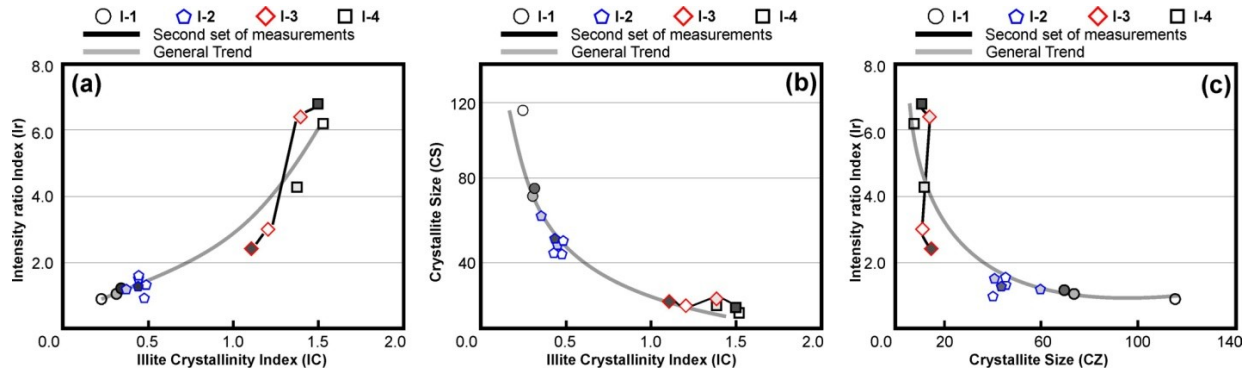

Figure 5-3. Variations in illite properties in the four outcrops analyzed. (a) IC vs. Ir plot. (b) IC vs. CS plot. (c) CS vs. Ir plot. Notice the differences between samples from localities I-1 and I-2 taken in the Zimapán Basin compared to samples from I-3 and I-4, taken in the Tampico-Misantla Basin. Also notice the positive correlation between Ir and CI and negative correlations between CS and IC and between Ir and CS.

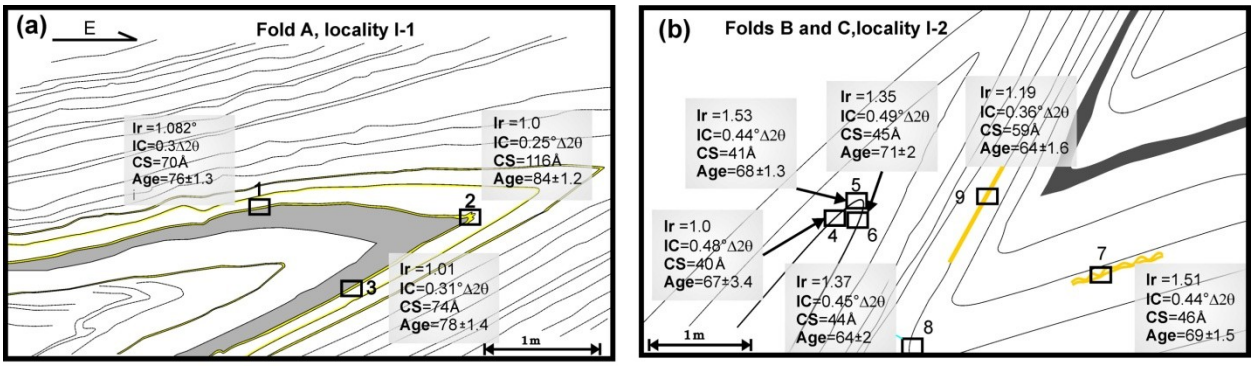

Figure 5-4. Sketches of the outcrops of folds where illite dating analysis was applied. (a) Recumbent fold in mudstone interbedded with shale and bentonite (near the top of Tamaulipas Fm.) locality I-1. (b) Asymmetrical steeply inclined chevron folds developed in limestone layers interbedded with chert bands, shale and bentonite, locality I-2. The numbers in the sampled boxes correspond to those in Table 5-2.

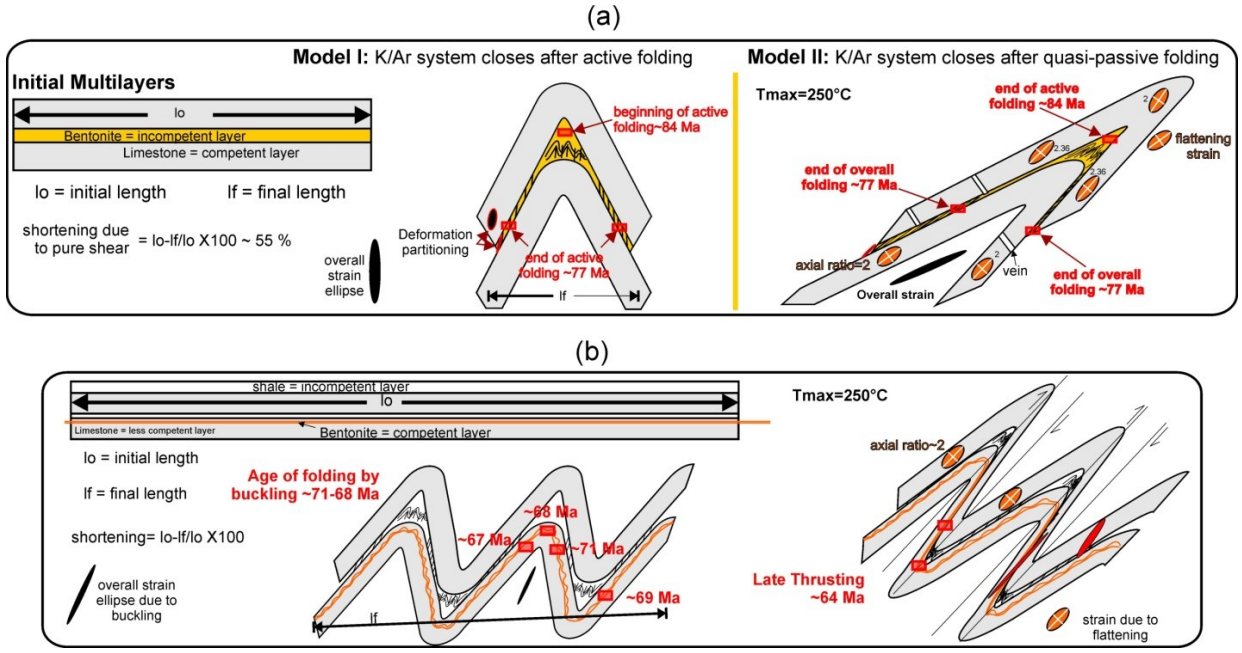

Fig. 5-5. Kinematic models to explain the distribution of ages around the folds. (a) Two models to explain the age distribution around the fold in I-1 (b) Model to explain the strain distribution around the folds in I-2. The explanation of this model is included in the text. Flattening-related strain ellipses (in orange) were estimated by measuring distortion in calcispherulid shells (Chapter 3).

Table 5-1. U-Th/He ages determined in detrital zircons from 7 localities along the studied cross-section. Sample locations are shown in Figure 5-1.

Locality	Zircon number	U-Th/He Age (Ma)	Error (Ma)	Detrital Zircon U/Pb Ages
Z1	Z1-1	76	2	Youngest zircon 269±5 Ma
	Z1-2	83	2	
Z2	Z2-1	75	1	140±5 Ma (*)
	Z2-2	59	1	
	Z2-3	95	2	
	Z2-4	72	1	
Z3	Z3-1	84	2	
	Z3-2	62	1	
Z4	Z4-1	58	1	149±4 Ma (*)
	Z4-2	60	1	
	Z4-3	61	1	
Z5	Z5-1	67	1	
	Z5-2	64	1	
	Z5-3	66	1	
Z5'	Z5'-1	55	1	
	Z5'-2	48	1	
Z6	Z6-1	143	3	
	Z6-2	52	1	
	Z6-3	43	1	
Z7	Z7-1	103	2	Youngest zircon 190±5 Ma
	Z7-2	93	2	
	Z7-3	54	1	
	Z7-4	62	1	

(*) Average U/Pb ages of detrital zircons from volcani-clastic sequences. The distribution ages in a probability plot indicate that most of the zircons come from the same source, probably related to monogenetic volcanism (Dávila-Alcocer *et al.*, 2009)

Locality	Sample	Mineralogy	IC	Ir	CS	Age (Ma) K/Ar
I-1	1	Illite, kaolinite and minor calcite	0.31	1.08	70	76.1±1.3
	2	Illite, kaolinite, calcite and quartz	0.25	0.87	116	84.8±1.2
	3	Illite, kaolinite and calcite	0.32	1.01	74	77.6±1.4
I-2	4	Smectite, Illite, kaolinite, calcite, quartz and minor chlorite	0.48	1	40	66.5±3.4
	5	Illite, kaolinite, smectite, quartz and calcite	0.44	1.53	41	68.3±1.3
	6	Smectite, Illite, kaolinite, calcite, quartz and almost no chlorite	0.49	1.35	45	71±2
	7	Illite, smectite, kaolinite and minor calcite, quartz and almost no chlorite	0.44	1.57	46	68.6±1.5
	8	Dominant illite and minor kaolinite, smectite, calcite and quartz	0.45	1.31	44	63.7±2
	9	Dominant illite and minor kaolinite, smectite, calcite, quartz and chlorite	0.36	1.19	59	63.8±1.6
I-3	10	Illite and minor smectite and kaolinite	1.2	3	12	
	11	Illite and minor smectite and kaolinite	1.1	2.4	15	
	12	Illite and minor smectite and kaolinite	1.4	6.4	14	
I-4	13	Smectite, illite, kaolinite and K feldspar	1.5	6.2	8	
	14	Smectite, illite, kaolinite, calcite and minor K feldspar	1.5	6.8	11	
	15	Smectite, illite, kaolinite, calcite and minor K feldspar	1.4	4.2	11	40.3±2.1

Table 5-2. Illite analysis. Mineralogy, illite Crystallinity (IC), intensity ratio index (Ir), crystallite size (CS) and K/Ar determined in the clay fractions smaller than 0.2 μm separated from bentonite samples.

Bibliography

Abdioglu, E. and Arslan, M. 2005. Mineralogy, geochemistry, and genesis of bentonites of the Ordu Area, NE Turkey. Clays and Clay Minerals, 40, 131-151.

Aller, J.; Bobillo-Ares, N. C.; Bastida, F.; and Lisle, R. J. 2008. Total bulk strain in flattened parallel folds. Journal of Structural Geology, 30-7, 827-838.

Allmendinger, R. W.; Brewer, J. A.; Brown, L. D.; Kaufman, S.; Oliver, J. E.; and Houston, R. S. 1982. COCORP profiling across the Rocky Mountain Front in southern Wyoming; Part 2, Precambrian basement structure and its influence on Laramide deformation. Geological Society of America Bulletin, 93-12, p.1253-1263.

Anderson, E.M. 1976. The dynamics of faulting, in: Voight, B. and Fairbridge, R. W. (Eds.), Mechanics of thrust faults and decollement. Dowden, Hutchinson, Ross, Stroudsburg, PA, United States (USA), United States (USA).

Anderson, T. H. and Silver, L. T. 2005. The Mojave-Sonora Megashear; field and analytical studies leading to the conception and evolution of the hypothesis. Special Paper-Geological Society of America, 393, 1-50.

Anderson, T. H. and Schmidt, A. 1983. The evolution of Middle America and the Gulf of Mexico-Caribbean Sea region during Mesozoic time. Geological Society of America Bulletin, 94-8, 941-966.

Armstrong, R. L. 1968. Sevier orogenic belt in Nevada and Utah. Geological Society of America Bulletin, 79-4, 429-458.

Armstrong, R. L. 1974. Magmatism, orogenic timing, and orogenic diachronism in the Cordillera from Mexico to Canada. Nature (London), 247, no. 5440, 348-351.

Bally, A. W.; Gordy, P. L. and Stewart, G. A. 1966. Structure, seismic data, and orogenic evolution of southern Canadian Rocky Mountains. Bulletin of Canadian Petroleum Geology, 14-3, 337-381.

Beaumont, C.; Fullsack, P. and Hamilton J. 1992. Erosion control of active compressional orogens: In McClay (Ed.) Thrust Tectonics. Chapman & Hall, 1-19.

Beck, R. A.; Vondra, C. F.; Filkins, J. E.; and Olander, J. D. 1988. Syntectonic sedimentation and Laramide basement thrusting, Cordilleran foreland; timing of deformation. Memoir - Geological Society of America, 171, 465-487.

Biot, M. A. 1965, Theory of viscous buckling and gravity instability of multilayers with large deformation. Geological Society of America Bulletin, 76-3, 371-378.

Bjørlykke, K.; Ramm, M. and Saigal, G. C. 1989. Sandstone diagenesis and porosity modification during basin evolution; Geologic modeling; aspects of integrated basin analysis and numerical simulation. Geologische Rundschau, 78, 243-268.

Bjørlykke, K. 1997. Lithological control on fluid flow in sedimentary basins, in: Jamtveit, B. and Yardley, B. (eds.), Fluid flow and transport in rocks: mechanisms and effects, Champman and Hall, Oxford, U.K, 15-34.

Bodnar, R. J. and Vityk, M. O. 1994. Interpretation of microthermometric data for H_2O-NaCl fluid inclusions, in: De Vivo, B. and Frezzotti, M. L.(eds.), Fluid Inclusions in Minerals, Methods and Applications, Virginia Tech, Blacksburg, VA, 117-130.

Bons, P. D. 2001. The formation of large quartz veins by rapid ascent of fluids in mobile hydrofractures; Fluids and fractures in the lithosphere. Tectonophysics, 336, 1-17.

Bons, P. D.; Jessell, M. W. and Urai, J. L. 2000. The formation of veins and their microstructures; Stress, strain and structure; a volume in honor of W. D. Means. Journal of the Virtual Explorer 2.

Boyer, S. E. 1995. Sedimentary basin taper as a factor controlling the geometry and advance of thrust belts. American Journal of Science, 295-10, 1220-1254.

Boyer, S. E. and Elliott, D. 1982. Thrust systems. AAPG Bulletin, 66, 196-1230.

Boyer, S. E. and Elliott, D. 1982, Thrust systems, AAPG Bulletin, 66-9, 196-1230.

Brewer, J. A.; Allmendinger, R. W.; Brown, L. D.; Oliver, J. E. and Kaufman, S. 1982. COCORP profiling across the Rocky Mountain Front in southern Wyoming; Part 1, Laramide structure. Geological Society of America Bulletin, 93-12, 1242-1252.

Burbank, D. W.; Verges, J.; Munoz, J. A.; Bentham, P. 1993. Coeval hindward- and forward-imbricating thrusting in the south-central Pyrenees, Spain; timing and rates of shortening and deposition. Geological Society of America Bulletin, 104, 3-17

Burkhard, M. 1993. Calcite twins, their geometry, appearance and significance as stress-strain markers and indicators of tectonic regime; a review; the geometry of naturally deformed rocks. Journal of Structural Geology, 15, 351-368.

Byerlee, J. 1978. Friction of rocks; Rock friction and earthquake prediction. Pure and Applied Geophysics, 116, 615-626.

Campa-Uranga, M. F. 1985. The tectonostratigraphic terranes and the thrust belt in Mexican territory. In: Howell, David G; Jones, David L; Cox, Allan; Nur, Amos M. (eds.) Stanford University Publications, Geological Sciences, 18, 44-46.

Campa-Uranga, M. F. 1983. The tectonostratigraphic terranes and the thrust belt in Mexican territory; Proceedings of the Circum-Pacific terrane conference. Stanford University Publications. Geological Sciences, 18, 44-46.

Cant. D. J. and Stockmal, G. D. 1999. A field guide to portions of the Jurassic Fernie-Kootenay Trens-Canada Highway section, Banff, Alberta; new sedimentological and structural observations and interpretations. Bulletin of Canadia Petroleum Geology, 47, 1-18.

Cardwell, R. K.; Chinn, D. S.; Moore, G. F. and Turcotte, D. L. 1978. Frictional heating on a fault zone with finite thickness. Geophysical Journal of the Royal Astronomical Society, 52(3), 525-530.

Carrillo-Martínez, M. 1989. Structural analysis of two juxtaposed Jurassic lithostratograpchic assamblages in the Sierra Madre Oriental fold belt of central Mexico. Geofísica Internacional, 28-5, 1007-1028.

Carrillo-Martínez, M. 1990. Geometría estructural de la Sierra Madre Oriental entre Peñamiller and Jalpan, Estado de Querétaro. Revista del Instituto de Geología, UNAM, 8, 62-70.

Carrillo-Martínez, M. 1997. Hoja Zimapán 14Q-e(7); resumen de la geología de la hoja Zimapán, estados de Hidalgo y Queretaro. Carta Geologica de Mexico, Serie de 1: 100,000, 24, 32 pp.

Carrillo-Martínez, M.; Valencia, J. J. and Vázquez, M. E. 2001. Geology of the southwestern Sierra Madre Oriental fold-and-thrust belt, east-central Mexico; a review. AAPG Memoir, 75,145-158.

Casciello E.; Cesarano, N. and Cosgrove, J. W. 2004. Shear deformation of pelitic rocks in a large-scale natural fault. Geological Society of London, 224, 113-125.

Castelltort, S.; Guillocheau, F.; Robin, C.; Rouby, D.; Nalpas, T.; Lafont, F.; and Eschard, R. 2003. Fold control on the stratigraphic record: a quantified sequence stratigraphic study of the

Pico del Aguila anticline in the south-western Pyrenees (Spain). Basin Research [Basin Res.], 15- 4, 527-551.

Cecil, M. R.; Ducea, M. N.; Reiners, P. W. and Chase, C. G. 2006. Cenozoic exhumation of the northern Sierra Nevada, California, from (U-Th)/He thermochronology. Geological Society of America Bulletin, 118, 1481-1488.

Chacko, T.; Cole, D. R. and Horita, J. 2001. Equilibrium oxygen, hydrogen and carbon isotope fractionation factors applicable to geologic systems: Stable isotope geochemistry. Reviews in Mineralogy and Geochemistry, 43, 1-81.

Chapple, W. M. 1978. Mechanics of thin-skinned fold-and-thrust belts. Geological Society of America Bulletin, 89, 1189–1198.

Chávez-Cabello, G.; Aranda-Gómez, J. J.; Garza-Molina, R. S.; Cossío-Torres, T.; Arvízu-Gutiérrez, I. R. and González-Naranjo, G. A. 2007. The San Marcos Fault: a Jurassic multireactivated basement structure in northeastern Mexico: Special Paper, Geological Society of America, 422, 261-286.

Clauer, N. and Chaudhuri, S. 1995. Clays in Crustal Environments. Isotope Dating and Tracing. Springer-Verlag, Berlin.

Clauer, N.; Liewig, N.; Ledesert, B.; Zwingmann, H. 2008. Thermal history of Triassic sandstones from the Vosges Mountains-Rhine Graben rifting area, NE France, based on K-Ar illite dating. Clay Minerals, 43, 363-379.

Cobbold, P. R.; Cosgrove, J. W. and Summers, J. M. 1971, Development of internal structures in deformed anisotropic rocks: Tectonophysics, 12-1, 23-53.

Cole, D. R. 2000. Isotopic exchange in mineral-fluid systems; IV, The crystal chemical controls on oxygen isotope exchange rates in carbonate-H_2O and layer silicate-H_2O systems. Geochimica et Cosmochimica Acta. 64, 921-931.

Compton, J. S.; Conrad, M. E. and Vennemann, T. W. 1999. Stable isotope evolution of volcanic ash layers during diagenesis of the Miocene Monterey Formation, California. Clays and Clay Minerals, 47, 84-95.

Coney, J. P. and Evenchick, C. A. 1994. Consolidation of the American Cordilleras: Journal of South American Earth Sciences. 7, 241-262.

Coney, P. J.; Jones, D. L.; and Monger, J. W. H. 1980. Cordilleran suspect terranes: Nature (London), 288-5789, 329-333.

Contreras, J. and Suter, M. 1990. Kinematic modeling of cross-sectional deformation sequences by computer simulation. Journal of Geophysical Research, 95-B13, 21,913-21,929.

Cosca, M. A.; Hunziker, J. C.; Huon, S.; and Massone, H. 1992. Radiometric age constraints on mineral growth, metamorphism, and tectonism of the Gummfluh Klippe, Brianconnais domain of the Prealps, Switzerland: Contributions to Mineralogy and Petrology, 112, 439–449.

Cosgrove, J.W. 1993. The interplay between fluids, folds and thrusts during the deformation of a sedimentary succession. Journal of Structural Geology, 15, 491-500.

Cox, S. F. 2007. Structural and isotopic constraints on fluid flow regimes and fluid pathways during upper crustal deformation; an example from the Taemas area of the Lachlan Orogen, SE Australia. Journal of Geophysical Research. 112, @B08208.

Cox, S. F.; Etheridge, M. A. and Wall, V. J. 1987. The role of fluids in syntectonic mass transport, and the localization of metamorphic vein-type ore deposits. Ore Geology Reviews, 2, 65-86.

Craig, H. 1961. Isotopic variations in meteoric waters. Science, 133, 1702-1703.

Cruz, L.; Teyssier, C.; Perg, L; Take, A. and Fayon. 2008. Deformation, exhumation, and topography of experimental doubly-vergent orogenic wedges subjected to asymmetric erosion. Journal of Structural Geology, 30, 98-115

Currie, J. B.; Patnode, H. W. and Trump, R. P, 1962. Development of folds in sedimentary strata. Geological Society of America Bulletin, 73, 655-674.

Dahlen, F. A. 1990. Critical taper model of fold and thrust belts and accretionary wedges: Annual Reviews Earth Planetary Sciences, 18, 55-99.

Dahlen, F. A.; Suppe, J. and Davis, D. 1984. Mechanics of Fold-and-Thrust Belts and Accretionary Wedges: Cohesive Coulomb Theory: Journal of Geophysical Research, 89-B12, 10,087-10,101.

Dahlen, F. A. and Barr, T. D. 1989. Brittle frictional mountain building 1: deformation and mechanical energy Budget: Journal of Geophysical Research, 94, 3923-3947.

Dahlen, F. A.; Suppe, J. and Davis, D. 1984. Mechanics of fold-and-thrust belts and accretionary wedges: cohesive Coulomb theory: Journal of Geophysical Research, 89, 10,087-10,101.

Dahlen, F. A. 1984. Non-cohesive Critical Coulomb Wedges: an exact solution: Journal of Geophysical Research, 89, 10 125-10 133.

Dahlen, F. A. and Barr, T. D. 1989. Brittle frictional mountain building 1: deformation and mechanical energy Budget: Journal of Geophysical Research, 94, 3923-3947.

Dahlstrom, C. D. 1969. Balanced cross-sections. Canadian Journal of Earth Sciences, 6-4, Part 1, 743-757.

Dahlstrom, C. D. 1970. A Structural geology in eastern margin of Canadian Rocky Mountains. The American Association of Petroleum Geologists Bulletin, 54-5, 843.

Dávila-Alcocer, M.; Centeno-García, E.; Valencia, V. and Fitz-Díaz, E. 2009. Una nueva interpretación de la estratigrafía de la Región de Tolimán, Estado de Querétaro (New interpretation of the stratigraphy in Tolimán región, Querétaro State). Boletín de la Sociedad geológica Mexicana, 63- 3. http://boletinsgm.igeolcu.unam.mx/epoca04/6103/DavilaGAL.pdf.

Davis, D.; Suppe, J. and Dahlen, F. A. 1983. Mechanics of fold-and-thrust belts and accretionary wedges. Journal of Geophysical Research, 88, 1,153-1,172.

DeCelles, P. G. 1994. Late Cretaceous-Paleocene synorogenic sedimentation and kinematic history of the Sevier thrust belt, Northeast Utah and Southwest Wyoming. Geological Society of America Bulletin. 106-1. 32-56.

DeCelles, P. G. 2004. Late Jurassic to Eocene evolution of the Cordilleran thrust belt and foreland basin system, western U.S.A. American Journal of Science, 304, 105-168.

DeCelles, P. G. 2009. Cyclicity in Cordilleran orogenic systems. Nature Geoscience, 469, 2. www.nature.com/naturegeoscience.

DeCelles, P. G.; Gray, M. B.; Ridgway, K. D.; Cole, R. B.; Pivnik, D. A.; Pequera, N.; and Srivastava, P. 1991. Controls on synorogenic alluvial-fan architecture, Beartooth Conglomerate (Palaeocene), Wyoming and Montana. Sedimentology, 38-4, 567-590.

DeCelles, P. G.; Lawton, T. F.; and Mitra, G. 1995. Thrust, timing, growth of structural culminations, and synorogenic sedimentation in the type Sevier orogenic belt, Western United States. Geology (Boulder), 23-8, 699-702.

Dewey, J. F. and Horsfield, B. 1970. Plate tectonics, orogeny and continental growth. Nature, 225, 521-525.

Dickinson W. 1971. Plate Tectonics for orogeny at continental margins. Nature, 232, 41-42.

Dickinson, W. R.; Klute, M. A.; Hayes, M. J.; Janecke, S. U.; Lundin, E. R.; McKittrick, M. A. and Olivares, M. D. 1988. Paleogeographic and paleotectonic setting of Laramide sedimentary basins in the central Rocky Mountain region. Geological Society of American Bulletin.100, 1023-1039.

Dixon, J. M. 2004. Physical (centrifuge) modeling of fold-thrust shortening across carbonate bank margins — timing, vergence, and style of deformation, in K. R. McClay ed., Thrust tectonics and hydrocarbon systems. AAPG Memoir, 82, 223–238.

Dixon, J. M. and Liu, S. 1992. Centrifuge modelling of the propagation of thrust faults. In: McClay, K.R. (ed.), Thrust Tectonics. Chapman and Hall, London, 53-69.

Dunnet, D. 1969. A technique of finite strain analysis using elliptical particles. Tectonophysics, 7-2, 117-136.

Durney, D. W. 1972. Solution-transfer, an Important Geological Deformation Mechanism. Nature (London), 235, 315-317.

Eardley, A. J. 1963. Relation of uplifts to thrusts in Rocky Mountains. Memoir - American Association of Petroleum Geologists, 209-219.

Eguiluz, S.; Aranda-Gómez, M. and Marret, R. 2000. Tectónica de la Sierra Madre Oriental, México. Boletín de la Sociedad Geológica Mexicana, LIII, 1-26.

Elliott, D. 1976. The motion of thrust sheets. Journal of Geophysical Research, 81, 949-963.

Elliott, D. 1976. The energy balance and deformation mechanisms of thrust sheets. Philosophical Transactions of the Royal Society of London, 283, 289-312.

Eslinger, E. V. and Yeh, H. 1986. Oxygen and hydrogen isotope geochemistry of Cretaceous bentonites and shales from the Disturbed Belt, Montana. Geochimica et Cosmochimica Acta, 50, 59-68.

Evenchick, C. A.; McMechan, M. E.; McNicoll, V. J. and Carr, S. D. 2007. A synthesis of the Jurassic-Cretaceous tectonic evolution of the central and southeastern Canadian Cordillera; exploring links across the orogen. Special Paper - Geological Society of America, 433, 117-145.

Faure, G. and Mensing, T. M. 2005. Isotopes; principles and applications. John Wiley & Sons, Hoboken, NJ, United States (USA), United States (USA).

Feinstein, S.; Kohn, B.; Osadetz, K. and Price, R. A. 2007. Thermochronometric reconstruction of the prethrust paleogeothermal gradient and initial thickness of the Lewis thrust sheet, southeastern Canadian Cordillera foreland belt. Special Paper - Geological Society of America, 433, 167-182.

Ferket, H.; Swennen, R. A. J.; Ortuño, S. and Roure, F. 2003. Reconstruction of the fluid flow history during Laramide foreland fold and thrust belt development in eastern Mexico; cathodoluminescence and $\delta^{18}O$-$\delta^{13}C$ isotope trends of calcite-cemented fractures. Journal of Geochemical Exploration, 78-79, 163-167.

Fischer, M. P.; Higuera-Diaz, I. C.; Evans, M. A.; Perry, E. C.; and Lefticariu, L. 2009. Fracture-controlled paleohydrology in a map-scale detachment fold; insights from the analysis of fluid inclusions in calcite and quartz veins. Journal of Structural Geology, 31, 1490-1510.

Fisher, D. M. and Brantley, S. L. 1992. Models of quartz overgrowth and vein formation; deformation and episodic fluid flow in an ancient subduction zone. Journal of Geophysical Research, 97, 20,043-20,061.

Fisher, D. M. and Byrne, T. 1990. The character and distribution of mineralized fractures in the Kodiak Formation, Alaska; implications for fluid flow in an underthrust sequence; Special section on the Role of fluids in sediment accretion, deformation, diagenesis, and metamorphism in subduction zones. Journal of Geophysical Research, 95, 9069-9080.

Fitz Díaz, E.; Hudleston, P. and Tolson, G. 2010. Comparison of tectonic styles in the Mexican and Canadian Rocky Mountain Fold-Thrust Belt, in: Poblet, J. and Lisle, R. (eds.), Kinematics and Tectonic Styles of Fold-Thrust Belt, Geological Society of London, Special Publication on (in press).

Foland, K.; Hubacher, F.A. and Arehart, G.B. 1992. $^{40}Ar/^{39}Ar$ dating of fine grained samples: An encapsulated-vial procedure to overcome the problem of ^{39}Ar recoil loss. Chemical Geology, 102, 269-276

Foreman, J. L. and Dunne, W. M. 1991. Conditions of vein formation in the Southern Appalachian foreland; constraints from vein geometries and fluid inclusions. Journal of Structural Geology, 13, 1173-1183.

Fyfe, W. S. and Kerrich, R. 1985. Fluids and thrusting. Chemical Geology, 49, 353-362.

Gabrielse H. and Taylor, G.C. 1982. Geological maps and cross sections of the northern Canadian Cordillera from southwest of Fort Nelson, British Columbia to Gravina Island, southeastern Alaska. Open-File Report 864- Geological Survey of Canada, 15p.

Giorgis, S.; McClelland, W.; Fayon, A.; Singer, B. S. and Tikoff, B. 2008. Timing of deformation and exhumation in the western Idaho shear zone, McCall, Idaho. Geological Society of America Bulletin, 120, 119-1133.

Goldstein, R. H. and Reynolds, T. J. 1994. Systematics of fluid inclusions in diagenetic minerals. SEPM Short Course Notes. 31, 199 p.

González-Sánchez, F.; Camprubí, A.; González-Partida, E.; Puente-Solís, R.; Canet, C.; Centeno-García, E. and Atudorei, V. 2009. Regional stratigraphy and distribution of epigenetic stratabound celestine, fluorite, barite and Pb–Zn deposits in the MVT province of northeastern Mexico. Miner Deposita, 44, 343-361.

Grant, N. T.; Banks, D. A.; McCaig, A. M. and Yardley, B. W. D. 1990. Chemistry, source, and behavior of fluids involved in Alpine thrusting of the central Pyrenees; Special section on the Role of fluids in sediment accretion, deformation, diagenesis, and metamorphism in subduction zones. Journal of Geophysical Research, 95, 9123-9131.

Gray, G. G.; Pottorf, R. J.; Yurewicz, D. A.; Mahon, K. I.; Pevear, D. R. and Chuchla, R. J. 2001. Thermal and chronological record of syn-to post-Laramide burial and exhumation, Sierra Madre Oriental, Mexico. AAPG Memoir, 75, 159-181.

Griffith, A.A. 1921, The phenomena of rupture and flow in solids, Philosophical Transactions of the Royal Society of London A 221, 163-198.

Hames, W. E. and Bowring, S. A. 1994. An empirical evaluation of the Ar diffusion geometry in muscovite. Earth and Planetary Science Letters, 124, 161-167.

Harrison, T. M. and Zeitler, P. K. 2005. Fundamentals of noble gas thermochronometry; Low-temperature thermochronology; techniques, interpretations, and applications. Reviews in Mineralogy and Geochemistry, 58, 123-149.

Hay, R. S. and Evans, B. 1988. Intergranular distribution of pore fluid and the nature of high-angle grain boundaries in limestone and marble. Journal of Geophysical Research, 93, 8959-8974.

Hernández-Jáuregui, R. 1997. Sedimentación Sintectónica de la Formación Soyatal (Turoniano Medio-Campaniano) y Modelado Cinemático de la Cuenca de Flexura de Maconí, Querétaro-Syntectonic sedimentation of Soyatal Formation (Middle Turonian-Campanian) and kinematic modeling the Maconi Flexural Basin, Queretaro. Instituto Politécnico Nacional, ESIA, Masters Thesis.

Hernández-Jáuregui, R. 1997, Sedimentación Sintectónica de la Formación Soyatal (Turoniano Medio-Campaniano) y Modelado Cinemático de la Cuenca de Flexura de Maconí, Querétaro-Syntectonic sedimentation of Soyatal Formation (Middle Turonian-Campanian) and kinematic modeling the Maconi Flexural Basin, Queretaro. Instituto Politécnico Nacional, ESIA, Masters Thesis.

Hernández-Jáuregui, R. 1997, Sedimentación sintectónica de la Formación Soyatal (Turoniano Medio-Campaniano) y modelado cinemático de la cuenca de flexura de Maconí, QuerétaroInstituto Politécnico Nacional, ESIA, Masters Thesis.

Hilgers, C.; Kirschner, D. L.; Breton, J. P.; and Urai, J. L. 2006. Fracture sealing and fluid overpressures in limestones of the Jabal Akhdar Dome, Oman Mountains, Geofluids, 6, 168-184.

Hodgkins, M. A. and Stewart, K. G. 1994. The use of fluid inclusions to constrain fault zone pressure, temperature and kinematic history; an example from the Alpi Apuane, Italy. Journal of Structural Geology, 16, 85-96.

Hossack, J. R. 1979. The use of balanced cross-sections in the calculation of orogenic contraction: A review. Journal of the Geological Society, 136, 705-711.

Hubbert, M. K., and Rubey, W. W., 1959, Mechanics of fluid-filled porous solids and its application to overthrust faulting, [Part 1] of Role of fluid pressure in mechanics of overthrust faulting. Geological Society of America Bulletin 70- 2, 115-166.

Hudleston P.J. and Treagus, S.H. in press, Information from folds: a review. Journal of Structural Geology.

Hudleston, P. J. 1989. The association of folds and veins in shear zones. Journal of Structural Geology, 11, 949-957.

Huiqi, L.; McClay, K.R. and Powell, D. 1992. Physical models of thrust wedges. In: McClay, K.R. (ed.) Thrust Tectonics. Chapman and Hall, London, 71-81.

Hyeong, K. and Capuano, R. M. 2004. Hydrogen isotope fractionation factor for mixed-layer illite/smectite at 60 degrees to 150 degrees C; new data from the northeast Texas Gulf Coast. Geochimica et Cosmochimica Acta, 68, 1529-1543.

Imlay, R. W. 1944. Correlations of the Cretaceous Formations of the Greater Antillas, Central America, and Mexico. Bulletin of the Geological Society of America, 55, 1005-1046.

Imlay, R. W. 1944, Cretaceous Formations of central America. Bulletin of the American Association of Petroleum Geologists, 28-8, 1107-1195.

Jessell, M. W.; Willman, C. E. and Gray, D. R. 1994. Bedding parallel veins and their relationship to folding. Journal of Structural Geology, 16, 753-767.

Johnson, A. M. and Fletcher, R. C. 1994. Folding of Viscous Layers. Columbia University Press, 461 p.

Kilsdonk, B. and Wiltschko, D. V. 1988. Deformation mechanisms in the southeastern ramp region of the Pine Mountain Block, Tennessee; with Suppl. Data 88-12. Geological Society of America Bulletin, 100, 653-664.

Kirschner, D. L.; Sharp, Z. D. and Teyssier, C. 1993. Vein growth mechanisms and fluid sources revealed by oxygen isotope laser microprobe. Geology (Boulder), 21, 85-88.

Kisch, H. J. and Merriman, R. J. 1991. Illite crystallinity; recommendation on sample preparation, X-ray diffraction settings, and interlaboratory samples; Very low-grade metamorphism. Journal of Metamorphic Geology, 9, 665-670.

Kisch, H. J. 1990. Calibration of the anchizone; a critical comparison of illite "crystallinity" scales used for definition. Journal of Metamorphic Geology, 8, 31-46.

Koons, P. O. 1990. Two sided orogen: Collision and erosion from the sandbox to the Southern Alps, New Zealand. Geology, 18, 679-682.

Kralik, M.; Klima, K. and Riedmueller, G. 1987. Dating fault gouges, Nature, 327, 6120, 315-317.

Kübler, B. and Jaboyedoff, M. 2000. Illite crystallinity. Comptes Rendus de l'Académie des Sciences, Série II.Sciences de la Terre et des Planètes, 331, 75-89.

Kübler, B. 1967. La cristallinité de l'illite et les zones tout à fait supérieures du metamorphisme. Étages tectoniques. Colloque de Neuchâtel, 18-21 avril 1966. Université de Neuchâtel, Institut de Géologie, 105-122.

Kübler, B. 1968. Évaluation quantitative du métamorphisme par la cristallinité de l'illite; état des progrès realisés ces dernières années. Centre de Recherches de Pau (Societé Nationale des Petôoles d'Aquitaine), Bulletin, 2, 385-397.

Lacroix, S. and Sawyer, E. W. 1995. An Archean fold-thrust belt in the northwestern Abitibi greenstone belt; structural and seismic evidence. Canadian Journal of Earth Sciences = Revue Canadienne des Sciences de la Terre, 32, 97-112.

Lawton, T. F and Trexler, J. H. 1991. Piggyback basin in the Sevier orogenic belt, Utah; implications for development of the thrust wedge. Geology (Boulder), 19- 8, 827-830.

Lebel, D.; Langenberg, W. and Mountjoy, E.W. 1996. Structure of the central Canadian Cordilleran thrust-and-fold belt, Athabasca-Brazeau area, Alberta; a large, complex intercutaneous wedge. Bulletin of Canadian Petroleum Geology, 44-2, 282-298.

Lee, Y. J. and Morse, J. W. 1999. Calcite precipitation in synthetic veins: implications for the time and fluid-volume necessary for vein filling, Chemical Geology, 156, 151-170.

Lerman A. and Clauer, N. 2005 Losses of radiogenic ^{40}Ar in the fine-clay size fractions of sediments. Clays and Clay Minerals. 53. 234-249.

Lisle, R.J. 1985. Geological Strain Analysis. Pergamon, 108 p.

López-Oliva, J. G.; Keller, G. and Stinnesbeck, W. 1998, El límite Cretácico/Terciario (K/T) en el noreste de México; extinción de foraminíferos planctónicos. The Cretaceous-Tertiary boundary in northeastern Mexico; extinction of planktonic Foraminifera. Revista Mexicana de Ciencias Geológicas, 15- 1, 109-113.

López-Ramos, E. 1983. Estratigrafia Cretacica y tectonica de una porcion del centro y noreste de Mexico. Cretaceous stratigraphy and tectonics of a portion of the central and northeast of Mexico. Boletin de la Sociedad Geologica Mexicana, 44-1, 21-31.

Lyons, J. B. and Snellenburg, J. 1971. K-Ar dates from authigenic illite in fault gouges. Geological Society of America Bulletin, 82, 1749-1751.

MacKay, P. A. 1996. The Highwood Structure; a tectonic wedge at the foreland edge of the southern Canadian Cordillera. Bulletin of Canadian Petroleum Geology, 44-2, 215-232.

Magoon, L. B.; Hudson, T. L. and Cook, H. E. 2001. Pimienta-Tamabra(!); a giant supercharged petroleum system in the southern Gulf of Mexico, onshore and offshore Mexico. AAPG Memoir, 75, 83-125.

McClay, K.R. ed. 1992. Thrust Tectonics. Chapman and Hall, 447 p.

McQuarrie, N. 2004. Crustal scale geometry of the Zagros fold–thrust belt, Iran. Journal of Structural Geology, 26-3, 519-535.

Meunier, A. 2005. Clays. Springer-Verlag. Berlin. 472 p.

Meunier, A.; Velde, B. and Zalba, P. 2004. Illite K-Ar dating and crystal growth processes in diagenetic environments: a critical review. Terra Nova [Terra Nova], 16, 296-304.

Mitchell, S. G. and Reiners, P. W. 2003. Influence of wildfires on apatite and zircon (U-Th)/He ages. Geology (Boulder), 31, 1025-1028.

Moore, D. M. and Reynolds, R. C. Jr. 1997. X-ray diffraction and the identification and analysis of clay minerals. Oxford University Press, Oxford, United Kingdom, 373p.

Moore, J. C.; Brown, K. M.; Horath, F.; Cochrane, G. R.; MacKay, M. and Moore, G. 1991. Plumbing accretionary prisms; effects of permeability variations. Philosophical Transactions of the Royal Society of London, Series A. Mathematical and Physical Science, 335, 275-288.

Moore, J. C. and Vrolijk, P. 1992. Fluids in accretionary prisms. Reviews of Geophysics, 30, 113-135.

Mugnier, J. L.; Baby, P.; Colletta, B.; Vinour, P.; Bale, P.; Leturmy, P. 1997. Thrust geometry controlled by erosion and sedimentation; a view from analogue models. Geology (Boulder), 25-5, 427-430.

Muñoz-Máximo, I. 2010. Análisis de inclusiones fluidas e isótopos estables en mega-vetas de calcita y su significado estructural en el área de Zimapán y Peñamiller, Estados de Hidalgo y Querétaro. Bachelor's thesis, Benemérita Universidad Autónoma de Puebla, 100 p.

Nurkowski, J. R. 1984. Coal quality, coal rank variation and its relation to reconstructed overburden, Upper Cretaceous and Tertiary plains coals, Alberta, Canada. AAPG Bulletin, 68-3, 285-295.

Ochoa-Camarillo, H. 1996. Geología del anticlinorio de Huayacocotla en la región de Molango, Estado de Hidalgo, Master's Thesis, UNAM, 91 p.

O'Neil, J. R.; Clayton, R. N. and Mayeda, T. K. 1969. Oxygen isotope fractionation in divalent metal carbonates. The Journal of Chemical Physics, 51, 5547-5558.

Ortega-Flores, B. 2010. Deformación por acortamiento en la Plataforma Valles-San Luís Potosí y en la Cuenca Tampico-Misantla; porción externa del Cinturón de Pliegues y Cabalgaduras Mexicano. Master's Thesis, Programa de Posgrado en Ciencias de la Tierra, Universidad Nacional Autónoma de México, 100p.

Padilla y Sánchez, R. J. 1986. Post-paleozoic tectonics of the northeast Mexico and its rule in the Evolution of the Golf of Mexico. Geofísica Internacional, 25-I, 157-206.

Pevear, D. R. 1999. Illite and hydrocarbon exploration. Proceedings of the National Academy of Sciences. 96. 3440-346.

Pfiffner, O. A. 2006. Thick-skinned and thin-skinned styles of continental contraction. Special Paper- Geological Society of America, 414, 153-177.

Philippe, Y.; Colletta, B.; Deville, E. and Mascle, A. 1996. The Jura fold-and-thrust belt; a kinematic model based on map-balancing. Memoires du Museum National d'Histoire Naturelle, 170, 235-261.

Phillips D. L.; Newsome, S. D. and Gregg J.W. 2005. Combining sources in stable isotope mixing models: alternative methods. Oecologia, 144, 520-527.

Price, R. A. 1981. The Cordilleran foreland thrust and fold belt in the southern Canadian Rocky Mountains. Geological Society of London, Special publication Thrust and Nappe Tectonics, edited by McClay, M. R. and Price, N. J., 427-448.

Price, R. A. 2001. An evaluation of models for the kinematic evolution of thrust and fold belts; structural analysis of a transverse fault zone in the Front Ranges of the Canadian Rockies north of Banff, Alberta. Journal of Structural Geology, 23, no. 6/7, 1079-1088.

Price, R. A. and Fermor, P. R. 1985. Structure section of the Cordilleran Foreland thrust and fold belt west of Calgary, Alberta, Geological Survey of Canada, 84-14, 1 sheet.

Ramos, A. 2009. Anatomy and global context of the Andes; main geologic features and the Andean orogenic cycle. Memoir - Geological Society of America, 204, 31-65.

Ramos-Velázquez, E.; Calmus, T.; Valencia, V.; Iriondo, A.; Valencia-Moreno, M. and Bellon, H. 2008. U/Pb and (super 40) Ar/ (super 39) Ar geochronology of the Coastal Sonora Batholith; new insights on Laramide continental arc magmatism. Revista Mexicana de Ciencias Geologicas, 25-2, 314-333.

Ramsay, J. G. 1967. Folding and fracturing of rocks. McGraw-Hill, New York, 658 p.

Ramsay, J. G. 1974. Development of chevron folds. Geological Society of America Bulletin, 85, 1741-1754.

Ramsay, J. G. 1980. The crack-seal mechanism of rock deformation. Nature (London). 284, 135-139.

Ramsay, J. G. and Huber, M. I. 1983. The Techniques of Modern structural Geology Volume 1: Strain Analysis. Academic Press, 307 p.

Reich, M.; Ewing, R. C.; Ehlers, T. A. and Becker, U. 2007. Low-temperature anisotropic diffusion of helium in zircon; implications for zircon (U-Th)/He thermochronometry. Geochimica Et Cosmochimica Acta, 71, 3119-3130.

Reiners, P. and Ehlers, T. A, eds. 2005. Low temperature Thermochronology: Techniques, interpretation and applications. Reviews in Mineralogy and Geochemistry, 58, 622.

Reiners, P. W. 2005. Zircon (U-Th)/He thermochronometry; Low-temperature thermochronology; techniques, interpretations, and applications. Reviews in Mineralogy and Geochemistry, 58, 151-179.

Reiners, P. W.; Ehlers, T. A. and Zeitler, P. K. 2005. Past, present, and future of thermochronology; Low-temperature thermochronology; techniques, interpretations, and applications. Reviews in Mineralogy and Geochemistry, 58, 1-18.

Reiners, P. W.; Zhou Zuyi; Ehlers, T. A.; Xu Changhai; Brandon, M. T.; Donelick, R. A. and Nicolescu, S. 2003. Post-orogenic evolution of the Dabie Shan, eastern China, from (U-Th)/He and fission-track thermochronology. American Journal of Science, 303, 489-518.

Reynolds, R. C., Jr. 1992. X-ray diffraction studies of illite/smectite from rocks, <1 μm randomly oriented powders, and <1 μm oriented powder aggregates; the absence of laboratory-induced artifacts. Clays and Clay Minerals, 40, 387-396.

Rich, J. L. 1934. Mechanics of low-angle overthrust faulting as illustrated by Cumberland thrust block, Virginia, Kentucky, and Tennessee. AAPG Bulletin, 18, 1584-1596.

Richards, I.; Connelly, J.; Gregory, R. and Gray, D. 2002. The importance of diffusion, advection, and host-rock lithology on vein formation: A stable isotope study from the Paleozoic Ouachita orogenic belt, Arkansas and Oklahoma. Bulletin of the Geological Society of America, 114, 1343-1355.

Roeder, D. 1983. Style zonation in fold-thrust belts. AAPG Bulletin, 67, 542p.

Rosales-Lagarde, L.; Centeno-García, E.; Dostal, J.; Sour-Tovar, F.; Ochoa-Camarillo, H. and Quiróz-Barroso, S. 2005. The Tuzancoa Formation: evidence of an Early Permian submarine continental arc in east-central Mexico. International Geology Review, 47-9, 901-919.

Rye, D. M. and Bradbury, H. J. 1988. Fluid flow in the crust: an example from a Pyrenean thrust ramp. American Journal of Science, 288, 197-235.

Sample, J. C. 2010. Stable isotope constraints on vein formation and fluid evolution along a recent thrust fault in the Cascadia accretionary wedge, Earth and Planetary Science Letters, 293, 300-312.

Sasseville, C.; Tremblay, A.; Clauer, N.; Liewig, N. 2008. K-Ar age constraints on the evolution of polydeformed fold-thrust belts; the case of the Northern Appalachians (southern Quebec). Journal of Geodynamics, 45, 99-119

Schmid, D.W. and Podladchikov, Y.Y. 2006. Fold amplification rates and dominant wavelength selection in multilayer stacks. Philosophical Magazine, 86 (21-22), 3409-3423.

Schmidt, C. J.; Chase, R. B. and Erslev, E. A. 1993. Laramide basement deformation in the Rocky Mountain foreland of the Western United States. Special Paper - Geological Society of America, 280, 365 p.

Schmoker, J. W. and Gautier, D. L. 1989. Compaction of basin sediments; modeling based on time-temperature history. Journal of Geophysical Research. 94, 7379-7386.

Scotese C. and Golonka, J. 1992. PALEOMAP Paleogeographic Atlas, PALEOMAP Progress Report No. 20, Department of Geology, University of Texas at Arlington, Arlington, Texas, 34 p.

Segerstrom, K. 1961. Geology of the Bernal-Jalpan area, Estado de Queretaro, Mexico: U. S. Geological Survey Bulletin, Report, B 1104-B, 19-86.

Selting, A. J. and Schmitt, J. G. 1999. Carbonate sedimentation in a foreland basin lake system, Upper Cretaceous Beaverhead Group, Southwest Montana. AAPG Bulletin, 83-7, 1188 p.

Shah, J. and Srivastava, D. C. 2006. Strain estimation from flattened parallel folds: application of the Wellman method and Mohr circle. Geological Magazine [Geol. Mag.], 143- 2, 243-247.

Simpson, D. H. G. 2009. Mechanical modeling of folding versus faulting in brittle-ductile wedges. Journal of Structural Geology, 31, 369-381.

Slotboom, R. T.; Lawton, D. C. and Spratt, D. A. 1996. Seismic interpretation of the triangle zone at Jumping Pound, Alberta. Bulletin of Canadian Petroleum Geology, 44-2, 233-243.

Smit, J. H. W.; Brun, J. P.; and Sokuotis, D. 2003. Deformation of brittle-ductile thrust wedges in experiments and nature. Journal of Geophysical Research 108, 949-963.

Solé, J. 2009. Determination of K-Ar ages in milligram samples using an infrared laser for argon extraction. Rapid Communications in Mass Spectrometry, 33, 3579-3590.

Solum, J. S. and Van der Pluijm, B. A. 2007. Reconstructing the Snake River-Hoback River Canyon section of the Wyoming thrust belt through direct dating of clay-rich fault rocks. Geological Society of America, Special Paper 433, 183-196.

Soule, G. S. and Spratt, D. A. 1996. En echelon geometry and two-dimensional model of the triangle zone, Grease Creek Syncline area, Alberta. Bulletin of Canadian Petroleum Geology, 44-2, 244-257.

Spotila, J. A. 2005. Applications of low-temperature thermochronometry to quantification of recent exhumation in mountain belts; Low-temperature thermochronology; techniques, interpretations, and applications. Reviews in Mineralogy and Geochemistry, 58, 449-466.

Spratt, D. A. and Lawton, D. C. 1996. Variations in detachment levels, ramp angles and wedge geometries along the Alberta thrust front. Bulletin of Canadian Petroleum Geology, 44-2, 313-323.

Spratt, D. A.; Lawton, D. C. and MacKay, P. A. 1993. The Triangle Zone and Turner Valley Structure west of Calgary, Alberta. Geological Association of Canada Field Trip A-1 Guidebook, 41.

Spratt, D. A.; Dixon, J. M. and Beattie, E. T. 2004. Changes in structural style controlled by lithofacies contrast across transverse carbonate bank margins; Canadian Rocky Mountains and scaled physical models. AAPG Memoir, 82, 259-275.

Srodon, J. and Eberl, D. D. 1984. Illite; Micas. Reviews in Mineralogy. 13, 495-544.

Srodon, J. 1984. X-ray powder differaction identification of illitic materials. Clays and Clay Minerals. 32, 337-349.

Srodon, J.; Elsass, F.; McHardy, W. J. and Morgan, D. J. 1992. Chemistry of illite-smectite inferred from TEM measurements of fundamental particles. Clay Minerals. 27, 137-158.

Stockmal, G. S.; Beaumont, C.; Nguyen, M. and Lee, B. 2007. Mechanics of thin-skinned fold and thrust belts; insights from numerical models. Special Paper, Geological Society of America, 433, 63-98.

Stockmal, G. S.; MacKay P. A.; Lawton, D. C.and Spratt, D. A. 1996. The Oldman triangle zone: a complicated tectonic wedge delineated by new structural mapping and seismic interpretation. Bulletin of Canadian Petroleum Geology, 44-2, 202-214.

Stockmal, G. S.; McMechan, M.E.; Lebel, D, and MacKay P. A. 2001. Structural style and evolution of the triangle zone and external foothills, southwestern Alberta; implications for thin-skinned thrust-and-fold belt mechanics. Bulletin of Canadian Petroleum Geology, 49-4, 472-496.

Storti, F.; McClay, K. 1995. Influence of syntectonic sedimentation on thrust wedges in analogue models. Geology [Geology]. 23- 11. 999-1002.

Suppe, J. 1983, Geometry and kinematics of fault-bend folding. American Journal of Science, 283-7, 684-721.

Suter, M. 1980. Tectonics of the external part of the Sierra Madre Oriental foreland thrust and fold belt Between Xilitla and the Moctezuma River (Hidalgo and San Luís Potosí states). UNAM, Revista del Instituto de Geología, 4, 19-31.

Suter, M. 1984. Cordilleran deformation along the eastern edge of the Valles- San Luis Potosi carbonate platform, Sierra Madre Oriental thrust and fold belt, east-central Mexico. Geological Society of America Bulletin, 95, 1387-1397.

Suter, M. 1987. Structural traverse across the Sierra Madre Oriental fold-thrust belt in east-central Mexico. Geological Society of America Bulletin, 98. 249-264.

Suter, M. 1990. Hoja Tamazunchale 14Q-(5), con geología de la hoja Tamazunchale, estados de Hidalgo, Querétaro y San Luís Potosí. UNAM, Instituto de Geología, Carta Geológica de México, serie 1:100,000, 56 p.

Sydney C. Jr. 1966. Handbook of Physical Constants (revised edition). Geological Society of America, Memoir, 97, 587.

Sydney P. C. Jr. 1966. Handbook of Physical Constants (revised edition). Geological Society of America, Memoir 97, 587 p.

Tagami, T. and O'Sullivan, P. B. 2005. Fundamentals of fission-track thermochronology; Low-temperature thermochronology; techniques, interpretations, and applications. Reviews in Mineralogy and Geochemistry, 58, 19-47.

Taylor, H. P. 1974. The Application of Oxygen and Hydrogen Isotope Studies to Problems of Hydrothermal Alteration and Ore Deposition. Economic Geology, 69, 843-883.

Thompson, R. I. 1979. A Structural interpretation across a part of the northern Rocky Mountains, British Columbia, Canada. Canadian Journal of Earth Sciences, 6, 1228-1241.

Thompson, R.I. 1981. The nature and significance of large 'blind' thrusts within the northern Rocky Mountains of Canada. Geological Society of London, Special publication Thrust and Nappe Tectonics, edited by K. R. McClay and N. J., Price, 449-462.

Tikoff, B. and Fossen, H. 1993. Simultaneous pure and simple shear: the unifying deformation matrix. Tectonophysics, 217, 267-283.

Tolson, G.; Chávez-Cabello, G.; Fitz-Díaz, E.; Bolaños-Rodríguez, D. E. and González-Naranjo, G. A. 2005. Thin- and thick-skinned tectonics in central Coahuila, northern Mexico; structural and stratigraphic considerations. Abstracts with Programs - Geological Society of America, 37-7, p.443.

Touret, J. L. R. 2001. Fluids in metamorphic rocks. Lithos, 55, 1-25.

Travé, A.; Labaume, P. and Vergés, J. 2007. Fluid systems in foreland fold-and-thrust belts; an overview from the southern Pyrenees, in: Lacombe, O.; Lave, J.; Roure, F.; Vergés, J.; Brun, J. P.; Oncken, O.; Weissert, H. and Dullo, C. (Eds.), Thrust belts and foreland basins; from fold kinematics to hydrocarbon systems. Springer.

Valencia-Islas, J. J. 1996. Implicaciones de la historia termica de la plataforma Valles-San Luis Potosí en la distribucion de los hidrocarburos y yacimientos minerales. Boletín de la Asociación Mexicana de Geólogos Petroleros, 45, 1-19.

Van der Pluijm, B. A.; Vrolijk, P. J.; Pevear, D. R.; Hall, C. M. and Solum, J. 2006. Fault dating in the Canadian Rocky Mountains; evidence for Late Cretaceous and early Eocene orogenic pulses. Geology (Boulder), 34-10, 837-840.

Vennemann, T. W. and O'Neil, J. R. 1993. A simple and inexpensive method of hydrogen isotope and water analyses of minerals and rocks based on zinc reagent. Chemical Geology, 103, 227-234.

Von Huene, R. and Lee, H. 1982. The possible significance of pore fluid pressures in subduction zones; Studies in continental margin geology. AAPG Memoir, 34, 781-791.

Vrolijk, P. and van der Pluijm, B. A. 1999. Clay gouge; questions in structural geology; 20th anniversary special issue. Journal of Structural Geology, 21(8-9), 1039-1048.

Vrolijk, P.; Myers, G. and Moore, J. C. 1988. Warm fluid migration along tectonic melanges in the Kodiak accretionary complex, Alaska. Journal of Geophysical Research, 93, 10,313-10,324.

Warr, L. N. and Rice, A. H. N. 1994. Interlaboratory standardization and calibration of clay mineral crystallinity and crystallite size data. Journal of Metamorphic Geology, 12, 141-152.

Wassenaar, L. I.; van Wilgenburg, S. L.; Larson, K. and Hobson, K. A. 2009. A groundwater isoscape $\delta D^{18}O$ for Mexico; Isoscapes; isotope mapping and its applications. Journal of Geochemical Exploration, 102, 123-136.

Weaver, C. E.; Grim, R. E. and Guven, N. 1979. Bentonites; geology, mineralogy, properties and use; book review. Sedimentary Geology, 24, 324-325.

Wellman, H. G. 1962. A graphic method for analyzing fossil distortion caused by tectonic deformation. Geological Magazine, 99, 348–52

Wilkerson, M. S.; Apotria, T. and Farid, T. 2002. Interpreting the geologic map expression of contractional fault-related fold terminations; lateral/oblique ramps versus displacement gradients. Journal of Structural Geology, 24-4, 593-607.

Wilson, J. R. and Ward, W. C. 1993. Early Cretaceous carbonate platforms of northeastern and east-central Mexico, in Simon, J. A. T.; Scott, R. W. & Masse, J.P., eds., Cretaceous carbonate platforms. American Association of Petroleum Geologists Memoir, 56, 35-50.

Yeh, H. W. 1980. D/H ratios and late-stage dehydration of shales during burial. Geochimica et Cosmochimica Acta, 44, 341-352.

Yonkee, W. A. 1992. Basement-cover relations, Sevier orogenic belt, northern Utah. Geological Society of America Bulletin, 104, 280-302.

Zwingmann, H. and Mancktelow, N. S. 2004. Timing of Alpine fault gouges. Earth and Planetary Science Letters, 223, 415-425.

Appendices

Appendix 4-1

Sample	Material analyzed	$\delta^{18}O$ SMOW	$\delta^{13}C$ VPDB	Dist. (m)
T1-1	Basinal limestone	23.2	0.2	20.0
T1-2	Basinal limestone	25.4	-1.7	19.0
T1-3	Basinal limestone	25.6	-3.3	16.0
T1-4	Basinal limestone	24.3	-3.2	14.0
T1-5	Basinal limestone	22.9	-5.6	12.0
T1-6	Basinal limestone	23.4	-2.8	10.0
T1-7	Basinal limestone	23.7	-3.3	8.0
T1-8	Microfractured mudstone	22.7	-1.2	6.0
T1-9	Cataclasite	20.0	-3.9	4.0
T1-10	Calcite megacrystals in vein	13.8	-3.1	2.0
T1-11	Calcite megacrystals in vein	11.5	-3.5	1.0
T1-12	Calcite megacrystals in vein	11.9	-4.0	0.8
T1-13	Calcite megacrystals in vein	11.7	-4.1	0.5
T1-14	Calcite megacrystals in vein	11.7	-3.6	0.3
T1-15	Calcite megacrystals in vein	12.0	-3.5	0.0
T1-16	Cataclasite	16.9	-0.5	-0.3
T1-17	Cataclasite	18.3	0.0	-0.5
T1-18	Sheared carbonate siltstone	16.9	0.0	-0.7
T1-19	Shaly limestone	19.8	-2.1	-1.0
T1-20	Shaly limestone	19.5	0.0	-2.0
T1-21	Shaly limestone	21.3	0.7	-3.0
T1-22	Shaly limestone	21.9	2.7	-5.0
T1-23	Shaly limestone	22.0	2.0	-7.0
T1-24	Shaly limestone	20.0	-0.3	-9.0
T1-25	Shaly limestone	21.3	0.7	-10.0
T2-1	Shaly limestone	22.0	-9.6	11.0
T2-2	Shaly limestone	21.6	-5.2	10.0
T2-3		20.8	-9.7	9.0
T2-4	Shaly limestone	21.2	-6.6	8.0
T2-5	Shaly limestone	21.0	-11.0	5.5
T2-6	Shaly limestone	21.5	-10.3	5.0
T2-7	Shaly limestone	20.9	-9.4	4.0
T2-8	Shaly limestone	21.7	-10.0	3.5
T2-9	Calcite from fthrust-related vein	20.3	-5.1	3.0
T2-10	Siltstone-calciarenite	21.1	-8.7	2.5
T2-11	Cataclasite	22.7	-22.8	2.3
T2-12	Cataclasite	21.6	-17.4	2.0
T2-13	Cataclasite	21.2	-9.5	1.8
T2-14	Cataclasite	20.1	-7.0	1.5
T2-15	Cataclasite	22.0	-13.0	1.0
T2-16	Cataclasite	23.5	-17.1	0.5
T2-17	Calcite from fthrust-related vein	15.7	-3.6	0.0
T2-18	Calcite from fthrust-related vein	10.9	-3.1	-0.5
T2-19	Calcite from fthrust-related vein	13.6	-3.5	-1.0
T2-20	Cataclasite	14.5	-4.3	-1.5
T2-21	Calcite from fthrust-related vein	24.1	-6.2	-2.0
T2-22	Calcite from fthrust-related vein	15.2	-4.6	-3.0
T2-23	Platformal limestone	25.2	-15.2	-4.0
T2-24	Platformal limestone	25.1	-13.2	-5.0
T2-25	Platformal limestone	24.3	-12.5	-6.0
T2-26	Platformal limestone	23.9	-14.2	-7.0
T2-27	Platformal limestone	24.8	-14.3	-8.0
T2-28	Platformal limestone	24.5	-15.0	-9.0
T3-1	Platformal limestone	23.7	0.4	14.0
T3-2	Platformal limestone	23.5	1.5	12.0

Sample	Material analyzed	$\delta^{18}O$ SMOW	$\delta^{13}C$ VPDB	Dist. (m)
T3-3	Platformal limestone	23.6	1.7	10.0
T3-4	Platformal limestone	24.0	1.1	7.0
T3-5	Platformal limestone	23.6	0.7	5.0
T3-6	Platformal limestone	23.4	1.4	3.0
T3-7	Calcite from fthrust-related vein	23.4	-1.5	1.6
T3-8	Cataclasite in platform limestone	22.8	2.0	1.2
T3-9	Calcite from fthrust-related vein	22.6	0.5	0.8
T3-10	Cataclasite	22.2	-4.6	0.7
T3-11	Cataclasite	22.3	-1.5	0.5
T3-12	Cataclasite	22.2	1.2	0.4
T3-13	Cataclasite	22.5	-3.4	0.3
T3-14	Cataclasite	22.7	-4.3	-0.2
T3-15	Calcite from fthrust-related vein	22.4	0.1	-0.6
T3-16	Cataclasite	22.0	-4.1	-0.8
T3-17	Calcite from fthrust-related vein	23.3	1.2	-1.2
T3-18	Siltstone and calciarenite	23.1	0.4	-1.8
T3-19	Siltstone and calciarenite	23.1	0.7	-2.2
T3-20	Siltstone and calciarenite	22.7	0.4	-2.8
T3-21	Siltstone and calciarenite	23.0	0.1	-3.8
T3-22	Siltstone and calciarenite	23.1	0.0	-4.8
T3-23	Siltstone and calciarenite	23.2	0.5	-5.4
T3-24	Siltstone and calciarenite	23.2	0.7	-6.0
T4-1	Basinal limestone	25.4	0.5	12.9
T4-2	Calcite from fthrust-related vein	25.9	-0.1	11.9
T4-3	Basinal limestone	25.5	-1.2	10.9
T4-4	Basinal limestone	25.5	-0.1	9.9
T4-5	Basinal limestone	24.1	0.2	8.9
T4-6	Basinal limestone	24.4	1.7	8.2
T4-7	Basinal limestone	24.5	1.6	7.5
T4-8	Basinal limestone	23.7	1.5	6.8
T4-9	Basinal limestone	23.5	1.3	6.3
T4-10	Calcite from fthrust-related vein	23.6	1.2	5.8
T4-11	Cataclasite	23.7	2.1	5.3
T4-12	Cataclasite	23.7	1.8	4.8
T4-13	Cataclasite	23.8	1.5	4.3
T4-14	Cataclasite	23.6	0.5	3.9
T4-15	Cataclasite	23.5	0.8	3.5
T4-16	Cataclasite	23.7	1.6	3.1
T4-17	Cataclasite	23.7	1.9	2.7
T4-18	Cataclasite	22.5	1.7	2.3
T4-19	Cataclasite	23.1	1.6	2.1
T4-20	Cataclasite	23.4	1.5	1.9
T4-21	Cataclasite	23.6	1.4	1.7
T4-22	Cataclasite	23.3	1.4	1.5
T4-23	Cataclasite	23.8	1.6	1.3
T4-24	Cataclasite	23.3	1.5	1.1
T4-25	Cataclasite	23.3	1.7	0.9
T4-26	Cataclasite	22.9	1.5	0.7
T4-27	Cataclasite	23.2	1.9	0.5
T4-28	Cataclasite	23.2	1.5	0.3
T4-29	Calcite from fthrust-related vein	23.2	2.0	0.1
T4-30	Siltstone and calciarenite	23.3	1.7	-0.1
T4-31	Calcite from fthrust-related vein	23.5	1.5	-0.5
T4-32	Calcite from fthrust-related vein	23.2	1.2	-1.0
T4-33	Siltstone and calciarenite	23.3	1.7	-1.5
T4-34	Calcite from fthrust-related vein	23.4	1.5	-2.0

Sample	Material analyzed	$\delta^{18}O$ SMOW	$\delta^{13}C$ VPDB	Dist. (m)
T1-1	Basinal limestone	23.2	0.2	20.0
T1-2	Basinal limestone	25.4	-1.7	19.0
T1-3	Basinal limestone	25.6	-3.3	16.0
T1-4	Basinal limestone	24.3	-3.2	14.0
T1-5	Basinal limestone	22.9	-5.6	12.0
T1-6	Basinal limestone	23.4	-2.8	10.0
T1-7	Basinal limestone	23.7	-3.3	8.0
T1-8	Microfractured mudstone	22.7	-1.2	6.0
T1-9	Cataclasite	20.0	-3.9	4.0
T1-10	Calcite megacrystals in vein	13.8	-3.1	2.0
T1-11	Calcite megacrystals in vein	11.5	-3.5	1.0
T1-12	Calcite megacrystals in vein	11.9	-4.0	0.8
T1-13	Calcite megacrystals in vein	11.7	-4.1	0.5
T1-14	Calcite megacrystals in vein	11.7	-3.6	0.3
T1-15	Calcite megacrystals in vein	12.0	-3.5	0.0
T1-16	Cataclasite	16.9	-0.5	-0.3
T1-17	Cataclasite	18.3	0.0	-0.5
T1-18	Sheared carbonate siltstone	16.9	0.0	-0.7
T1-19	Shaly limestone	19.8	-2.1	-1.0
T1-20	Shaly limestone	19.5	0.0	-2.0
T1-21	Shaly limestone	21.3	0.7	-3.0
T1-22	Shaly limestone	21.9	2.7	-5.0
T1-23	Shaly limestone	22.0	2.0	-7.0
T1-24	Shaly limestone	20.0	-0.3	-9.0
T1-25	Shaly limestone	21.3	0.7	-10.0
T2-1	Shaly limestone	22.0	-9.6	11.0
T2-2	Shaly limestone	21.6	-5.2	10.0
T2-3		20.8	-9.7	9.0
T2-4	Shaly limestone	21.2	-6.6	8.0
T2-5	Shaly limestone	21.0	-11.0	5.5
T2-6	Shaly limestone	21.5	-10.3	5.0
T2-7	Shaly limestone	20.9	-9.4	4.0
T2-8	Shaly limestone	21.7	-10.0	3.5
T2-9	Calcite from fthrust-related vein	20.3	-5.1	3.0
T2-10	Siltstone-calciarenite	21.1	-8.7	2.5
T2-11	Cataclasite	22.7	-22.8	2.3
T2-12	Cataclasite	21.6	-17.4	2.0
T2-13	Cataclasite	21.2	-9.5	1.8
T2-14	Cataclasite	20.1	-7.0	1.5
T2-15	Cataclasite	22.0	-13.0	1.0
T2-16	Cataclasite	23.5	-17.1	0.5
T2-17	Calcite from fthrust-related vein	15.7	-3.6	0.0
T2-18	Calcite from fthrust-related vein	10.9	-3.1	-0.5
T2-19	Calcite from fthrust-related vein	13.6	-3.5	-1.0
T2-20	Cataclasite	14.5	-4.3	-1.5
T2-21	Calcite from fthrust-related vein	24.1	-6.2	-2.0
T2-22	Calcite from fthrust-related vein	15.2	-4.6	-3.0
T2-23	Platformal limestone	25.2	-15.2	-4.0
T2-24	Platformal limestone	25.1	-13.2	-5.0
T2-25	Platformal limestone	24.3	-12.5	-6.0
T2-26	Platformal limestone	23.9	-14.2	-7.0
T2-27	Platformal limestone	24.8	-14.3	-8.0
T2-28	Platformal limestone	24.5	-15.0	-9.0
T3-1	Platformal limestone	23.7	0.4	14.0
T3-2	Platformal limestone	23.5	1.5	12.0

Sample	Material analyzed	$\delta^{18}O$ SMOW	$\delta^{13}C$ VPDB	Dist. (m)
T3-3	Platformal limestone	23.6	1.7	10.0
T3-4	Platformal limestone	24.0	1.1	7.0
T3-5	Platformal limestone	23.6	0.7	5.0
T3-6	Platformal limestone	23.4	1.4	3.0
T3-7	Calcite from fthrust-related vein	23.4	-1.5	1.6
T3-8	Cataclasite in platform limestone	22.8	2.0	1.2
T3-9	Calcite from fthrust-related vein	22.6	0.5	0.8
T3-10	Cataclasite	22.2	-4.6	0.7
T3-11	Cataclasite	22.3	-1.5	0.5
T3-12	Cataclasite	22.2	1.2	0.4
T3-13	Cataclasite	22.5	-3.4	0.3
T3-14	Cataclasite	22.7	-4.3	-0.2
T3-15	Calcite from fthrust-related vein	22.4	0.1	-0.6
T3-16	Cataclasite	22.0	-4.1	-0.8
T3-17	Calcite from fthrust-related vein	23.3	1.2	-1.2
T3-18	Siltstone and calciarenite	23.1	0.4	-1.8
T3-19	Siltstone and calciarenite	23.1	0.7	-2.2
T3-20	Siltstone and calciarenite	22.7	0.4	-2.8
T3-21	Siltstone and calciarenite	23.0	0.1	-3.8
T3-22	Siltstone and calciarenite	23.1	0.0	-4.8
T3-23	Siltstone and calciarenite	23.2	0.5	-5.4
T3-24	Siltstone and calciarenite	23.2	0.7	-6.0
T4-1	Basinal limestone	25.4	0.5	12.9
T4-2	Calcite from fthrust-related vein	25.9	-0.1	11.9
T4-3	Basinal limestone	25.5	-1.2	10.9
T4-4	Basinal limestone	25.5	-0.1	9.9
T4-5	Basinal limestone	24.1	0.2	8.9
T4-6	Basinal limestone	24.4	1.7	8.2
T4-7	Basinal limestone	24.5	1.6	7.5
T4-8	Basinal limestone	23.7	1.5	6.8
T4-9	Basinal limestone	23.5	1.3	6.3
T4-10	Calcite from fthrust-related vein	23.6	1.2	5.8
T4-11	Cataclasite	23.7	2.1	5.3
T4-12	Cataclasite	23.7	1.8	4.8
T4-13	Cataclasite	23.8	1.5	4.3
T4-14	Cataclasite	23.6	0.5	3.9
T4-15	Cataclasite	23.5	0.8	3.5
T4-16	Cataclasite	23.7	1.6	3.1
T4-17	Cataclasite	23.7	1.9	2.7
T4-18	Cataclasite	22.5	1.7	2.3
T4-19	Cataclasite	23.1	1.6	2.1
T4-20	Cataclasite	23.4	1.5	1.9
T4-21	Cataclasite	23.6	1.4	1.7
T4-22	Cataclasite	23.3	1.4	1.5
T4-23	Cataclasite	23.8	1.6	1.3
T4-24	Cataclasite	23.3	1.5	1.1
T4-25	Cataclasite	23.3	1.7	0.9
T4-26	Cataclasite	22.9	1.5	0.7
T4-27	Cataclasite	23.2	1.9	0.5
T4-28	Cataclasite	23.2	1.5	0.3
T4-29	Calcite from fthrust-related vein	23.2	2.0	0.1
T4-30	Siltstone and calciarenite	23.3	1.7	-0.1
T4-31	Calcite from fthrust-related vein	23.5	1.5	-0.5
T4-32	Calcite from fthrust-related vein	23.2	1.2	-1.0
T4-33	Siltstone and calciarenite	23.3	1.7	-1.5
T4-34	Calcite from fthrust-related vein	23.4	1.5	-2.0

Appendix 4-2

Sample	Material analyzed	$\delta^{18}O$ SMOW	$\delta^{13}C$ PDBB	δD SMOW	E-$\delta^{18}O$ SMOW
TMB1-R1	Basinal limestone	26.36	26.36		
TMB1-R2	Basinal limestone	25.93	25.93		
TMB1-R3	Basinal limestone	25.97	25.97		
TMB1-R4	Basinal limestone	26.15	26.15		
TMB1-R5	Basinal limestone	25.85	25.85		
TMB1-R6	Basinal limestone	26.26	26.26		
TMB1-ben1	Illite and Smectite from bentonite layers			-41.0	
TMB1-ben2	Illite and Smectite from bentonite layers			-44.0	
TMB1-V1a-1	Calcite from vein V1a	26.3	1.6		
TMB1-V1a-2	Calcite from vein V1a	26.0	2.1		
TMB1-V1a-3	Calcite from vein V1a	24.7	2.7		
TMB1-V1a-4	Calcite from vein V1a	25.5	2.6		
TMB1-V1a-5	Calcite from vein V1a	26.8	2.3		
CO_2 in fluid inclusions from calcite decrep. at 400°C				$\delta^{13}C$ =-34‰	
H_2O from fluid inclusions in calcite decrepitated at 400°C				-8.4	5±1
H_2O from fluid inclusions in cal. decrepitated at 400°C +HC				-11.2	5±1
H_2O from fluid inclusions in calcite step heated at 200°C				NF	
H_2O from fluid inclusions in calcite step heated at 300°C				-22.5	
H_2O from fluid inclusions in calcite step heated at 400°C				-0.6	
TMB1-V2-1	Calcite from vein V2	25.47	2.48	-31.5	
TMB1-V2-2	Calcite from vein V2	26.42	2.31		
TMB1-V2-3	Calcite from vein V2	26.21	2.52		
TMB1-V2-4	Calcite from vein V2	25.60	2.47		
H2O from fluid inclusions in calcite decrepitated at 400°C				-31.5	6±1
TMB1-V2-5	Calcite from vein V2	26.33	2.32		
TMB2-R1	Basinal limestone	26.62	4.03		
TMB2-R2	Basinal limestone	26.98	4.17		
TMB2-R3	Basinal limestone	26.62	4.16		
TMB2-R4	Basinal limestone	27.04	4.41		
TMB2-R5	Basinal limestone	26.71	4.08		
TMB2-R6	Basinal limestone	26.00	4.17		
TMB2-V1a-1	Calcite from vein V1a	26.49	3.85		
TMB2-V1a-2	Calcite from vein V1a	26.07	4.04		
TMB2-V1a-3	Calcite from vein V1a	26.93	4.33		
TMB2-V1a-4	Calcite from vein V1a	26.44	4.15		
TMB2-V1a-5	Calcite from vein V1a	26.54	3.97		
TMB2-V1a-6	Calcite from vein V1a	27.30	3.74		
TMB2-V2-1	Calcite from vein V2	26.97	4.15		
TMB2-V2-2	Calcite from vein V2	26.72	4.06		
TMB2-V2-3	Calcite from vein V2	26.40	4.02		
TMB2-V2-4	Calcite from vein V2	26.62	4.25		
TMB2-V2-5	Calcite from vein V2	27.24	3.97		
TMB2-V2-6	Calcite from vein V2	26.95	4.05		
TMB3-R1	Basinal limestone	25.31	1.95		
TMB3-R2	Basinal limestone	25.73	1.80		
TMB3-R3	Basinal limestone	24.52	1.63		
TMB3-R4	Basinal limestone	24.61	1.65		
TMB3-R5	Basinal limestone	24.93	1.54		
TMB3-V1a-1	Calcite from vein V1a	24.87	1.45		

Sample	Material analyzed	$\delta^{18}O$ SMOW	$\delta^{13}C$ PDBB	δD SMOW	E-$\delta^{18}O$ SMOW
TMB3-V1a-2	Calcite from vein V1a	25.08	1.85		
H_2O from fluid inclusions in calcite decrepitated at 400°C				-33.2	10±.5
TMB3-V1a-3	Calcite from vein V1a	24.62	1.55		
TMB3-V1a-4	Calcite from vein V1a	24.68	1.45		
TMB3-V1a-5	Calcite from vein V1a	24.65	1.50		
TMB3-V2-1	Calcite from vein V2	25.27	1.59		
TMB3-V2-2	Calcite from vein V2	24.99	1.43		
TMB3-V2-3	Calcite from vein V2	24.15	1.60		
TMB3-V2-4	Calcite from vein V2	23.52	1.82		
CO_2 in fluid inclusions from calcite decrep. at 400°C				$\delta^{13}C$ =-6‰	
H_2O from fluid inclusions in calcite decrepitated at 400°C				-36.75	9±.4
H_2O from fluid inclusions in cal. decrepitated at 400°C +HC				-43.54	9±.5
TMB3-V2-5	Calcite from vein V2	23.67	1.44		
TMB3-V2-6	Calcite from vein V2	24.91	1.84		
TMB4-R1	Basinal limestone	26.83	2.11		
TMB4-R2	Basinal limestone	26.91	2.17		
TMB4-R3	Basinal limestone	26.75	2.27		
TMB4-R4	Basinal limestone	27.31	2.13		
TMB4-R5	Basinal limestone	26.70	2.23		
TMB4-V1a-1	Calcite from vein V1a	26.28	2.26		
TMB4-V1a-2	Calcite from vein V1a	26.33	2.42		
TMB4-V1a-3	Calcite from vein V1a	26.47	2.45		
TMB4-V1a-4	Calcite from vein V1a	26.68	2.49		
TMB4-V1a-5	Calcite from vein V1a	25.93	2.41		
TMB4-V2-1	Calcite from vein V2	26.52	2.39		
TMB4-V2-2	Calcite from vein V2	26.37	2.51		
TMB4-V2-3	Calcite from vein V2	26.33	2.50		
TMB4-V2-4	Calcite from vein V2	26.16	2.46		
TMB4-V2-5	Calcite from vein V2	26.47	2.65		
TMB4-V2-6	Calcite from vein V2	26.29	2.41		
VP1-R1	Platformal limestone	25.14	2.29		
VP1-R2	Platformal limestone	26.86	3.58		
VP1-R3	Platformal limestone	26.33	2.17		
VP1-R4	Platformal limestone	27.65	4.01		
VP1-R5	Platformal limestone	28.40	4.47		
VP1-R6	Platformal limestone	26.93	3.00		
VP1-V1-1	Calcite from vein V1	22.69	-6.45		
VP1-V1-2	Calcite from vein V1	22.15	-4.75		
VP1-V1-3	Calcite from vein V1	25.81	0.26		
VP1-V1-4	Calcite from vein V1	22.17	-5.40		
VP1-V1-5	Calcite from vein V1	22.76	-7.85		
VP1-V2-1	Calcite from vein V2	23.46	1.94		
VP1-V2-2	Calcite from vein V2	22.28	-6.36		
VP1-V2-3	Calcite from vein V3	23.00	-5.31		
VP1-V2-4	Calcite from vein V4	20.89	-2.74		
VP1-V2-5	Calcite from vein V5	22.70	-5.92		
VP1-V2-6	Calcite from vein V6	20.60	1.61		
ZB1-R1	Basinal limestone	26.52	0.83		

Sample	Material analyzed	$\delta^{18}O$ SMOW	$\delta^{13}C$ PDBB	δD SMOW	E-$\delta^{18}O$ SMOW
ZB1-R2	Basinal limestone	26.54	0.85		
ZB1-R3	Basinal limestone	26.49	1.01		
ZB1-R4	Basinal limestone	26.84	1.52		
ZB1-R5	Basinal limestone	26.75	1.27		
ZB1-R6	Basinal limestone	26.44	0.92		
ZB1-V1a-1	Calcite from vein V1a	25.72	3.95		
H_2O from fluid inclusions in calcite step heated at 200°C				-61.4	
H_2O from fluid inclusions in calcite step heated at 300°C				-58.4	
H_2O from fluid inclusions in calcite step heated at 400°C				-57.0	
H_2O from fluid inclusions in quartz decrepitated at 400°C				-61.5	
H_2O from fluid inclusions in quartz step heated at 200°C				NFI	
H_2O from fluid inclusions in quartz step heated at 300°C				-57.4	
H_2O from fluid inclusions in quartz step heated at 400°C				-60.6	
H_2O from fluid inclusions in quartz step heated at 500°C				-59.8	
H_2O from fluid inclusions in quartz step heated at 600°C				-56.8	
ZB1-V1a-3	Calcite from vein V1a	25.8	4.3		
ZB1-V1a-4	Calcite from vein V1a	25.9	4.2		
ZB1-V1a-5	Calcite from vein V1a	25.8	3.6		
ZB1-V2-1	Calcite from vein V2	26.7	1.4		
ZB1-V2-2	Calcite from vein V2	26.7	1.2		
ZB1-V2-3	Calcite from vein V2	26.9	1.2		
ZB1-V2-4	Calcite from vein V2	26.9	1.3		
ZB1-V2-5	Calcite from vein V2	26.9	1.5		
H_2O from fluid inclusions in calcite decrepitated at 400°C				-41.91	18±1
ZB1-V3-1		26.2	3.9		
ZB1-V3-2		26.4	4.2		
ZB1-V3-3		26.4	4.4		
H_2O from fluid inclusions in calcite decrepitated at 400°C				-59.83	5.6±0.5
ZB1-V3-4		26.6	4.5		
H_2O from fluid inclusions in calcite decrepitated at 400°C				-70.38	5.9±0.5

ZB2-R1	Basinal limestone	24.99	4.10		
ZB2-R2	Basinal limestone	25.17	4.19		
ZB2-R3	Basinal limestone	25.79	4.38		
ZB2-R4	Basinal limestone	25.58	4.17		
ZB2-R5	Basinal limestone	25.49	3.96		
ZB2-R6	Basinal limestone	25.36	3.99		
ZB2-Ben1	Illite and Smectite from bentonite layers			-44.0	
ZB2-Ben2	Illite and Smectite from bentonite layers			-48.0	
ZB2-Ben3	Illite and Smectite from bentonite layers			-47.0	
ZB2-V1a-1	Calcite from vein V1	25.72	3.99		
H_2O from fluid inclusions in calcite decrepitated at 400°C				-44.11	17±0.5
ZB2-V1a-2	Calcite from vein V1a	25.51	4.03		
ZB2-V1a-3	Calcite from vein V1a	25.61	4.25		
ZB2-V1a-4	Calcite from vein V1a	25.60	3.69		
ZB2-V1a-5	Calcite from vein V1a	25.26	3.54		
ZB2-V1a-6	Calcite from vein V1a	25.97	4.23		
ZB2-V2a-1	Calcite from vein V2a	25.73	3.77		
ZB2-V2a-2	Calcite from vein V2a	25.71	3.21		
ZB2-V2a-3	Calcite from vein V2a	25.84	3.46		
ZB2-V2a-4	Calcite from vein V2a	26.00	4.03		

Sample	Material analyzed	$\delta^{18}O$ SMOW	$\delta^{13}C$ PDBB	δD SMOW	E-$\delta^{18}O$ SMOW
ZB2-V2a-5	Calcite from vein V2a	25.92	3.62		
H_2O from fluid inclusions in calcite decrepitated at 400°C				-43.25	18.2±2
ZB2-V2b-1	Calcite from vein V2b	25.70	3.46		
ZB2-V2b-2	Calcite from vein V2b	25.93	3.67		
ZB2-V2b-3	Calcite from vein V2b	25.32	3.29		
ZB2-V2b-4	Calcite from vein V2b	25.51	2.85		
ZB2-V2b-5	Calcite from vein V2b	25.62	3.41		
H_2O from fluid inclusions in calcite decrepitated at 400°C				-45.3	18±2
H_2O from fluid inclusions in quartz decrepitated at 400°C				-52.1	
ZB2-V2b-6	Calcite from vein V2b	25.75	3.86		

ZB3-R1	Basinal limestone	26.42	3.35		
ZB3-R2	Basinal limestone	26.02	2.94		
ZB3-R3	Basinal limestone	26.31	3.17		
ZB3-R4	Basinal limestone	26.31	3.20		
ZB3-R5	Basinal limestone	25.77	3.40		
ZB3-B1	Illite and Smectite from bentonite layers			-53.0	
ZB3-B2	Illite and Smectite from bentonite layers			-49.0	
ZB3-B3	Illite and Smectite from bentonite layers			-49.0	
ZB3-V1a-1	Calcite from vein V1a	26.46	3.39		
H_2O from fluid inclusions in calcite decrepitated at 400°C				-48.2	18±2
H_2O from fluid inclusions in quartz decrepitated at 400°C				-62.5	
ZB3-V1a-2	Calcite from vein V1a	26.72	3.46		
ZB3-V1a-3	Calcite from vein V1a	25.88	3.21		
ZB3-V1a-4	Calcite from vein V1a	25.63	2.82		
ZB3-V1a-5	Calcite from vein V1a	26.77	3.35		
ZB3-V1a-6	Calcite from vein V1a	25.60	3.26		
ZB3-V2a-1	Calcite from vein V2a	26.30	2.87		
ZB3-V2a-2	Calcite from vein V2a	26.43	3.15		
ZB3-V2a-3	Calcite from vein V2a	26.41	3.30		
ZB3-V2a-4	Calcite from vein V2a	26.62	3.15		
H_2O from fluid inclusions in calcite step heated at 200°C				-57.3	
H_2O from fluid inclusions in calcite step heated at 300°C				-44.6	
H_2O from fluid inclusions in calcite step heated at 400°C				-42.8	18.8±2
H_2O from fluid inclusions in quartzz heated at 200&300°C				NF	
H_2O from fluid inclusions in quartz step heated at 400°C				-59.5	
H_2O from fluid inclusions in quartz step heated at 600°C				44.2	17.7±1
ZB3-V2a-5	Calcite from vein V2a	26.03	3.98		
ZB3-V2a-6	Calcite from vein V2a	26.12	3.18		
ZB3-V2b-1	Calcite from vein V2b	26.44	3.45		
ZB3-V2b-2	Calcite from vein V2b	25.80	3.47		
ZB3-V2b-3	Calcite from vein V2b	26.22	3.55		
ZB3-V2b-4	Calcite from vein V2b	26.22	3.10		
H_2O from fluid inclusions in calcite decrepitated at 400°C				-46.1	18.6±2
H_2O from fluid inclusions in calcite step heated at 200°C				-61.9	
H_2O from fluid inclusions in calcite step heated at 300°C				-45.4	
H_2O from fluid inclusions in calcite step heated at 400°C				-41.8	
ZB3-V2b-5	Calcite from vein V2b	26.21	4.12		
H_2O from fluid inclusions in calcite decrepitated at 400°C				40.1	18.4±2
H_2O from fluid inclusions in calcite step heated at 200°C				NFI	
H_2O from fluid inclusions in calcite step heated at 300°C				-43.5	

Sample	Material analyzed	$\delta^{18}O$ SMOW	$\delta^{13}C$ PDBB	δD SMOW	E-$\delta^{18}O$ SMOW
H_2O from fluid inclusions in calcite step heated at 400°C				NFI	
ZB3-V3-1	Calcite from vein V3	25.92	4.15		
ZB3-V3-2	Calcite from vein V3	25.61	4.21		
ZB3-V3-3	Calcite from vein V3	25.65	4.11		
ZB3-V3-4	Calcite from vein V3	25.75	4.01		
ZB3-V3-5	Calcite from vein V3	25.41	3.47		
ZB4-R1	Basinal limestone	25.42	1.04		
ZB4-R2	Basinal limestone	24.21	0.73		
ZB4-R3	Basinal limestone	25.86	0.86		
ZB4-R4	Basinal limestone	24.71	0.46		
ZB4-R5	Basinal limestone	25.72	0.72		
ZB4-B1	Illite and Smectite from bentonite layers			-64.0	
ZB4-B2	Illite and Smectite from bentonite layers			-72.0	
ZB4-B3	Illite and Smectite from bentonite layers			-69.0	
ZB4-V1a-1	Basinal limestone	25.93	0.67		
ZB4-V1a-2	Calcite from vein V1	25.64	0.56		
ZB4-V1a-3	Calcite from vein V1	25.54	-0.49		
ZB4-V1a-4	Calcite from vein V1	25.83	1.29		
ZB4-V1a-5	Calcite from vein V1	24.65	0.44		
ZB4-V2-1	Calcite from vein V2	26.31	1.65		
ZB4-V2-2	Calcite from vein V2	25.96	1.76		
ZB4-V2-3	Calcite from vein V2	26.03	1.87		
ZB4-V2-4	Calcite from vein V2	26.05	0.37		
ZB4-V2-5	Calcite from vein V2	26.15	0.69		
ZB4-V2-6	Calcite from vein V2	25.70	-0.03		
ZB4-V2-7	Calcite from vein V2	26.19	0.69		
ZB4-V2-8	Calcite from vein V2	25.90	0.81		
ZB3-V3-4	Calcite from vein V3	25.75	4.01		
ZB3-V3-5	Calcite from vein V3	25.41	3.47		
ZB4-V3-1	Calcite from vein V3	19.23	-2.14		
ZB4-V3-2	Calcite from vein V3	19.05	-0.59		

E-$\delta^{18}O$ SMOW	Estimated $\delta^{18}O$ in fluid inclusions assuming equilibrium conditions with the host mineral and equations by O'Neil *et al.* (1969) and Zheng (1994) and using the $\delta^{18}O$ values analyzed in the host mineral (calcite) and temperature of deformation for each locality

Sample	Material analyzed	$\delta^{18}O$ SMOW	$\delta^{13}C$ PDBB	δD SMOW	E-$\delta^{18}O$ SMOW
ZB4-V3-3	Calcite from vein V3	25.41	-0.96		
ZB4-V3-4	Calcite from vein V3	17.55	-1.39		
ZB4-V3-5	Calcite from vein V3	22.53	-5.38		
DP1-R1	Platformal limestone	24.78	0.14		
DP1-R2	Platformal limestone	25.69	2.21		
DP1-R3	Platformal limestone	25.91	-0.30		
DP1-R4	Platformal limestone	25.53	-1.31		
DP1-R5	Platformal limestone	23.70	-0.44		
DP1-V1a-1	Calcite from veins V1a	24.53	-1.84		
DP1-V1a-2	Calcite from veins V1a	25.94	0.62		
H_2O from fluid inclusions in calcite decrepitated at 400°C				-57.0	18.1±2
DP1-V1a-3	Calcite from veins V1a	22.96	1.54		
DP1-V1a-4	Calcite from veins V1a	25.28	0.00		
DP1-V1a-5	Calcite from veins V1a	25.41	-2.04		
DP1-V1a-6	Calcite from veins V1a	25.59	-0.52		
DP1-V1a-7	Calcite from veins V1a	25.95	-1.89		
DP1-V1a-8	Calcite from veins V1a	25.31	-2.08		
DP1-V2a-1	Calcite from vein V2	24.56	0.53		
H_2O from fluid inclusions in calcite decrepitated at 400°C				-58.69	18.2±2
DP1-V2a-2	Calcite from vein V2	25.20	0.41		
DP1-V2a-3	Calcite from vein V2	26.21	0.70		
DP1-V2a-4	Calcite from vein V2	25.63	0.03		
DP1-V2a-5	Calcite from vein V2	25.62	0.17		
DP1-V2a-6	Calcite from vein V2	25.30	-0.12		
DP1-V2b-1	Calcite from vein V2	25.51	0.05		
DP1-V2b-2	Calcite from vein V2	25.46	-0.30		
DP1-V2b-3	Calcite from vein V2	25.70	-0.02		
DP1-V2b-4	Calcite from vein V2	25.59	0.11		
DP1-V2b-5	Calcite from vein V2	25.11	-0.13		
DP1-V2b-6	Calcite from vein V2	25.56	0.25		
DP1-V3-1	Calcite from vein V3	15.72	-1.47		
DP1-V3-2	Calcite from vein V3	14.22	-2.35		
DP1-V3-3	Calcite from vein V3	16.56	-2.92		
DP1-V3-4	Calcite from vein V3	16.16	-2.74		
DP1-V3-5	Calcite from vein V3	15.73	-2.05		
DP1-V3-6	Calcite from vein V3	15.08	-1.45		